UNIVERSITE D'ORLEANS

ÉCOLE DOCTORALE SCIENCES ET TECHNOLOGIES
Laboratoire PRISME

THÈSE présentée par :

Jianxi ZHOU

Soutenue le :
Pour obtenir le grade de : **Docteur de l'université d'Orléans**
Discipline : Mécanique et Energétique

Etude de l'effet du taux d'oxygène sur la combustion en moteur à allumage commandé suralimenté

THÈSE dirigée par :

Mme Christine MOUNAÏM-ROUSSELLE Professeur, Université d'Orléans
M Fabrice FOUCHER Maitre de Conférences, Université d'Orléans

RAPPORTEURS :

M. Marc BELLENOUE	Professeur ENSMA Poitiers
M. Bernard LEDUC	Professeur université libre de Bruxelles

JURY :

M. Marc BELLENOUE	Professeur, ENSMA Poitiers
M. Bernard LEDUC	Professeur, Université Libre de Bruxelles
M. Guillaume DAYMA	Professeur, Université d'Orléans
M. Gilles CABOT	Maître de Conférences, HdR, Université de Rouen
M. Erwann SANSON	Ingénieur de Recherche, PSA Peugeot Citroën
Mme. C. MOUNAÏM-ROUSSELLE	Professeur, Université d'Orléans
M. Fabrice FOUCHER	Maître de Conférences, HdR, Université d'Orléans

Remerciements

Cette thèse, cofinancée par la région Centre et PSA Peugeot Citroën, a été réalisée au sein de l'équipe Energie, Combustion et Moteur du laboratoire PRISME (Pluridisciplinaire de Recherche Ingénierie des Systèmes Mécanique, Energétique) de l'université d'Orléans.

Je tiens tout abord à remercier Christine Mounaïm-Rousselle, qui a dirigé cette étude, de m'avoir accueilli au sein de son équipe, de m'avoir donné l'opportunité de réaliser ce travail de thèse et de m'avoir soutenu au cours de cette thèse.

Je tiens à exprimer ma profonde reconnaissance à Fabrice Foucher, qui a codirigé cette thèse, pour son excellent encadrement, sa disponibilité, sa confiance et son soutien. Je le remercie aussi pour les agréables moments en dehors du laboratoire (Congrès, Ski …).

Je remercie Erwann Samson, ingénieur recherche du groupe PSA Peugeot Citroën, pour avoir soutenu ce projet et pour les discussions scientifiques et ses précieux conseils.

Je tiens à remercier Stéphane Richard, ingénieur recherche d'IFP Energies Nouvelles, pour les discussions et son aide sur la partie simulation LMS Amesim.

Je tiens à remercier également tous les membres de jury qui ont accepté de juger ma thèse: B. Leduc, M. Bellenoue, G. Dayma, G. Cabot, E. Sanson et tout particulièrement les deux rapporteurs, B. Leduc et M. Bellenoue pour avoir accepté d'examiner le mémoire.

Je souhaiterais ensuite exprimer tout ma reconnaissance pour tous les membres des équipes techniques et administratives du laboratoire pour leur aide précieuse à ce travail : Sylvie Plessard, Nicolas Dumuis, Yahia Haidous, Benoit Bellicaud, Benoit Clavier et Pierre. Je souhaiterais exprimer ma grand merci à Bruno Moreau et Julien Lemaire, avec qui j'ai appris sur la conception et la mise en place des dispositifs expérimentaux, surtout, durant les moments difficiles, moteur cassé, problème de baies d'analyse de gaz ...

Je voudrais aussi dire mon profond merci à tous les amis et collègues: Jérémie, Toni, les deux excellents amis et collègues dans le même bureau au début de ma thèse, grâce à eux, je me suis initié aux connaissances du moteur. Guillaume, J-B, Pierre, Padipan, Antonio, Shadi, Benedicte, Etienne, Mathieu, les amis et collègues dans même bureau de 'open space'. Je tiens aussi à exprimer mon merci à tous les amis dans le labo PRISME : Christophe, Chao, Jamil, Haïfa, Yan-Aël, Amine, Audrey, Arnaud, comme compagnons de tous les jours, pour les discussions, les cafés, les soirées et les autres sorties.

Je souhaiterais aussi encore remercier à les amis dans le labo Coria (où j'ai fait deux stages), François-Xavier, mon encadrant, qui m'appris les outils numériques et notion de programmations. François, Guillaume, Jieshen, Jérémie, Arnaud, Bruno, pour les discussions et les soirées poker et foot.

Je voudrais finir par remercier toute ma famille, tout particulièrement mes parents qui m'ont permis de poursuivre mes études par leur soutien moral et financier. Et ma femme Suli, merci pour les soutiens des moments difficiles, et merci pour m'avoir donné le plus beau cadeau, mon fils.

Table of contents

Introduction générale 17

1 Chapter 1 General study of bibliography 23

1.1 Actual emission problems and fuel economy 24

1.2 Introduction to SI engine and its new technologies 25

1.3 Normal Combustion in SI engine 28

1.3.1 Laminar premixed combustion 28

1.3.2 Turbulent premixed combustion 31

1.4 Abnormal combustion 35

1.4.1 Pre-ignition 36

1.4.2 Engine knock 36

1.5 Application of Oxygen-Controlled combustion in downsized SI engine 38

2 Study of oxygen controlled combustion in engine 45

2.1 Introduction 45

2.2 Experimental setup 45

2.2.1 Engine characteristics 45

2.2.2 Engine control and measurement 47

2.3 Combustion analysis 47

2.3.1 Single zone analysis model 47

2.4 Emission analysis 49

2.4.1 Converting humid gas type to dry gas type 49

2.4.2 Equivalence ratio of 5 gases 50

2.5 Operating conditions and engine parameters 52

2.6 Results and discussion 55

2.6.1 Indicated mean effective pressure 55

2.6.2 HC emissions 58

2.6.3 NO_x emissions 60

2.6.4 CO emissions 62

2.6.5 CO_2 emissions 64

2.6.6 Combustion characteristics 66

2.7 Conclusions 67

3 Characteristics parameters of combustion for oxygen-controlled fuel mixture 71
3.1.1 Laminar burning velocity 71
3.1.2 Correlations of laminar burning velocity 75
3.2 Experimental set-up 78
3.3 Methodology to analyze flame propagation 80
3.3.1 Laminar burning velocity determination 80
3.3.2 Markstein Length 82
3.4 Validation of the methodologies: case of iso-octane/air mixture. 83
3.5 Results and discussion 84
3.5.1 Effect of oxygen enrichment 84
3.5.2 Effect of CO_2 addition 85
3.5.3 Effect of O_2 and CO_2 on adiabatic flame temperature 86
3.5.4 Markstein lengths 87
3.5.5 Experimental correlation for laminar burning velocity 89
3.6 Conclusions 89
3.7 Data avalaible : 90
3.8 Auto-ignition delay of Isooctane/O_2/N_2/CO_2 mixtures 91
3.9 Conclusions 94
4 Combustion modeling 97
4.1 Introduction 97
4.2 Combustion modeling using Amesim 98
4.2.1 Energy conservation equations 98
4.2.2 Combustion heat release 99
4.2.3 Tabulation of the mean flame surface $\boldsymbol{Sm}$ 100
4.2.4 Flame wrinkling 101
4.2.5 Knock modeling 101
4.2.6 Knock intensity estimation 103
4.3 Adaptation of Amesim model for oxygen controlling engine 104
4.3.1 Laminar flame speed correlation 105
4.4 Calibration process 106
4.5 Amesim model results 108
4.5.1 Validation of pure compression cycle 108
4.5.2 Studied cases 109

4.5.3 Calibration of in-cylinder pressure 111
4.5.4 Combustion characteristics 118
Effect of O_2 percentage on combustion characteristics 118
Effect of equivalence ratio on combustion characteristics 123
Effect of IMEP on combustion characteristics 125
Parametric study of combustion characteristics 127
4.5.5 Knock estimation and sensitivities 132
4.6 Conclusions 138
5 Conclusions and perspectives 141
Conclusions et perspectives (version français) 144
6 ANNEXES 154
Engine efficiencies and energy losses 156
Engine puissance, specific fuel consummation and mean pressure indicators 157

List of figures

Figure 1-1. Evolution of mean CO2 emission value for new cars in Europe 25
Figure 1-2 the structure of a SI engine with turbo-compressor.....26
Figure 1-3 diagrams for illustrating engine efficiency 26
Figure 1-4. mechanism of a laminar premixed combustion.....29
Figure 1-5. Structure of a laminar premixed combustion.....29
Figure 1-6. the structure of energy cascade (Bougrine 2012).....31
Figure 1-7. Peters-Borghi Diagram of combustion regime (Borghi et al. 1984) 34
Figure 1-8. Cylinder pressure curves for normal and abnormal combustion (Winklhofer 2009) 35
Figure 1-9. Time-series of high speed direct combustion images with the H_2-O_2-Ar mixture (equivalence ration=1.0, P0=40kPa, T0=323K, θ_i = 355 deg and knock intensity KI = 1.173Mpa)(Kawahara 2009).....37
Figure 1-10. Comparison of current EGR dilution system (left), oxygen controlled by membranes (middle) and oxygen controlled with CO_2 dilution (right). 39
Figure 1-11. effects of equivalence ratio ϕ on CSI, η_i ,IMEP (left) and CO, HC, NOx emissions (right).....40
Figure 2-1. Scheme of EP6 mono-cylinder engine 46
Figure 2-2. Real Image of engine.....46
Figure 2-3. Equivalence between N2 dilution (O2 < 20.9%) or O2 enrichment (O2 > 20.9%) and EGR percentage for a fixed equivalence ratio 54
Figure 2-4. Presentation of the different operation points employed in engine test bench 55
Figure 2-5. the evolution of indicated specific fuel consummation (SFC) versus equivalence ratio with different IMEP (a. IMEP=400kPa, b. IMEP=600kPa, c. IMEP=800kPa, d. IMEP=1000kPa) 57
*Figure 2-6. the evolution of indicated specific HC emissions versus equivalence ratio with different IMEP (a. IMEP=400kPa, b. IMEP=600kPa, c. IMEP=800kPa, d. IMEP=1000kPa)*59
*Figure 2-7. the evolution of indicated specific NOx emissions versus equivalence ratio with different IMEP (a. IMEP=400kPa, b. IMEP=600kPa, c. IMEP=800kPa, d. IMEP=1000kPa)*61
Figure 2-8. Evolutions of the indicated specific NO_x emission versus O_2 percentage with different Indicated mean pressure at stoichiometry 62
Figure 2-9. Evolutions of the indicated specific NOx emission versus exhaust temperature with different Indicated mean pressure at stoichiometry 62
*Figure 2-10. the evolution of indicated specific CO emissions versus equivalence ratio with different IMEP (a. IMEP=400kPa, b. IMEP=600kPa, c. IMEP=800kPa, d. IMEP=1000kPa)*64
*Figure 2-11. the evolution of indicated specific CO_2 emissions versus equivalence ratio with different IMEP (a. IMEP=400kPa, b. IMEP=600kPa, c. IMEP=800kPa, d. IMEP=1000kPa)*66
Figure 2-12. combustion characteristics for three different cases(a. $\phi = 1$, IMEP 10 bar, b. 21% O2, IMEP =10 bar, c. $\phi = 1$, 21% O2) 67
Figure 3-1. description of the structure of spherically expanding laminar flame front 72
Figure 3-2. Scheme of the experimental setup (Zhou et al. 2011) 80

Figure 3-3. Example of the flame front at 9ms, 15ms and 21ms after start of ignition. 80
Figure 3-4. Flame radius as a function of time for different experimental condition 81
Figure 3-5. Unstretched propagation flame speed determination for different experimental conditions. Square symbol: experimental velocity as function of flame stretch. Continuous lines: linear methodology. Dashed line: nonlinear methodology. 82
Figure 3-6. Experimental laminar burning velocities of isooctane-air mixture at two initial temperatures (300 K and 400 K).Comparation with previous studies in the literature(Davis et al. 1998) (Huang et al. 2004) (Freeh et al. 2004; Kumar et al. 2007) (Bradley et al. 1998; Halter et al. 2010). 83
Figure 3-7. Markstein length versus the equivalence ratio for isooctane mixture. Comparison with previous studies (Bradley et al. 1998; Halter et al. 2010). 84
Figure 3-8. Laminar burning velocities as function of the amount of oxygen in air-isooctane mixture for 3 equivalence ratios (Tini = 373 K, Pini = 1 atm). 85
Figure 3-9. Laminar burning velocities versus O2 and CO2 percentage at stoichiometric equivalence ratio (Tini = 373 K, Pini = 1 atm). 86
Figure 3-10. Simulated adiabatic flame temperature versus O2 (7a) and CO2 (7b) percentage at stoichiometric equivalence ratio (Tini = 373 K, Pini = 1 atm). 87
Figure 3-11. Laminar flame velocity as a function of the adiabatic temperature 87
Figure 3-12. Markstein length evolution versus O2 (a) and CO2 (b) percentage for 3 different cases (Tini = 373 K, Pini = 1 atm) 88
Figure 3-13. Comparison between estimated values (dotted lines) and experimental data for various CO_2 and O_2 percentages. 89
Figure 3-14. Ignition delays versus O_2 and CO_2 percentage for stoichiometric iso-octane/O_2/N_2/CO2 mixture with 1000/T=1.5 (1/K), P=20 bar. Comparison between simulation data and correlation results. 92
Figure 3-15. Ignition delays versus pressure for iso-octane/O_2/CO_2/N_2 mixture (with 20% CO_2, 21% O2 and T = 666 K).....93
Figure 3-16. Ignition delays versus temperature for iso-octane/O_2/CO_2/N_2 mixture (with 20% CO_2, 21% O2 and P=60 bar).....93
Figure 4-1. Evolution of mean flame surface –based on real configuration 100
Figure 4-2. Example of knock crank angle θk with spark advance before and after top dead center (red line: an example of in-cylinder pressure at 10 bar IMEP and 27%O_2, black line: supposed pressure).....104
Figure 4-3. Amesim model for oxygen controlling engine.....105
Figure 4-4. illustration of simulation process.....107
Figure 4-5. Validation of pure compression process. From bottom to up, the intake pressures are from 6 bars to 16 bars with the steps of 2 bars.....109
Figure 4-6. Presentation of the different operation points employed in engine test bench and the Amesim combustion model calibration process (1400 rpm). 109
Figure 4-7. Intake pressure(a) and spark advance (b) versus equivalence ratio for different cases of O_2 percentages.....111
Figure 4-8. Fuel mass flow rate versus equivalence ratio for different cases of O_2 percentages 111

Figure 4-9. Comparison between experimental and simulated cylinder pressure curve for different engine load at 1400 rpm. 113
Figure 4-10. Comparison between experimental and simulated cylinder pressure curve for different equivalence ratio at 1400 rpm. 113
Figure 4-11. Relative error of IMEP (a) and maximum in-cylinder pressure (b) as function of IMEP. 114
Figure 4-12. Relative error of IMEP (a) and maximum in-cylinder pressure (b) as function of equivalence ratio. 114
Figure 4-13. Relative error of IMEP (a) and maximum in-cylinder pressure (b) as function of O_2 precentage. 115
Figure 4-14. integral length scales and tumble values obtained by optimizing the in-cylinder pressure. 116
Figure 4-15. integral length scales and tumble values obtained by optimizing the in-cylinder pressure at IMEP=10 bar. 116
Figure 4-16. integral length scales and tumble values obtained by optimizing the in-cylinder pressure at unit equivalence ratio. 117
Figure 4-17. integral length scales (a) and tumble values (b) versus intake pressure for IMEP at 10 bar. 118
Figure 4-18. Evolution of the mean in-cylinder pressure at stoichiometric and IMEP=1000kPa 119
Figure 4-19. Laminar burning velocity versus crank angle degree with different O_2 percentages at stoichiometric and IMEP=1000kPa 119
Figure 4-20. Flame surface (a) and flame wrinkling (b) versus Crank angle with different O_2 percentages at unit equivalence ratio and IMEP=1000kPa 120
Figure 4-21. Evolution of turbulent flame velocity with different O_2 percentages at stoichiometric equivalence ratio and IMEP=1000kPa 121
Figure 4-22. Ratio of the characteristic length and velocity scales versus crank angle degree for different O2 percentages. 121
Figure 4-23. Ratio of the characteristic length and velocity scales versus O_2 percentage for two crank angle degree cases 122
Figure 4-24. Comparison of the combustion traces in the Peters-Borghi diagram for different O_2 percentages 123
Figure 4-25. Operating conditions for combustion analysis 124
Figure 4-26. Ratio of the characteristic length and velocity scales versus crank angle degree for different equivalence ratios. 124
Figure 4-27. Ratio of the characteristic length and velocity scales versus equivalence ratio for two crank angle degree cases 124
Figure 4-28. Comparison of the combustion traces in the Peters-Borghi diagram for different equivalence ratios at IMEP=10 bar 125
Figure 4-29. Operating conditions of different IMEP for combustion analysis 125
Figure 4-30. Ratio of the characteristic length and velocity scales versus crank angle degree for different IMEP. 126
Figure 4-31. Ratio of the characteristic length and velocity scales versus IMEP for two crank angle degree cases 126

Figure 4-32. Comparison of the combustion traces in the Peters-Borghi diagram for different equivalence ratios 127
Figure 4-33. Evolution of in-cylinder pressure varying laminar flame speed with two different cases of equivalence ratio at IMEP=10bar 128
Figure 4-34. evolution of in-cylinder pressure varying spark ignition advance for three different cases of O2 percentage at IMEP=10bar and stoichiometric equivalence ratio (X=1, 2, 3)......130
Figure 4-35. Evolution of in-cylinder pressure varying the intake temperature for three different cases of O_2 percentage at IMEP=10bar and stoichiometric equivalence ratio (X=1, 2, 3).....131
Figure 4-36. Laminar burning velocity versus crank angle for two different cases. Left: variation of spark advance, Right: variation of intake temperature.....132
Figure 4-37. Behavior of spark advance (left) and intake temperature (right) in Peters-Borghi diagram. 132
Figure 4-38. Examples of absolute (left hand) and high-passed filtered with 4 kHz cut-off frequency (right hand) cylinder pressure traces at IMEP 10 bar and $\phi = 1$......134
Figure 4-39. High-passed filtered cylinder pressure traces for 100 consecutive cycles at IMEP 10 bar and $\phi = 1$. 135
Figure 4-40. Absolute values of experimental indicators (left) and normalized MAPO, IMPO, simulated KI (right) versus O_2 percentage.....136
Figure 4-41. Evolution of knock intensity (KI) by varying laminar flame speed and auto-ignition delay.....137
Figure 4-42. Evolution of knock intensity (KI) by varying spark advance with adv= Adv_{ref} $+\Delta CA$.....138
Figure 4-43. Evolution of knock intensity (KI) by varying intake temperature with T_{intake}= $T_{intake,ref} + \Delta T_{intake}$.....138
Figure 6-1. An example of Clapeyron diagram with operating conditions as: engine speed 1400 rpm, Pintake = 0.6 bar, Spark advance = 21 CAD.....155

List of tables

Table 1-1. European anti-pollution standards (in g/km) for gasoline engine cars (http://en.wikipedia.org/wiki/European_emission_standards). 24
Table 1-2. Engine parameters influencing knock tendency.(Ferguson 1986) 38
Table 2-1. determination of the volume fraction of air, O2 and N2 for different cases. 52
Table 2-2. Equivalence between N2 dilution (O2 < 20.9%) or O2 enrichment (O2 > 20.9%) and EGR percentage for a fixed equivalence ratio. 54
Table 3-1. values of the constants $b1, b2, b3$ *for different dilution at stoichiometric condition.* 78
Table 3-2. values of the constants αT *and* βP *for different equivalence ratios.* 78
Table 3-3. A summary of various experimental conditions for isooctane ignition delay test (Scott 2009) 91
Table 4-1. Correlation parameters in laminar flame speed correlation. 106
Table 4-2. Operation conditions of engine bench tests at 10 IMEP 110
Table 4-3. Operating conditions for combustion analysis 119

Nomenclature

Latins Symboles

A_L	laminar flame surface	m^2
A_T	turbulent flame surface	m^2
c	progress variable of combustion	-
C	constant coefficient	-
CAxx	Crank angle degree when xx% of fresh air/fuel mixture is burned	CAD
C_p	specific heat coefficient at constant pressure	-
C_v	specific heat coefficient at constant volume	-
Da	Damköhler number	-
D_{th}^u	heat diffusivity of fresh gases	$m^2.s^{-1}$
E	energy spectrum	J
h	mass enthalpy	J/kg
k	turbulent kinetic energy	$m^2.s^{-2}$
K	total stretch rate	1/s
Ka	Karlovitz number	-
l	size of eddies	m
L_b	burned gas Markstein length	m
Le	Lewis numbers	-
Le_D	Lewis numbers of the deficient	-
Le_E	Lewis numbers of the excess	-
l_t	turbulent integral length scale	m
m	Mass	kg
n	constant coefficient	-
N_{eng}	engine rotation speed	rpm^{-1}
P	pressure	pa
PCI	heating value of fuel	J/kg
q'	turbulent intensity	m/s
Q_c	heat produced by combustion	J
Q_p	wall heat loss	J
r	Flame rayon	m
Re	Reynolds number	-
S_c	Schmidt number	-
S_L	laminar flame speed	m/s
S_m	mean flame surface	m^2
S_t	turbulent flame surface	m^2
t	time	s
T	temperature	K
T_c	chemical time scales	s
T_t	characteristic time of turbulent	s
u', v', w'	velocity fluctuations	m/s
V	volume, volume fraction	m^3
V_n	stretched propagation flame velocity	m/s
V_n^0	unstretched propagation flame velocity	m/s
W	work applies to piston, molecular weight	J
X	mass fraction	-

x, y, z	spatial coordinate	m
Y	mass fraction	-

Grecs Symboles

α	constant coefficient	-
θ	Crank angle degree	CAD
δ	Flame thickness, characteristic thermal thickness	m
γ	isentropic coefficient	-
ϕ	equivalence ratio	-
Δ	variation	-
$\Delta\theta_c$	Crank angle duration of combustion	CAD
$\Delta\theta_\mathrm{d}$	Crank angle duration of initial flame development	CAD
$\Delta\theta_\mathrm{m}$	half crank angle degree of the combustion	CAD
β	Zeldovich number, constant coefficient	-
ρ	density	kg/m^3
λ	fresh gases heat conductivity	$W.m^{-1}.K^{-1}$
Ξ	flame wrinkling factor	-
v	kinematic viscosity	$m^2.s^{-1}$
η_k	Kolmogorov length scale	m
η_{comb}	combustion efficiency	-
ϵ	dissipation rate	m^2/s^3
χ_{res}	residual gas mass fraction	-
σ	the expansion factor	-
ϑ_i	stoichiometric coefficient of species i	-
Γ	efficiency function of the turbulent flow on the flame strain	-

Indice

b	burned gases
c	chemical, combustion
cyl	cylinder
$carb$	carburant
eff	effective
fg	Fresh gases
i	inflammation
L	laminar
t	turbulent
u	unburned gases

Abbreviations

0D	zero-dimensional
AST	after spark timing

ATDC	after top dead center
BTDC	before top dead center
BMF	burned mass fraction
CAD	crank-angle degree
CAXX	crank angle degree for which XX% of the cumulative heat release is released
CO	carbon monoxide
CO_2	carbon dioxide
CoV	coefficient of variation
CFD	Computational Fluid Dynamics
EGR	Exhaust Gaz Recirculation
HCCI	Homogeneous Charge Compression Ignition
IC	internal combustion
IMEP	indicated mean effective pressure
KI	knock intensity
LES	Large Eddy Simulation
LIF	Laser Induced Fluorescence
MN	methane number
N_2	nitrogen
NO_x	nitrogen oxide
O_2	oxygen
OST	optimum spark timing
RON	research octane number
RPM	Round per minute
SFC	Specific fuel consumption
SI	spark ignition
ST	spark timing
TDC	top dead center
UHC	unburned hydrocarbon

Introduction générale

Le moteur à combustion interne, que ce soit à allumage par étincelle ou par compression, a su s'imposer comme source motrice pour la plupart des véhicules de transports et notamment des automobiles. Ce système a donc pu profiter de nombreux développements depuis plus d'un siècle permettant d'atteindre des performances exceptionnelles en termes de rendement énergétique et d'émissions polluantes. Malgré ces améliorations constantes, le transport, dû à l'utilisation des moteurs à combustion interne, est l'une des sources majeures d'émissions de gaz à effets de serre et d'autres émissions polluantes nocives pour notre planète et notre santé.

Parallèlement à l'enjeu de réduction des émissions polluantes, la diminution certaine et relativement proche de nos ressources mondiales pétrolières nécessite de trouver de nouveaux procédés de motorisation et/ou de modes de combustion afin de réduire la consommation en carburant des moteurs à combustion interne, challenge qu'essayent de tenir les constructeurs automobiles et les organismes de recherche. L'objectif scientifique de l'équipe Energétique, Combustion et Moteurs du laboratoire PRISME est en parfaite symbiose avec ce challenge soit en apportant des éléments nouveaux sur les phénomènes mis en jeu, soit en proposant des nouveaux systèmes de motorisations ou encore en optimisant le contrôle-moteur, maillon final d'optimisation du groupe moto-propulseur.

Actuellement, l'une des voies potentiellement envisagées pour augmenter le rendement, et donc par là-même diminuer la consommation en carburant, est de suralimenter massivement les moteurs. Ainsi, tout en maintenant constante la puissance, l'augmentation du rendement est obtenue par la conjoncture de deux effets : un remplissage optimum de la chambre de combustion grâce à l'utilisation d'un turbocompresseur permettant de suralimenter l'admission et la diminution des frottements mécaniques résultant de la diminution de la taille et de la masse des pièces mécaniques en mouvement. Ainsi, grâce à ce concept, dénommé «Downsizing», les gains de rendement peuvent atteindre jusqu'à 20%.

Malgré la simplicité apparente de ce concept, de nombreuses questions liées au déroulement de cette combustion restent en suspens. En effet, la combustion se déroule dans des plages de pression et de température beaucoup plus importantes que dans un moteur conventionnel ; de plus, ce mode de combustion est très souvent associé à une dilution massive des gaz frais par l'utilisation de l'EGR (Exhaust Gas Recirculation). Expérimentalement, il a été observé que la conjoncture de ces deux points pouvait générer des combustions anormales pouvant mener à la destruction du moteur, ou inversement des combustions dégradées et incomplètes.

L'objectif de cette thèse est donc d'étudier la combustion in-situ dans le cas de fonctionnement d'un moteur à allumage commandé suralimenté mais en contrôlant le taux d'oxygène afin d'en étudier son effet. Peu d'études expérimentales et numériques existent à ce jour permettant de prédire le développement de la combustion dans ces conditions si particulières.

Le premier chapitre de ce mémoire est consacré à l'étude bibliographique de manière générale sur le fonctionnement du moteur allumage commandé et plus particulièrement dans des conditions de suralimentation. Une attention particulière est portée sur les deux paramètres importants pour les conditions de cliquetis : la vitesse de combustion laminaire et le délai d'auto-inflammation.

Le deuxième chapitre est consacré à la description du dispositif expérimental et des méthodes d'analyse numérique pour le traitement des résultats. Les résultats expérimentaux obtenus sur banc moteur monocylindre en variant le taux d'oxygène à l'admission y sont présentés et analysés.

Le troisième chapitre expose l'étude réalisée pour estimer les paramètres caractéristiques de la combustion. Dans ce chapitre, l'enrichissement de l'oxygène sur la combustion laminaire de l'iso-octane avec l'oxygène dans des conditions proches des Conditions moteurs y est discuté. Des comparaisons des mesures de vitesse de combustion laminaire avec les données issues d'une simulation avec le logiciel Cantera appliquée avec deux schémas chimiques y sont discutées. Les données concernant la longueur Markstein y sont également présentées. Un mélange enrichi en oxygène semble être très intéressant pour augmenter la vitesse de combustion laminaire et la stabilité de la flamme. Le délai d'auto-inflammation a aussi été déterminé pour les mélanges d'Isooctane/O2/N2/CO2, en utilisant l'outil Senkin. Ensuite, pour obtenir une correction plus précise pour le cas de la simulation AMESIM, les conditions initiales des mélanges Isooctane/O_2/N_2 ont été définies en tenant compte des données calculées et expérimentales de pression et de température.

Le quatrième chapitre est dédié à la présentation du logiciel commercial AMESim, au développement nécessaire pour simuler les variations des taux d'oxygène à l'admission en particulier les paramètres tels que la vitesse de combustion laminaire et le délai d'auto-inflammation. La prédiction de l'évolution de la vitesse de combustion turbulente dans le cylindre durant le cycle a permis ainsi de classifier la combustion dans un diagramme de combustion turbulente (type Peters-Borghi) et d'estimer l'intensité du Cliquetis et sa sensibilité avec différents paramètres.

En conclusion, les résultats principaux sont synthétisés pour dégager les principales analyses faites sur les modes de combustion essence à taux d'oxygène contrôlé, et pour proposer des perspectives d'études.

Chapter one

General study of bibliography

1 Chapter 1 General study of bibliography

Considering lack of oil storage and stringent legislation on emission, improving the engine efficiency in combination with a decrease of air pollution becomes a significant challenge for engine manufacturers. For Spark-Ignition (SI) engine, one of the potential solutions is to shift towards 'downsizing' engine. In order to maintain the engine power output, boosting technologies, either supercharging or turbo-charging, are generally employed because they allow more air to be pumped into the engine and therefore increase the engine power density.

In this thesis, engine combustion with controlling oxygen concentration in air is discussed. In one hand, for oxygen-enriched combustion, engine power density can be improved with same intake pressure level. Thus, oxygen-enriched combustion can be used either as a kind of boosting way for increasing engine output or as a combustion enhancer when engine works in low load or cold start. Several studies performed with oxygen enrichment in SI engines showed positive effects: Reduction in Unburned Hydrocarbon fuel (UHC) and CO (Kajitani et al. 1993; Ng et al. 1993; POOLA et al. 1995; Poola et al. 1996), Optimization of downsizing due to the direct effect on the combustion process and overall engine thermodynamics(Caton 2005), Increase in flame propagation velocity (Quader 1978; Kajitani et al. 1992; Poola et al. 1998) and so on. In the other hand, low oxygen concentration in air (or N2 dilution) can be considered as an alternative to exhaust gas recirculation (EGR) which is widely investigated in recent years (Van Blarigan et al. 2012; Mounaïm-Rousselle et al. 2013).

Moreover, controlling oxygen concentration in air can be done by selective permeation through a non-porous polymeric membrane, air can be recomposed with oxygen enrichment or nitrogen dilution for engine applications (Koros et al. 1987).this kind of polymeric membrane technology is now extensively researched and applied (Poola et al. 1998; Coombe et al. 2007; Favre et al. 2009).

Thus, the first purpose of this thesis is to investigate the impact of oxygen concentration controlled on engine performance and emissions using bench tests, and give a global overview of optimized engine operation points with lowest SFC and exhaust gas emissions.

In order to study more details of engine combustion with oxygen controlling, containing turbulent flame velocity in engine, flame wrinkling, knock prediction and so on, the Amesim commercial software, with the combustion model developed by IFP-EN was employed. Compare to the other two zone models, Amesim combustion provides the following advantages: firstly, Amesim enables us to address the various physical domains involved in vehicle and engine system simulation with a high level of details (IFP-engine library, 2008). Thanks to this advantage, Amesim model can be set up with reference to the experimental configuration, for example, intake and exhaust tube, engine valves, turbo-compressors and so on. Secondly, the combustion model proposed and developed by IFP-EN gives an accurate description of physical processes. Although this combustion model is based on weak assumption for the mean flame geometry, the employment of the flame surface, turbulent intensity, and laminar and turbulent flame speed gives a realistic physical signification for the in-cylinder combustion process.

Thus, this chapter is dedicated to

- ✓ Firstly discuss about actual emission problems and fuel economy
- ✓ give a brief introduction of SI engine and new technologies

- ✓ study the normal combustion in SI engine
- ✓ study the abnormal combustion in SI engine
- ✓ investigate the Oxygen-Controlled combustion in engine

1.1 Actual emission problems and fuel economy

Nowadays, vehicle exhaust gas emissions become a serious problem with shapely increasing of car numbers. In present, the main pollutant emission refers to CO, HC, NOx, and PM (particulate matter). Carbon monoxide, produced mainly by incomplete combustion, can reduce the oxygen percentage in the bloodstream and is particularly dangerous for people with heart disease. Hydrocarbon is mainly due to incomplete or no combustion of fuel. It can form ground-level ozone with the presence of nitrogen oxides. Moreover, it is also toxic, with the potential to cause cancer. Nitrogen oxide is the main factor of ozone formation. The well known principal mechanism of Nitrogen oxide formation is the Zeldovich one, which depends on high temperature condition which could be inside engine. Particulate matter which is smaller than order of 10 micrometers can penetrate the deepest part of lung and cause health problem.
Since the first pollutant standard in 1972, the restriction has become more and more stringent. European pollutant standards (in g/km) for gasoline engine cars are exhibited in ***Table 1-1***. From 1992 to now, the norm of CO is reduced about three times and the norm of $HC+NO_x$ is reduced more than six times. In Euro 3, HC and NO_x are considered separately. From Euro 5, NMHC (non-methane hydrocarbons) is also separately counted from THC (total hydrocarbon) and PM emission is regulated for the first time.

standard	date	CO	THC	NMHC	NO_x	$HC+NO_x$	PM
Euro 1	07/1992	2,72	-	-	-	0,97	-
Euro 2	01/1996	2,2	-	-	-	0,5	-
Euro 3	01/2000	2,3	0,2	-	0,15	-	-
Euro 4	01/2005	1,0	0,1	-	0,08	-	-
Euro 5	09/2009	1,0	0,1	0,068	0,06	-	0,005
Euro 6	09/2014	1,0	0,1	0,068	0,06	-	0,005

Table 1-1. European anti-pollution standards (in g/km) for gasoline engine cars (http://en.wikipedia.org/wiki/European_emission_standards).

Meanwhile, Carbon dioxide (CO_2), a normal combustion product, which can trap the earth's heat and thus produces the green house effect. The European Union has set itself the target of reducing emissions by 20% global CO_2 emissions between 1990 and 2020. For automobile sector, an average reduction of 40% of the CO_2 emissions of new vehicles is required between 2007 and 2020. In ***Figure 1-1***, the evolution of mean CO_2 emission value for new cars in Europe is described. France and Portugal are both countries which reached 140 g/km of CO_2 emission value in 2008. However, many efforts should be done for the next several years. The European objective of 2015 and 2020 are respectively 130g CO_2/km and 95g CO_2/km for average vehicle emissions, which is far away from general European trend as showed in ***Figure 1-1***. As CO_2 is one of the main products of combustion, the best way to meet the objective is to have less fuel consumption while maintaining the output power.

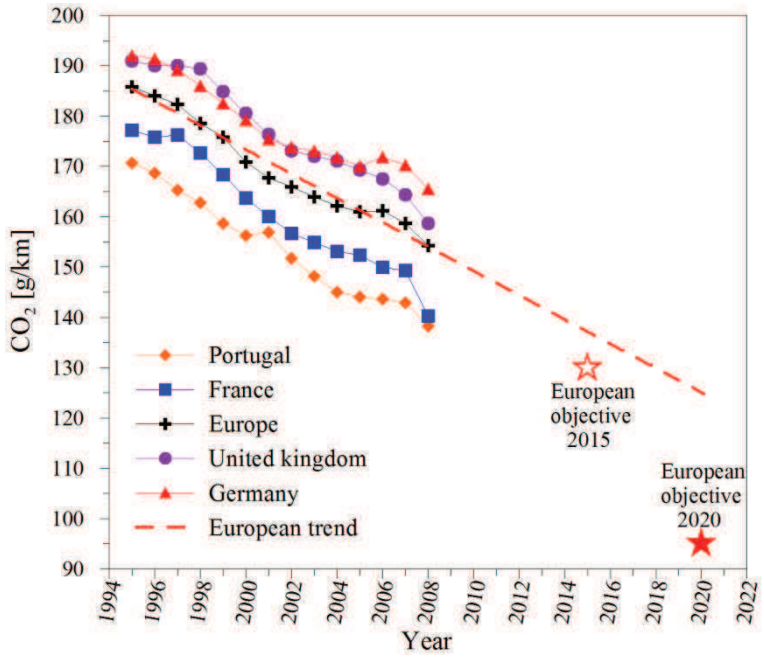

Figure 1-1. Evolution of mean CO2 emission value for new cars in Europe

(Source CCFA http://www.developpement-durable.gouv.fr/IMG/pdf/ccfa.pdf)

Therefore, facing to these environmental and human health problems, it is necessary to optimize the engine operation to minimize pollutant emissions while providing better engine performance and less fuel consumption. Following these strategic clues, in car manufacture, vehicle engine is studied in details using both experimental and numerical methods, and new technologies are well developed for new engine generation.

1.2 Introduction to SI engine and its new technologies

In SI engine, the power is produced by the combustion of an air/fuel mixture inside a cylinder, in which the piston moves in a reciprocating motion. ***Figure 1-2*** describes the structure of a SI engine with turbo-compressor. The engine is supplied with an air/fuel mixture, obtained by intake port injection or direct injection inside the cylinder. The amount of admitted air is controlled by a valve located in the intake pipe. One of main factor for engine power release is the quantity of introduced air/fuel mixture. Engine load is normally characterized by air filling in cylinder, which is the ratio between real air mass presented in cylinder and ideal air mass could be contained in cylinder under standard conditions (i.e. atmosphere pressure, 20 °C). Inside the cylinder, the air and vaporized fuel are transformed into a gas mixture. Ignition can then be triggered by an electrical spark, causing a local rise of temperature, initialing radicals' formation, and then a flame front propagating in the chamber.

Recently, more and more vehicles are equipped with Turbo-compressor in order to improve the power output with same engine capacity. As showed in ***Figure 1-2***, exhaust gas is used to drive the Turbine, while the waste-gate controls the functionality of turbine. By the mechanical connection between turbine and compressor, compressor is driven to compress the ambient air into the intake tube with higher boosted pressure (P_{boost}).

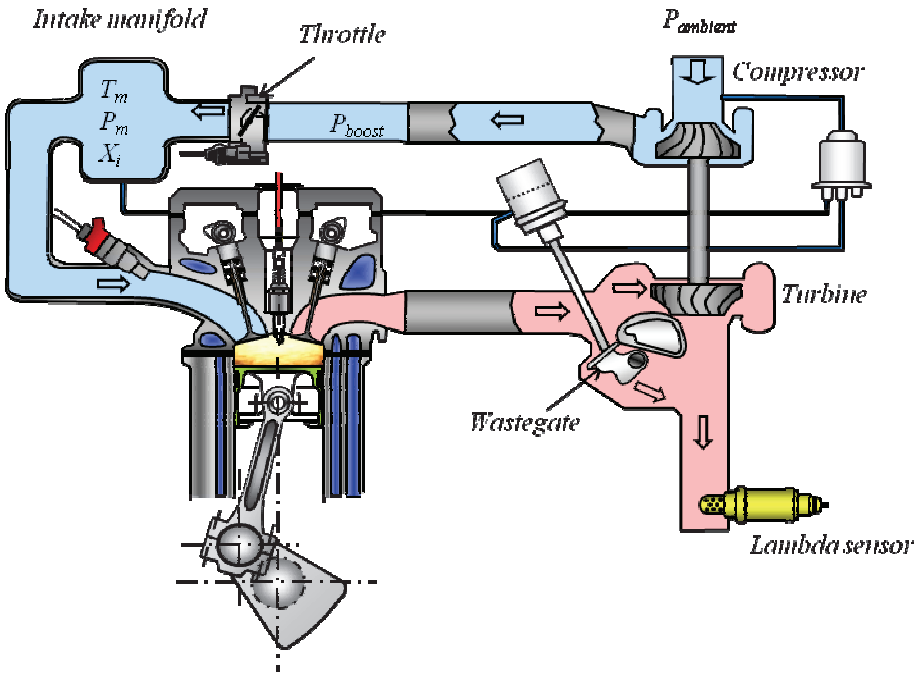

Figure 1-2 the structure of a SI engine with turbo-compressor

In order to meet regulation standards, two ways can be employed practically(CITEPA 2010). The first way is to reduce the pollution emission by combustion control (ex. control the temperature and pressure of admission gas mixture, the EGR rate, spark timing and etc). The other way is the pollution post-treatment. For gasoline engine, three-way catalytic (TWC) is normally used to minimize the pollutants emission. Although the pollution post-treatment can solve nearly 100% of the pollution, the relative cost is much higher (2 to 5 times) than combustion control (CITEPA 2010) . Thus, investigation of pollutants emission using combustion control is still necessary to meet future emission regulation.

Apart from pollutants emissions, another major challenge for car manufactures is to increase engine efficiency while improving fuel economy, which is also the main strategy for the reduction of CO_2 emission. Engine efficiency is the ratio of the amount of energy used to perform useful work to the total energy contained in the fuel .As described in diagram ***Figure 1-3***, the energy efficiency of an internal combustion (IC) engine depends mainly on:

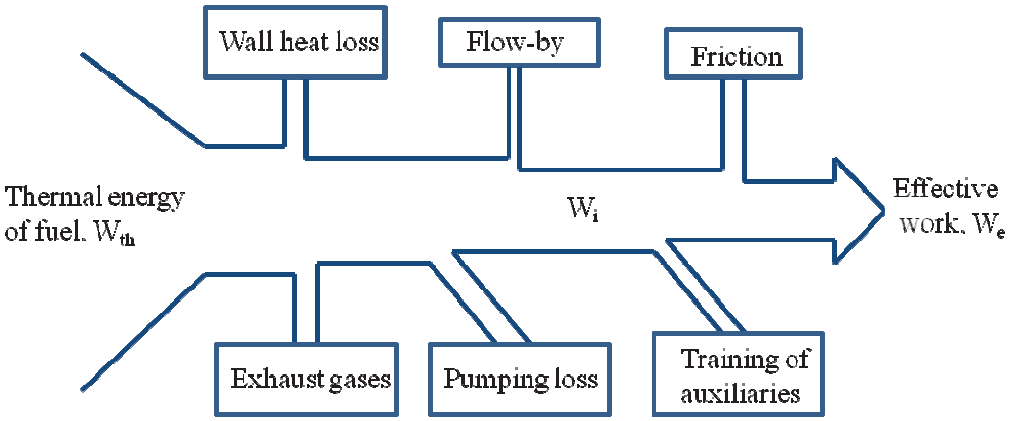

Figure 1-3 diagrams for illustrating engine efficiency

- Its compression ratio and the isentropic coefficient of gases mixture, which are the two parameters determining theoretical thermal efficiency.
- Heat loss during the compression and expansion phases
- Pumping losses of the gas stream during the intake and exhaust stroke.
- Energy loss by exhaust gases and blow-by
- Losses due to non-instantaneous combustion and cycle variation
- Mechanical losses due to friction
- Energy used for training of auxiliaries

In order to increase the engine efficiency as well as reduce pollutants emission, several new technologies are invented for SI engine in recent years. These new technologies are either changing engine architectures or using new concept of air/fuel mixture. The former catalog can be globally summarized as:

- Gasoline Direct Injection (GDI): The fuel is injected directly into the chamber by high pressure injectors (100 to 200 bars). The idea of GDI is to reduce the consumption by decreasing pumping losses due to gas transfer. Moreover, the spray evaporation cools the fuel-air mixture down, which may push back knock occurrence and therefore enable the use of higher volumetric compression ratios to improve the engine efficiency. Compare to port fuel injection, GDI has also the advantage of allowing a precise control of the fuel quantity injected in each cylinder. A major challenge of such a technology is to obtain a homogeneous air-fuel mixing and to avoid interactions between the spray and the engine walls.

- Downsizing concept: The engine volume is reduced and the engine volumetric efficiency is improved by combining two key technologies: direct injection and turbo-charging. As the engine size is reduced, wall heat loss and friction can therefore be decreased. Generally, direct injection can not only decrease the in-cylinder temperature, that may prevent knock occurrence, but also give a better control of the injected fuel quantity as function of the trapped air quantity. Moreover, turbo-charging decreases pumping losses and improves exhaust gas scavenging which consequently allows a reduction of knock occurrence at high loads. Finally, higher high-pressure loops can be normally obtained in downsized engines which may lead to a better engine efficiency.

- Variable Valve Timing (VVT): It allows the lift, duration or timing of intake and/or exhaust valve to be changed via the Engine Control Unit (ECU) during engine operation. VVT approaches are generally performed by adjusting geometrically the camshaft phasing. Normally the valve timing is well set for adapting different phases of engine operation mode: at idle phase, the inlet camshaft opens late and consequently, closes late as well, and the exhaust camshaft is set much before Top Dead Center (TDC). So that the air filing is minimized, this leads to smooth idling. At power phase, the exhaust valves are open late to maintain the expansion of burned gases pushing against the piston longer. Meanwhile the inlet valves open after TDC and close well after BDC to let the dynamic self-charging effect of the entering air increase power. At torque phase, Inlet valves need open early, so it close early as well, which avoids pressing out the fresh gases to achieve maximum torque. And the exhaust camshafts close just before TDC, to avoid the residual gases trapped in the cylinder.

The other new technologies of this catalog are also widely discussed and researched such as Variable Compression Ratio (VCR), Hybrid electric vehicle (HEV) and so on. For the later catalog of new technology, new concept of air/fuel mixture is investigated:

- Exhaust Gases Recirculation (EGR): The major benefits of EGR are mainly due to several aspects: first, reduce piping lose via increased inlet manifold pressure for a given power output. Second, the pick combustion temperature is lowered, which can reduce both wall heat lose and NO_x formation. Finally, high knock resistance in the case of EGR can therefore enable the use of higher compression ratio to improve engine efficiency. However, EGR would reduce the intake power density, and consequently reduce peak power output at high load. And it would also cause unstable combustion when high EGR level is used or at idle phase (low speed, zero load).

- Stratified Combustion: a mixture sufficiently rich for ignition is available in the vicinity of the spark plug, whereas poor mixture is formed in the rest of the cylinder. A stratified charge engine, the power output is no longer controlled by the intake air amount, but the amount of fuel injected as a Diesel engine.

In one developed engine, several new technologies might be used. Downsizing concept SI engine are normally combined with turbo-charging, direct injection, and EGR. The structures of engine normally become more and more complicated for new vehicle generation. This is also a challenge for engineers and researchers to develop new experimental and simulation tools for updating the renewable technologies.

The Downsized Spark-Ignition Engine is one of the most promising solutions to reduce the CO_2 emissions. And in order to optimize the operation of the engine regardless the engine load, the dilution by the exhaust gases recirculation (EGR) is one of the best way to decrease the pumping losses, to limit abnormal combustion and decrease the NOx emissions. However, the dilution obtained by EGR requires a cooling exchanger to control the temperature of fresh gas which can cause a number of technological problems such as those related to the water vapor condensation and the fouling of the EGR circuit. In addition, the mastery of the composition of the re-circulated gases and the response time of the loop EGR can disrupt the management of engine control.

1.3 Normal Combustion in SI engine

In Spark Ignition engine, before the combustion is initiated by the spark, fuel and oxidizer are mixed by turbulence to nearly the molecular level; after the ignition, a flame kernel grows at first by laminar and then by turbulent flame propagation. Thus, this section aims at presenting some basic knowledge about laminar and turbulent premixed combustion.

1.3.1 Laminar premixed combustion

Laminar premixed combustion is considered as a fundamental study of turbulent combustion for both experimental and numerical investigations because of its simplicity and importance. ***Figure 1-4*** shows the mechanism of a laminar premixed combustion. The premixed mixture is ignited on the left hand of container. By propagating of the laminar flame, the gases are separated into two zones: fresh gases zone and burned gases zone. The reaction zone is in middle of these two zones, where chemical reactions take place. The chemical reactions take

place when the temperature of mixture exceeds T_i, called ignition temperature. In this mechanism, heat transfer plays a major role since it elevates the temperature of unburned gases, which are just near the reaction zone. The gases are heated up then ignite and continue to perform as a hot source to heat transfer.

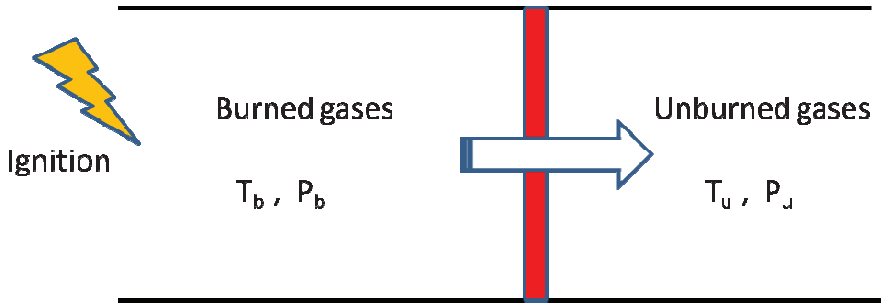

Figure 1-4. mechanism of a laminar premixed combustion

Laminar flame thickness

The structure of a laminar premixed combustion is firstly described by Mallard and Chatelier (Mallard et al. 1983). In order to calculate analytically the combustion rate, the flame is divided into two zones:

- Preheated zone with thickness of δ_p : in this area, the diffusion and convection processes are predominant and the chemical reactions are therefore negligible.
- Reaction zone with thickness of δ_r: very thin area in which the heat releases due to chemical reactions. In this zone, the conduction phenomena are then negligible compare to diffusion.

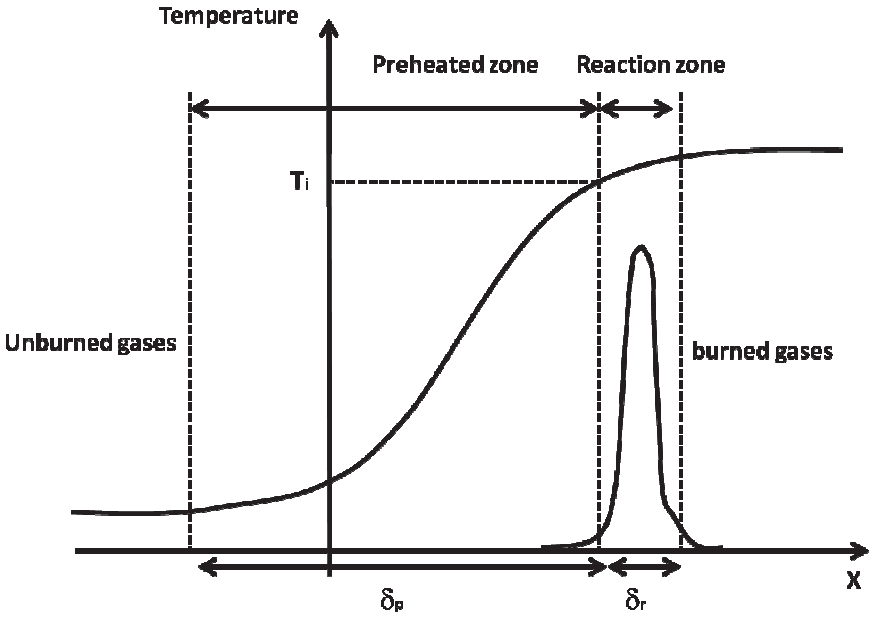

Figure 1-5. Structure of a laminar premixed combustion

Thus, the total laminar flame thickness can be expressed as the sum of the thickness of preheating and reaction zones:

$$\delta_L = \delta_p + \delta_r \qquad \text{Equation 1-1}$$

The thickness of the reaction zone can be deduced from the thickness of the preheating zone by the relationship $\delta_r = \delta_p/\beta$. The Zeldovich number β is infinitely large relative to the thickness of the preheating zone, thence one can considered that the thickness of the reaction zone is negligible.

The definition of the thickness proposed by Spalding (Spalding 1955) is base on the temperature profile. It is defined by the ratio of temperature difference between burned gases and fresh gases to the maximum temperature gradient of the temperature profile:

$$\delta_l^{Spalding} = \frac{T_b - T_u}{\max\left(\left|\frac{\partial T}{\partial x}\right|\right)} \qquad \text{Equation 1-2}$$

Where $\delta_l^{Spalding}$ is Spalding thickness, also called diffusion thickness, and T_b, T_u are the burned and fresh gases temperature respectively. The advantage of this definition is that the thickness may be calculated locally along the flame front. According to the study of Poinsot et al.(Poinsot et al. 1991), this definition of the laminar flame thickness is a convenient way to define the mesh resolution of the numerical calculations. The major drawback of this definition is that a first computation of laminar flame is needed to post-process temperature profile. Therefore, in order to determine the laminar flame thickness before the computation, correlations should be employed.
Among these correlations, the zeldovich expression is wildly used. This expression is obtained by assuming that all of the energy produced by the combustion is used to raise the temperature of the fresh gases which present in the preheating zone:

$$\delta_l^{Zeldovitch} = \frac{\lambda_u}{\rho_u Cp_u S_L} = \frac{D_{th}^u}{S_L} \qquad \text{Equation 1-3}$$

Where λ_u, ρ_u, Cp_u, S_L, D_{th}^u are respectively the fresh gases heat conductivity, density, heat capacity, laminar flame speed and heat diffusivity. In this expression, as soon as the flame speed S_L is known, the thickness of the flame can be calculated easily before any computation.

Another correlation proposed by Blint (Blint 1986) is supposed to be closer to Splading thickness:

$$\delta_l^{Blint} = 2\frac{\lambda_u}{\rho_u Cp_u S_L}\left(\frac{T_b}{T_u}\right)^{0.7} \qquad \text{Equation 1-4}$$

In this correlation, burned gas temperature T_b is approximated by considering the enthalpy balance between fresh and burned gases:

$$T_b = T_u + \frac{QY_F^0}{Cp} \qquad \text{Equation 1-5}$$

Where Q is the heat of reaction per unit mass, and Y_F^0 is the initial fuel mass fraction.

The determination of laminar premixed combustion parameters will be presented in third chapter. Different methods for estimation of laminar burning velocity will be introduced.

1.3.2 Turbulent premixed combustion

Turbulent basics

Turbulence is a flow regime characterized by chaotic and stochastic property changes. Because of its pseudo-random and apparently unpredictable nature, it is considered as one of the most challenging problems in fluid dynamics. Numerous scientists have made great effort in the observation, description and understanding of turbulent flows.

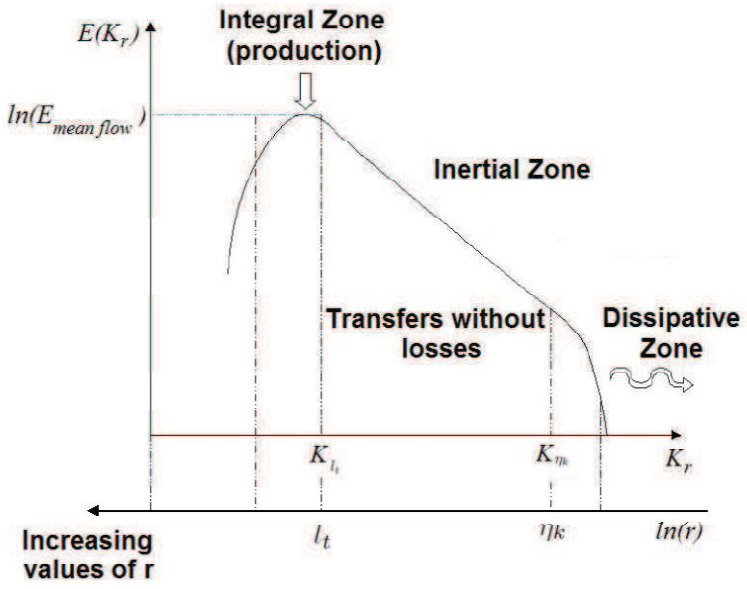

Figure 1-6. the structure of energy cascade (Bougrine 2012)

Kolmogorov (Kolmogorov 1941) proposed the first statistical theory of turbulence, based on the aforementioned notion of the energy cascade and the concept of self-similarity. In his theory, a turbulent flow is composed by different sizes of eddies defined by characteristic length, velocity and time scales (eddies turnover time). As described in ***Figure 1-6***, large scale eddies are produced by the kinetic energy which is supposed to be injected by an external force. The large eddies are deformed and stretched by the fluid dynamics, until they break into smaller eddies. The kinetic energy of the large eddies is divided and transferred to the small ones. This process is repeated such that energy is transported to smaller and smaller structures. Thus the energy is transferred from the largest length scale (the integral length l_t) to smaller ones until reaching the smallest length scale (Kolmogorov length scale η_k) such that the viscosity of the fluid can effectively dissipate the kinetic energy into heat.

A classical way to describe turbulent flows is to split the three components of velocity and the scalar quantities like the temperature and mass fractions measured at a point x into a mean and a fluctuation, for example the velocity $U(x,t)$ can be expressed as:

$$U(x,t) = \overline{U}(x,t) + u'(x,t) \qquad \text{Equation 1-6}$$

Where $\overline{U}(x,t)$ is the mean value of $U(x,t)$, $u'(x,t)$ is the fluctuation value which is obtained by subtracting the mean from the instantaneous value and $\overline{u'}(x,t) = 0$ by definition.

The turbulent kinetic energy k is then given by:

$$k = \frac{1}{2} < u_i u_i >= \frac{1}{2}\left(\overline{u'^2} + \overline{v'^2} + \overline{w'^2}\right)$$ Equation 1-7

To calculate the turbulent kinetic energy distributed among the eddies of different sizes, usually the energy spectrum $E(K)$ is introduced. Here, $E(K)$ is the energy contained in eddies of size l, and wave number K defined as: $2\pi/l$. Then by definition, k is the integral of $E(K)$ over all wave numbers:

$$k = \int_0^\infty E(K)dK$$ Equation 1-8

As showed in ***Figure 1-6***, three different zones with different range of scales can thus be indentified:

- Integral zone

  The integral zone also called the energy containing zone has eddies of size integral length scale l_t which is considered as the largest length scale among all the turbulent eddies. By the definition of wave number K, largest length scale l_t corresponds to the lowest wave number. More importantly, the integral scale is the scale at which turbulent energy is introduced into the system. Eddies of this scale obtain energy from the mean flow and also from each other. They have large velocity fluctuations ($u' = \sqrt{2/3k}$) and low frequencies. Thus, it can be summarized as following: velocity $u' \approx k^{1/2}$, length scale l_t and time scale $T_t = l_t / u'$. Moreover, the dissipation rate is imposed by large structures of the turbulent flow: $= \frac{k}{T_t} \approx \frac{u'^3}{l_t}$.

- Inertial zone

  The second zone contains the transitive scales, also called Taylor scales. It refers to scales between Kolmogorov length scale η_k and the integral length l_t. These scales are independent of the forcing scales, are dominated by inertial forces rather than viscosity. Moreover, these scales contain and dissipate very little turbulent energy. The main action is transfer energy from the large scales to the very small ones.

- Dissipative zone

  The dissipative zone related to the scales under the Kolmogorov structure. At these length scales, viscous effects start to strongly damp the turbulent motion. The end of the curve is characterized by a rapid, almost exponential drop off in energy content, which also accounts for the bulk of energy dissipation within the turbulent cascade. Because the small scales are high in frequency, turbulence can be considered locally as isotropic and homogeneous. The velocity, the length scale and the time scale can then be expressed as: $u_k = \nu^{1/4}\epsilon^{1/4}$, $\eta_k = \nu^{3/4}\epsilon^{-1/4}$, $T_k = \nu^{1/2}\epsilon^{-1/2}$.

Turbulent combustion

Premixed turbulent combustion differs from the laminar combustion, which depends not only on the physicochemical properties of the mixture, but also properties of the flow. The interaction between the turbulent flow and combustion makes this phenomenon even complicated: the turbulence changes the behavior of the flame front; the changes in the flow

may take place by the expansion of the burned gases and the spread of flame; the velocity gradient by changes in densities and viscosities and etc. However, it is evidence that the turbulence can extend the surface of the flame and also improves the diffusivity of the mixture, hence increase the burning rate.

As the same way for the study of laminar flames, the turbulent premixed flame is characterized by flame speed, denoted S_t and flame thickness, denoted δ_t . Similar to the laminar burning velocity, turbulent flame speed represents the rate of consumption of fresh gases per unit area. Turbulent flame speed was a subject of a large amount of investigations for many years due to their fundamental importance for premixed combustion theory.

In literature, a simple model was found that the turbulent flame speed was directly related to the turbulent intensity by a linear relationship:

$$S_t = S_L^0 + Cq' \qquad \text{Equation 1-9}$$

Where C is a constant coefficient and q' is the turbulent intensity. Damköhler (Damköhler 1940) firstly explained that the effect of turbulence is to wrinkle the flame front in the case of low turbulence intensity and large scale (flamelet regime). Thus, a simple equality formula was proposed to link the relationship between flame speed ratio and flame area ratio:

$$\frac{S_t}{S_L^0} = \frac{A_T}{A_L} = \Xi \qquad \text{Equation 1-10}$$

Where A_T is the turbulent flame surface and A_L is the laminar flame surface corresponding to A_T. Ξ is the flame wrinkling factor which represents the increase of the turbulent flame speed S_T due to the increase of the total flame surface A_T. In other words, the turbulent flame speed is supposed to be influenced by laminar flame speed and flame front wrinkling.

The diversity and complexity of the phenomena encountered in reactive flows make it impossible to treat the problems as a whole. For the development of combustion models, it is then necessary to understand what phenomena is predominant in a given configuration, and what are the different interactions between them. Thus, determining the combustion regime and the structure of the reactive flow becomes an important task in the study of premixed turbulent combustion. Many authors have proposed combustion regime diagrams in term of length, velocity and time ratios (Borghi et al. 1984; Peters 1988; Poinsot et al. 1991), as described in ***Figure 1-7***. The turbulent combustion can therefore be characterized as five different zones: laminar flame zone, wrinkled flamelets zone, corrugated flamelets zone, thin reaction zone and broken reaction zone. Dimensionless numbers are employed to characterize the different combustion regimes, such as the turbulent Reynolds number Re_t, the Damköhler number Da , and the Karlovitz number Ka.

Turbulent Reynolds number: representing the ratio of turbulent transport to viscous forces, turbulent Reynolds number can be expressed as following:

$$Re_t = \frac{u' l_t}{v} \qquad \text{Equation 1-11}$$

In this function, the velocity scale u' can be obtained by the mean square root of the velocity fluctuations. l_t is the turbulent integral length scale and v is the kinematic viscosity of the flow. Generally, flow is considered as turbulent when the turbulent Renolds number is larger than unit. Therefore, the turbulent Reynolds number can differentiate the field of laminar premixed flames ($Re_t < 1$) and that of turbulent premixed flames ($Re_t > 1$). By the

assumption of unit flame Reynolds number ($Re_f = \delta_L S_L/\nu = 1$), $Re_t = u' l_t/\ \delta_L S_L$, so the boundary between laminar and turbulent flame is the straight line with slop of -1 as showed in Peters-Borghi diagram.

Karlovitz number: Karlovitz number is defined by the ratio between chemical reaction time scales and Kolmogorov time scales:

$$\mathrm{Ka} = \frac{T_c}{T_k} = \frac{\delta_L}{\eta_k}\,\frac{u_k}{S_L} \qquad \text{Equation 1-12}$$

By using the equations of velocity and length scale of Kolmogorov structure $u_k = \nu^{1/4}\epsilon^{1/4}$, $\eta_k = \nu^{3/4}\epsilon^{-1/4}$, Karlovitz number can be written as:

$$\mathrm{Ka} = \frac{\delta_L}{\eta_k}\,\frac{u_k}{S_L} = \left(\frac{\epsilon}{\nu}\right)^{1/2}\frac{\delta_L}{S_L} \qquad \text{Equation 1-13}$$

In order to build the relationship between Karlovitz number and integral scales, the unity flame Reynolds number ($Re_f = \delta_L S_L/\nu = 1$) and the expression of dissipation rate ($\epsilon = u'^3/l_t$) are employed. Finally, the Karlovitz number can also be written as:

$$\mathrm{Ka} = \left(\frac{u'}{S_L}\right)^{3/2}\left(\frac{\delta_L}{l_t}\right)^{1/2} \qquad \text{Equation 1-14}$$

The Karlovitz number is employed to define the Klimov-Williams criterion, related to Ka = 1. The condition Ka <1 means that the combustion rate is sufficiently high to compensate the stretch undergoing by the reaction zone, therefore there is no phenomena of local extinction of the flame. In the reverse situation Ka >1, the turbulent flow can produce the flame stretching and then cause extinction events, and small flow structures are able to penetrate the internal structure of the flame which corresponds to both reaction zone and preheated zone (Peters 1999). With regards to Equation 1-14, the line Ka = 1 has a slop of 1/3 in Peters-Borghi diagram.

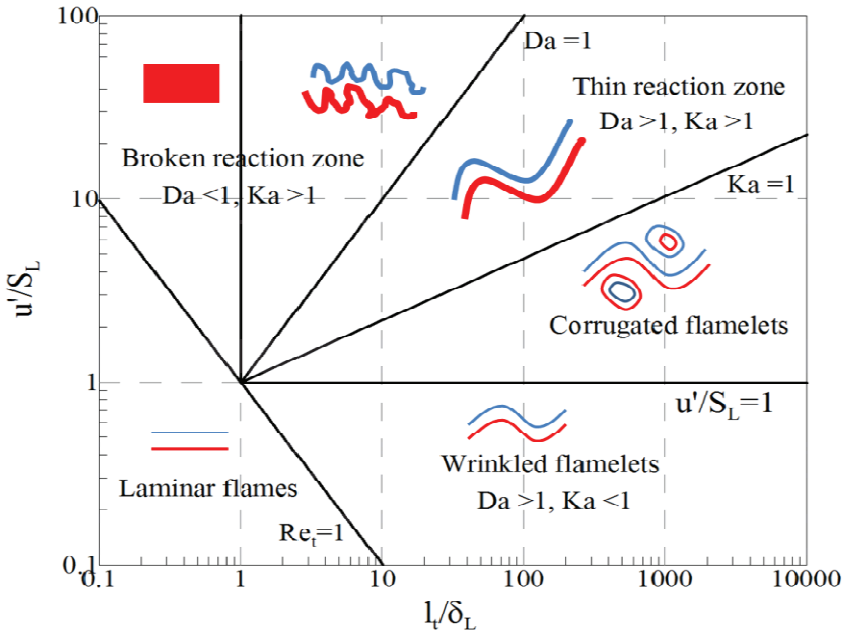

Figure 1-7. Peters-Borghi Diagram of combustion regime (Borghi et al. 1984)

Damköhler number: the ratio of the turnover time of an eddy at the integral length scale (characteristic time of turbulent $T_t = l_t/u'$) and the chemical time scale ($T_c = \delta_L/S_L$):

$$Da = \frac{T_t}{T_c} = \frac{l_t}{u'}\frac{S_L}{\delta_L} \qquad \text{Equation 1-15}$$

In case of large Damköhler number (Da>>1), the chemical reaction time is negligible compared to the turbulent one, which related to a thin reaction zone wrinkled and convected by the flow field. The internal structure of the flame can be described as a laminar flame element embodied by the turbulent flow. This structure can then be qualified as 'flamelet' regime. Otherwise, for a small Damköhler number (Da<<1), the characteristic time of turbulent is short compared to the chemical reaction time. As the chemical reactions are very slow, the effect of turbulent becomes predominant inside the flame, which makes the reactants and products mix perfectly. This regime can then be classified as distributed combustion. With regards of Equation 1-15, the line $Da = 1$ has a slop of 1 in Peters-Borghi diagram.

Based on the above dimensionless number analyses, the premixed combustion can be divided into several zones:

- Laminar flame zone: $Re_t < 1$
- Wrinkled flamelets : $Re_t > 1$, Da > 1, Ka < 1, $u'/S_L < 1$
- Corrugated flamelets: $Re_t > 1$, Da > 1, Ka < 1, $u'/S_L > 1$
- Thin reaction zone: $Re_t > 1$, Da > 1, Ka > 1, $u'/S_L > 1$
- Broken reaction zone: $Re_t > 1$, Da < 1, Ka > 1, $u'/S_L > 1$

1.4 Abnormal combustion

For spark ignition engine, normal combustion (also called regular combustion) is started by the spark plug plasma which is precisely timed and located by controlling the parameter 'spark advance'. Fixing the other parameters (such as intake temperature, intake pressure, equivalence ratio and etc), spark advance can be adjusted to develop peak pressure in the cylinder at the ideal time for producing maximum work from the expanding gases. Then after the spark, a small flame kernel is formed and glows rapidly by consumption of unburned gases. Due to the influence of turbulence, the flame front has a much greater surface area and propagates much faster than laminar propagation speed. The pressure curve of normal combustion is showed in ***Figure 1-8*** with green color. The pressure curve rises smoothly by consuming fresh air fuel mixture, and falls down after the arrival of peak pressure as the piston descends.

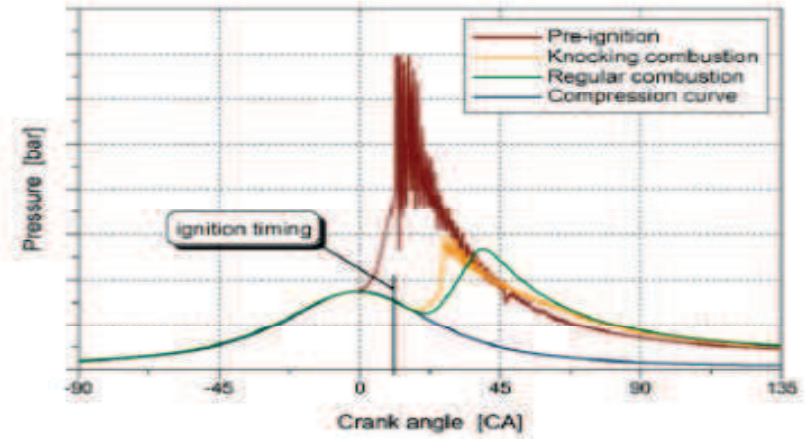

Figure 1-8. Cylinder pressure curves for normal and abnormal combustion (Winklhofer 2009)

Abnormal combustion is commonly considered as two different kinds of phenomena: engine knocking and surface ignition (which contains pre-ignition and post-ignition). As post-ignition is difficult to distinguish with engine knocking, few literature discusses in this domain.

1.4.1 Pre-ignition

Pre-ignition (also called mega-knock) is initiated by an ignition source before the spark plug firing. The ignition source can be hot spots in the combustion chamber, a spark plug that runs too hot for application, or carbonaceous deposits in the combustion chamber heated by previous engine cycle and so on (Mogi et al. 1998). In ***Figure 1-8***, the red curve presents the in cylinder pressure of pre-ignition, the flame propagates suddenly and results in rapid pressure increase and high magnitude of pressure oscillation. High pressure during the pre-ignition generally causes serious damage, thus pre-ignition must be avoided. High charging pressures and low engine speeds favor to pre-ignition, because low engine speeds provide more time for auto-ignition chemistry and supercharged pressure will shorten the auto-ignition timing.

1.4.2 Engine knock

Knocking phenomenon is an acknowledged limitation to improve engine efficiency. The intake pressure should be well controlled in order to avoid engine knock, which will directly influence the engine power density, and gives a main barrier for turbo-charged technology. Engine knock can also result in severe damage on engine elements. If knock occurs over a long period of time or under a serious knocking condition, some harmful effects can be produced: piston erosion or even melting, breakage of piston rings, cylinder head erosion etc.

As wildly considered, the onset of knock is caused mainly by the auto-ignition of fresh gases ahead of the normal spark-ignited flame front, which could be related to engine design or operating conditions, or to the work gas composition(the gas octane number, or gas quality…). According to the study of Konig et al. (Konig et al. 1990), the auto-ignition of end gases can be ranged into three modes: deflagration, thermal explosion, and detonation. The first mode is corresponding to a light knock, the second one associated to a moderate knock and the third one can cause severe knock. Under knock, combustion can be extremely violent and can reach a speed of 5 to 25 times higher than during a normal combustion (Heywood 1988). Thus the major part of fresh gas at knock onset will be consumed by knocking combustion.

Kawahara et al (Kawahara 2009) used a high-speed monochrome video camera (with operating speed: 250,000 frame/s) to measure the pressure wave propagation. They examined the auto-ignition process of hydrogen fuels in a specially designed SI engine with various equivalence ratios. ***Figure 1-9*** shows time-series images at specific crank angle for knocking engine cycle. After ignition sparks, a bluish-colored flame, which propagated in a circular shape towards the end gas region, was observed as in frame E and F. In frame G, the auto-ignited kernel of end gas appeared in front of the flame propagation in the upper left corner. At the instance of knock, as showed in frame H, the unburned gas region suddenly flashed white and expanded towards the blue colored region of the burned gas with higher luminous flame density.

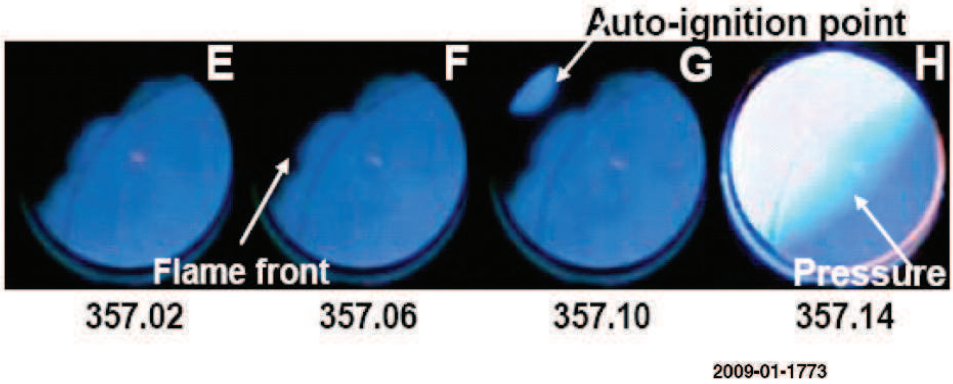

Figure 1-9. Time-series of high speed direct combustion images with the H_2-O_2-Ar mixture (equivalence ration=1.0, P0=40kPa, T0=323K, θ_i = 355 deg and knock intensity KI = 1.173Mpa)(Kawahara 2009)

The in-cylinder pressure histories of the knocking can be showed in ***Figure 1-8*** with yellow curve. Pressure oscillation is observed nearly after the pressure peak. Concerning the harmful effects of engine knock, it must be detected and then avoid by controlling the engine operation conditions or gas mixture quantity.

Engine knock can be detect by many different methods, which is summarized by Zhen et al (Zhen et al. 2012), in-cylinder pressure analysis (Millo 1998), cylinder block vibration analysis(Ettefagh et al. 2008), exhaust gas temperature analysis(Abu-Qudais 1996), intermediate radicals and species analysis(Merola et al. 2007), heat transfer analysis(Grandin 2000), and etc. The major drawbacks of pressure analysis are: high cost of the sensors, short lifetime of the sensors while working in high temperature and high pressure. As non-homogeneities take place when knock occurs, thus local pressure can not present the global domain, various accessories should be employed which may increase the cost and complicity of measurements. Cylinder block vibration analysis and exhaust gas temperature analysis give an indirectly measurement of knock parameters. Both of the two methods are very convenient, low cost and excellent durability. But the precision of the two methods should still be discussed. Engine knock can also detect by intermediate radicals and species analysis. As markers of normal combustion phases, the radicals CH, HCO, HCHO, and OH can be identified by spectroscopic and chemiluminescence measurements(Merola et al. 2007). CH and OH are considered as markers of normal combustion reaction and burned zone respectively. HCO can be detected in the end gas and in the reaction zone of ignition surface at onset of knocking. Heat transfer analysis can be another method to detect engine knock, Grandin (Grandin 2000) found that heat transfer to the walls of the combustion chamber is increased by engine knock. When knock intensities was above 0.2 MPa, the heat flux was influenced. At knock intensities above 0.6 MPa, the peak heat flux was 2.5 times higher than for a non-knocking cycle.

In order to avoid knock, engine parameters which can affect this phenomenon should be studied. Ferguson (Ferguson 1986) listed the parameters which can affect knock and their tendency on knock occurrence as showed in ***Table 1-2***. Engine speed, expressed as RPM (Round per minute) has a dual character for knock tendency. On the one hand, at low engine speeds the flame velocity is slow and thus the burn time is long, this results in more time for auto-ignition. However on the other hand, at high engine speeds there is less heat loss so the unburned gas temperature is higher which promotes auto-ignition. These are competitive effects: some engines show an increase in propensity to knock at high speeds while others

don't. All parameters listed bellow can influence the end gas thermodynamic conditions, which directly or indirectly change the end gas auto-ignition phenomenon. Moreover, fuel quality is also one of the main factors for the engine knock occurrence. The gas quality of the fuel, for example its ability to resist knock, is commonly represented by the methane number (MN). Normally, it is valued 100 for pure methane and 0 for pure hydrogen. For the liquid form of fuel, research octane number (RON) is employed to represent fuel knock resistance. It is usually equal to 100 for pure isooctane and 0 for n-heptanes.

Engine factor	Variation	Knock tendency
Compression ratio	Increase	+
Spark time	Advanced	+
Load	Increase	+
RPM	Increase	+/-
Combustion speed	Increase	-
AFR	Lean	-
	Lightly rich	+
	Very rich	-
Inlet temperature	Increase	+
Inlet pressure	Increase	+
Cooling temperature	Increase	+

Table 1-2. Engine parameters influencing knock tendency.(Ferguson 1986)

1.5 Application of Oxygen-Controlled combustion in downsized SI engine

Oxygen-enriched combustion is applied in various domains, including industrial furnaces, chemical processing, or biotechnology. It could also be a promising technique for further internal combustion engine developments (Kajitani et al. 1993; Poola et al. 1995; Caton 2005; Wu et al. 2007). The inexpensive production of O_2 is not straightforward, however, and requires close attention. Koros et al. (Koros et al. 1987) proposed a mechanism to supply oxygen-enriched air based on the use of a non-porous polymeric membrane, which is now extensively researched and applied (Poola et al. 1998; Coombe et al. 2007; Favre et al. 2009).

Several studies performed with oxygen enrichment in Spark-Ignition (SI) engines showed positive effects, which are summarized below:

- Reduction in UHC (Unburned Hydrocarbon fuel) and CO observed by Kajitani et al. (Kajitani et al. 1993) with an enrichment of 2% in 02, and confirmed by other authors (Ng et al. 1993; Poola et al. 1995; Poola et al. 1996).
- Optimisation of downsizing due to the direct effect on the combustion process and overall engine thermodynamics. Simulation results by Caton (Caton 2005) showed that with an enrichment of 10%, a 25% reduction in the displaced volume can be obtained.
- Increase in flame propagation velocity. This effect has been established by several previous studies in oxygen-enriched combustion for SI engines (Quader 1978; Kajitani et al. 1992).

A major drawback, however, is the increase in NO_x emission due to the higher flame temperature. One solution could be to dilute the charge, not with N_2, air or global Exhaust Gas

Recirculation but with carbon dioxide. As the heat capacity of CO_2 is higher than that of the other components of EGR, it may decrease the flame temperature and avoid high levels of NO_x emission. Moreover, the effects of oxygen-enriched combustion could be minimized by the addition of CO_2 (Zhu et al. 1989). The balance between these two effects appeared therefore to be worthy of further investigation for application to S.I. engines.

A new idea is to control the oxygen concentration combining with the polymer membrane technology. It can help to simplify the loop dilution of inlet gas of traditional EGR system, or even avoid it and respond in part to the different technological barriers that are still rising, such as increased performance, the control of abnormal combustion, the cycle to cycle fluctuations, the adequacy SI engine to the alternative fuels (CNG, alcohol ...) and hybrid vehicles that require a critical optimization of emissions regulated or non-regulated related to the increase of the turn off of the engine during the driving cycle.

In this context, this thesis aims to investigate the potential of the control of oxygen levels at the intake air. Indeed, the use of polymer membranes allows selective management of nitrogen/oxygen along the intake of the engine. These membranes which have a high potential of development, developed recently to solve a part of the CO_2 sequestration problem for fixed-site power generation for example, would deplete or enrich oxygen in the intake air while being compact, lightweight, embeddable in the vehicle and inexpensive by overcoming current problems of a loop EGR. The essential mechanisms are presented in ***Figure 1-10***. Three different concepts are depicted: current EGR dilution system, oxygen controlled by membrane and oxygen controlled with CO_2 dilution. Different from the current EGR dilution system, air is pre-selected to meet N_2 dilution or O_2 enrichment level as desired for oxygen controlled by membrane. For oxygen controlled with CO_2 dilution, CO_2 and a part of N_2 are re-circulated by membrane to dilute the O_2 enrichment combustion.

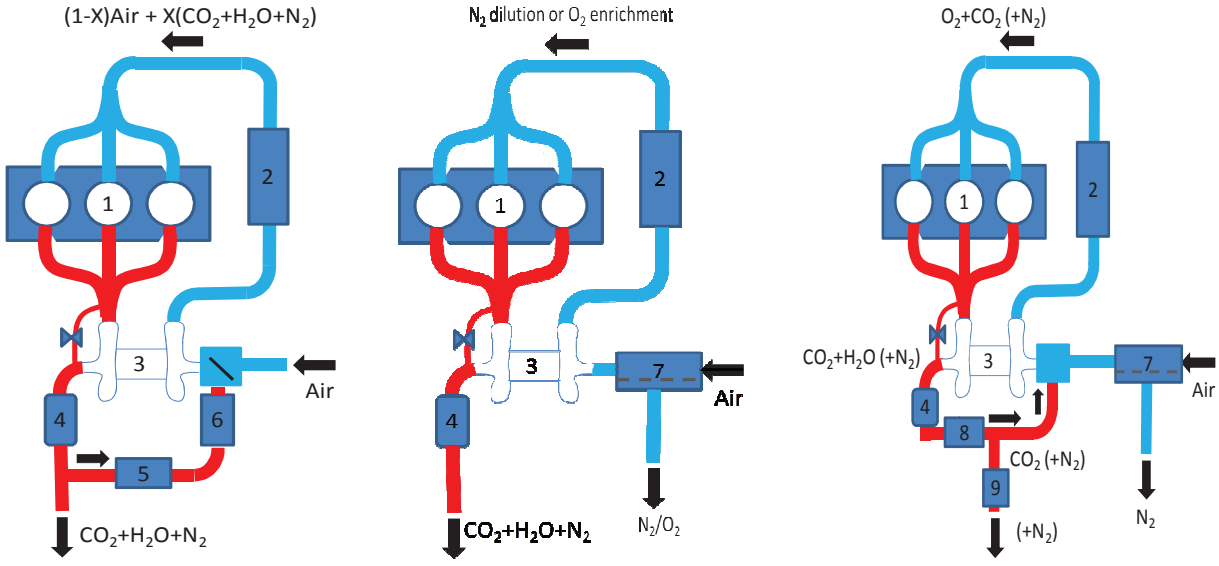

1: SI engine, 2: intercooler, 3: turbocharger, 4: three-ways Exhaust after treatment, 5: filter, 6: intercooler, 7: polymer membrane system, 8: condenser, 9: ceramic membrane

Figure 1-10. Comparison of current EGR dilution system (left), oxygen controlled by membranes (middle) and oxygen controlled with CO_2 dilution (right).

The advantages of oxygen controlled by membrane with/without CO_2 compare to current EGR loop are potentially:

- no clogging of the inlet due to the presence of soot and water vapor in the exhaust (stratified GDI increases the formation of soot)
- no heat exchanger to cool the re-circulated gases or to filter some of them which can damage the compressor
- no problem of homogeneity of the air-diluents
- better control of gas composition allowed to optimize the combustion process
- decreasing potentially the response time of gas dilution

In our study, firstly, oxygen controlled combustion (the middle case of ***Figure 1-10***) with various equivalence ratios in a downsizing engine is first studied. The controlling of oxygen percentage in air and equivalence ratios will both change the quality of the isooctane/air mixture. The advantages of lean mixture combustion in SI engine can be summarized as follow: first, pumping loses can be minimized especially when engine works in low load; second, the thermodynamic efficiency can be improved by decreasing wall heat loses and/or by increasing compression ratio. The two advantages corresponding to the engine performance can be explained by the left graph of ***Figure 1-11***. The lean mixture leads to higher efficiency, lower specific consumption, lower indicated mean effective pressure (IMEP). The decrease of IMEP is obvious, whereas the super-charge can be an effective way to settle this problem. The third advantage of lean mixture combustion is to minimize the engine pollutant emissions. As showed in the right hand of ***Figure 1-11***, the CO, HC, and NO_x emissions can all be minimized at equivalence ratio of 0.8.

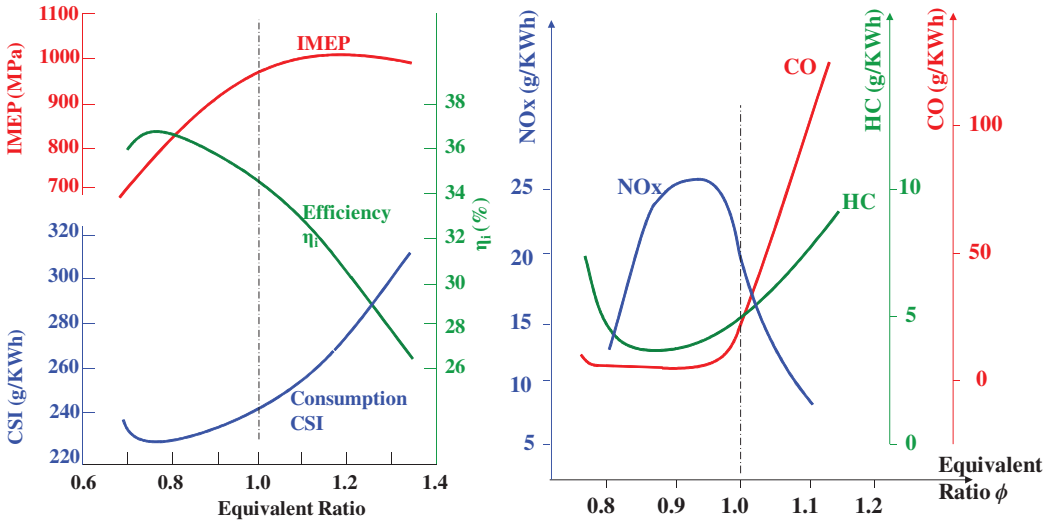

Figure 1-11. effects of equivalence ratio ϕ on CSI, η_i ,IMEP (left) and CO, HC, NOx emissions (right)

However, operating in lean mixture would be challenged by the problem of misfire and combustion stability. Thus, the oxygen enriched combustion can be a potential way to answer this problem. As we known, no work has been done to answer the coupling of oxygen enriched combustion with lean mixture. Therefore, one of our objectives is to analyze the coupling effect of oxygen enriched combustion and lean condition in downsized SI engine (chapter two). Moreover, the depletion of O_2 which can be considered also as N_2 dilution is also discussed.

In the second part of work (chapter three), we mainly focus on the characteristics of combustion for oxygen controlled fuel mixture. In all combustion processes, combustion behavior is linked to the laminar flame velocity. Knowledge of this fundamental parameter can provide a better understanding of the potential of oxygen enrichment. The objective of this study is therefore to investigate the effect of oxygen enrichment and N_2 dilution (19% O_2) on the laminar flame velocity in the case of iso-octane as fuel. The dilution by CO_2 is also considered here. The auto-ignition delay of same mixture will also be estimated using Senkin in this chapter. The estimation of two predominant parameters will then provide the basic data for engine combustion simulations.

The last part of this thesis (chapter four) is devoted to numerical simulation study of engine combustion. The combustion characteristics such as laminar/turbulent burning velocity, flame wrinkling, in-cylinder pressure will be discussed. Moreover, by controlling the gas quality (oxygen and equivalence ratio controlling), we can change the two predominant parameters for knock occurrence: laminar flame speed and auto-ignition delay. By varying equivalence ratio, the effective RON of the mixture can be changed: equivalence ratio bigger or smaller than unity can give an effective RON bigger than the RON of the fuel(Lafossas 2002). However the effect of oxygen percentage on knock is not clear. So the knock estimation and knock sensibility is investigated in the last part of chapter four.

Chapter two

Study of oxygen-controlled combustion in engine

2 Study of oxygen controlled combustion in engine

2.1 Introduction

The second chapter is devoted to describing experimental tools: both experimental setups and numerical analysis methods for the post treatment of results, and to analyze our experimental results on engine.

The first part of this chapter describes in details the single cylinder engine and all the other elements annexes to it, and then describes schematically the experimental setup used to perform all the experiments. A Matlab program was employed in order to analyze the heat release and study the progress of combustion from the pressure measurement. It was assumed that the mixture enclosed in the combustion chamber remains homogenous during combustion. The temperature and pressure of the mixture are supposed to be uniform.

In the second part of this chapter, experimental investigations on effects of oxygen controlled combustion in spark-ignition engine will be discussed for different rates of oxygen percentage (15% to 27% by volume in the total mixture of gases except evaporated fuel) and equivalence ratios (from 0.45 to 1). The study of the impact of oxygen controlled combustion with variation of equivalence ratios on combustion characteristics and emissions was performed with engine speeds at 1400 tr/min, and several different loads(from 4 to 10 in steps of 2). For each operation point, the spark advance and the intake pressure were varied simultaneously in order to maintain a constant engine load and obtain a minimum value of indicated specific consumption (SFC) at a fixed oxygen percentage and equivalence ratio.

2.2 Experimental setup

2.2.1 Engine characteristics

Experiments were carried out in a single-cylinder S.I. engine (PSA EP6) characterized by a four-valve pent-roof chamber with a displacement volume (V_{cyl}) of 399.5 cm^3 and a compression ratio of 10.5. A scheme of the engine is presented in ***Figure 2-1***. The bore, stroke and connecting rod length were 77 mm, 85.8 mm and 138.5 mm respectively. The engine was driven by an electric motor at a fixed engine speed, and equipped with an optical encoder mounted on the main shaft, giving a 0.1 Crank Angle Degree (CAD) as resolution. A conventional spark plug with an electrode space of 1mm was used. A timer card ensured synchronization of the various trigger signals and data acquisition systems. The engine sucks in the air through a thermal mass flowmeter and all other flows were evaluated from this reference flow. Oxygen, nitrogen and air flows were measured by using thermal mass flowmeters with an accuracy of ±0.7% for the instantaneous flow. Before the intake pipe, all the gases passed through a plenum volume, to avoid pressure oscillations inside the intake port. The iso-octane quantity was regulated by using a 0-8 kg/h Bronkhorst Coriolis mass flow controller with a maximum combined standard uncertainty of ±1% for the minimum flow rate considered in the present work. To provide a premixed air-fuel mixture inside the intake pipe, the fuel was vaporized and mixed inside the intake pipe just after the plenum to obtain a homogeneous air-fuel mixture. The air-fuel mixture temperature was kept constant at 70 °C by an electric heater. Cylinder pressure was recorded with a water-cooled AVL quartz pressure transducer connected to a charge amplifier at 0.1 CAD resolutions. The linearity (<±0.6%) of the transducer was verified starting from a maximum pressure of 10MPa (>maximum pressure in the engine). In this work, the absolute cylinder pressure was deduced

by equalizing the in-cylinder pressure at 20 CAD after inlet valve opening timing to the intake mean absolute pressure. Thus, 100 consecutive cycles of cylinder pressure data were acquired by a PC equipped with a National Instruments acquisition board.

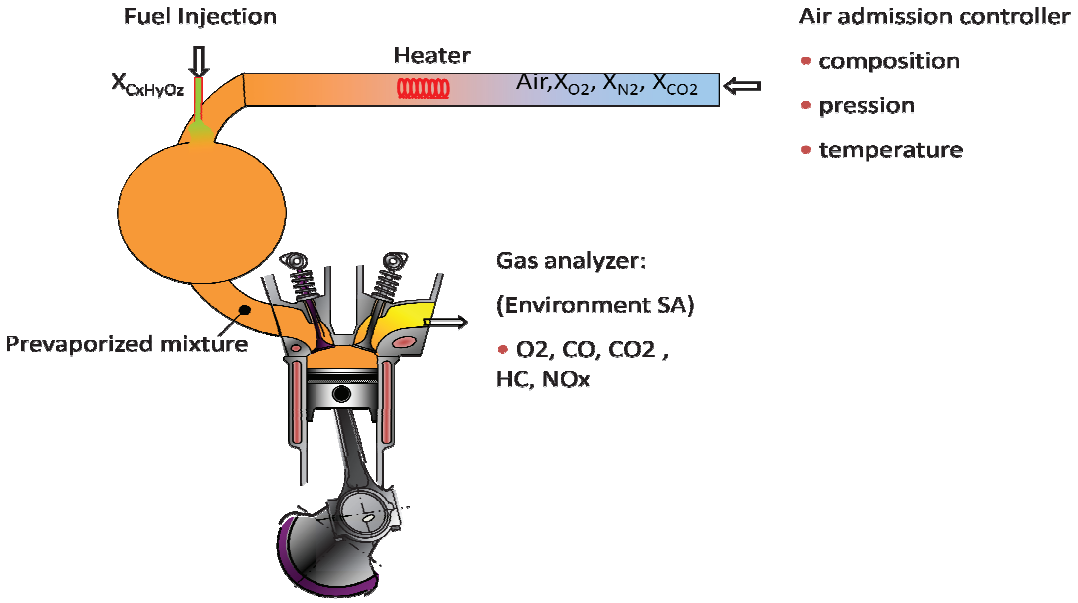

Figure 2-1. Scheme of EP6 mono-cylinder engine

The exhaust emissions of gases (NO_x, HC, CH_4, CO, CO_2, O_2) were measured by a classical emission analyzer (from Environment S.A) with an accuracy <2% of the measured value and 1% of full scale. O_2 emissions were determined by the polarization mode dispersion measuring technique. NO_x were measured by the chemiluminescent method. CO and CO_2 were detected by the non-dispersive infrared method while HC and CH_4 emissions were determined by the heated flame ionization detector method.

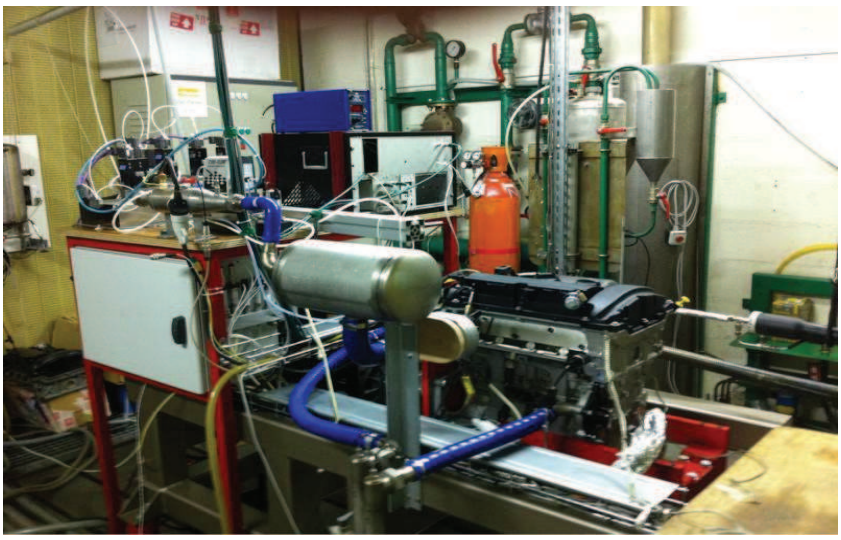

Figure 2-2. Real Image of engine

2.2.2 Engine control and measurement

In order to control and acquire a maximum of parameters during engine operation, the engine was equipped with different systems of measurement and monitoring, which can be grouped into three categories:

- Engine control: according to a desired operating point, the engine control should define and maintain all the control parameters. The engine was coupled to a direct current electric generator (32.4 KW), which can either drive the electric motor or became a brake receiver according to the torque delivered by the engine. The generator enslaved by an electronic control unit allows maintaining engine speed constant within ± 0.1%. A control interface developed by Labview can handle independently of all engine parameters.
- Slow acquisitions: slow acquisition is employed to measure the physical constants during an experimental operation, such as pollution emission, the ignition timing etc… thermocouples of type Pt100 were used for controlling the intake air(70 ° C), coolant (75 ° C) and engine oil (80 ° C). A thermocouple of type K was placed in the exhaust pipe so as to measure the temperature of exhaust gases. Pressure sensors provide absolute pressure average measurements of the coolant, engine oil and fuel pressure. All of these data are acquired via a controller and transmitted via an Ethernet port to the control computer. The control interface retrieves all values of these measurements and puts alarms on each of them to guarantee safety of the installation.
- Rapid acquisitions: Rapid acquisitions allow us to measure physical quantities which change rapidly during an engine operation. The pressure in the combustion chamber was measured by a piezoelectric sensor (0-250 bar) located in the cylinder head. An amplifier conditions the signal from the sensor to provide a signal with voltage, which is proportional to the pressure. Note that this type of sensor does not record the absolute value of the pressure but only the relative value. Then it is necessary to adjust this value relative to an absolute pressure. The absolute value of the admission pressure is, for its part, measured by a Kistler sensor Type 4005AA5 (0-5 bars). The data measured by the sensors was collected and stored on a second computer via a National Instrument acquisition unit. A visualization interface retrieved all the values of these measures, and the alarms on every value were set to guarantee the safety of the installation.

2.3 Combustion analysis

The analysis of physical quantities related to the engine, particularly cylinder pressure, allows us to obtain information on combustion characteristics. The employment of thermodynamic laws allows us to deduce other physical quantities from in-cylinder pressure such as: temperature, heat release rate, burned mass fraction and so on.

Analysis models in our study are based on cylinder pressure measurement. For the absolute value of the in-cylinder pressure, it is necessary to readjust the recorded signals respect to a reference. Based on the work of Burnt et al., the cylinder pressure in the vicinity of dead bottom center during intake stroke can be assumed to be equal to the pressure measured in the intake manifold. Because the pressure measurement carried out in the intake manifold provides an absolute value, the in-cylinder pressure can be deduced by calibrating the measured in-cylinder value to intake manifold pressure.

2.3.1 Single zone analysis model

The single zone model is considered zero-dimensional and follows several hypothesis:

- During the combustion process, the gas mixture inside the combustion chamber remains homogeneous and does not distinguish between unburned and burned gas.
- Pressure and temperature of gas mixture are considered uniform and the thermodynamic state of the mixture is defined in terms of average properties.
- Each element of the combustion gases is therefore instantly mixed with fresh gas and the gas previously burned.
- The thermodynamic transformations are no mass transfer, but with an energy exchange with the surroundings (walls of the combustion chamber, the piston and the cylinder head).
- The phenomena of leakage during combustion, causing mass loss in the combustion chamber, and the effects of crevices are assumed negligible.

According to the first law of thermodynamics, the energy balance equation for combustion chamber can be expressed as:

$$\frac{dU}{d\theta} = \frac{dQ_c}{d\theta} + \frac{dW}{d\theta} + \frac{dQ_p}{d\theta} \qquad \text{Equation 2-1}$$

Where U is the internal energy of gases in the combustion chamber, θ: the crank angle, Q_c: the heat produced by combustion, W: the work applies to piston, and Q_p: the wall heat loss. Then with the ideal gas assumption, the simplified heat release rate can be deduced by:

$$\frac{dQ_c}{d\theta} = \frac{\gamma}{\gamma-1} P_{cyl} \frac{dV_{cyl}}{d\theta} + \frac{1}{\gamma-1} V_{cyl} \frac{dP_{cyl}}{d\theta} \qquad \text{Equation 2-2}$$

Where γ is the isentropic coefficient of gases in the chamber, P_{cyl} and V_{cyl} are the in-cylinder pressure and volume respectively. In this study, the gas mixture can be considered as a mixture of ideal gases and specific heat coefficients C_p and C_v depend only on temperature. The thermodynamic properties of each species are approximated by polynomial JANAF tables.

Heat losses represent a significant proportion of the energy released during the combustion (between 20 and 30% of the energy introduced). In thermodynamic models, the heat flow is determined from a transfer coefficient which includes the radiative and convective term. The radioactive term is neglected here because it is usually approximately 3-4% of transfers (Trapy 1981). The burned mass fraction (BMF) is the degree of progression of combustion and is defined as the ratio of heat release on the energy introduced:

$$BMF = \frac{1}{m_{carb}.PCI.\eta_{comb}} \int_{RFA}^{AOE} \left(\frac{dQ_c}{d\theta} + \frac{dQ_p}{d\theta} \right) \qquad \text{Equation 2-3}$$

Where m_{carb} is the mass of fuel introduced into the chamber, PCI is the heating value of fuel, η_{comb} is the combustion efficiency, RFA is the delay in closure of admission and AOE is the exhaust valve opening advance.

From the burned mass fraction, the CA05, CA10, CA50 and CA90 which are necessary to characterize the combustion duration can be determined. The CA05, CA10, CA50 and CA90 represent the crankshaft angles for which 5%, 10%, 50% and 90% of the total energy were identified respectively.

The crank angle degree duration of the flame development is often considered as the period from the moment of ignition to 10% of burned mass fraction (Heywood 1988; Gupta et al. 1996).

$$\Delta\theta_d = CA10 - ignition\ advance \quad \text{Equation 2-4}$$

The first half crank angle degree of the combustion is defined by the relation:

$$\Delta\theta_m = CA50 - CA10 \quad \text{Equation 2-5}$$

Then the total combustion crank angle degree is defined by:

$$\Delta\theta_c = CA90 - CA10 \quad \text{Equation 2-6}$$

2.4 Emission analysis

The exhaust emissions of NO_X, HC, CH_4, CO, CO_2, and O_2 from the test engine were measured by a classical emission analyzer (from Environment S.A). There are two different type of measurement: one is dry gas type for CO, CO_2 and O_2 measurements and the other is humid gas type for NO_x and HC measurements. Thus, firstly we should convert humid gas type to dry gas type by defining a parameter K_b. Then to verify and give a more precise value of equivalence ratio of gas mixture, equivalence ratio of 5 gases is deduced by exhaust emissions analysis.

2.4.1 Converting humid gas type to dry gas type

For specie X, the molar percentage of dry gas basis can be expressed as:

$$[X]_{dry} = [X]_{humid}/K_b \quad \text{Equation 2-7}$$

Thus,

$$\frac{n_X}{n_{tot\ hum}} = \frac{1}{K_b}\frac{n_X}{n_{tot\ dry}} \quad \text{Equation 2-8}$$

Finally, the parameter K_b can be deduced by following equation:

$$K_b = \frac{n_{tot\ dry}}{n_{tot\ hum}} \quad \text{Equation 2-9}$$

To calculate the Kb, several hypotheses are employed: HC is considered as formula $C_\alpha H_\beta$, and a chemical equilibrium is used for giving a relationship between H2 and CO percentages, $[H_2] = \delta\,[CO]$, with and NO_x is supposed to be NO_w.

For a fuel of basic formula CH_yO_Z, the global reaction of the mixture can be defined as follows:

$$\phi.CH_YO_Z + \left(1+\frac{Y}{4}-\frac{Z}{2}\right).(O_2+\chi.N_2) \rightarrow n_{CO2}.CO_2 + n_{CO}.CO + n_{H2}.H_2 + n_{O2}.O_2 + n_{H2O}.H_2O + n_{C_\alpha H_\beta}.C_\alpha H_\beta + n_{N2}.N_2 + n_{NOx}.NO_w$$

Equation 2-10

Where ϕ is fuel equivalence ratio, χ is the mole proportion of N_2 and O_2, with $\chi = [N_2]/[O_2]$. By atom balancing of C and H, following equation can be established:

$$\phi = n_{CO_2} + n_{CO} + \alpha.n_{C_\alpha H_\beta} \quad \text{Equation 2-11}$$

$$\phi Y = 2.n_{H_2} + 2.n_{H_2O} + \beta.n_{C_\alpha H_\beta} \quad \text{Equation 2-12}$$

Combining these above balancing equations, the following equation can be written:

$$Y\left(n_{CO_2} + n_{CO} + \alpha.n_{C_\alpha H_\beta}\right) = 2.n_{H_2} + 2.n_{H_2O} + \beta.n_{C_\alpha H_\beta} \quad \text{Equation 2-13}$$

With the condition of $n_{H_2O} = n_{tot\ hum} - n_{tot\ dry}$, and dividing the above equation by $\frac{n_{tot\ dry}}{100}$:

$$Y\left([CO_2]^{\%}_{sec} + [CO]^{\%}_{sec} + \alpha.[C_\alpha H_\beta]^{\%}_{sec}\right) = 2.[H_2]^{\%}_{sec} + 200.\left(\frac{1}{K_b} - 1\right) + \beta.[C_\alpha H_\beta]^{\%}_{sec} \quad \text{Equation 2-14}$$

This expression can then be simplified by using the hypotheses:

$$[H_2]_{sec} = \delta.[CO]_{sec}$$

$$[C_\alpha H_\beta]_{sec} = \frac{1}{K_b}[C_\alpha H_\beta]_{hum}$$

$$[C_\alpha H_\beta]^{\%} = \frac{1}{\alpha}.10^{-4}.[HC]_{ppmc}$$

So the balancing equation can be expressed as:

$$Y[CO_2]^{\%}_{sec} + (Y - 2\delta)[CO]^{\%}_{sec} = 200\left(\frac{1}{K_b} - 1\right) + \left(\frac{\beta}{\alpha} - Y\right)\frac{1}{K_b}.10^{-4}.[HC]^{ppmc}_{hum} \quad \text{Equation 2-15}$$

From this equation, Kb can be finally deduced:

$$K_b = \frac{200 + \left(\frac{\beta}{\alpha} - Y\right)[HC]^{ppmc}_{hum}}{200 + Y[CO_2]^{\%}_{sec} + (Y - 2\delta).[CO]^{\%}_{sec}} \quad \text{Equation 2-16}$$

If we suppose $\frac{\beta}{\alpha} = \frac{y}{x} = Y$, which x and y are the number of atoms of fuel formula as $C_xH_yO_z$ before simplifying by CH_YO_z:

$$Kb = \frac{200}{200 + Y.[CO_2]^{\%}_{sec} + (Y - 2\delta).[CO]^{\%}_{sec}} \quad \text{Equation 2-17}$$

In above equation, we can deduce Kb from CO_2 and CO measurement, and then by using this parameter K_b, the measurement of humid type can then be converted to dry gas type.

2.4.2 Equivalence ratio of 5 gases

During the experiments, the equivalence ratio can be set by Labview program, thus with this equivalence ratio, the program determined the necessary fuel quantity for injection. This equivalence ratio called 'equivalence ratio of flow meter' is influenced by mass flow meter, and therefore maybe have less precision than equivalence ratio of 5 gases. Moreover,

equivalence ratio of 5 gases can also be a factor for verifying the validity of our experimental results.

In this part, the calculation of equivalence ratio by the method of the five gases (CO_2, CO, HC, O_2, NO_x) is discussed. This method is based on analyzes of dry gas and takes into account the presence of nitrogen oxides in exhaust gases. The average formula of the fuel is CH_YO_Z, it ignores the presence of nitrogen (N) in the fuel.

With the measurement of emission analyzer (from Environment S.A) and the parameter K_b, the dry exhaust gas concentrations (% CO_2, % CO, %O_2, % NO_x, %HC) can be determined. Here, the gas concentrations are expressed by gas volume percentages, which is considered as same as numbers of moles of 100 moles total dry gas with ideal gas assumption. It is estimated the compositions statistics of unburned hydrocarbons (HC) and nitrogen oxides (NOx) in exhaust gas by the values of a, b and w. In this case, the basic chemical formula of HC and Nox can be written C_aH_b, NO_w respectively. It is assumed that, regardless of equivalence ratio and oxygen percentage in air, the equilibrium composition of H_2 and CO can be determined by the relation: % H_2=δ. % CO. the humidity of the total gas is estimated as ε%. Writing the balance sheets of different elements results in the following equations:

(1) $Bilan\,C$ $\quad \Phi = n_{CO2} + n_{CO} + \alpha . n_{C\alpha H\beta}$

(2) $Bilan\,H$ $\quad \Phi . Y = 2.n_{H2} + 2.n_{H2O} + \beta . n_{C\alpha H\beta}$

(3) $Bilan\,O$ $\quad \Phi . Z + 2.\left(1 + \frac{Y}{4} - \frac{Z}{2}\right) = 2.n_{CO2} + n_{CO} + 2.n_{O2} + w.n_{NOx} + n_{H2O}$

(4) $Bilan\,N$ $\quad 2.\chi.\left(1 + \frac{Y}{4} - \frac{Z}{2}\right) = 2.n_{N2} + n_{NOx}$

(5) $Bilan \quad dry \quad gas \quad concentrations$ $\quad 100 - \varepsilon = n_{CO2} + n_{CO} + n_{H2} + n_{O2} + n_{C\alpha H\beta} + n_{NOx} + n_{N2}$

Thus, with the above balance equations, the equivalence ration of 5 gases can be deduced:

$$\Phi = 1 + \chi . \frac{A - B}{C}$$

Equation 2-18

Where A, B, C can be expressed as:

$$A = CO_2(\%) + CO(\%) + 10^{-4}.HC\ (ppmC)$$

$$B = \frac{1-\delta}{2}.CO\ (\%) + CO_2(\%) + O_2(\%) - \frac{1}{4}.\left(\frac{\beta}{\alpha}\right).10^{-4}.HC(ppmC) + \frac{1}{2}.w.10^{-4}.NO_x(ppm)$$

$$C = 100 - \varepsilon\ (\%) - (1+\delta).CO\ (\%) - CO_2(\%) - O_2(\%) - \frac{1}{\alpha}.10^{-4}.HC\ (ppmC) - \frac{1}{2}.10^{-4}.NO_x(ppm)$$

In this equation of the equivalence ratio, the formula of the fuel is not involved; it means that this expression can be used commonly for any kind of fuel. But in our case of study, mole proportion of N_2 and O_2 (χ) changes when oxygen concentration in air is varied.

For isooctane fuel, the parameters mentioned above can be determined:

- $\alpha = 8,\ \beta = 18$

- $w = 1.2$, this formula implies a distribution: $NO_x = 80\%NO + 20\%NO_2$. This distribution takes into account of the NO oxidation when the gas transfers to the analyzer, although, practically, only NO is formed in the engine.
- $\delta = 0.3$
- $\varepsilon = 1\%$

2.5 Operating conditions and engine parameters

The oxygen controlling is realized by adding oxygen or nitrogen in air of ambient. For simplification, we suppose that air is consist of 21% O_2 and 79% N_2, in this case, if we need O_2 percentage more than 21%, O_2 should be supplied by a compressed O_2 high pressure tank. Otherwise, if we want O_2 percentage less than 21%, than N_2 will be produced by a N_2 producing machine. Here, the percentage is defined as volume fraction:

$$X_{O_2} = \frac{V_{O_2}}{V_{O_2}+V_{N_2}}.100\% \qquad \text{Equation 2-19}$$

Thus, for $X_{O_2} > 21\%$, we have:

$$X_{O_2} = \frac{0.21V_{air}+V_{O_2}}{V_{air}+V_{O_2}} \qquad \text{Equation 2-20}$$

And we suppose: $V_{air} + V_{O_2} = 1$

For $X_{O_2} < 21\%$, we have:

$$X_{O_2} = \frac{0.21V_{air}}{V_{air}+V_{N_2}} \qquad \text{Equation 2-21}$$

And we suppose: $V_{air} + V_{N_2} = 1$

Then, the volume fraction of air, O_2 and N_2 can be determined for a given O_2 percentage:

for $X_{O_2} > 21\%$	$V_{O_2} = \frac{X_{O_2} - 0.21}{0.79}$
	$V_{air} = \frac{1.21 - X_{O_2}}{0.79}$
for $X_{O_2} < 21\%$	$V_{N_2} = \frac{0.21 - X_{O_2}}{0.21}$
	$V_{air} = \frac{X_{O_2}}{0.21}$

Table 2-1. determination of the volume fraction of air, O2 and N2 for different cases.

The equivalence ratio was defined, based on the quantity of oxygen and not on the quantity of air.

$$\phi = \frac{Stoichiometric \quad O_2 / fuel \quad ratio}{actual \quad O_2 / fuel \quad ratio} \qquad \text{Equation 2-22}$$

As the global reaction of the mixture can be defined as follows:

$$C_8H_8 + \frac{12.5}{\phi}\left(O_2 + \frac{X_{N_2}}{X_{O_2}}N_2\right)$$

$$\rightarrow \frac{8}{\phi}CO_2 + \frac{9}{\phi}H_2O + \frac{12.5}{\phi}\frac{X_{N_2}}{X_{O_2}}N_2 + M, \text{ for rich mixture}$$

$$\rightarrow 8CO_2 + 9H_2O + 12.5\frac{X_{N_2}}{X_{O_2}}N_2 + M, \text{ for lean mixture}$$

With M, the quantity of excess air or unburned fuel for lean or rich mixtures respectively. CO_2 in air was not investigated here, so X_{CO_2} is zero. Thus, for a given equivalence ratio ϕ, fuel mass flow rate is directly linked to O_2 mass flow rate.

In order to compare N_2 dilution (O_2 < 20.9%) or O_2 enrichment (O_2 > 20.9%) to EGR percentage for a fixed equivalence ratio, the equivalence between them was calculated with the approximation of replacing the inert gases CO_2 and H_2O by N_2. Based on the study of Dubreuil (Dubreuil 2008), the one step reaction can be written:

$$C_xH_y + \underbrace{\left[\frac{(1-\tau)(1+e)-\tau}{1-\tau}\right]}_{\textbf{E+1}}\left(x+\frac{y}{4}\right)(O_2 + 3.78N_2) + \frac{\tau}{1-\tau}\left(xCO_2 + \frac{y}{2}H_2O + 3.78\left(x+\frac{y}{4}\right)N_2\right)$$

$$\longrightarrow \frac{1}{1-\tau}\left(xCO_2 + \frac{y}{2}H_2O + 3.78\left(x+\frac{y}{4}\right)N_2\right) + \underbrace{\left[\frac{(1-\tau)(1+e)-1}{1-\tau}\right]}_{\textbf{E}}\left(x+\frac{y}{4}\right)(O_2 + 3.78N_2)$$

In this equation, we can assign E as:

$$E = \frac{(1-\tau)(1+e)-1}{1-\tau} \qquad \text{Equation 2-23}$$

Using the similarity of equation of combustion without EGR, the equivalence ratio can be deduced by:

$$\phi_\tau = \phi = \frac{1}{1+E} \qquad \text{Equation 2-24}$$

By consuming one unity mole number of fuel, the mole quantities of species can be summarized below:

Fuel	1
Air	$4.78(E+1)\left(x+\frac{y}{4}\right)$
CO_2	$x\left(\frac{\tau}{1-\tau}\right)$
H_2O	$\frac{y}{2}\left(\frac{\tau}{1-\tau}\right)$
N_2(except N2 in air)	$3.78\left(x+\frac{y}{4}\right)\left(\frac{\tau}{1-\tau}\right)$
Total O_2	$(E+1)\left(x+\frac{y}{4}\right)$
Total 'N_2'	Air - Total O2 + CO2+ H2O+ N2

Once the equivalence ratio ϕ_τ and EGR dilution rate τ are set, the O_2 percentage can be get by: Total O_2/ (Total 'N_2'+ Total O_2). By reverse calculation, EGR dilution rate τ can be calculated once O_2 percentage and equivalence ratio are set.

Equivalence between N_2 dilution (O_2 < 20.9%) or O_2 enrichment (O_2 > 20.9%) and EGR percentage for a fixed equivalence ratio is presented in Table 2.2 and Figure 2.3. Negative dilution presents the O_2 enrichment, which also means that the N2 is taken away from air. Thus the quantities of CO_2 , H_2O, N_2(except N_2 in air) can be negative values.

O2 %	Phi=1	Phi=0.9	Phi=0.8	Phi=0.7	Phi=0.6	Phi=0.5
15	26.87%	28.95%	31.45%	34.40%	37.95%	42.35%
17	17.65%	19.25%	21.15%	23.45%	26.35%	30.00%
19	8.60%	9.45%	10.50%	11.85%	13.55%	15.85%
21	-0.35%	-0.40%	-0.45%	-0.50%	-0.60%	-0.70%
23	-9.20%	-10.30%	-11.75%	-13.65%	-16.30%	-20.25%
25	-17.90%	-20.30%	-23.40%	-27.65%	-33.85%	-43.55%
27	-26.50%	-30.30%	-35.45%	-42.65%	-53.65%	-72.05%

Table 2-2. Equivalence between N2 dilution (O2 < 20.9%) or O2 enrichment (O2 > 20.9%) and EGR percentage for a fixed equivalence ratio.

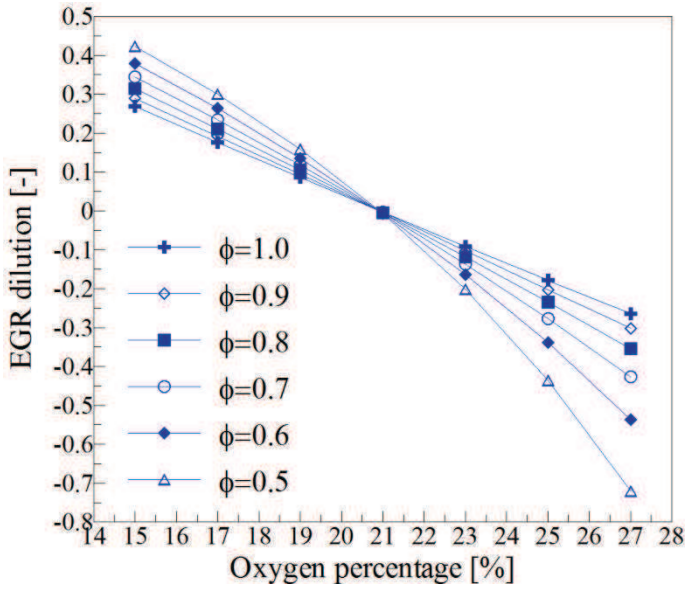

Figure 2-3. Equivalence between N2 dilution (O2 < 20.9%) or O2 enrichment (O2 > 20.9%) and EGR percentage for a fixed equivalence ratio

The different operation points employed in engine test bench are presented in ***Figure 2-4***. The figure on the left hand presents varies conditions of Indicated mean effective pressure and oxygen percentage. For conditions which marked with rounded rectangle, different equivalence ratios for fixed IMEP 8 bar are exhibited on the right hand of the ***Figure 2-4***. In the same case, equivalence ratios for IMEP 4 bar, 6 bar, and 10 bar were also investigated, although the operation points are not presented here.

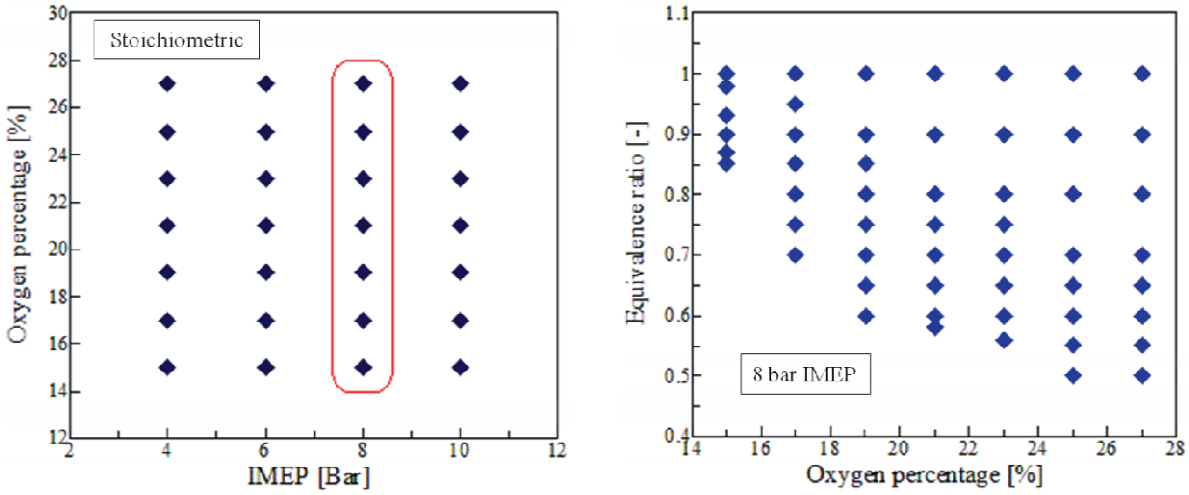

Figure 2-4. Presentation of the different operation points employed in engine test bench

For the test, indicated mean effective pressure (IMEP) was adjusted to be a quasi constant value, and the spark ignition was set at the optimum spark timing (OST), which makes engine have lower specific fuel consummation (SFC). The intake pressure was also adjusted during the operation. So that for given equivalence ratio and O_2 percentage, the IMEP is adjusted by advance spark timing and the intake pressure, meanwhile, the exhaust pressure was set as the same value as intake pressure, to simulate the same condition of a turbocharger. The value of COV_{imep} was used as a criterion in this study to determine the lean and N_2 dilution operation limits. COV_{imep} is defined as:

$$COV_{imep} = \frac{std_{imep}}{imep_n}.100\% \qquad \text{Equation 2-25}$$

Where std_{imep} is the standard deviation of the net IMEP ($imep_n$). COV_{imep} exceed 5% was considered as the operation limits.

2.6 Results and discussion

2.6.1 Indicated mean effective pressure

The evolution of indicated specific fuel consummation (SFC) versus equivalence ratio is presented in ***Figure 2-5*** for different indicated mean effective pressures (IMEP) (400 kPa, 600kPa, 800kPa and 1000 kPa). In these figures, the O_2 percentage in air varies from 15 to 27 percents. For each O_2 percentage, equivalence ratio is descended to reach the lean operation limits. With the decrease in the equivalence ratio, SFC was decreased for a fixed O_2 percentage, although the operation limits normally accompany with an expected SFC increase.

On the right hand of the graphs, the SFC and optimal SFC value are presented versus O_2 percentage. Optimal SFC is defined by the minimum SFC value of different equivalence ratio at a fixed O_2 percentage.

For IMEP 400 kPa and 600kPa (***Figure 2-5a*** and ***Figure 2-5b***), by increasing the O_2 percentage in air and decreasing the equivalence ratios, a lower SFC can be obtained. Compared to the conventional operating point (with 21% O_2, and stoichiometric case), SFC can be reduced by 15%. The lowest SFC is found at an O_2 percentage around 25% and 27% with an equivalence ratio of 0.5 to 0.55, which means that oxygen-enriched combustion with a low equivalence ratio can be a potential method for improving fuel efficiency.

For IMEP 800 kPa (***Figure 2-5c***), and an O_2 percentage from 15% to 19%, a lower SFC can be obtained by increasing the O_2 percentage while reducing the equivalence ratio, which is similar to the cases of IMEP 400 kPa and 600kPa. But for an O_2 percentage from 21% to 27%, this tendency is reversed. The lowest SFC for IMEP 800kPa is found at 19% O_2 with an equivalence ratio 0.7.

For IMEP 1000 kPa (***Figure 2-5d***), the lowest SFC is obtained at 15% O_2 with an equivalence ratio of 0.9. In this case, the dilution of N_2 will be a better way than oxygen enrichment to limit fuel consumption. Compared to the regular operating point (with 21% O_2, and a unit equivalence ratio), N_2 dilution has a potential for achieving about 10% of fuel economy.

It can therefore be concluded that for low IMEP (400kPa, 600kPa), oxygen enrichment is a potential way to improve fuel efficiency, whereas for high IMEP (800kPa, 1000kPa), N_2 dilution should be used to have a better fuel economy.

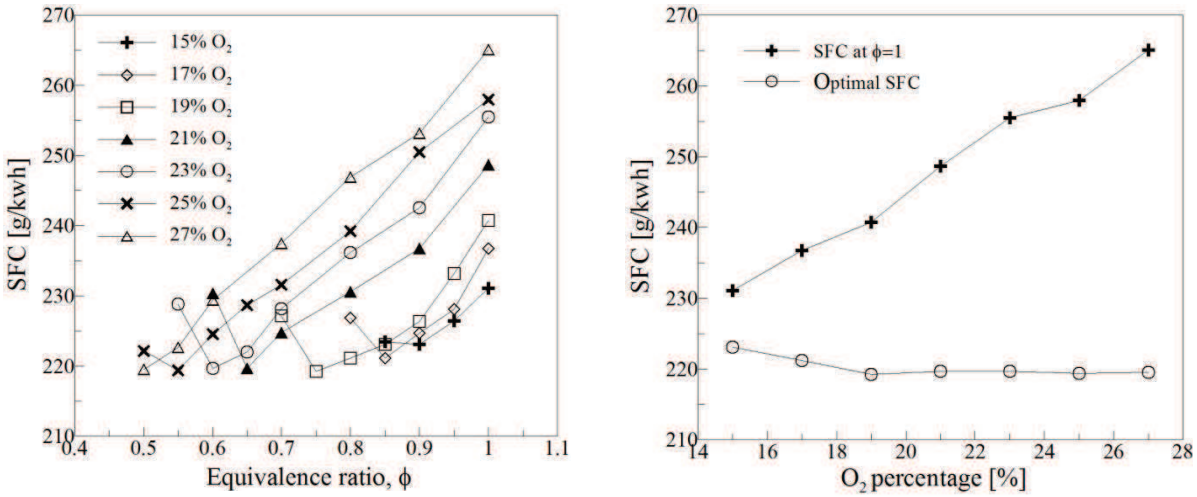

Figure 2-5a. IMEP=400kPa

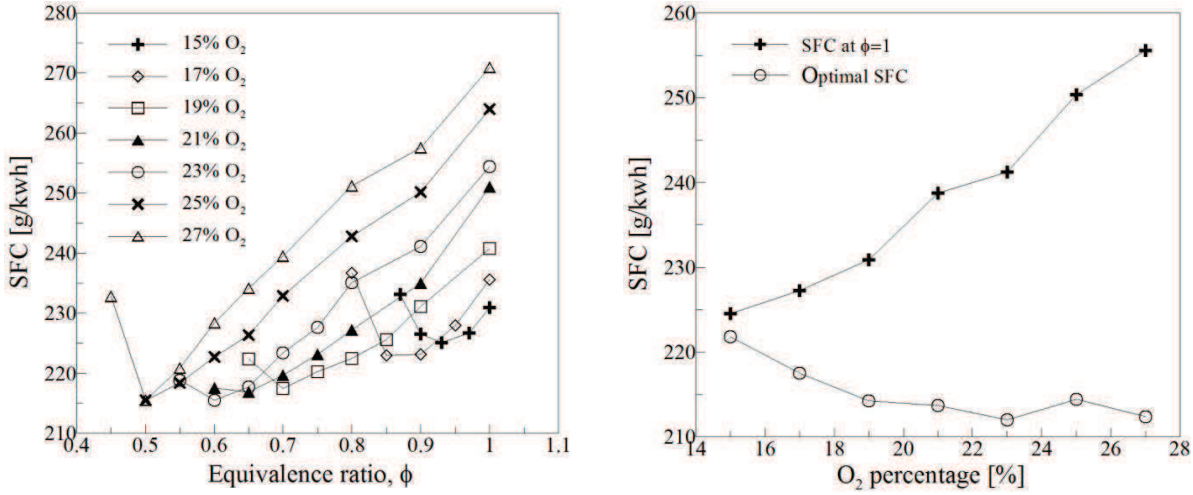

Figure 2-5b. IMEP=600kPa

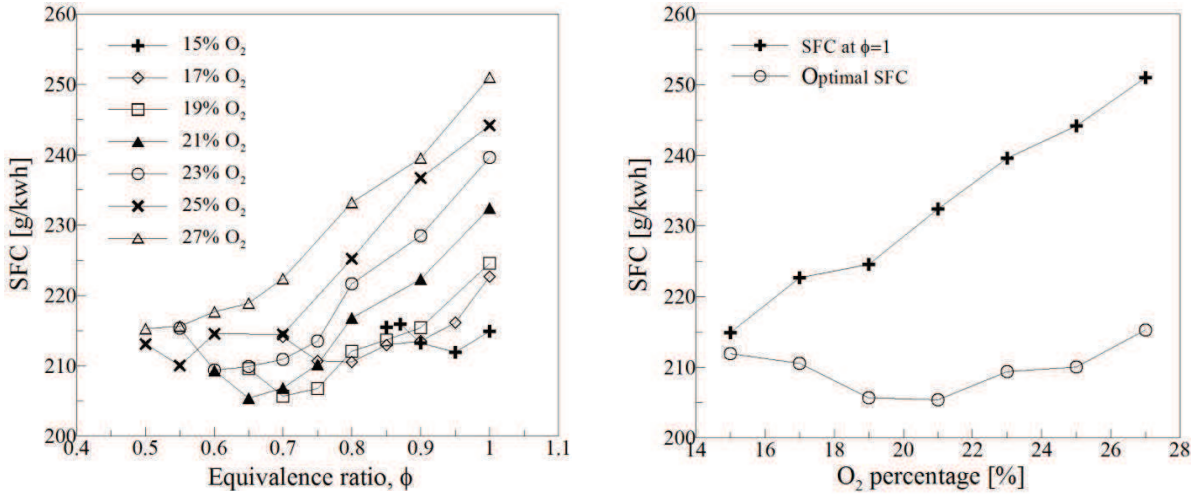

Figure 2-5c. IMEP=800kPa

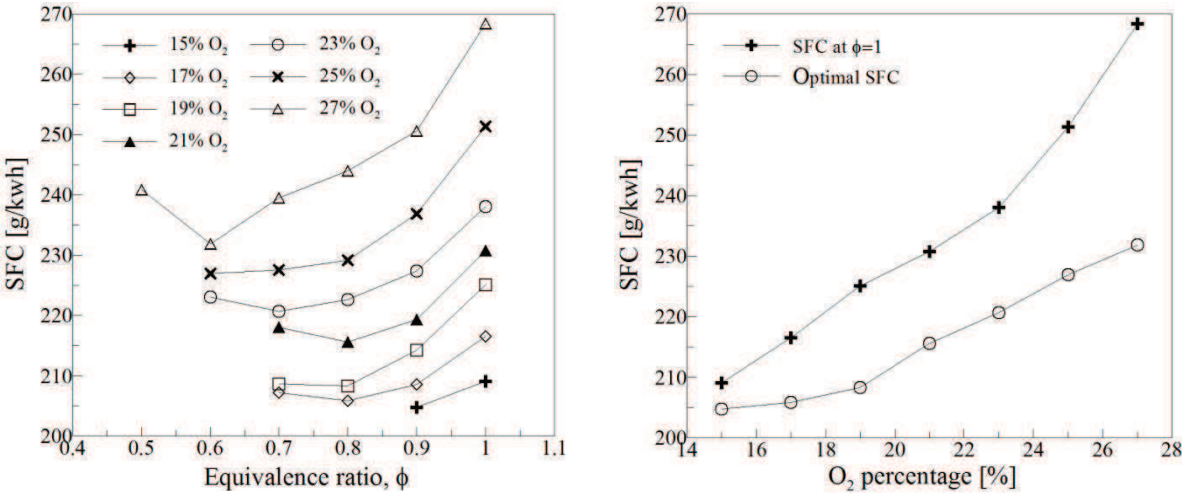

Figure 2-5d. IMEP=1000kPa

Figure 2-5. the evolution of indicated specific fuel consummation (SFC) versus equivalence ratio with different IMEP (a. IMEP=400kPa, b. IMEP=600kPa, c. IMEP=800kPa, d. IMEP=1000kPa)

2.6.2 HC emissions

There are four possible HC emissions formation mechanisms for spark ignition engine: first, flame quenching at the combustion chamber walls, which leaves a layer of unburned fuel-air mixture adjacent to the wall; second, the crevice volumes provide spaces for unburned mixture to escape the primary combustion process; third, absorption of oil layers during intake and compression strokes and the desorption of fuel vapor into cylinder during expansion and exhaust strokes. Finally, incomplete combustion in a fraction of the engines operating cycles.

Figure 2-6 represents the evolution of indicated specific HC emissions versus equivalence ratio with four different IMEP (a. IMEP=400kPa, b. IMEP=600kPa, c. IMEP=800kPa, d. IMEP=1000kPa).

The effect of oxygen enrichment on HC emissions is obvious. For every fixed equivalence ratio, the HC emission decreases with the increase in the O_2 percentage and the lowest values always are found at 27% O_2. One of the reasons is that oxygen enrichment provides higher combustion velocity, which improves the combustion efficiency. Furthermore, oxygen enrichment can also decrease the quenching distance of the mixture. In the study by Friedman et al. (Friedman et al. 1950), quenching distance was found to be a decreasing function of flame temperature, and it is well known that the flame temperature increases in the case of oxygen enrichment (Zhou et al. 2011). Mazas et al. (Mazas et al. 2011) also showed that quenching effects at the flame foot are reduced due to the increase in the flame temperature when the oxygen-enrichment ratio is increased. Thus oxygen enrichment allows the flame to propagate much closer to the cylinder wall than does the N_2 dilution mixture.

The specific HC emission increases when the equivalence ratio varies from 0.9 to 1. However, the HC emission decreases from the lean limits to an equivalence ratio of 0.9. The lowest value can be found around an equivalence ratio of 0.9.

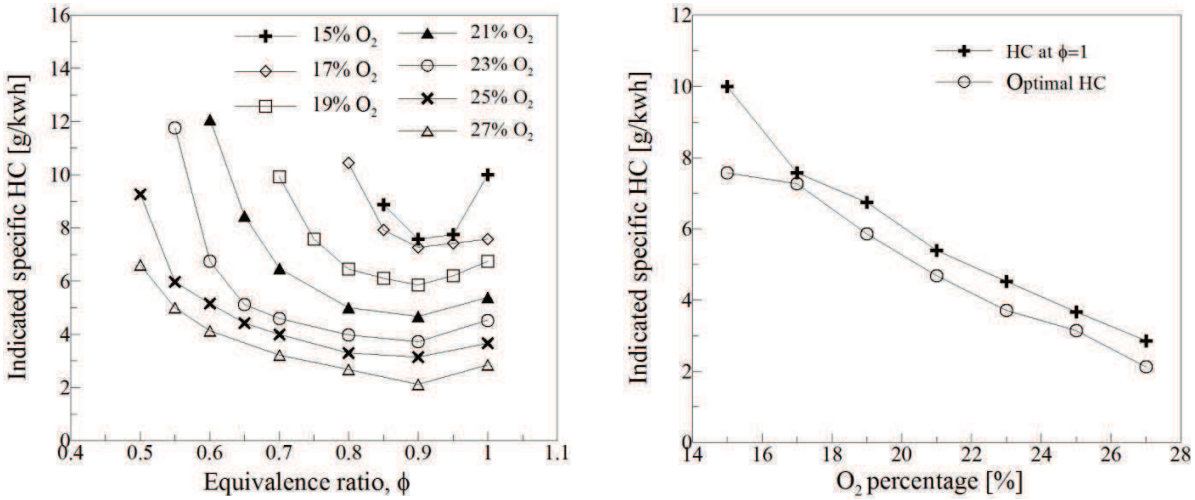

a. IMEP=400kPa

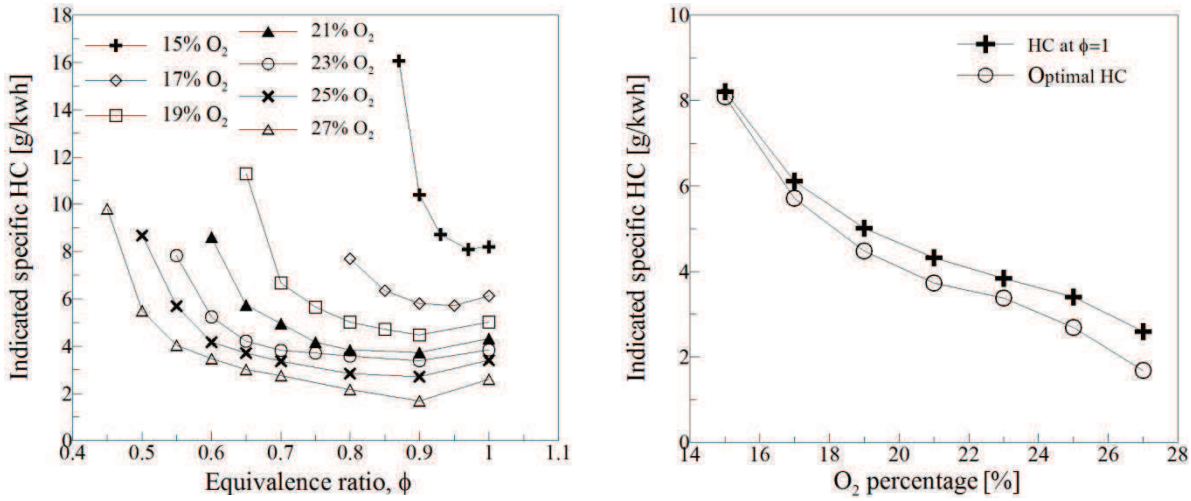

b. IMEP=600kPa

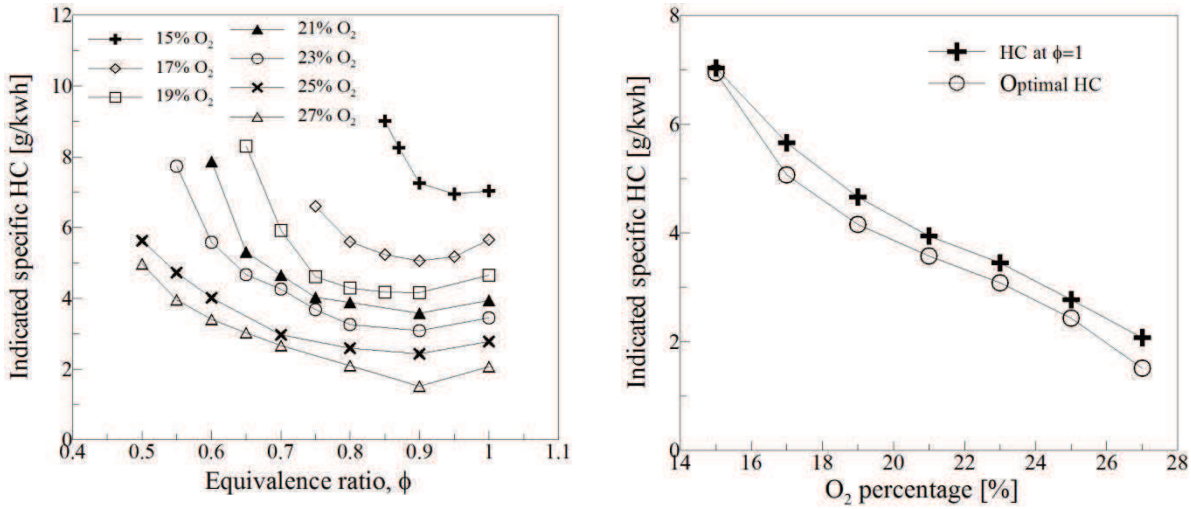

c. IMEP=800kPa

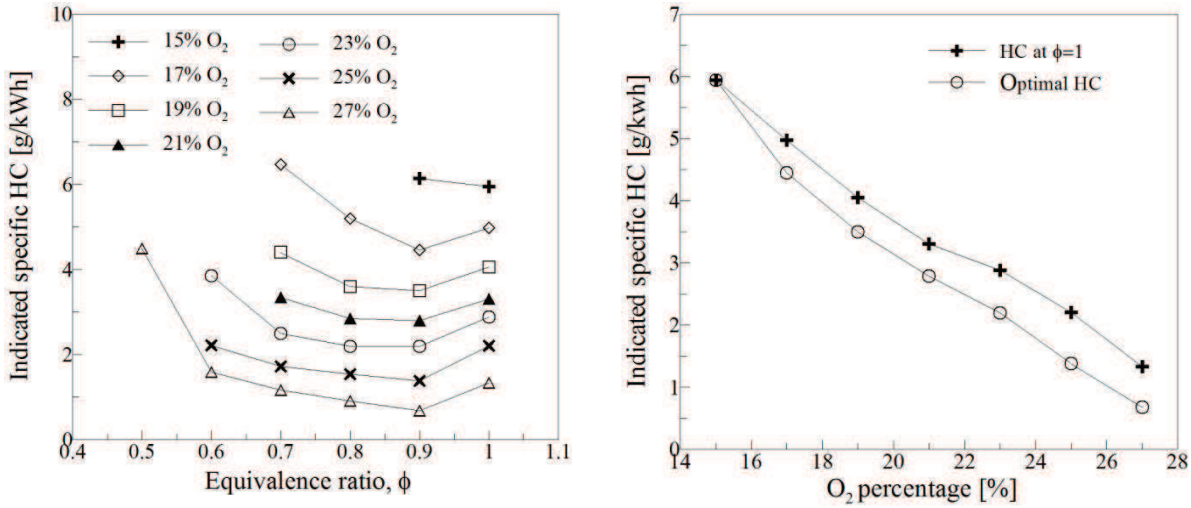

d. IMEP=1000kPa

Figure 2-6. the evolution of indicated specific HC emissions versus equivalence ratio with different IMEP (a. IMEP=400kPa, b. IMEP=600kPa, c. IMEP=800kPa, d. IMEP=1000kPa)

2.6.3 NO_x emissions

The evolution of NO_x emissions versus equivalence ratio is presented in ***Figure 2-7***. Contrary to HC emissions, at a fixed equivalence ratio value, NO_x emissions increase when the oxygen percentage is increased, with the exception of a few points which may be due to measurement error. As the formation of NO_x depends mainly on the burned gas temperature, due to the thermal formation process, the higher the burned gas temperature, the higher the rate of NO_x formation is. Thus the higher emission of NO_x for oxygen enrichment can be explained by the high temperature of the burned gases.

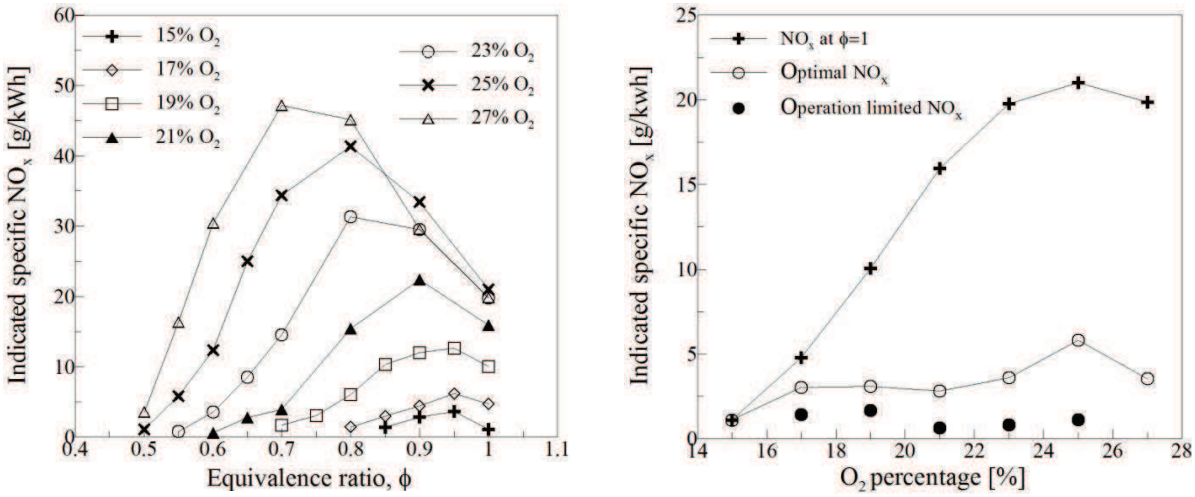

Figure 2-7a. IMEP=400kPa

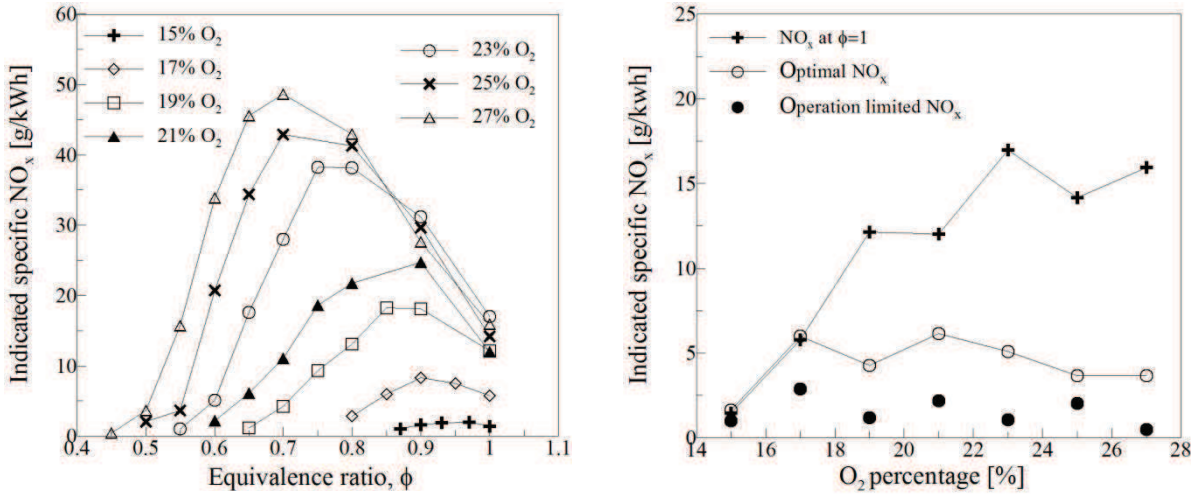

Figure 2-7b. IMEP=600kPa

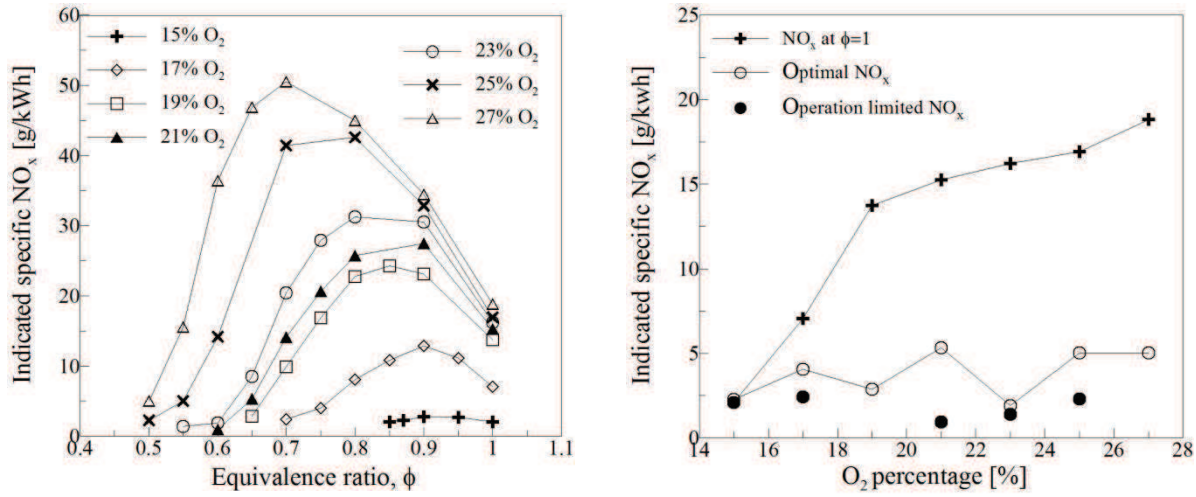

Figure 2-7c. IMEP=800kPa

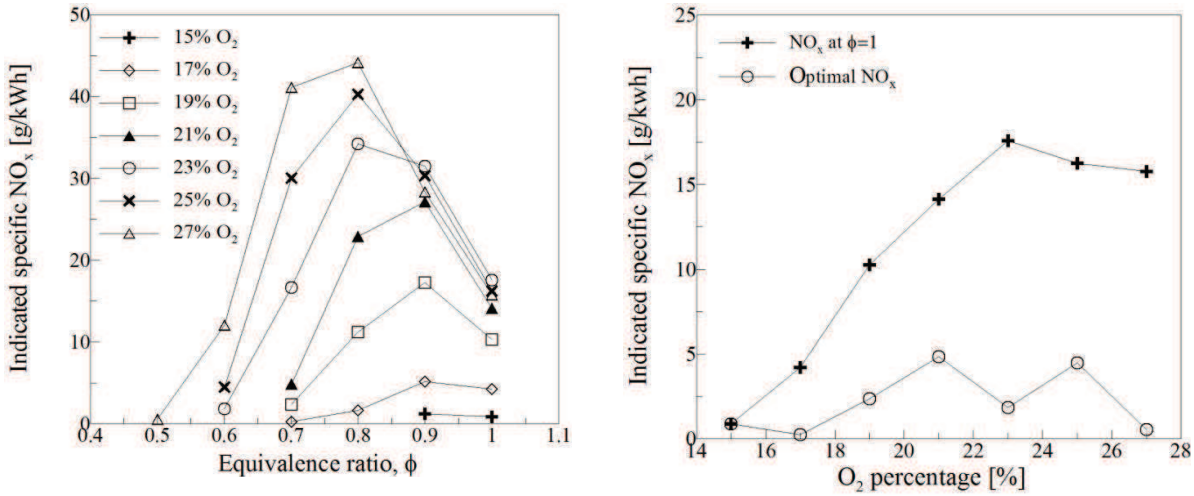

Figure 2-7d. IMEP=1000kPa

Figure 2-7. the evolution of indicated specific NOx emissions versus equivalence ratio with different IMEP (a. IMEP=400kPa, b. IMEP=600kPa, c. IMEP=800kPa, d. IMEP=1000kPa)

The evolutions of the indicated specific NO_x emission versus O_2 percentage (***Figure 2-8***) and exhaust gas temperature (***Figure 2-9***) with different Indicated mean pressure at stoichiometry is presented. The increase of O_2 leads to higher NO_x emission for all the four different IMEP cases. The exhaust gas temperature is investigated to study more about the thermal effect on NO_x formation, as the exhaust gas temperature has a correspondent value with in-cylinder temperature. For certain IMEP, higher value of NO_x is found for higher exhaust gas temperature.

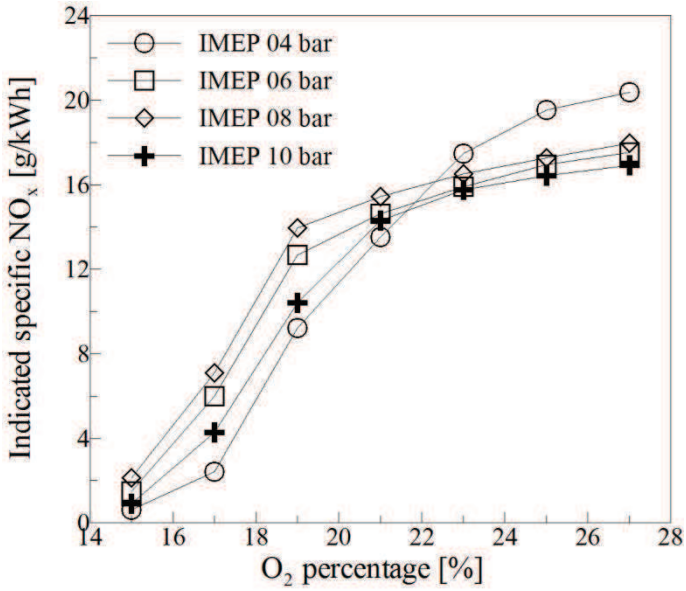

Figure 2-8. Evolutions of the indicated specific NO_x emission versus O_2 percentage with different Indicated mean pressure at stoichiometry

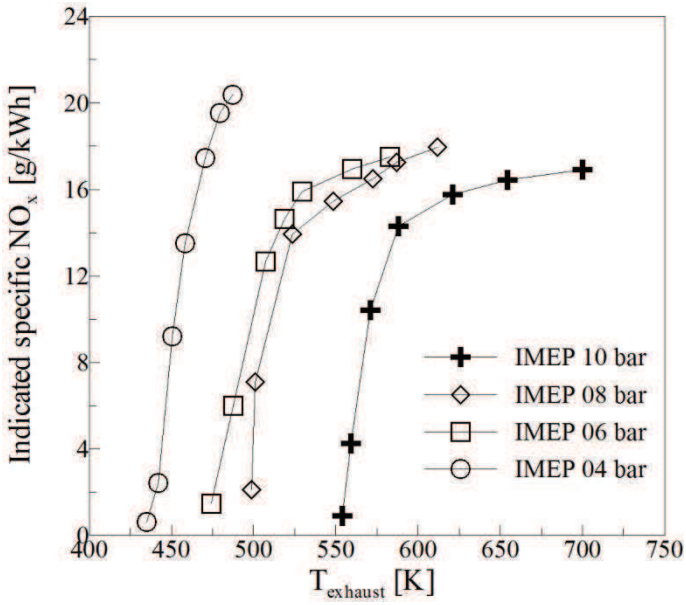

Figure 2-9. Evolutions of the indicated specific NOx emission versus exhaust temperature with different Indicated mean pressure at stoichiometry

2.6.4 CO emissions

Figure 2-10 represents the evolution of indicated specific CO emissions versus equivalence ratio with different IMEP (a. IMEP=400kPa, b. IMEP=600kPa, c. IMEP=800kPa, d. IMEP=1000kPa). CO emissions are mainly affected by the equivalence ratio ϕ, especially for ϕ near unit value , they decrease in lean conditions due to the increase in O_2 concentration which helps the oxidation of CO into CO_2. On the right hand of the graphs, the CO emissions at unit equivalence ratio and optimal CO value are presented versus O_2 percentage. Optimal

CO is defined by the minimum CO value of different equivalence ratio at a fixed O_2 percentage.

Compared to the equivalence ratio, the O_2 percentage in air does not present a clear tendency. In Figure 8a, the local slope of equivalence ratio between 0.95 and 1 for 17% O_2 can reach 240 (the closer it is to the unit ϕ value, the greater it is), which means that with one percent variation in the equivalence ratio, the CO emission will have a more than 2.4 g/kWh discrepancy. Conversely, the biggest variation from 15% to 27% O_2 is about 7 g/kWh. Thus, to ensure precise CO measurement, the equivalence ratio should be controlled and the precision of the mass flow meters of fuel and gases should be checked.

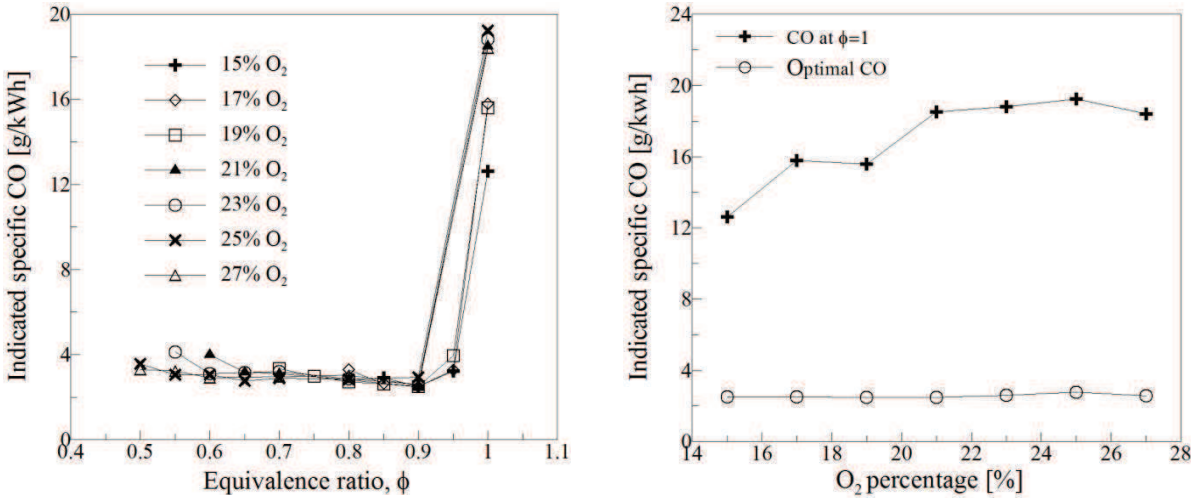

Figure 2-10a. IMEP=400kPa

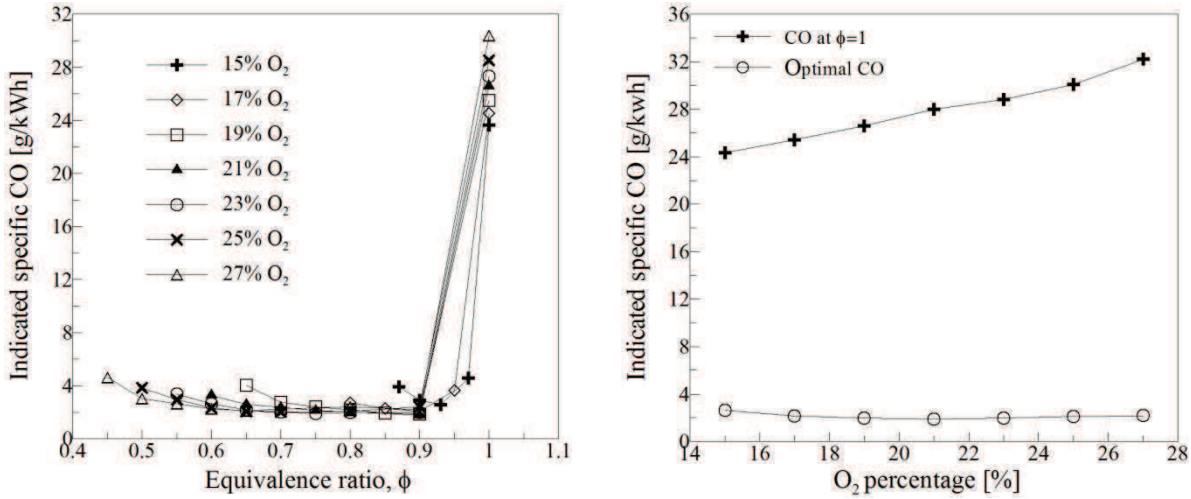

Figure 2-10b. IMEP=600kPa

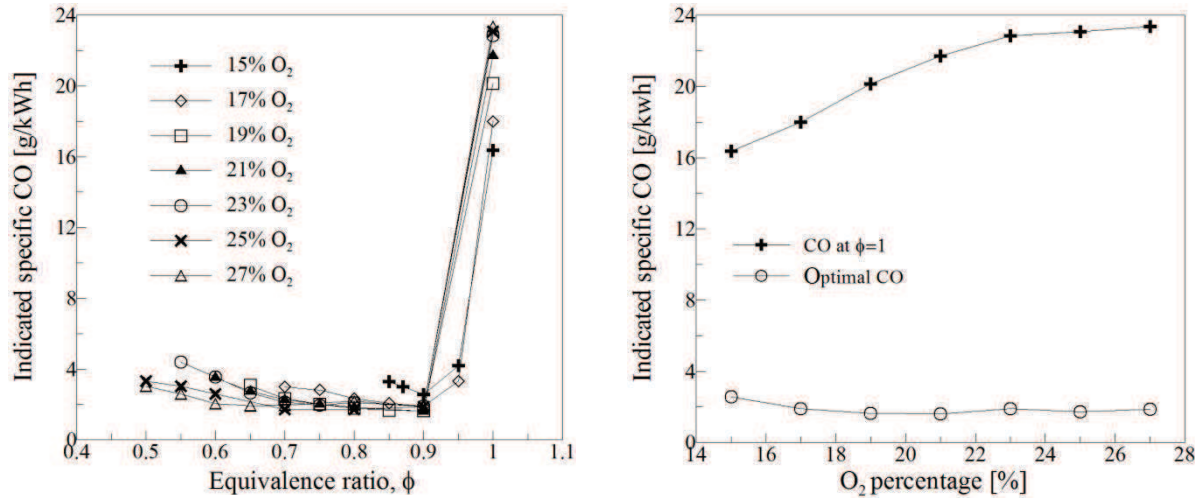

Figure 2-10c. IMEP=800kPa

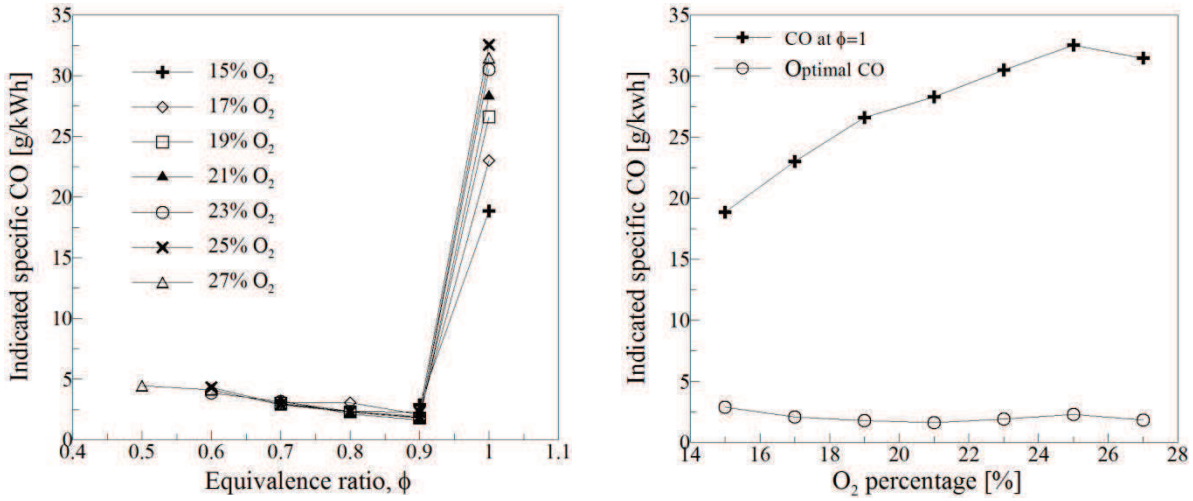

Figure 2-10d. IMEP=1000kPa

Figure 2-10. the evolution of indicated specific CO emissions versus equivalence ratio with different IMEP (a. IMEP=400kPa, b. IMEP=600kPa, c. IMEP=800kPa, d. IMEP=1000kPa)

2.6.5 CO_2 emissions

The CO_2 emissions depend mainly on specific fuel consumption (SFC), although the tendencies are affected by CO, HC, soot emissions. For equivalence ratio near unit value, some CO is not converted to CO_2, as previously described in CO emission section. Thus, the increases of CO_2 emissions at equivalence ratio from 0.9 to 1 are less obvious compared to the general tendency. Furthermore, HC and soot emissions which can be considered as unburned or not completely burned fuel have also effect on CO_2 emissions. As CO_2 emissions depend mainly on SFC, the major way to reduce it to increase the engine efficiency.

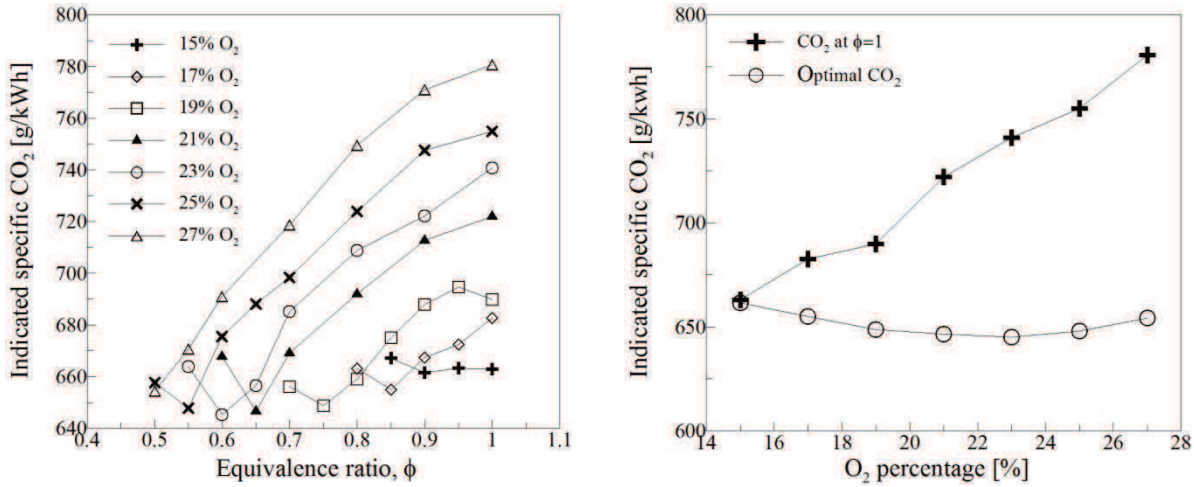

Figure 2-11a. IMEP=400kPa

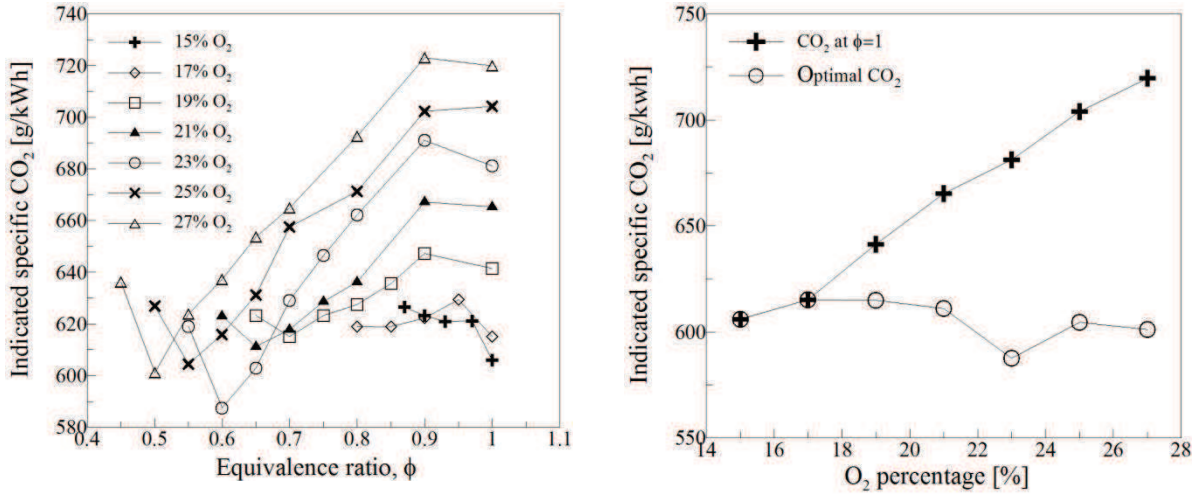

Figure 2-11b. IMEP=600kPa

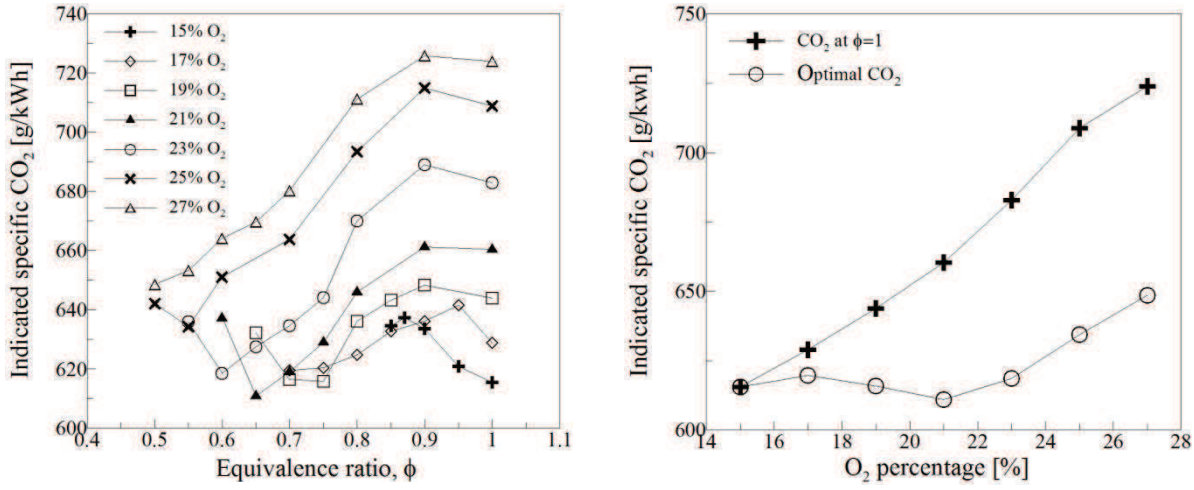

Figure 2-11c. IMEP=800kPa

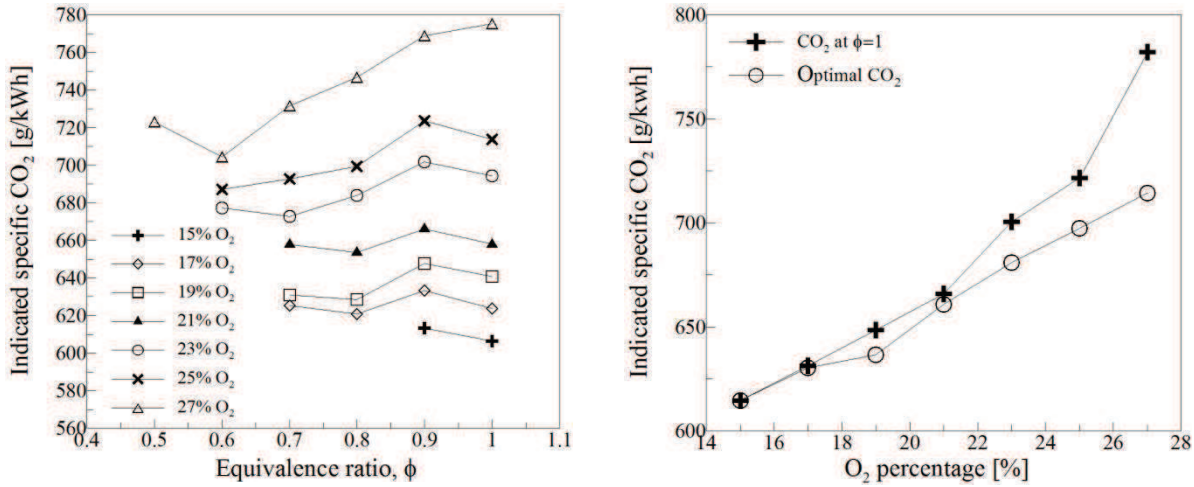

Figure 2-11d. IMEP=1000kPa

Figure 2-11. the evolution of indicated specific CO_2 emissions versus equivalence ratio with different IMEP (a. IMEP=400kPa, b. IMEP=600kPa, c. IMEP=800kPa, d. IMEP=1000kPa)

2.6.6 Combustion characteristics

The combustion characteristics are presented in ***Figure 2-12*** for three different cases: a. $\phi = 1$, IMEP 10 bar, b. 21% O_2, IMEP =10 bar, c. $\phi = 1$, 21% O_2. In ***Figure 2-12***a, different characteristic combustion timings are plotted versus O_2 percentage. The spark timing (ST) increases with the increase of O_2 percentage. CA10 shows a slightly decrease in the dilution side and increases linearly in the side of oxygen enrichment. Similar to CA10, CA50 also decreases in the dilution side and increase linearly in the other side. The difference between CA50 and CA10 (or ST) (which represents first part of combustion duration) decreases with the increase of O_2, which indicates that, the first half of combustion takes longer time for the dilution cases. However, CA90-CA10 which normally employed as combustion duration shows an increase trend (except 15% O_2) in dilution side, and decreases in the oxygen enrichment side. Thus, combustion duration (or second half of combustion time) for both dilution and enrichment side are smaller than 21% O_2. This phenomenon is mainly due to two reasons: first, for O_2 enrichment, laminar flame speed is much higher than 21% O_2, which gives a shorter combustion time for both first and second half of combustion time. For dilution side, although the first half of combustion is slower, the total combustion is faster, which mainly due to the higher turbulence level with high intake pressure and high spark advance.

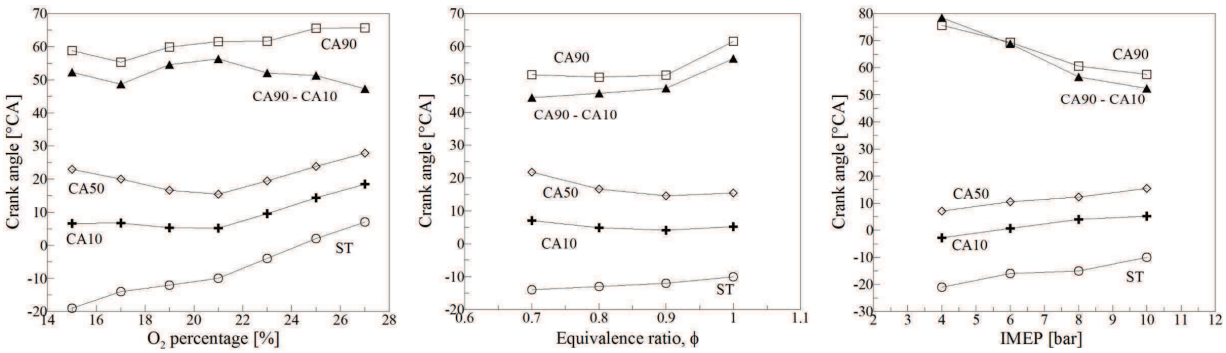

a. $\phi = 1$, IMEP 10 bar b. 21% O_2, IMEP =10 bar c. $\phi = 1$, 21% O_2

Figure 2-12. combustion characteristics for three different cases(a. $\phi = 1$, IMEP 10 bar, b. 21% O2, IMEP =10 bar, c. $\phi = 1$, 21% O2)

In ***Figure 2-12***b, for the operating point of 21% O_2 and IMEP=10 bar, similar to the dilution case as mentioned above, the first half of combustion time is longer, but the total combustion time is shorter for lean mixture.

In ***Figure 2-12***c, for the operating point of 21% O_2 and stochiometry. ST, CA10, and CA50 show an almost parallel tend and increase linearly with the increase of IMEP. However, the values of CA90 and CA90-CA10 are decreased. This indicates that the second half of combustion time is much shorter for high IMEP level.

2.7 Conclusions

In this chapter, the effect of controlling oxygen concentration in air on the performance and emissions in a downsized engine is presented and discussed using experimental tests.

Experimental results indicate that, by increasing the O_2 percentage in air and decreasing the equivalence ratios, lower fuel consumption can be reached for indicated mean effective pressures of 400 and 600kPa. However, for 800 and 1000 kPa, the lowest fuel consumption is obtained for 19% O_2 at 0.7 of equivalence ratio and 15% O_2 at 0.9 respectively. It can be concluded that for low loads, oxygen enrichment has a real potential to improve fuel efficiency, whereas for relatively high IMEP, N_2 dilution still remains the best way. For all equivalence ratios, the HC emission decreases with the increase in O_2 percentage and the lowest value can always be found at 27% O_2 but in this case, NO_x emissions increase.

To better understand the effect of O_2 on the combustion, a part of this study described in next chapter was dedicated to the determination of the laminar combustion characteristics, Moreover, these parameters are needed to model with AMESim simulation.

Characteristics parameters of combustion for oxygen-controlled fuel mixture

3 Characteristics parameters of combustion for oxygen-controlled fuel mixture

This part is dedicated to the determination of two main parameters: the laminar burning velocity and the auto-ignition delay both obtained as function of different oxygen rates in the mixture. For the first part concerning the velocity, major part blow is published in Combustion and Flame journal Titled as: 'Experimental estimate of the laminar burning velocity of iso-octane in oxygen-enriched and CO_2-diluted air'.

The parameters of laminar premixed combustion :

3.1.1 Laminar burning velocity

Laminar burning velocity, considered as one of the most important parameters of premixed flame, plays key roles in determining several aspects of the combustion process in SI engine: for instance, the minimum ignition energy, the thickness of the wall quenching layer, the ignition delay, the engine knock and so on. Many different experimental devices are used for determination of the laminar flame velocity: the planar flame burner (Powling 1949), the counter-flow configuration (Yu et al. 1986) (Freeh et al. 2004), the Bunsen-type burner (Kobayashi et al. 1996)and the spherical bomb (Babkin et al. 1967; Gulder 1983; Bradley et al. 1998). Among these experimental methods, the spherical bomb is the one currently most used for determining the laminar burning velocity.

In this literature review, we primarily interested in the work undertaken in spherical bomb as we used this kind of experimental device for our study. Although the spherical method does not allow us to measure laminar burning velocity directly, it gives a well defined stretch rate which is uniform over the surface. In this configuration, see ***Figure 3-1***, the flame is initialized by an energy source point (electrode was used for our configuration) in the center of the bomb. The outer and inner boundary of the preheated zone is a sphere of radius r_u and r_b, the distance between inner and outer boundary is the flame thickness δ_p. V_n, V_b are the flame speed with respect to the unburned and burned gas separately. And u_g is the gas velocity due to the flame expansion at r_u.

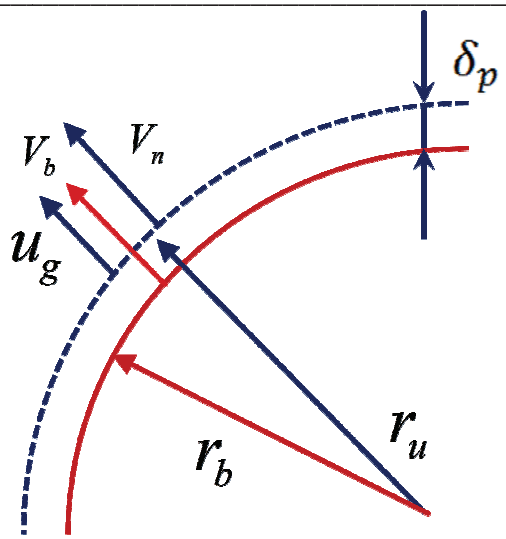

Figure 3-1. description of the structure of spherically expanding laminar flame front

The burning rate of spherical flame propagation is defined as the rate of consumption of reactants at an initial unburned gas density ρ_u and radius r_u, which can be expressed as follow:

$$\frac{dm_u}{dt} = -4\pi {r_u}^2 \rho_u S_L \qquad \text{Equation 3-1}$$

Where m_u is the mass of unburned gas. And u_n is the stretched laminar burning velocity. In the case of a spherically outwardly expanding flame, the variation of the mass contained in the sphere of radius r_u can be expressed as:

$$\frac{dm_u}{dt} = -\frac{d}{dt}\left(\int_0^{r_u} 4\pi r^2 \, \rho dr\right) \qquad \text{Equation 3-2}$$

Where ρ is the density at radius r. Combining the two equations above (Equation 3-1, Equation 3-2), the stretched laminar burning velocity can be written:

$$S_L = \frac{1}{{r_u}^2 \rho_u}\frac{d}{dt}\left(\int_0^{r_u} r^2 \, \rho dr\right) \qquad \text{Equation 3-3}$$

To solve this equation, the spatial distribution and temporal evolution of density should be found within the sphere of radius r_u. Bradley et al. (Bradley et al. 1996) proposed that the gas within the sphere of radius r_u might be considered as comprised of a mixture of burned gas at its adiabatic temperature with a density of ρ_b, and unburned gas with a density of ρ_u. Thus, the fraction of unburned and burned gas can be determined by $(\rho_b - \rho)/(\rho_b - \rho_u)$ and $(\rho - \rho_u)/(\rho_b - \rho_u)$ respectively. By this approach, Equation 3-3 can be decomposed into two parts:

$$S_L = \frac{1}{{r_u}^2 \rho_u}\frac{d}{dt}\left[\int_0^{r_u} r^2 \, \rho_u \left(\frac{\rho_b - \rho}{\rho_b - \rho_u}\right) dr + \int_0^{r_u} r^2 \, \rho_b \left(\frac{\rho - \rho_u}{\rho_b - \rho_u}\right) dr\right] \qquad \text{Equation 3-4}$$

The first part represents the rate of entrainment of unburned gas which remains unburned by the flame front; the second part represents the rate of unburned gas formation. Thus the burning velocity which expresses the rate of appearance of completely burned gas can be defined using the second term:

$$u_{nr} = \frac{1}{r_u{}^2 \rho_u} \frac{d}{dt}\left(\int_0^{r_u} r^2 \rho_b \left(\frac{\rho-\rho_u}{\rho_b-\rho_u}\right) dr\right) \quad \text{Equation 3-5}$$

By combining the equations (Equation 3-3, Equation 3-4, Equation 3-5), u_{nr} can be simplified as:

$$u_{nr} = \frac{\rho_b}{\rho_b-\rho_u}\left(u_n - \frac{dr_u}{dt}\right) \quad \text{Equation 3-6}$$

By the definition of V_n,

$$V_n = \frac{dr_u}{dt} \quad \text{Equation 3-7}$$

Equation 3-6can be written as:

$$u_{nr} = \frac{\rho_b}{\rho_b-\rho_u}(u_n - V_n) \quad \text{Equation 3-8}$$

The relationship of u_n, u_g, and V_n can be written as:

$$S_L = V_n - u_g \quad \text{Equation 3-9}$$

The burning velocity that represents the rate of appearance of completely burned gas can be derived from:

$$u_{nr} = \frac{\rho_b}{\rho_b-\rho_u}.u_g \quad \text{Equation 3-10}$$

Experimental measurements normally focus on the unstretched laminar burning velocity. In the case of a spherically outwardly expanding flame, the laminar burning velocity can be deduced via the stretch rate, including the flow field aerodynamic strain rate and curvature effect at the cold front of flame propagation (Bradley et al. 1998). The key to flame analysis is to introduce an equation to determine the stretch rate and to link the stretch rate to the laminar burning velocity. For a premixed propagation flame, Williams (Williams 1974) proposed that the total stretch rate could be represented by the temporal rate of flame surface variation, expressed as:

$$K = \frac{1}{A}.\frac{dA}{dt} \quad \text{Equation 3-11}$$

where K is the total stretch rate, and A is the flame front surface area. By assuming a spherical flame development, K can be expressed as follows:

$$K = \frac{2}{r_u}.\frac{dr_u}{dt} \quad \text{Equation 3-12}$$

where r_u is the diameter of the flame front on the unburned gases side. In the case of thin flames, r_u can be replaced by r_b, the diameter of the flame front on the burned gases side.

To link the local burning speed and the local stretch rate, two methodologies can be used (Tahtouh et al. 2009) (Halter et al. 2010). The linear methodology, first proposed by Markstein (Markstein 1951) is expressed as:

$$V_n = V_n^0 - L_b.K \qquad \text{Equation 3-13}$$

In this expression, V_n is the stretched propagation flame velocity, V_n^0 the unstretched propagation flame velocity, and L_b the burned gas Markstein length.

The second methodology, the nonlinear one, proposed by Buckmaster (Buckmaster 1977) and Sivashinsky (Sivashinsky 1977), is based on the asymptotic hypothesis. The structure of the considered flames is characterized by a small flame thickness, to which all the reactions are confined. Furthermore, deformations occur on a long scale of the order of dimensionless activation energy. The nonlinear equation is expressed as:

$$\left(\frac{V_n}{V_n^0}\right)^2 . ln\left[\left(\frac{V_n}{V_n^0}\right)^2\right] = -\frac{2L_b.K}{V_n^0} \qquad \text{Equation 3-14}$$

Therefore, unstretched propagation flame speed and burned gas Markstein length can be deduced by minimization of the following expression (Halter et al. 2010):

$$\sum_1^N \left|\left(\frac{V_n}{V_n^0}\right)^2 . ln\left[\left(\frac{V_n}{V_n^0}\right)^2\right] + \frac{2L_b.K}{V_n^0}\right| \qquad \text{Equation 3-15}$$

The unstretched laminar burning velocity can be deduced from unstretched flame speed by considering mass continuity at the unstretched flame condition (Clavin 1985):

$$S_L^0 = \frac{\rho_b}{\rho_u}.V_n^0 \qquad \text{Equation 3-16}$$

Different methods might be employed to determine the unstretched laminar buring velocity by different authors: Bradley et al. (Bradley et al. 1996) detected the flame radius r_{sch} by schlieren ciné photography. In their study, the flame radius r_{sch} was considered as 450K isotherm of flame front, while the cold front r_u, was defined as the isotherm which is 5K above the temperature of the reactants. Thus the cold front r_u can be derived by following correlation:

$$r_u = r_{sch} + 1.95\delta_l \left(\frac{\rho_u}{\rho_b}\right)^{0.5} \qquad \text{Equation 3-17}$$

Where δ_l is the laminar flame thickness given by $\delta_l = \upsilon/S_L^0$, in which υ is the kinematic viscosity of the unburned mixture, S_L^0 is the unstretched laminar burning velocity. Once unburned flame radius r_u has been deduced from measured r_{sch} data, the flame speed V_n is found from unburned flame radius versus time data as Equation 3-7. Then from Equation 3-13, a best straight line fit can be found with experimental data of the flame speed V_n and stretch rate K. V_n^0 and L_b are straight the line fit constants. Finally, the unstretched laminar burning velocity can be deduced by Equation 3-16.

Another method proposed by Bradley et al. (Bradley et al. 1998) was employed by Balusamy et al. (Balusamy et al. 2011) to derive the laminar burning velocity. This method is based on the fresh gas velocity near the preheat zone using Equation 3-10:

$$u_{nr}^0 = \frac{\rho_b}{\rho_b - \rho_u} . u_g^0$$ Equation 3-18

Where u_{nr}^0 is the unstretched burning velocity for appearance of completely burned gas. Although different value can be found for stretched laminar burning velocity S_L (derived from Equation 3-4) and u_{nr} (derived from Equation 3-5), u_{nr}^0 and S_L^0 tends to be the same value. That is because at small radii the flame thickness effect is important, while as the radious tends to infinity (stretch rate K tends to zero), the flame thickness effect can be neglected. u_g^0 is the fresh gas velocity near the preheat zone of the unstretched flame front. Gas velocity $u_g$was measured by PIV unit, and by exploiting the stretch rate K tends to zero, u_g^0 can then be determined.

In their study, the laminar burning velocity was also determinate as the difference between the flame speed S_b and the fresh gas velocity u_g as a function of flame stretch (Balusamy et al. 2011).

$$S_L(K) = V_b(K) - u_g(K)$$ Equation 3-19

This equation is derived from Equation 3-9 by replacing V_n to V_b. Numerical study of Bradley et al. (Bradley et al. 1996) showed that the flame speed is almost independent of the chosen isotherm. Thus, replacing V_n by V_b should not affect the experimental results of laminar burning velocity. The advantage of this method is the laminar burning velocity can be measured directly from the flame speed and fresh gas velocity without using any fuel properties.

In our study, the flame images were obtained by shadowgraphy. The burned gas radius r_b was recorded by high intensity of luminosity, thus the measured flame speed is considered as the flame speed with respect to the burned gas V_b. With thin flames assumption, the stretch rate K and flame speed can be deduced by r_b and its time evolution data. Nonlinear methodology (Equation 3-14) was employed for data post-processing to determine V_b^0 and L_b. Finally, the unstretched laminar burning velocity can be deduced from Equation 3-16.

3.1.2 Correlations of laminar burning velocity

In many combustion models, the laminar burning velocity should be employed to solve the system. Experimental data normally give the discontinue value with certain limited initial conditions. Thus correlations are needed to provide the intermediate points not measured by experiments and extend the initial conditions. Simulation data of laminar burning velocity are normally obtained by solving complex chemical reactions, which need a long time of calculation. Compare to simulation data, the correlations data may calculated directly by a given equation.

Correlation of Metghalchi and Keck

In case of isooctane fuel, the correlation of Metghalchi and Keck (Metghalchi et al. 1982) is the one most used for determining laminar burning velocity. The proposed empirical correlation estimate the laminar burning velocity for a pressure ranging from 1 to 50 bar, temperature ranging from 350 to 700 Kelvin, equivalence ratio ranging from 0.7 to 1.1, and dilution from 0 to 20% by mass quantity. In their study, the dilution is simulated by a mixture

composed of 15% CO_2 and 85% N_2 in volume. The proposed correlation for a mixture of isooctane/air with dilution is of the following form:

$$S_L^0 = S_{L0}^0 \left(\frac{T_u}{T_0}\right)^{\alpha} \left(\frac{P_u}{P_0}\right)^{\beta} (1 - 2.1\chi_{res}) \qquad \text{Equation 3-20}$$

Where S_{L0}^0 is the unstretched laminar burning velocity with reference thermodynamic conditions ($T_0 = 298\text{K}$, $P_0 = 1atm$), α and β are the coefficients associated with the equivalence ratio , χ_{res} is the residual gas mass fraction. In the above correlation, S_{L0}^0 is expressed by the relation as follow:

$$S_{L0}^0 = C_1 + C_2(\phi - \phi_m)^2 \qquad \text{Equation 3-21}$$

Where C_1, C_2 and ϕ_m are coefficients related to the type of fuel. The coefficient C_2 is always negative, ϕ_m represents the equivalence ratio that gives the maximum value of laminar burning velocity. For isooctane fuel, $C_1 = 33.73cm/s$, $C_2 = -110.82$ and $\phi_m = 1.13$.

The coefficients α and β depend on equivalence ratio ϕ with the following expression:

$$\alpha = 2.18 - 0.8(\phi - 1)$$
$$\beta = -0.16 + 2.22(\phi - 1)$$

Correlation of Müller et al.

Unlike the previous correlation, the correlation of Müller et al. (Müller et al. 1997) doesn't result from experimental data but are derived from different simulations. The proposed empirical correlation estimate the laminar burning velocity for a pressure ranging from 1 to 40 bar, temperature ranging from 298 to 800 Kelvin, equivalence ratio ranging from 0.5 to 1.0. The proposed correlation to estimate the laminar burning velocity of isooctane/air is of the form as follow:

$$S_L^0 = A(T^0) Y_{F,u}^m \frac{T_u}{T^0} \left(\frac{T_b - T^0}{T_b - T_u}\right)^n \qquad \text{Equation 3-22}$$

The function $A(T^0)$ depends on the thermodynamic and kinetic properties. T^0 is the inner layer temperature, representing the crossover temperature between chain-branching and chain-breaking reactions. $Y_{F,u}$ is the mass fraction of fuel in fresh gas, given by:

$$Y_{F,u} = \frac{\phi}{\phi + \frac{1 - Y_{F,St}}{Y_{F,St}}} \qquad \text{Equation 3-23}$$

Where $Y_{F,St}$ is the fuel mass fraction at stoichiometric condition. Assuming that the inner layer temperature T^0 depends only on the pressure, Müller et al. determine a value of T^0 for each pressure studied to obtain the best correlation. The relation of pressure, inner layer temperature T^0, and $A(T^0)$ is given below:

$$P = Bexp\left(-\frac{E}{T^0}\right)$$ Equation 3-24

$$A(T^0) = Fexp\left(-\frac{G}{T^0}\right)$$ Equation 3-25

Replacing T^0 by pressure P, $A(T^0)$ is given by:

$$A(T^0) = Fexp\left[\frac{G\left(ln(P)-ln(B)\right)}{E}\right]$$ Equation 3-26

For isooctane fuel, the constants of this correlation are listed as: $B = 3.80 \times 10^7\ bar$, $E = 20906.00K$, $F = 2926.00\ cm/s$, $G = -25.60K$, $m = 0.5578,\ n = 2.5214$.

The burnt gas temperature is defined as the adiabatic flame temperature at chemical equilibrium. It is then approximated for lean flames as a function of equivalence ratio as:

$$T_b = aT_u + b + c\phi + d\phi^2 + e\phi^3$$ Equation 3-27

The coefficients a to e for isooctane fuel are: $a = 0.61$, $b = 936K$, $c = -1127K$, $d = 5326K$, $e = -3044K$.

Correlation of Babkin et al.

The correlation proposed by Babkin et al. (Babkin et al. 1967) to estimate the laminar burning velocity of isooctane/air is of the form as follow:

$$S_L^0 = (404.log(T_u) - 1008)P_u^{-0.39+0.40(T_u/100)}$$ Equation 3-28

This empirical correlation estimate the laminar burning velocity for a pressure ranging from 1 to 100 bar, temperature ranging from 423 to 650 Kelvin, at stoichiometric condition.

Correlation of Ryan et al.

The correlation proposed by Ryan et al. (Ryan et al. 1980) to estimate the laminar burning velocity of isooctane/air is of the form as follow:

$$S_L^0 = b_1 P_u^{b_2} exp(-b_3/T_u)$$ Equation 3-29

Where b_1, b_2, b_3 are constants related to the type of fuel, equivalence ratio and dilution. The values of coefficients b_1, b_2, b_3 are listed in table 1-1:

Dilution	b_1	b_2	b_3
0.00	2965.5	-0.051	2008.8
0.10	2511.4	-0.246	1895.4
0.20	308.0	0.198	1516.2

0.30	112.7	0.181	1271.8

Table 3-1. values of the constants b_1, b_2, b_3 for different dilution at stoichiometric condition.

This empirical correlation estimate the laminar burning velocity for a pressure ranging from 4 to 18 bar, temperature ranging from 470 to 600 K, equivalence ratio ranging from 0.7 to 1.3, and dilution from 0 to 30%.

Correlation of Bradley et al.

The correlation proposed by Bradley et al. (Bradley et al. 1998) to estimate the laminar burning velocity of isooctane/air is of the form as follow:

$$S_L^0 = S_{L0}^0 \left(\frac{T_u}{T_0}\right)^{\alpha_T} \left(\frac{P_u}{P_0}\right)^{\beta_P} \qquad \text{Equation 3-30}$$

Where S_{L0}^0 is the unstretched laminar burning velocity with reference thermodynamic conditions ($T_0 = 358\text{K}, P_0 = 1atm$), α_T and β_P are the coefficients associated with the equivalence ratio ϕ, as listed in table 1-2:

Equivalence ratio	α_T	β_P
0.8	1.01	-0.282
1.0	1.07	-0.348

Table 3-2. values of the constants α_T and β_P for different equivalence ratios.

This empirical correlation estimate the laminar burning velocity for a pressure ranging from 1 to 10 bar, temperature ranging from 358 to 450 Kelvin, equivalence ratio ranging from 0.8 to 1.0.

3.2 Experimental set-up

The laminar flame velocity measurements were made by using a stainless steel spherical combustion chamber with an inside volume of 4.2 L, as described in our pervious study (Zhou et al. 2011). Four windows provided optical access into the chamber. Before filling the chamber, a vacuum was first created. The amount of gas introduced into the chamber was controlled with a thermal mass flow controller. Synthetic air (79% N2 and 21% O2) was used for the experiments. The mixture was made with high purity gas (>99.9%). High-purity isooctane (>99% pure from Aldrich) was injected through a Coriolis mass flow meter. The mixture was heated up to 450K to guarantee full vaporization of the liquid, and the temperature of the chamber was maintained at 373 K to avoid any condensation of isooctane on the chamber walls. In these conditions the quantity of fuel injected was fully vaporized for all cases. An electric fan, located inside the chamber, mixes all the gases. The quantity of each gas was regulated by volume percentage of the total value, excluding the fuel. The volume fraction can be defined as follows:

$$X_{O_2} = \frac{V_{O_2}}{V_{O_2} + V_{N_2} + V_{CO_2}}.100\%$$

Equation 3-31

$$X_{N_2} = \frac{V_{N_2}}{V_{O_2} + V_{N_2} + V_{CO_2}}.100\%$$

Equation 3-32

$$X_{CO_2} = \frac{V_{CO_2}}{V_{O_2} + V_{N_2} + V_{CO_2}}.100\%$$

Equation 3-33

As the global reaction of the mixture can be defined as follows:

$$C_8H_{18} + \frac{12.5}{\phi}\left(O_2 + \frac{X_{N_2}}{X_{O_2}}N_2 + \frac{X_{CO_2}}{X_{O_2}}CO_2\right)$$
$$\rightarrow \left(\frac{8}{\phi} + \frac{12.5}{\phi}\frac{X_{CO_2}}{X_{O_2}}\right)CO_2 + \frac{9}{\phi}H_2O + \frac{12.5}{\phi}\frac{X_{N_2}}{X_{O_2}}N_2 + M, \quad \textit{for rich mixture}$$
$$\rightarrow \left(8 + 12.5\frac{X_{CO_2}}{X_{O_2}}\right)CO_2 + 9H_2O + 12.5\frac{X_{N_2}}{X_{O_2}}N_2 + M, \quad \textit{for lean mixture}$$

Equation 3-34

with M, the quantity of excess air or unburned fuel for lean or rich mixtures respectively, an equivalence ratio ϕ was defined, based on the quantity of oxygen and not on the quantity of air.

$$\phi = \frac{Stoichiometric \quad O_2 / fuel \quad ratio}{actual \quad O_2 / fuel \quad ratio}$$

Equation 3-35

Two tungsten electrodes, with a 1 mm gap, connected to a conventional capacitive discharge ignition system, were used to produce spark ignition at the centre of the chamber. For each condition, the measurements were repeated three times.

The flame images were obtained by shadowgraphy. Parallel light was created with an Ar-Ion laser beam with two plano-convex lenses (25 mm and 1000 mm focal lengths). The shadowgraphic images were recorded using a high speed video CMOS camera (Photron APX) operating at 10000 frames per second with an exposure time of 20 μs. The temporal evolution of the expanding spherical flame was then analyzed. ***Figure 3-2*** presents a schematic overview of the system.

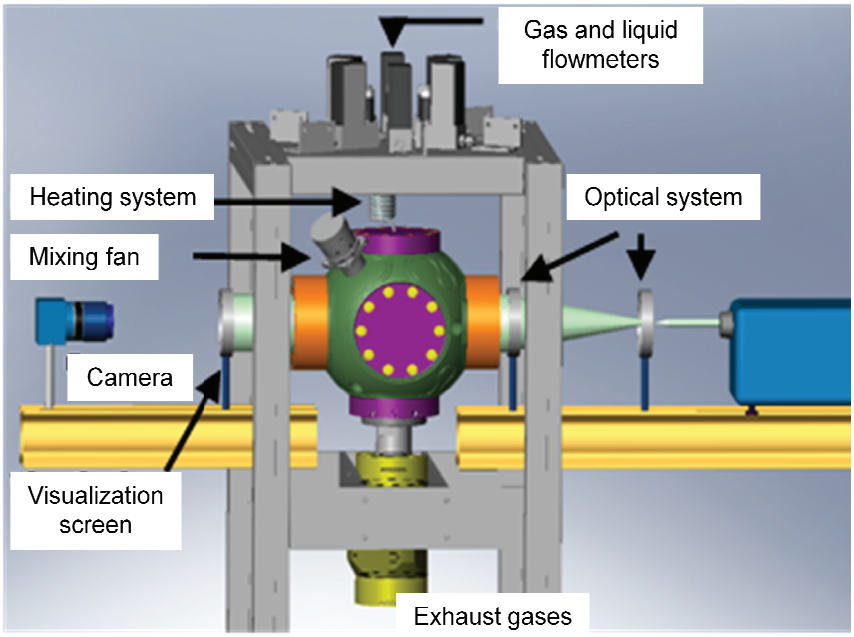

Figure 3-2. Scheme of the experimental setup (Zhou et al. 2011)

Figure 3-3 presents some examples of flame front propagation. The luminous circle represents the maximum derivative of the temperature gradient and is an image of the instantaneous flame front: burned gases are inside the circle and unburned ones outside. The images with flame radii less than 7 mm were not analyzed to determine the laminar flame velocities, so as to avoid the effect of the initial spark energy deposit (Bradley et al. 1998). During the initial stage of flame expansion, the total chamber pressure was constant, so flame radii greater than 25 mm were not taken into account, corresponding to a total volume of burned gases less than 1.6% of the chamber volume.

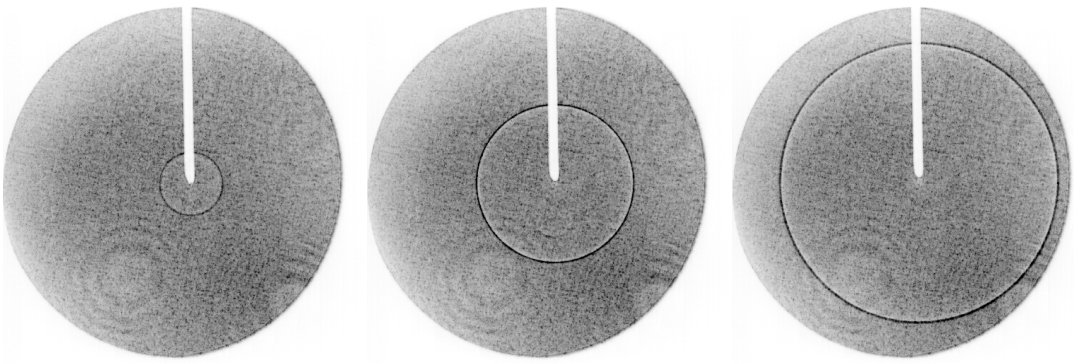

Figure 3-3. Example of the flame front at 9ms, 15ms and 21ms after start of ignition.

3.3 Methodology to analyze flame propagation

3.3.1 Laminar burning velocity determination

In the case of a spherically outwardly expanding flame, the laminar burning velocity can be deduced via the stretch rate, including the flow field aerodynamic strain rate and curvature effect at the cold front of flame propagation (Bradley et al. 1998). The key to flame analysis is to introduce an equation to determine the stretch rate and to link the stretch rate to the laminar

burning velocity. For a premixed propagation flame, Williams (Williams 1974) proposed that the total stretch rate could be represented by the temporal rate of flame surface variation, expressed previously in Equation 3-11. In the case of thin flames, r_u can be replaced by r_b, the diameter of the flame front on the burned gases side. For these different conditions, the radii r_b were extracted as a function of time with very good confidence and the number of images was enough to determine the history of the flame radius (***Figure 3-4***).

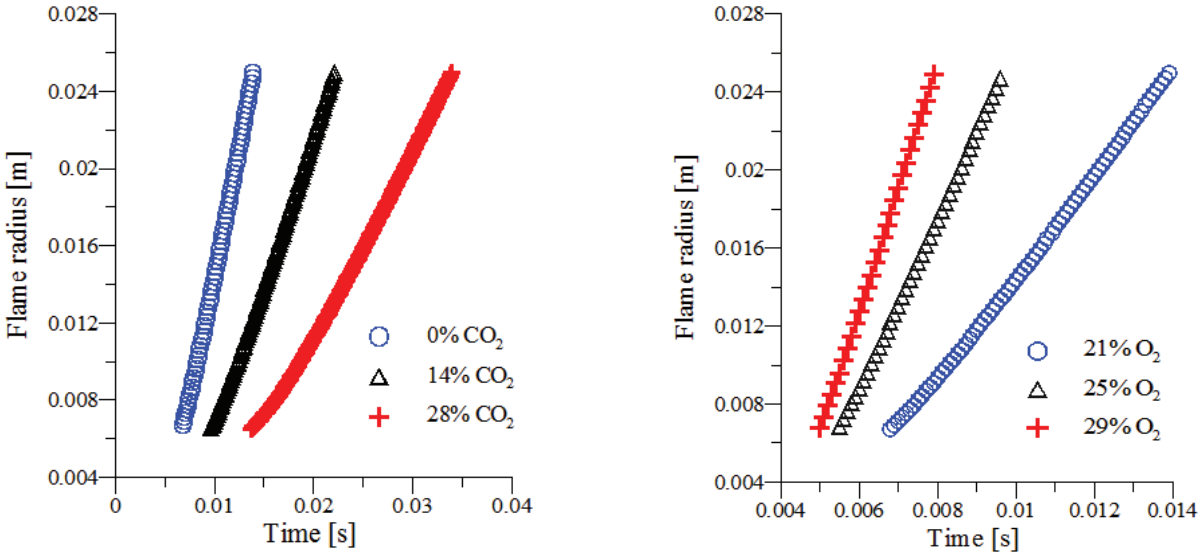

Figure 3-4. Flame radius as a function of time for different experimental condition

To link the local burning speed and the local stretch rate, two methodologies can be used (Tahtouh et al. 2009) (Halter et al. 2010). The linear methodology, first proposed by Markstein (Markstein 1951) is expressed as:

$$V_s = V_s^0 - L_b.K \qquad \text{Equation 3-36}$$

In this expression, V_s is the stretched propagation flame speed, V_s^0 the unstretched propagation flame speed, and L_b the burned gas Markstein length.

The second methodology, the nonlinear one, proposed by Buckmaster (Buckmaster 1977) and Sivashinsky (Sivashinsky 1977), is based on the asymptotic hypothesis. The structure of the considered flames is characterized by a small flame thickness, to which all the reactions are confined. Furthermore, deformations occur on a long scale of the order of dimensionless activation energy. The nonlinear equation is expressed as:

$$\left(\frac{V_n}{V_n^0}\right)^2 . ln\left[\left(\frac{V_n}{V_n^0}\right)^2\right] = -\frac{2L_b.K}{V_n^0} \qquad \text{Equation 3-37}$$

Therefore, unstretched propagation flame speed and burned gas Markstein length can be deduced by minimization of the following expression:

$$\Sigma_1^N \left|\left(\frac{V_n}{V_n^0}\right)^2 . ln\left[\left(\frac{V_n}{V_n^0}\right)^2\right] + \frac{2L_b.K}{V_n^0}\right| \qquad \text{Equation 3-38}$$

As the unstretched propagation flame speed is already known, for constant pressure flame propagation, the laminar burning velocity can be deduced:

$$S_L^0 = \frac{\rho_b}{\rho_u}.V_s^0$$ Equation 3-39

With ρ_b, ρ_u the density of burned and unburned gases respectively.

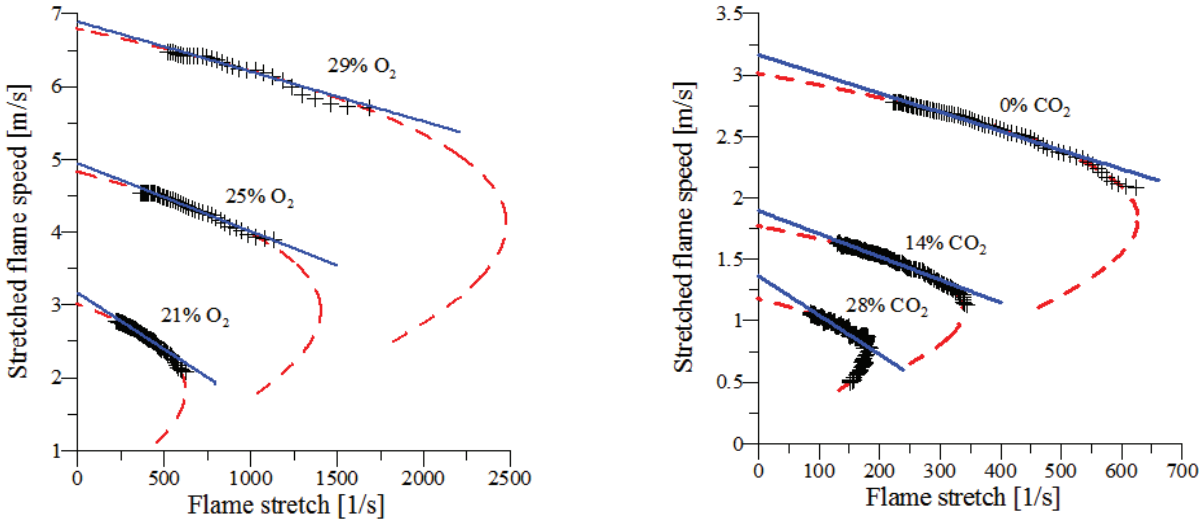

Figure 3-5. Unstretched propagation flame speed determination for different experimental conditions. Square symbol: experimental velocity as function of flame stretch. Continuous lines: linear methodology. Dashed line: nonlinear methodology.

A comparison between linear and nonlinear methodology is presented in ***Figure 3-5*** . Error between the two methodology increases with the decrease of the flame velocity. All the data presented in this study are deduced from the nonlinear methodology. The uncertainties among the operating point are less than 2 cm/s.

3.3.2 Markstein Length

The Markstein length, a coefficient of the same order as the flame thickness, represents the dependence of the flame propagation speed on the stretch rate. Its value can be obtained by minimising equation Equation 3-38, as described above. It can also be deduced from the conservation equations (Matalon et al. 1982). Bechtold and Matalon (Bechtold et al. 2001) provided an explicit expression for the Markstein length in terms of physico-chemical parameters including the thermal expansion coefficient, the effective Lewis number of the mixture, and the global activation energy of the chemical reaction.

Therefore, the Markstein Length, L, can be calculated analytically as:

$$L = \delta\left[\alpha - (\sigma - 1)\gamma_1 / \sigma\right]$$ Equation 3-40

$$\alpha = \gamma_1 + \frac{1}{2}\beta\left(Le_{eff} - 1\right)\gamma_2$$ Equation 3-41

$$\gamma_1 = \frac{2\sigma}{\sqrt{\sigma}+1} \quad \text{and} \quad \gamma_2 = \frac{4}{\sigma - 1}\left\{\sqrt{\sigma} - 1 - \ln\left[\frac{1}{2}(\sqrt{\sigma}+1)\right]\right\}$$ Equation 3-42

With $L = L_b/\sigma$, σ the expansion factor $= \rho_u/\rho_b$, δ the characteristic thermal thickness of the laminar flame $\delta = D_{th}/S_L^0$, β the Zeldovich number, and D_{th} the thermal diffusivity of the mixture. By assuming the thermal conductivity equal to $\lambda = T^{1/2}$ as suggested by Bechtold

and Matalon (Bechtold et al. 2001), Le_{eff} is the weighted average of the Lewis numbers of the deficient, Le_D , and excess, Le_E, reactants:

$$Le_{eff} = 1 + \frac{(Le_E - 1) + (Le_D - 1)A}{1 + A} \qquad \text{Equation 3-43}$$

with $A = 1 + \beta(\Phi - 1)$ and Φ the mass ratio of excess-to-deficient reactants in the fresh mixture. Under stoichiometric conditions, A=1, Le_{eff} is equal to the mean value of Le_E and Le_D. For non-stoichiometric mixtures, A>1, and the Lewis number corresponding to the deficient reactant is weighted more heavily.

The thermal and molecular diffusivities were estimated by using a CHEMKIN sub-routine with Jerzembeck's chemical kinetics mechanisms (Jerzembeck et al. 2009).

3.4 Validation of the methodologies: case of iso-octane/air mixture.

To validate all the experimental procedures, the laminar burning velocity for an air-isooctane mixture at atmospheric pressure and two initial temperatures, 300 and 400 K, was investigated and compared with data available in the literature. The results are presented in ***Figure 3-6***. At Tini = 300 K, our measured data are in very good agreement with those of Davis and Law (Davis et al. 1998), especially for an equivalence ratio range from 0.8 to 1.2. The agreement is poorer in the case of rich mixtures at Tini = 400 K: the measured data give greater values for a lean mixture but are in good agreement with those of Halter (Halter et al. 2010) in the rich mixture case. The differences are mainly due to the different experimental set-up and methodologies for data post-processing, confirming that flame velocity measurement must be still improved.

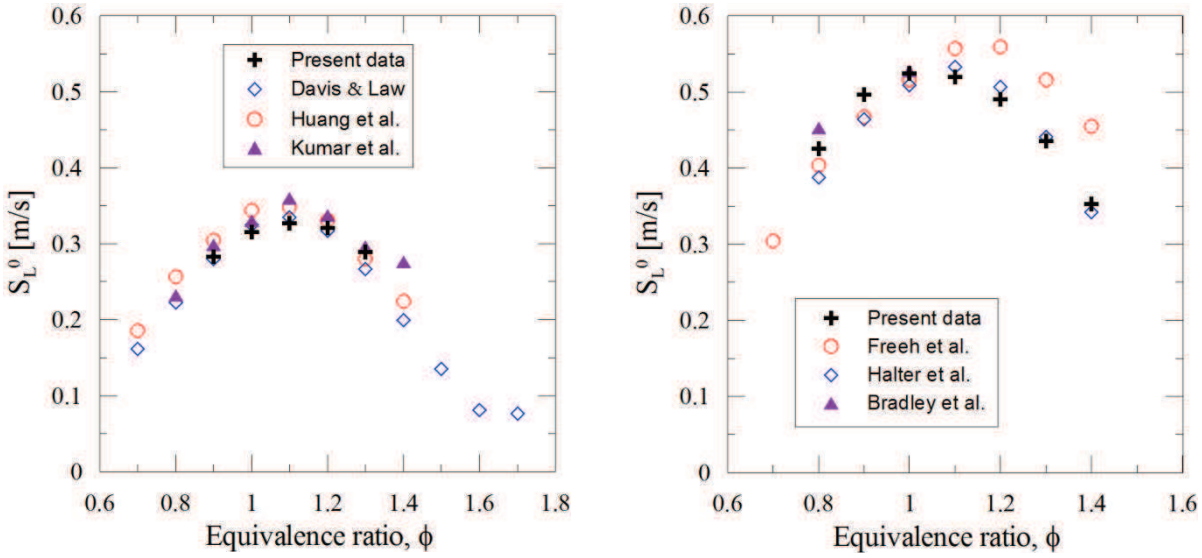

(a) T_{ini} = 300 K (b) T_{ini} = 400 K

Figure 3-6. Experimental laminar burning velocities of isooctane-air mixture at two initial temperatures (300 K and 400 K).Comparation with previous studies in the literature(Davis et al. 1998) (Huang et al. 2004) (Freeh et al. 2004; Kumar et al. 2007) (Bradley et al. 1998; Halter et al. 2010).

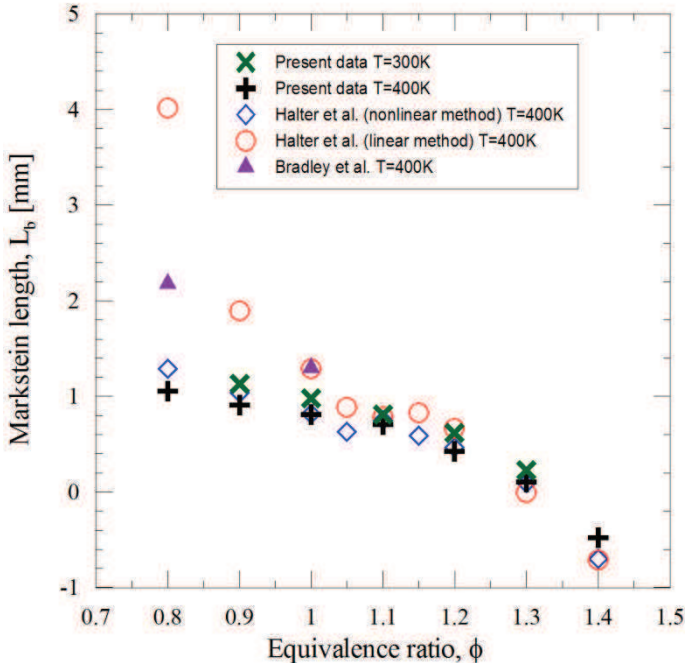

Figure 3-7. Markstein length versus the equivalence ratio for isooctane mixture. Comparison with previous studies (Bradley et al. 1998; Halter et al. 2010).

Figure 3-7 presents the evolution of Markstein length versus the equivalence ratio for the same conditions (300K and 400K). The Markstein length decreases with the increase in the equivalence ratio for both cases, indicating that the propagation velocity is more sensitive to the stretch rate for lean isooctane-air mixtures. A negative value is observed at the equivalence ratio of 1.4 as the flame becomes unstable, as observed during the experiments. As the Markstein lengths are quite sensitive to the flame radii, the smooth variation in Markstein length validates our data. Although Markstein lengths determined from the linear methodology (Bradley et al. 1998) (Halter et al. 2010) are higher than those evaluated with the nonlinear methodology for lean equivalence ratios, our experimental data correspond well with those obtained by Halter (Halter et al. 2010) with the same methodology.

3.5 Results and discussion

3.5.1 Effect of oxygen enrichment

In ***Figure 3-8***, the experimental values of the laminar burning velocity obtained for 3 different equivalence ratios (0.8, 1 and 1.2) are presented as a function of O_2 quantity inside the mixture. The scale of N_2 content is also added to visualize the effect of dilution. The evolution is quasi linear. By comparing with the air gas (21% O_2), 8% of additional oxygen induces an increase by a factor 2 in the value of the combustion velocity for all the cases of equivalence ratio.

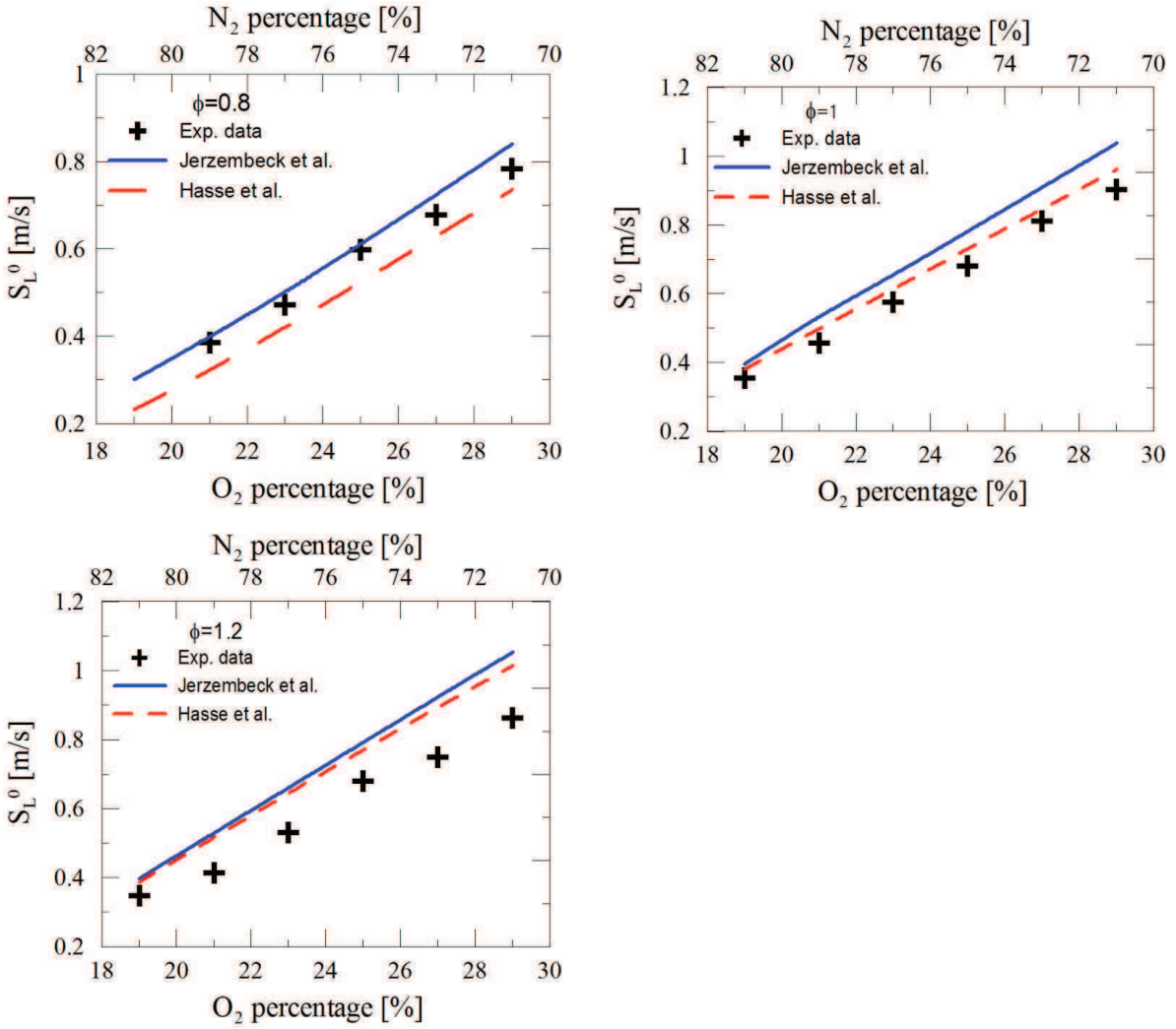

Figure 3-8. Laminar burning velocities as function of the amount of oxygen in air-isooctane mixture for 3 equivalence ratios (Tini = 373 K, Pini = 1 atm).

Numerical simulations were also performed with Jerzembeck's (669 reactions and 99 species) (Jerzembeck et al. 2009) and Hasse's (48 reactions and 29 species) (Hasse et al. 2000) kinetic schemes with Cantera software. All the values predicted by Jerzembeck's scheme are overestimated especially in the case of rich fuel mixture, whereas for Hasse's scheme lower values than those of the experimental data are obtained in the case of lean fuel mixture and higher values than experimental data for rich fuel mixture. Although the discrepancies are very marked for both kinetic schemes, the tendency of the effect of oxygen-enriched combustion is well predicted and quasi-linear evolutions are confirmed.

3.5.2 Effect of CO_2 addition

The effect of dilution by CO_2 in the case of oxygen-enriched combustion was also studied but only for the stoichiometric ratio case. ***Figure 3-9***a presents the evolution of the laminar burning velocity as a function of O_2 percentage for different CO_2 percentages. The laminar burning velocity increases quasi linearly with the increase in the percentage of O_2, whatever the CO_2 quantity.

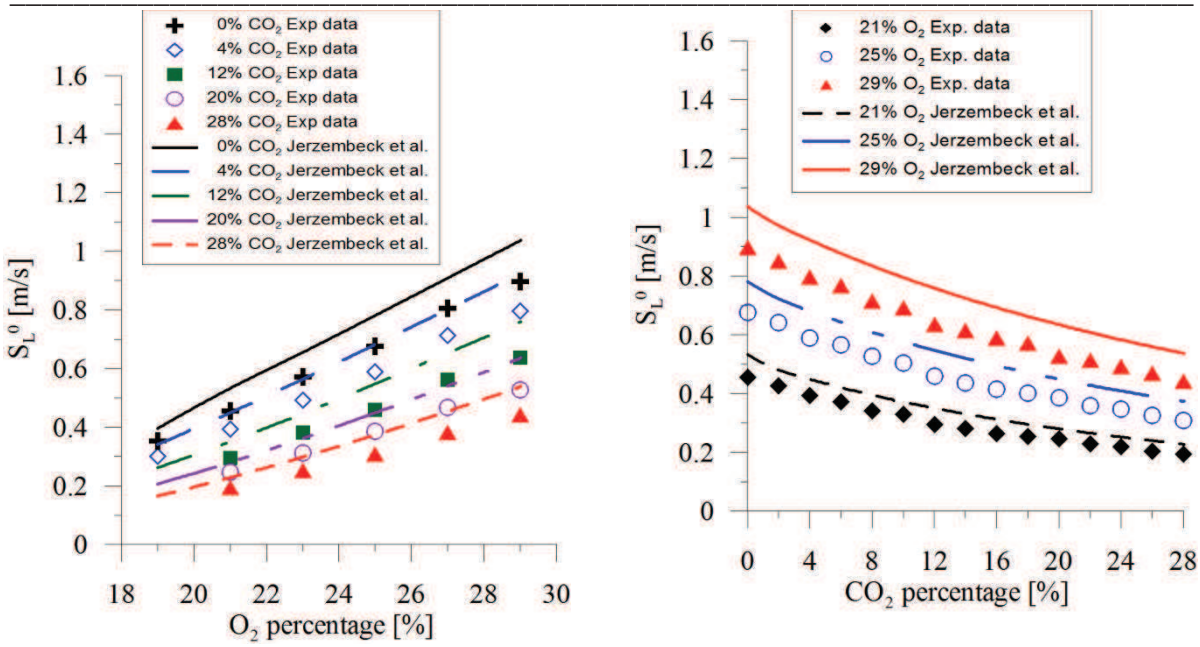

(***Figure 3-9a***) (***Figure 3-9b***)

Figure 3-9. Laminar burning velocities versus O2 and CO2 percentage at stoichiometric equivalence ratio (Tini = 373 K, Pini = 1 atm).

If one plots the same data but as function of the CO_2 percentage, it can be seen that the laminar burning velocities decrease with the increase in CO_2 percentage (***Figure 3-9***b). This decreasing trend slows down with increasing CO_2 dilution. The laminar burning velocity is more sensitive to oxygen enrichment than to CO_2 dilution. For example, it is necessary to add up to 28% of CO_2 to decrease the laminar burning velocity by about 50%, whereas increasing the percentage of O_2 from 21% to 29% suffices to double the laminar burning velocity. Although the predicted values from Jerzembeck's scheme provide higher values than the experimental data, the overall trends are in very good agreement.

3.5.3 Effect of O_2 and CO_2 on adiabatic flame temperature

Figure 3-10 presents the simulated adiabatic flame temperature (using Jerzembeck's kinetic scheme, and assuming a constant pressure problem) versus the variations in O_2 and CO_2 percentage. As expected, the adiabatic flame temperature increases with the increase in O_2 percentage and decreases with dilution by CO_2. The increase in the adiabatic flame temperature is significant for oxygen-enriched combustion. Unfortunately, in terms of magnitude, the decrease in adiabatic flame temperature is much less sensitive to CO_2 dilution.

Laminar flame velocity evolves as a function of the O_2 and CO_2 concentrations and also as a function of the adiabatic temperature. However, as represented in ***Figure 3-11***, for a constant adiabatic temperature, S_L^0 is sensitive to the CO_2 dilution effect.

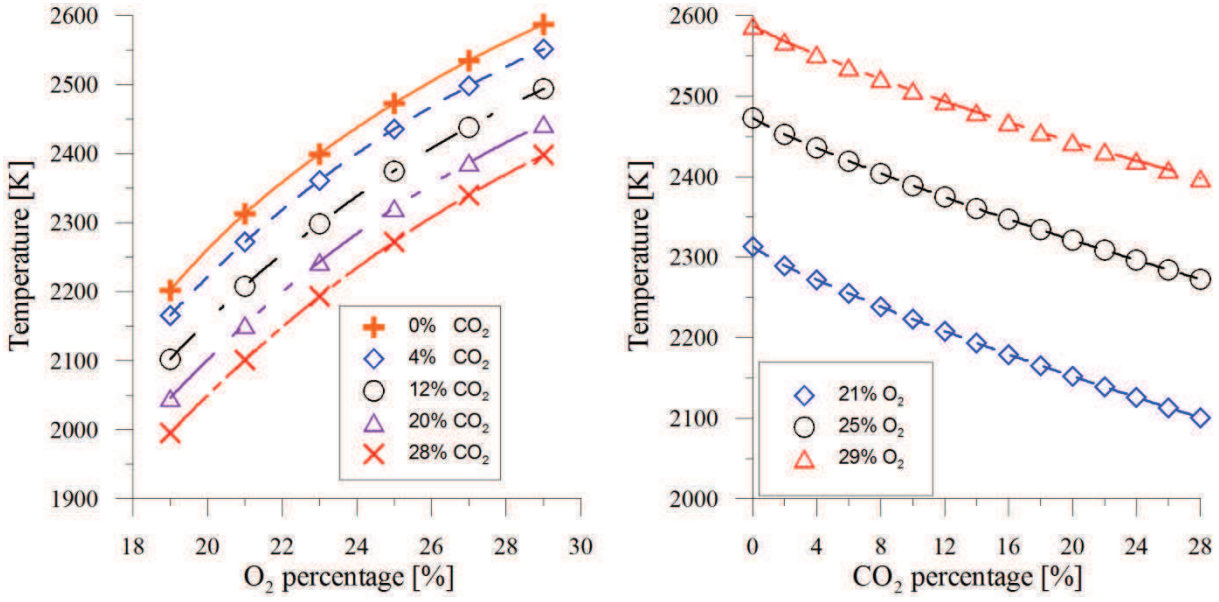

(Figure 3-10a) *(Figure 3-10b)*

Figure 3-10. Simulated adiabatic flame temperature versus O2 (7a) and CO2 (7b) percentage at stoichiometric equivalence ratio (Tini = 373 K, Pini = 1 atm).

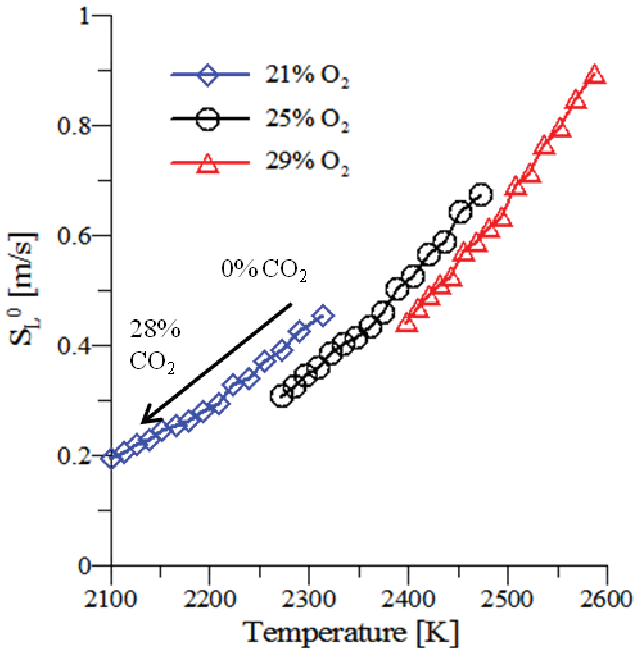

Figure 3-11. Laminar flame velocity as a function of the adiabatic temperature

3.5.4 Markstein lengths

Experimental and analytical values of burned gas Markstein length are presented in ***Figure 3-12***a as a function of O_2 amount and for three CO_2 dilution levels (0%, 14% and 28%). For analytical calculation, the experimental data of S_L^0were used to determine the characteristic thermal flame thickness; fluctuations in the analytical values are therefore due to the inverse variation of S_L^0. It can be seen that Markstein length decreases with O_2 percentage for both

analytical and experimental results. The evolution is very similar although the analytical values are lower. It can be concluded that as the amount of O_2 increases, the flame becomes less and less affected by the stretch rate. This is an interesting result which enhances the interest of oxy-combustion in which a high stretch rate can be reached, as for example in IC combustion engines.

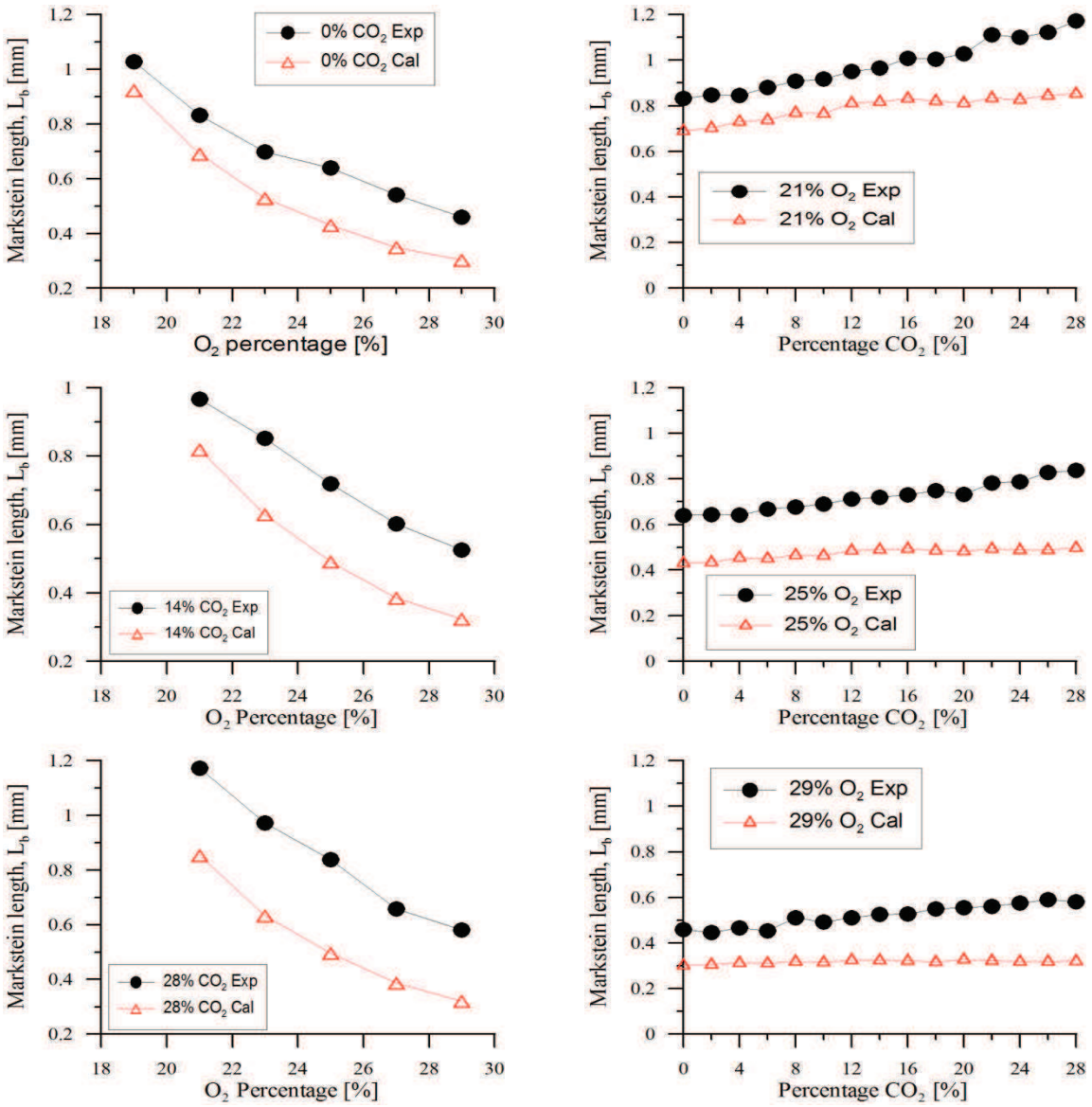

a. Markstein length evolution versus O_2 percentage for 3 amounts of CO_2

b. Markstein length versus CO2 percentage for 3 cases of O2 percentage amounts

Figure 3-12. Markstein length evolution versus O2 (a) and CO2 (b) percentage for 3 different cases (Tini = 373 K, Pini = 1 atm)

Figure 3-12b presents the evolution of the Markstein length values versus CO_2 percentage for three different amounts of O_2. It can be concluded that the Markstein length is slightly affected by CO_2 dilution.

3.5.5 Experimental correlation for laminar burning velocity

In order to predict the trend, an experimental correlation to predict the laminar burning velocity as a function of O2 and CO2 quantities in fresh gas mixtures for T_{ini} = 373 K and P_{ini} = 1 atm is proposed here as follows:

$$S_L^0 = aX_{CO_2}^2 + bX_{CO_2}X_{O_2} + cX_{CO_2} + dX_{O_2} + e \qquad \text{Equation 3-44}$$

with a = 2.553, b = -8.392, c = 0.1223, d = 5.405, e = -0.6743 (correlation coefficient R = 0.9975)

In the above expression, at a fixed CO_2 percentage, the laminar burning velocity is a linear function of the O_2 percentage and a polynomial function of the CO_2 percentage at a given O_2 percentage.

Figure 3-13 shows the values obtained with this correlation (dotted lines) with our experimental data (symbols). The correlation shows a perfect agreement with our experimental data: the RMS between correlation prediction values and our experimental ones is less than 1%. Same laminar burning velocities can be found with combination of different O_2 and CO_2 percentages: S_L^0 (21% O_2, 0% CO_2) ≅ S_L^0 (23% O_2, 8% CO_2) ≅ S_L^0 (25% O_2, 14% CO_2) ≅ S_L^0 (27% O_2, 26% CO_2) as showed in ***Figure 3-13***b.

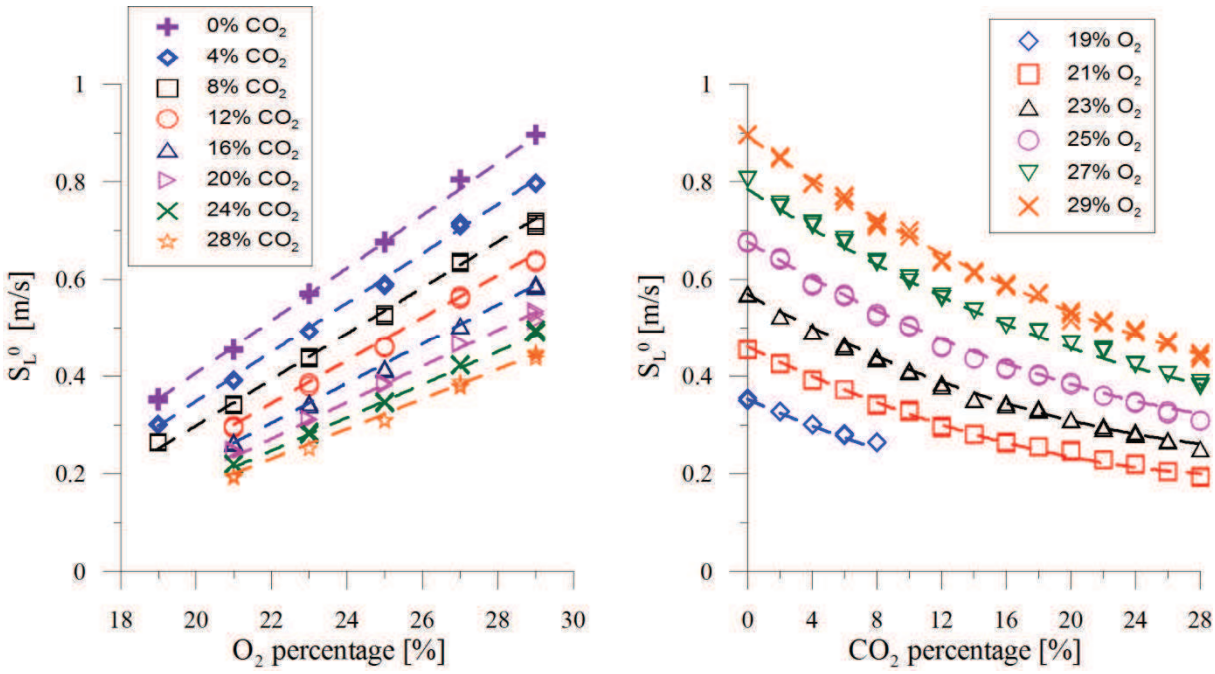

(a) (b)

Figure 3-13. Comparison between estimated values (dotted lines) and experimental data for various CO_2 and O_2 percentages.

3.6 Conclusions

In this chapter, the enrichment of iso-octane combustion with oxygen for combustion process applications such as IC engines has been discussed. Experimental data for laminar burning velocities are given for an initial O_2-N_2-CO_2-isooctane mixture at an initial temperature of

373K and pressure of 1 atm. Numerical data were obtained by using Cantera and two chemical schemes. Although discrepancies between experimental and numerical data exist on numerous points, the trends are very well predicted. As expected, the increase in laminar burning velocities with an increasing O_2 percentage or decreasing CO_2 is observed. The analytical and experimental data of Markstein length are also discussed. An oxygen-enriched mixture could be very interesting to significantly increase the laminar burning velocity and stability of the flame. An experimental correlation is proposed for balancing the O_2 and CO_2 percentages with constant laminar burning velocities. Even if the percentage of oxygen is greater than 21% in the non-reactive mixture, adiabatic temperature and laminar burning velocity could be controlled by adding CO_2.

Estimation of the auto-ignition delay:

3.7 Data avalaible :

As one of key parameters of knock, the auto-ignition delay is wildly employed for knock timing simulation. Livengood and Wu (Livengood et al. 1955) proposed a knock risk prediction method by solving following equation: $\int_0^{KOCA} \frac{1}{\tau}\, d\theta = 1$, where KOCA represents the predicted knock occurrence crank angle during the combustion, τ is an auto-ignition delay function, θ is crank angle. This method requires a correlation of the auto-ignition delay of the type $\tau = \tau(T, P)$. For 0 D two zones model, T is the temperature of fresh gases, and pressure P is supposed to be uniform for both burned and unburned zones. Noda et al (Noda, Hasegawa et al. 2004)considered that thermo-dynamic conditions severely evolve during the compression and combustion strokes so that the knock occurrence cannot be predicted directly by the integral of Livengood and Wu (Noda et al. 2004). Thus, a precursor described by its mass fraction in fresh gases is proposed to predict the knock occurrence by Lafossas et al (Lafossas et al. 2002). Although different methods are used between Livengood and Lafossas, auto-ignition delay showed a great important to predict the knock occurrence.

A summary of various experimental conditions for isooctane ignition delay test is presented in Table ***3-3*** (Scott 2009). There are mainly two kinds of experimental device to determine ignition delay times in literature. The rapid compression machine (RCM), allows the compression of a homogeneous fuel oxidizer mixture in a very short interval of time, thereby rapidly raising its pressure and temperature. This device consists of a driver piston, a reaction chamber, a hydraulic motion control cylinder, and a driving tank. More details of this device can be found in (Mittal 2006). The measurement of ignition delay times in shock tube (ST) has been described in several papers (Fieweger et al. 1997; Würmel et al. 2007; Shen et al. 2008). In the shock tube, the reactant mixture is heated by a shock wave in about 1 ns to pre-selected temperature and pressures. The shock wave is usually produced by rupture of a diaphragm, which is used to separate reaction and driver parts. The driver part usually contains helium at high pressure state.

As showed in Table ***3-3***, only Wooldridge and co-workers at the University of Michigan investigated the oxygen mole fractions covered oxygen enrichment and nitrogen dilution (variation from 9% to 42%). In their study, Rapid compression facility was used to investigate the ignition behavior of mostly lean isooctane charges in the intermediate temperature regime (900-1025K) and with the effective pressure ranged from 4.7 to 10 atm, with some up to 23 atm. However, the experiment data in literature are not sufficient for our study with pressure and temperature relevant to engine operation environment.

Group	Device	P [atm]	T[K]	ϕ	χ_{O2}	Refs.
UST-Lille	RCM	10.7-16.0	650-900	0.8,1.0, 1.2	21%	(Minetti et al. 1996; Minetti et al. 1996; Vanhove et al. 2006)
U. Michigan	RCF	4.7-23	900-1025	0.2-1.0	9-42%	(He et al. 2005; He et al. 2006; Walton et al. 2007)
MIT	RCM	40	798-878	0.2-0.5	21%	(Tanaka et al. 2003)
CWU	RCM	12-17	685-880	1.0	21%	(Mittal et al. 2007; Mittal et al. 2008)
NUIG	RCM	13.2-16.4	660-1020	1.0	21%	(Petersen et al. 2007; Dooley 2008)
IAM	ST	13-44	700-1300	0.5, 1.0, 2.0	21%	(Blumenthal et al. 1996; Fieweger et al. 1997)
Stanford	ST	1.3-59	855-2009	0.5, 1.0, 2.0	0.125-12.5%	(Davidson et al. 2002; Gauthier et al. 2004; Oehlschlaeger et al. 2004; Davidson et al. 2005)
CNRS	ST	9.9	1420-1773	1.0	1.25%	(Yahyaoui et al. 2007)
U. Tokyo	ST	2	1200-1600	1.0	5%	(Sakai et al. 2007)
U. Dayton	ST	~1	900-1400	1.0	18.5%	(Kahandawala et al. 2006)
RPI	ST	8-58	900-1300	0.25-1.0	21%	(Shen et al. 2008)

Table 3-3. A summary of various experimental conditions for isooctane ignition delay test (Scott 2009)

Thus, in our study, firstly auto-ignition delay was investigated for the mixtures of Isooctane/O_2/N_2/CO_2, as same mixture as experimental investigation of laminar speed, by using detail kinetics mechanism with Senkin tool. Then, to give a more precise correction for AMESIM simulation case, the initial conditions of the Isooctane/O_2/N_2 mixtures is defined considering the calculated and experimental data of pressure and temperature.

3.8 Auto-ignition delay of Isooctane/O_2/N_2/CO_2 mixtures

The auto ignition delays are calculated using Senkin with chemical kinetic schemes of Curran (Curran et al. 2002), over the same mixtures as the investigation of laminar flame speed. The Curran's kinetic schemes provide a broad range of validation with the initial pressure ranged from 1 to 45 atm, the temperature from 550K to 1700k and nitrogen-argon dilution from 70% to 99%, which can be adapted to study our engine operation conditions. Furthermore, good predictions were found by Curran et al. (Curran et al. 2002)compared to several previous experimental studies(Vermeer et al. 1972; Dagaut et al. 1993; Fieweger et al. 1994; Fieweger et al. 1997).

A correlation of auto-ignition can also be used, based on the traditional Arrhenius formula:

$$\tau = AP^{-n} X_{O_2}^{-B} (1 - X_{CO_2})^{-C} \exp(\frac{D}{T_{fg}})$$

Where P is pressure of the mixture, T_{fg} is the temperature of fresh gas and A, n, B, C, D are the correlation coefficients. From all data obtained by kinetic simulation, the correlation coefficients are: A=3.6962e-007, n=0.3334, B=0.4828, C=0.1057, D=1.0948e+004.

Figure 3-14 presents the auto-ignition delay times versus O_2 and CO_2 percentage for stoichiometric iso-octane/O_2/N_2/CO_2 mixture. The figure shows that under certain initial conditions of temperature and pressure, auto-ignition delay times decrease with increase of O_2 percentage with 20% CO_2 in gas mixture. Comparing with the effect of O_2 to auto-ignition delay, the addition of CO_2 becomes less important, although an increase trend is observed. Regardless of complex chemical reactions, as we used stoichiometric mixture, the addition of

O_2 was accompanied with increasing of iso-octane quantity, which means the quantities of reactants were both increased, but for the addition of CO_2, the reactants quantity remains the same, only the N_2 quantity decreased. The slight increase of ignition delay times is due to the fact that CO_2 is one of main reaction products which prevent the reaction activation. The discrepancies between the simulation data and correlation are acceptable, as the numerous data varying with several variables, the precision of the correlation is decreased as expected.

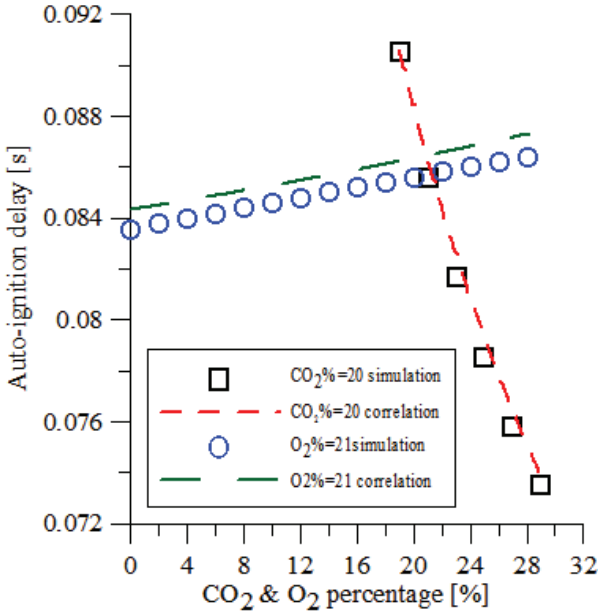

Figure 3-14. Ignition delays versus O_2 and CO_2 percentage for stoichiometric iso-octane/O_2/N_2/CO2 mixture with 1000/T=1.5 (1/K), P=20 bar. Comparison between simulation data and correlation results.

Figure 3-15 and ***Figure 3-16*** show ignition delays versus pressure and temperature respectively for iso-octane/O_2/CO_2/N_2 mixture. From 20 to 60 bar, ignition delay decreases gradually with the increase of the initial pressure and increase tremendously with increase of inverse of the temperature. The optimised correlation predicts very well both effects of pressure and temperature.

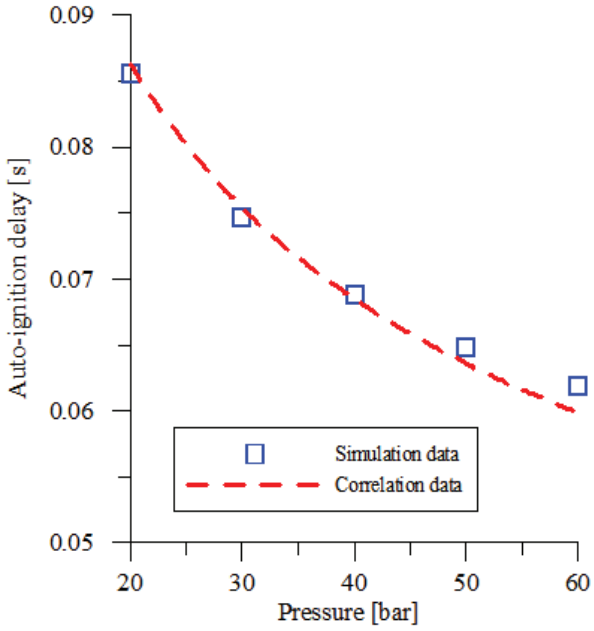

Figure 3-15. Ignition delays versus pressure for iso-octane/O_2/CO_2/N_2 mixture (with 20% CO_2, 21% O2 and T = 666 K)

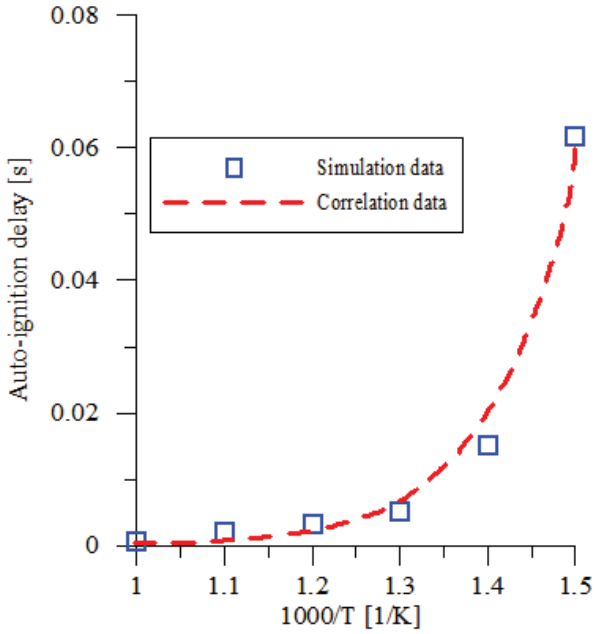

Figure 3-16. Ignition delays versus temperature for iso-octane/O_2/CO_2/N_2 mixture (with 20% CO_2, 21% O2 and P=60 bar)

Considering these parameters, i.e. pressure, temperature, O_2 and CO_2 percentage, it can be concluded that with increase of initial pressure, laminar flame speed decreases, as showed in several previous study (Bradley et al. 1998; Hasse et al. 2000; Jerzembeck et al. 2009), and auto-ignition delay decreases as well. Both effects favourite knock onset in downsizing SI engine. With increase of initial temperature, laminar flame speed increases (Bradley et al. 1998; Freeh et al. 2004), but auto-ignition delay decreases sharply as showed in ***Figure 3-16***. With increase of O_2 percentage, the increase of laminar flame speed becomes very important, and the decrease of auto-ignition delay can be neglected comparing the effect of temperature

to auto-ignition delay. With increase of CO_2 percentage, laminar flame speed decreases and auto-ignition delay remains nearly the same. Generally, the more effective way to prevent engine knock is reduce compression ratio, which can be explained by effect of initial pressure to flame speed and auto-ignition delay. Therefore, the addition of O_2 with or without reducing the compression ratio gives a great prospect to prevent knock onset for downsized SI engine.

3.9 Conclusions

A kinetic scheme of Curran et al. (Curran et al. 2002) was used to simulate the auto-ignition delay at various initial conditions (temperature, pressure, volume fraction of O_2 and CO_2). A new correlation based on the traditional Arrhenius formula is also proposed to take into account O_2 and CO_2 concentration in the mixture.

Combustion modeling

4 Combustion modeling

4.1 Introduction

Zero-dimensional (zero-D) model is one of commonly used engine simulation tools thanks to its simplicity and rapidity. Without considering the dimensional variables, this kind of models is normally only based on time resolutions (crank angle for engine modeling). These time-depended variables which calculated by zero-D model can easily employed to compare with recorded experimental data. Meanwhile, experimental data can also be used for calibrating the model in order to find out the principal unknown parameters. The significant roles for experimentally based zero-D models are not only to identify the unknown parameters which cannot be measured experimentally due to some technical issues, (for example, measurement of unburned and burned gas temperature, engine knock occurrences and its intensities and so on), but also to provide some qualitative trends in a predictive manner for some engine operation points not measured and for new engine with similar design for time saving or engine protection (ex. prevent engine rupture by knock). Thus, experimentally based zero-D models are useful for engine design and development.

Different categories of zero-D models can be found in the literature by dividing the work fluid into different number of zones: single-zone model (Descieux et al. 2007; Zheng et al. 2012), two-zone model and multi-zone models(Komninos et al. 2007; Rakopoulos et al. 2008; Rakopoulos et al. 2008; Verhelst et al. 2009). Multi-zone models are normally consists of zones which are allotted spatial location within the combustion. There are a lot of studies which focus on the two-zone.

- For single-zone model, no distinction is made between burned and unburned gas during the combustion phase inside the cylinder, which cannot adapt for studying the auto-ignition phenomena due to the unknown of the unburned gas thermodynamic properties.
- Two-zone model: normally, the work fluid is separated into unburned and burned zones. Two-zone model were employed in different previous researches for different purposes: Guezennec et al. (Guezennec et al. 1999) used a two-zone based model consistent with engine reverse modeling approach to extract heat release rate from in-cylinder pressure data. The study of Lounici et al. (Lounici et al. 2011) aims to investigate the effect of the different heat transfer correlations on their two-zone model and find the best correlation by comparing the experimental data with their modeling results. In the previous work of Soylu (Soylu 2005), knock model was incorporated with the zero-dimensional two zone model in order to predict the engine knock and its knock intensity. Nonetheless, Wiebe function was used for representing the burned mass fraction, which does not take account the meaningful in-cylinder combustion parameter, such as flame speed and turbulent intensity and so on.
- Multi-zone model: this kind of model is often used to simulate the engine-out emissions. Rakopoulos et al. (Rakopoulos et al. 2008) developed a zero-dimensional, multi-zone combustion model to predict the performance and nitric oxide (NO) emissions for a SI engine. In the model the burned gas zone is divided into several distinct zones for considering the effect of temperature and chemical species stratification. In our present simulation study, the effects of engine pollution will not be discussed.

In order to provide more details about the specificity of combustion with oxygen control, such as turbulent flame velocity evolution during the engine cycle or flame wrinkling, the AMESim commercial software with the combustion model developed by Richard et al. (Richard et al. 2009) was used. The AMESim software provides the following advantages: first, it enables the various physical domains involved in engine system simulation to be addressed with a high level of detail(IFP-EN 2008). Thanks to this advantage, an AMESim model can be set up with reference to the experimental configuration, for example, intake and exhaust tubes, engine valves, turbo-compressors and so on. Secondly, the combustion model developed by Richard et al. (Richard et al. 2009) gives an accurate description of the physical processes. Although this combustion model is based on a weak assumption for the mean flame geometry, the combustion parameters (i.e. flame surface, turbulent intensity, laminar and turbulent burning velocities) provided by the model give a realistic physical meaning for the in-cylinder combustion process.

4.2 Combustion modeling using Amesim

The combustion model used in this work is a physical 0-dimensional model, obtained by reduction of the 3D Coherent Flame Model (CFM) (Richard et al. 2009). CFM formalism distinguishes two zones: fresh and burned gases, which are separated by a flame front propagating from the burned gases towards the fresh mixture. Chemical reactions of fuel oxidation occur in the flame front, a very thin layer compared to all scales of the turbulent flow, and post-flame chemistry takes place in the burned gases. The main assumptions made to derive the 0D model are the following (Richard et al. 2009; Bougrine et al. 2011):

- In each zone, the mixture composition is assumed to be homogeneous and hence to have uniform properties.
- The pressure is uniform throughout the cylinder in both zones
- The gaseous mixture consists of 15 species (Fuel, N_2, O_2, H_2, H_2O, CO, CO_2, NO, NO_2, HC, NH_3, soot, O, H, OH).
- The gases considered are ideal gases.
- The turbulent kinetic energy field is assumed to be uniform in the cylinder.

4.2.1 Energy conservation equations

The energy conservation equation for the whole combustion chamber and fresh gases zone can be expressed respectively as Equation 4-1 and Equation 4-2:

$$\frac{dmh}{dt} = V\frac{dP}{dt} + \frac{dQ_c}{dt} - \frac{dQ_w}{dt} + \sum_{in,out} h_j \frac{dm_j}{dt} \qquad \text{Equation 4-1}$$

Where m is enclosed mass in cylinder, h is the mass enthalpy, V is the total cylinder volume, and P is the pressure which is link to the mean temperature T by first gas law. Q_c is the heat released by combustion processes, Q_{wall} refers to heat loses at the walls, and the last term of the above equation represents refers to enthalpy exchanges at inlet and outlet such as valves, and injector.

$$\frac{dmh_{fg}}{dt} = \frac{\rho}{\rho_{fg}}\frac{dP}{dt}V + \frac{dQ_{wall}^{fg}}{dt} \qquad \text{Equation 4-2}$$

Equation 4-2 is deduced from the 3D enthalpy balance equation for fresh gases by Colin et al. (Colin et al. 2003). Where subscript fg is abbreviation of fresh gas, and ρ is gas density. In this equation, density of the fresh gas can be calculated by dividing mass of fresh gas to fresh

gas volume, and then fresh gas volume is deduced by pressure and temperature of fresh gas employing the perfect gas equation.

For calculating the variables for burned gas zone, a progress variable c is used to account for the evolution of chemical reactions in the flame front. Then the burned gases enthalpy can be calculated by follow equation:

$$mh = (1-c)m_{fg}h_{fg} + cm_{bg}h_{bg} \qquad \text{Equation 4-3}$$

Where, c is the progress variable deduced by expression $c = 1 - \frac{m_{fg}}{m}$, and $m_{bg} = \sum_i m_i^{bg}$, with $m_i^{bg} = m_i - m_i^{fg}$.

Once enthalpy of fresh gases or burned gases is known, the temperature of both gases can be deduced by inversion from burned gases composition and enthalpy.

4.2.2 Combustion heat release

Following the hypothesis of the extension of a 0-dimensionnal coherent flame model (E-CFM)(Colin et al. 2003; F.-A. Lafossas et al. 2005), called CFM 1D, the combustion heat release can be expressed as(Richard et al. 2009):

$$\frac{dQ_{comb}}{dt} = \sum_i h_{f_i}\left(\left.\frac{dm_i}{dt}\right|_{ff} + \left.\frac{dm_i}{dt}\right|_{pf}\right) \qquad \text{Equation 4-4}$$

Where h_{f_i} is the formation enthalpy of specie i, $dm_i|_{ff}$ is the mass variations of this species in the flame front, which can be deduced by equation

$$\left.\frac{dm_i}{dt}\right|_{ff} = \vartheta_i \frac{W_i}{W_f}\left.\frac{dm_{fuel}}{dt}\right|_{ff} \qquad \text{Equation 4-5}$$

with ϑ_i is the stoichiometric coefficient of species i, W represents the molecular weight. And $dm_i|_{pf}$ is the mass variation of species due to post flame chemistry reactions, which coupled with pollutant formation processes.

In Equation 4-5, the unknown term $\left.\frac{dm_{fuel}}{dt}\right|_{ff}$ can be solved by using these following two equations:

$$\left.\frac{dm_{fuel}}{dt}\right|_{ff} = \left.\frac{dm_{fuel}^{fg}}{dt}\right|_{ff} - T_{fuel}^{fg\to bg} \qquad \text{Equation 4-6}$$

Where dm_{fuel}^{fg} is the fuel lost by the fresh gas zone through the flame and $T_{fuel}^{fg\to bg}$ is the transfer of fuel from fresh to burned zone in very rich cases. Then dm_{fuel}^{fg} can be calculated by:

$$\left.\frac{dm_{fuel}^{fg}}{dt}\right|_{ff} = -\rho_{fg}Y_{fuel}^{fg}S_L S_t \qquad \text{Equation 4-7}$$

Where S_t is turbulent flame surface, S_L is the laminar flame speed, and Y_{fuel}^{fg} is fuel mass fraction in fresh gases.

Finally, the turbulent flame surface S_t can be simply expressed as:

$$S_t = \Xi S_m \qquad \text{Equation 4-8}$$

Where Ξ presents flame wrinkling, and S_m is the mean flame surface.

In next two section, for determining the turbulent flame surface S_t, mean flame surface evolution is determined by tabulating piston position and the burnt gas volume using CFM1D tool of Amesim(IFP-EN 2008) with the engine parameters. And the flame front wriking model is discussed.

4.2.3 Tabulation of the mean flame surface S_m

The flame front is supposed to propagate spherically from the spark plug position in the cylinder following the experimental investigation of Baritaud(Baritaud 1989). In our case, parameter setting for engine characteristics is from real engine database, which is exhibited as follow:

Bore (mm)	77
Stroke (mm)	85.8
Compression ratio	10.5
Connecting-rod length (mm)	138.5

The mean flame surface was tabulated as a function of the piston position and the burnt gas volume. In this case, at each time step, the mean flame surface is obtained by interpolation in this table, knowing the current piston position and burned gases volume as in Figure 1, where the red surface represents the mean flame one (blue the chamber wall, orange the piston).

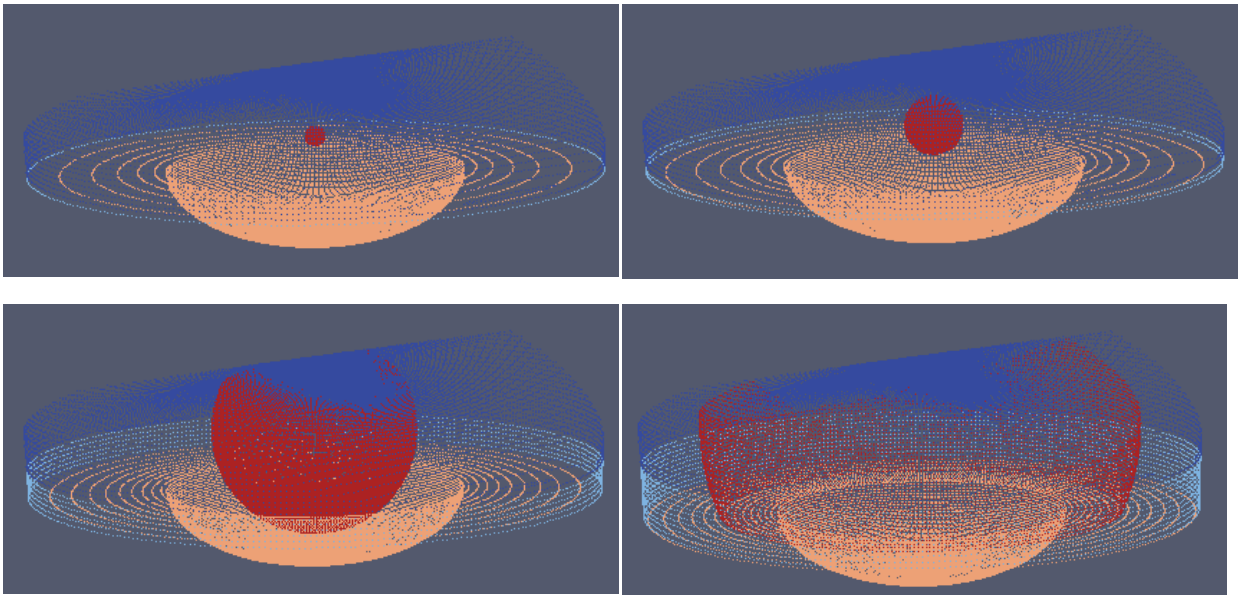

Figure 4-1. Evolution of mean flame surface –based on real configuration

Once the CFM model is run, the files for visualization are created and the two files Surfflm.dat and Rayonflm.dat are produced for later simulation.

4.2.4 Flame wrinkling

Two flame wrinkling models are included in Amesim model. First, a model using classical Damkoler's formation based on an equilibrium assumption for flame wrinkling is introduced as bellow(Boger M. 1998; F.-A. Lafossas et al. 2005):

$$\Xi=\left(1+2\frac{u'}{U_l}\sqrt{\frac{\Gamma C}{S_c}}\right)g(r_{bg}) \qquad \text{Equation 4-9}$$

Where u' is the instantaneous velocity fluctuation, Γ is the efficiency function of the turbulent flow on the flame strain, C a modeling constant, S_c the Schmidt number, r_{bg} the current mean flame radius and g a function accounting for the laminar-turbulent transition of the flame front. The second method is obtained by reduction of the 3D CFD equation for the flame density(Richard et al. 2007). This method gives the temporal evolution of the flame wrinkling.

$$\frac{1}{\Xi}\frac{d\Xi}{dt}=\Gamma(u'/U_l,\ \ l_t/\delta_l)\frac{u'}{l_t}\left(\frac{\Xi_{equ}-\Xi}{\Xi_{equ}-1}\right)-\frac{2}{r_{bg}}(1+\tau)(\Xi-1)U_l \qquad \text{Equation 4-10}$$

Where l_t is the turbulence integral length scale, δ_l is the laminar flame thickness, τ is the thermal expansion rate, r_{bg} is the current radius of burned gases with expression $r_{bg}=\sqrt[3]{3V_{bg}/4\pi}$. In this model, l_t is supposed to be constant and equal to its value at spark timing during the whole combustion stroke. And for both methods, the instantaneous velocity fluctuation u' is calculated by $u'=\sqrt{2/3\,k}$ with k derived by Equation 4-11.

$$k=C_{turb}.\frac{E_{kin,diss}}{m} \qquad \text{Equation 4-11}$$

Where m is the mass in the cylinder and C_{turb} is a modeling constant and is set as unit value, $E_{kin,diss}$ is the dissipated kinetic energy, and can be expressed as:

$$\frac{dE_{kin,diss}}{dt}=\frac{dE_{kin}}{dt}-C_{diss}.E_{kin,diss} \qquad \text{Equation 4-12}$$

Where C_{diss} is a modeling constant. Then, the evolution of the kinetic energy is calculated assuming the tumble motion decrease linearly from the intake valve closure (IVC) to the top dead centre, and it can be expressed as follow:

$$\frac{dE_{kin}}{dt}=\frac{1}{8}.m.\omega_{eng}^2.\left[L^2.\frac{dN_{tumble}}{dt}+2N_{tumble}.L\frac{dL}{dt}\right] \qquad \text{Equation 4-13}$$

Where ω_{eng} is the engine speed in rad/s. L is the distance between the piston and the cylinder head and N_{tumble} is the tumble number at IVC and corresponds to an initial condition for the compression stroke.

4.2.5 Knock modeling

For S.I. engine application, one of major challenges upon increasing efficiency in the most obvious way is to prevent knock occurrences. As an abnormal combustion in SI engine, knock is wildly known as the auto-ignition of one part of the end gas before the arrival of flame front.

As one of key parameters of knock, the auto ignition delay is wildly employed for knock timing simulation. Livengood and Wu (Livengood et al. 1955) proposed a knock risk

prediction method by solving following equation. $\int_0^{KOCA} \frac{1}{\tau}\, d\theta = 1$, where KOCA represents the predicted knock occurrence crank angle during the combustion, τ is an auto ignition function, θ is crank angle. This method requires a correlation of the auto-ignition delay of the type $\tau = \tau(T, P)$. For 0 D two-zone model, T is the temperature of fresh gases, and pressure P is supposed to be uniform for both burned and unburned zone. Noda et al (Noda, Hasegawa et al. 2004)considered that thermo-dynamic conditions severely evolve during the compression and combustion strokes so that the knock occurrence cannot be predicted directly by the integral of Livengood and Wu (Noda et al. 2004) . Thus, a precursor described by its mass fraction in fresh gases is proposed to predict the knock occurrence by Lafossas et al (Lafossas et al. 2002).

Although different methods are used between Livengood and Lafossas, auto-ignition delay showed a great important to predict the knock occurrence. In our study, the auto ignition delays were calculated using Senkin with chemical kinetic schemes of Curran (Curran et al. 2002), over the same mixtures as the investigation of laminar flame speed. The correlation of auto-ignition delay determined in chapter 4 is used:

$$\tau = AP^{-n}.{\chi_{O_2}}^{-B}.\left(1-\chi_{CO_2}\right)^{-C} exp\left(\frac{D}{T_{fg}}\right) \qquad \text{Equation 4-14}$$

Where P is pressure of the mixture, T_{fg} is the temperature of fresh gas and with A=3.6962e-007, n=0.3334, B=0.4828, C=0.1057, D=1.0948e+004.

In order to apply the auto-ignition delay for SI engine conditions, the above correlation was extended for various equivalence ratios and residual gas mass fractions:

$$\tau = A\left(\frac{R_{eff}}{100}\right)^{3.402} {P_{eff}}^{-n}.{\chi_{O_2}}^{-B}.\left(1-\chi_{CO_2}\right)^{-C} exp\left(\frac{D}{T_{fg}}\right) \qquad \text{Equation 4-15}$$

In this expression, $R_{eff} = RON.exp\left(0.1\, K_{far}(\phi-1)\right)^2$, $P_{eff} = P/(1+K_{rbg}X_{rbg})$. Both two definitions that firstly used by Lafossas et al.(Lafossas et al. 2002; Lafossas 2002), take account the effect of different equivalence ratios and residual gas mass fractions. The parameters K_{far}, K_{rbg}, are modeling constants: $K_{far} = 1, K_{rbg} = 10$.

Once the auto-ignition correlation is defined, a precursor is applied to calculate the knock timing(Lafossas et al. 2002):

$$\frac{dY_p}{dt} = Y_{fuel}^0 F(\tau) \qquad \text{Equation 4-16}$$

Where Y_{fuel}^0 is the fuel masse fraction in the fresh gases before the start of the combustion: $Y_{fuel}^0 = m_{fuel}^0/m_{fg}^0$. $F(\tau)$ is expressed as bellow:

$$F(\tau) = \frac{\sqrt{\alpha^2\tau^2 + 4(1-\alpha\tau)\frac{Y_p}{Y_{fuel}}}}{\tau} \qquad \text{Equation 4-17}$$

In the above equation, $\alpha = 1\, s^{-1}$ is a modeling constant. Auto-ignition occurs when the condition $Y_p = Y_{fuel}^0$ is satisfied. And then, the corresponding knock intensity is calculated using the estimation method described in next section.

4.2.6 Knock intensity estimation

Many different methods, using either experimental or simulation tools, have been proposed and developed in literature to qualify the knock intensity. Experimentally, two main broad approaches can be adopted for detecting and quantifying engine knock by manipulating the engine testing bench data: methods based on in-cylinder pressure measurements (Hudson et al. 2001) and on engine structural vibration measurements(Ettefagh et al. 2008). Hudson et al. (Hudson et al. 2001) used an average energy method based on in-cylinder pressure signal analyses to determine the logarithmic knock intensity (LKI).

As knock depends strongly on the temperature, fuel and residual gases distribution in the combustion chamber, the prediction of knock via heat release rate using 0D models became even roughly, especially, for a wide range of operation conditions.

Thus, in this study, a correlation is utilized to estimate the knock intensity. As the previous study of Richard et al. (Richard et al. 2009), several effects were take into account:

- ✓ Effect of fresh gas mass fraction: the knock is strongly depended by spontaneous auto-ignition of remaining fresh charge at the knock timing.
- ✓ Effect of combustion in rich mixture: combining the effect of fresh gas mass fraction, this effect take account the effect of unburned fuel due to the rich mixture.
- ✓ Effect of the cylinder volume at the instance of knock: the influence of the cylinder volume at the knock timing is previously taken account by several authors (Halstead et al. 1977; Karim 2004; Noda et al. 2004).
- ✓ Effect of knock phasing in the expansion stroke: the crank angle at which the knock occurs has an important effect of knock intensity.
- ✓ Effect of engine speed: in order to correlate the KI for different engine speed, a correlation term was employed by the study of Richard et al. (Richard et al. 2009)

Finally, the correlation of knock intensity can be written as:

$$KI = C_1(1 - bmf.\max(1,\emptyset))(\Pi - 1)\sqrt{1 - \frac{\theta_k}{C_2}}N_{eng} \qquad \text{Equation 4-18}$$

Where C_1 is a constant parameter for tuning the global knock intensity level with unit of rpm^{-1}. C_2 is the maximum crank angle for which knock is still audible and generally set to 40-50 cad. N_{eng} is the engine rotation speed.

However, for oxygen controlling combustion, the previous correlation doesn't work well in case of N_2 dilution and O_2 enrichment, as previous study mainly focused on engine combustion with air. Thus, a new correlation was proposed based on the previous correlation:

$$KI = C_1.\left(\frac{\chi_{O_2}}{0.21}\right)^{\alpha}(1 - bmf.\max(1,\emptyset))(\Pi - 1)\sqrt{1 - \frac{\theta_k + \beta(0.21 - \chi_{O_2})}{C_2 - \gamma(0.21 - \chi_{O_2})}}N_{eng} \qquad \text{Equation 4-19}$$

In this correlation the term $\left(\frac{\chi_{O_2}}{0.21}\right)^{\alpha}$ represents the KI increase with the increase of O_2 percentage in air. As showed in our experimental study, increasing of oxygen percentage may lead to smaller spark advance with the limit of engine knock. Spark advance has an important influence on knock crank angle θ_k as engine combustion gives an intense pressure and temperature rise. The term $\theta_k + \beta(0.21 - \chi_{O_2})$ takes account the effect of O_2 increase on retard of spark advance. For instant, in some cases of high level of O_2 percentage, the spark ignition timing should be set after the top dead center (TDC) as showed in ***Figure 4-2*** (the red

line of in-cylinder pressure). Compare to the black line, knock crank angle θ_k is retarded $\Delta\theta_k$, thus, the estimated KI using previous correlation gives too much lower KI value. So, in this case, the term $\beta(0.21 - \chi_{O_2})$ can be used to produce a higher KI value. In case of low level of O_2 percentage, even the spark advance is much advanced, the KI value increases very slightly. So the term $\beta(0.21 - \chi_{O_2})$ can be used to produce a lower KI value for low level of O_2 percentage. The term $-\gamma(0.21 - \chi_{O_2})$ gives a positive value when O_2 enrichment, which enlarges the knock crank angle limit.

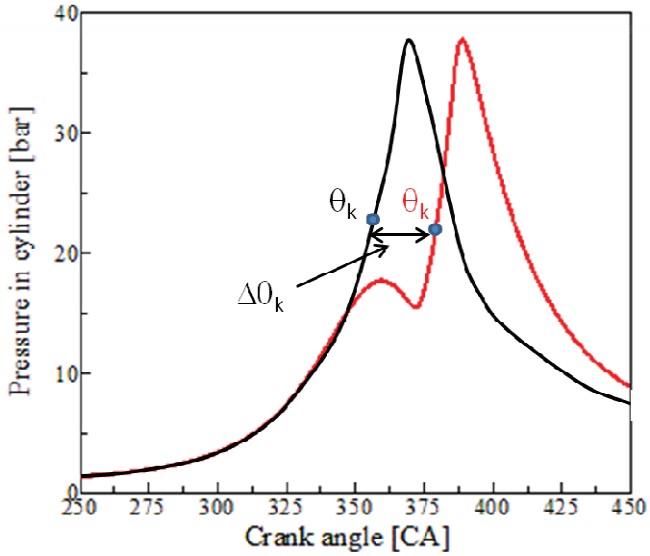

Figure 4-2. Example of knock crank angle θ_k with spark advance before and after top dead center (red line: an example of in-cylinder pressure at 10 bar IMEP and 27%O_2, black line: supposed pressure)

. And then four levels of knock intensity can be distinguished:

- $KI < 0.5$: no knock
- $0.5 \leq KI < 1$: trace knock
- $1 \leq KI < 1.5$: medium knock
- $KI \geq 1.5$: strong knock

In next section, firstly an Amesim model for oxygen controlling engine is presented.

4.3 Adaptation of Amesim model for oxygen controlling engine

Figure 4-3 is the diagram of Amesim model, the left hand of the diagram is the intake part, the exhaust part of engine is on the right hand, in the middle of the diagram is the main engine block, containing the intake and exhaust valves model, engine 12 gases model, crank model and etc.

In this Amesim model, four parts of subroutine (marked as 1 to 4) were modified to adapt the oxygen controlling calculation using advanced Amesim tool, called 'Ameset':

- 1 and 2 are pipe models, they transform the mixture of 3 gases (air, fuel, burned gases) to 12 specie (Fuel, N_2, O_2, H_2, H_2O, CO, CO_2, NO, NO_2, HC, NH_3, soot) when gases pass though intake or exhaust pipe to engine block. Inversely, from engine block to intake or exhaust side, 12 gases are transformed to 3 gases. In the pipe model, an integer parameter for O_2 mole percentage was defined, thus, by changing this

parameter above or less than 21%, air can be considered as oxygen enrichment or nitrogen dilution respectively.

- In the model of 12 gases engine fluid data, marked as number 3 in figure 1, instead of stoichiometric air-fuel ratio for fuel, stoichiometric oxygen-fuel ratio is calculated to determine the equivalence ratio based on oxygen as defined previously in chapter two. This equivalence ratio ϕ was defined, based on the quantity of oxygen and not on the quantity of air.

$$\phi = \frac{Stoichiometric \quad O_2 / fuel \quad ratio}{actual \quad O_2 / fuel \quad ratio}$$

Equation 4-20

- In block 4, an integer parameter for O_2 mole percentage is also employed to control the oxygen percentage in air and as a variable for laminar flame speed correlation and auto-ignition delay time correlation.

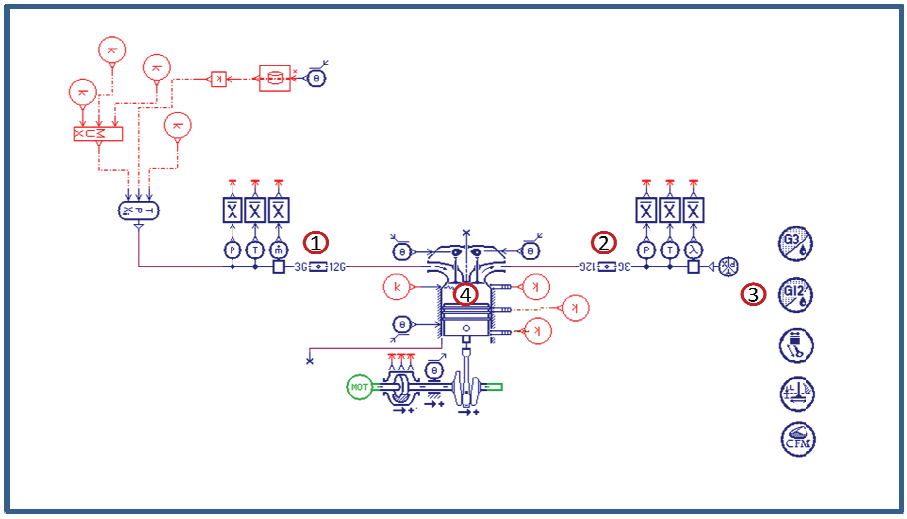

Figure 4-3. Amesim model for oxygen controlling engine

4.3.1 Laminar flame speed correlation

The laminar burning velocity for different quantities of O_2 was investigated experimentally in previous studies (Zhou et al. 2011; Galmiche et al. 2012). In order to take into account the effect of oxygen control on the engine combustion simulation, a correlation based on an experimental estimation (Galmiche et al. 2012) was implemented in the AMESim model:

$$S_L^0 = S_{Lref}^0 \left(\frac{T_i}{T_{ref}}\right)^{\alpha_s} \left(\frac{P_i}{P_{ref}}\right)^{\beta_s}$$

Equation 4-21

In the above relationship, S_{Lref}^0 is a function of equivalence ratio:

$$S_{Lref}^0 = A + B(\phi - \phi_m) + C(\phi - \phi_m)^2 + D(\phi - \phi_m)^3 + E(\phi - \phi_m)^4$$

Equation 4-22

And,

$$\alpha_s = \alpha_1 + \alpha_2(\phi - \phi_m)$$

$$\beta_s = \beta_1 + \beta_2(\phi - \phi_m)$$

T_{ref}, P_{ref} are the reference temperature and pressure respectively and S^0_{Lref} is the laminar burning velocity of these conditions. In this correlation, pressure, temperature and laminar burning velocity are respectively expressed in bar, K, and cm/s.

In the study by Galmiche et al. (Galmiche et al. 2012), an empirical term was added to take into account both the effect of N_2 dilution and O_2 enrichment:

$$S_L^0(v_{O_2}) = S_L^0(v_{O_2 ref})\left(\frac{v_{O_2}}{v_{O_2 ref}}\right)^{\gamma} \qquad \text{Equation 4-23}$$

Where $\gamma = \gamma_1 + \gamma_2(\phi - \phi_m)$, with two constant values of γ_1 , γ_2. $v_{O_2}$is the percentage in air defined by:

$$v_{O_2} = \frac{n_{O_2(synthetic\ air)}}{n_{O_2(synthetic\ air)} + n_{N_2(synthetic\ air)} + n_{N_2(diluent)}}.100 \qquad \text{Equation 4-24}$$

for N_2 dilution,

$$v_{O_2} = \frac{n_{O_2(synthetic\ air)} + n_{O_2(enrichment)}}{n_{O_2(synthetic\ air)} + n_{N_2(synthetic\ air)}}.100 \qquad \text{Equation 4-25}$$

for O_2 enrichment.

$v_{O_2 ref}$ is the reference percentage of O_2 in air, i.e. the percentage of O_2 in the synthetic air. The parameters used in the correlation are listed in ***Table 4-1***.

parameter	Optimized value
A	56.21
B	-14.44
C	-214.08
D	43.47
E	267.17
α_1	1.88
α_2	-0.19
β_1	-0.24
β_2	0.27
γ_1	2.67
γ_2	0.17
ϕ_m	1.07

Table 4-1. Correlation parameters in laminar flame speed correlation.

In order to apply this correlation in engine combustion calculation, the effect of residual gas can be defined by:

$$S_L^0(v_{O_2}) \text{ with residual gas} = S_L^0(v_{O_2})(1 - 2.1\chi_{residual}) \qquad \text{Equation 4-26}$$

where $\chi_{residual}$ is the residual gas in engine.

4.4 Calibration process

The calibrations were accomplished by coupling Amesim with Matlab program which was employed for arranging the experimental results to facilitate the input of simulation,

simulating and calibrating all the simulation points using the boucle for time saving, and plotting and saving the simulation results.

Figure 4-4 illustrates the simulation process for all the engine operation points. Firstly, bench data (such as intake pressure, intake temperature, exhaust pressure, exhaust gas temperature, equivalence ratio, advanced ignition crank angle, and in-cylinder pressure…) were read by a Matlab program. In this program, Matlab-AMEsim coupling was used for optimizing the in-cylinder data.

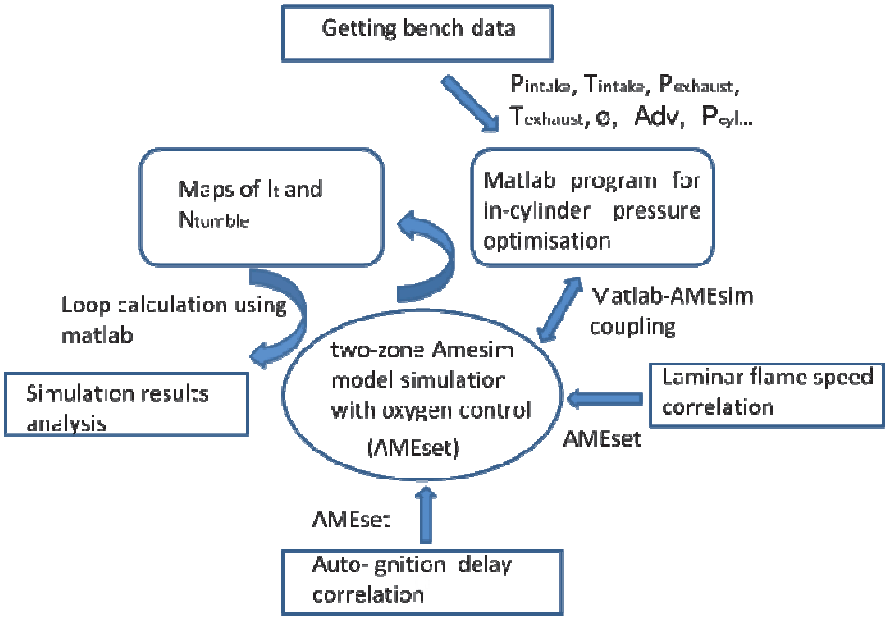

Figure 4-4. illustration of simulation process

The second part of this algorithm is focused on two-zone Amesim model simulation with oxygen control. In this part, the AMEsim developing tool AMEset was applied, on one hand, to induce laminar flame speed and auto-ignition delay correlations inside the main combustion model as the sub-routines, on the other hand, the main two-zone combustion model was modified to adapting the oxygen control.

Multi-cycle simulations were performed with the initial 'guess value' of the integral scale and tumble value, and then the simulation results of in-cylinder pressure of the last simulation cycle were compare to the experimental data for a range of crank angle from 250 to 450 CAD. the discrepancy between the two values can be calculated by:

$$error = \sum_{i=250\,^{\circ}CA}^{450\,^{\circ}CA}(P_{cyl}(simu) - P_{cyl}(expe))^2 + \alpha * (P_{max}(simu) - P_{max}(expe))^2$$

Equation 4-27

The second term of the above expression gives a more precision of P_{max} calibration with regards to the importance of P_{max} for heat release and exhaust gas emission. The parameter α gives a flexible value for considering more or less effect of P_{max}.

Once the error between simulation and experimental in-cylinder data was minimized, the value of lt and Ntumber can be found. By loop calculation, the maps of of lt and Ntumber can therefore be obtained. The last part of this algorithm is re-using the above obtained maps to calculate the simulation results.

Differing from the calibration process methodology employed by Richard et al. (Richard et al. 2009), which used an automatic calibration tool, IFP-Optilab, the present algorithm avoids the step of residual gas calibration. In their study, calculations start at IVC and end at EVO in their first step of calibration, thus the initial conditions at IVC should be well estimated by several assumptions: the residual gas temperature at Intake Valve Opening (IVO) is calculated assuming an adiabatic expansion of the residual burnt gases. And the temperature at IVC is then computed by a balance equation of sensible enthalpy. However, in present study, the initial conditions that concern the mass fraction of air, the mass fraction of the isooctane fuel, intake pressure and temperature are directly taken from experimental data. Residual burned gases, which have a significant impact on combustion process (heat release, knock, pollutants...), were estimated by muti-cycle simulation with five cycles of engine operation. Thus, only the results of the last cycle were adopted for calculating the error of in-cylinder data between simulation and bench data, and analyzing the engine performance, exhaust gases emission, and engine knock.

4.5 Amesim model results

4.5.1 Validation of pure compression cycle

In order to validate the simulation model, pure compression cycle was employed as the first test case.

Figure 4-5 shows that the simulation results of the in-cylinder pressure are perfectly correspond to the bench ones for a range of 6 bars to 16 bars with the steps of 2 bars. In this case, several parameters were calibrated due to their uncertainties.

The Compression ratio, an important parameter, cannot be defined as the same value of the engine estimated one. The discrepancy between the simulation value and the estimated one is about 5% because of the two main reasons following: firstly, the effect of crevice flow was not taken into account in present Amesim models. The mechanism of crevice process was described by Heywood as below: when the cylinder pressure rises during compression, unburned mixture or air is forced into each crevice region; during the combustion while the pressure continues to raises, unburned mixture or air continues to flow into these crevice volumes. This mechanism will increase the real dead volume of the engine, and thus decrease the real compression ratio. The crevice volume stated by Heywood for V-6 engine is about 3.5% of total clearance volume. Secondly, the effect of blow-by can also affect the precision of compression ratio. In practice, during the test bench, blow-by was recorded about a value of 1% to 2% of total intake mass of gas in the cylinder, which depends on different operation conditions.

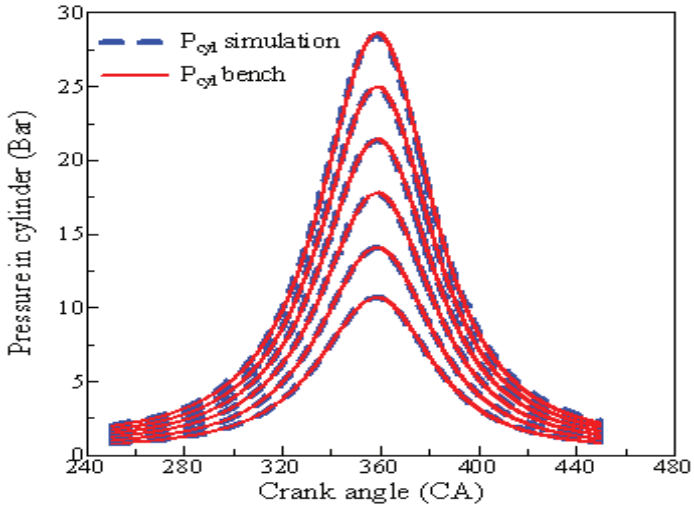

Figure 4-5. Validation of pure compression process. From bottom to up, the intake pressures are from 6 bars to 16 bars with the steps of 2 bars

Another parameter employed in calibration is the coefficient for correction on heat exchange. This parameter makes it possible to correct the calculated heat flow, for example, to take account the dispersion between cylinders (IFP Engine library (IFP-EN 2008)). In our test bench, mono-cylinder was realized by not running the three other cylinders with four cylinders engine. Thus, the wall heat exchange will be more efficient than normal mono-cylinder one.

4.5.2 Studied cases

The different operation points employed in engine test bench and the Amesim combustion model calibration process are presented in ***Figure 4-6***. The figure on the left hand presents various conditions of Indicated Mean Effective Pressure and oxygen percentage. For conditions inside the rounded rectangle, different values of equivalence ratios for fixed IMEP 8 bar were tested, as indicated on the right hand of the ***Figure 4-6***. In the same case, equivalence ratios for IMEP 4 bar, 6 bar, and 10 bar were also investigated, although the operation points are not presented here.

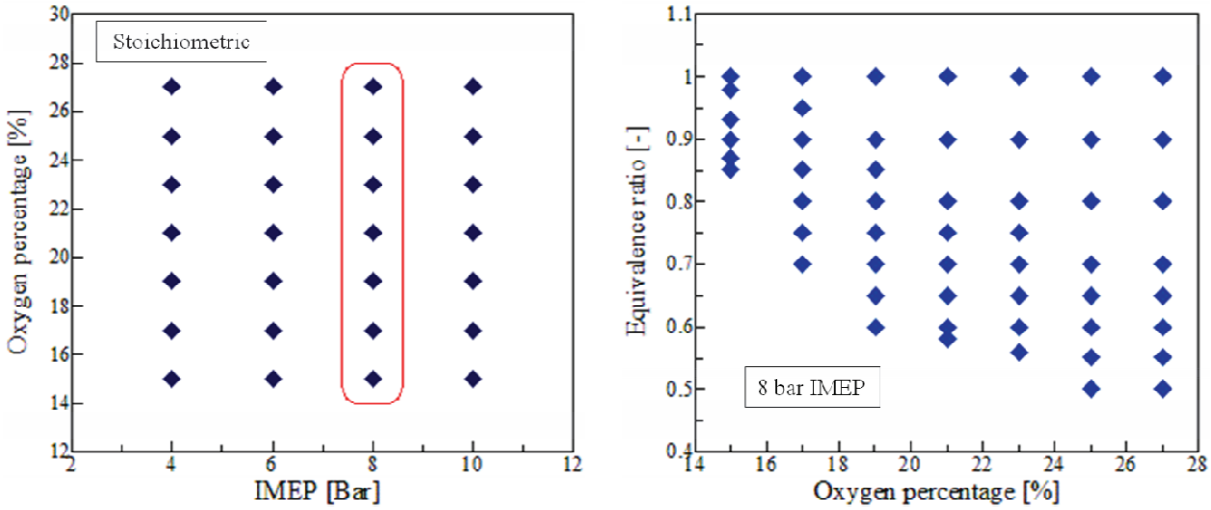

Figure 4-6. Presentation of the different operation points employed in engine test bench and the Amesim combustion model calibration process (1400 rpm).

Operation conditions of engine bench tests at 10 IMEP are showed in ***Table 4-2***. Generally, the range of equivalence ratio becomes larger while increasing the O_2 percentage. For each operation point, the spark advance and the intake pressure were adjusted simultaneously in order to maintain the load and obtain a minimum value of indicated specific fuel consumption (SFC).

O_2 percentage	Equivalence ratio	intake pressure	Spark advance	Fuel mass flowrate[kg/h]	Fuel mass flowrate[mg/cp]	l_t	N_{tu}
15	1	1.6	-19	0.9774	23.2710	0.1382	1.9745
15	0.9	1.78	-25	0.9526	22.6814	0.1027	1.7301
17	1	1.385	-14	1.0086	24.0154	0.1708	1.9244
17	0.9	1.49	-16	0.9733	23.1729	0.1660	1.9057
17	0.8	1.71	-20	0.9630	22.9286	0.1481	1.6340
17	0.7	1.89	-24	0.9697	23.0876	0.1356	1.5773
19	1	1.27	-12	1.0520	25.0476	0.1886	2.0439
19	0.9	1.352	-15	1.0040	23.9048	0.1804	2.0271
19	0.8	1.5	-16	1.0010	23.8333	0.1644	1.9438
19	0.7	1.68	-19	0.9860	23.4762	0.1406	1.7401
21	1	1.185	-10	1.0840	25.8095	0.2160	2.2088
21	0.9	1.262	-12	1.0340	24.6190	0.1988	2.1666
21	0.8	1.387	-13	1.0120	24.0952	0.1795	2.0615
21	0.7	1.598	-14	1.0250	24.4048	0.1493	1.8985
23	1	1.13	-4	1.1193	26.6497	0.2269	2.2962
23	0.9	1.2	-5	1.0663	25.3883	0.2116	2.2592
23	0.8	1.33	-6	1.0576	25.1809	0.1840	2.1503
23	0.7	1.471	-8	1.0394	24.7482	0.1526	1.9665
23	0.6	1.701	-12	1.0443	24.8643	0.1705	1.9841
25	1	1.12	2	1.1930	28.4048	0.2362	2.3413
25	0.9	1.15	0	1.1120	26.4762	0.2221	2.3260
25	0.8	1.25	-2	1.0820	25.7619	0.2016	2.2928
25	0.7	1.4	-3	1.0690	25.4524	0.1546	2.0799
25	0.6	1.63	-6	1.0740	25.5714	0.0970	2.0277
27	1	1.12	7	1.2770	30.4048	0.2556	2.3503
27	0.9	1.15	5	1.1870	28.2619	0.2433	2.4149
27	0.8	1.25	4	1.1580	27.5714	0.2150	2.3563
27	0.7	1.38	2	1.1300	26.9048	0.1561	2.1458
27	0.6	1.549	-2	1.0960	26.0952	0.1192	1.8703
27	0.5	1.88	-8	1.1100	26.4286	0.1093	1.4361

Table 4-2. Operation conditions of engine bench tests at 10 IMEP

In ***Figure 4-7***, intake pressure, spark advance and fuel mass flow rates versus equivalence ratio for different cases of O_2 percentages are presented. Normally, by increasing the O_2 percentage, intake pressure decreases for maintaining the IMEP value constant as showed in ***Figure 4-7***a. nevertheless, in case of 27% O_2, especially for higher equivalence ratio (0.8, 0.9, 1.0), the Intake pressures were set to be near the value of 25% O_2 in order to lower the spark advance while keeping the IMEP value constant. This operation is mainly for preventing engine knock

as knock is active at 27% O_2. ***Figure 4-7***b shows that at a fixed equivalence ratio, spark advance is always decreased by increasing O_2 percentage in order to maintain the load and obtain a minimum value of indicated specific fuel consumption (SFC). Fuel mass flow rate depends deeply in indicated specific fuel consumption (SFC) as engine load maintains constant. Thus fuel mass debit showed in figure ***Figure 4-8*** corresponds well with the SFC, which was presented in chapter 2.

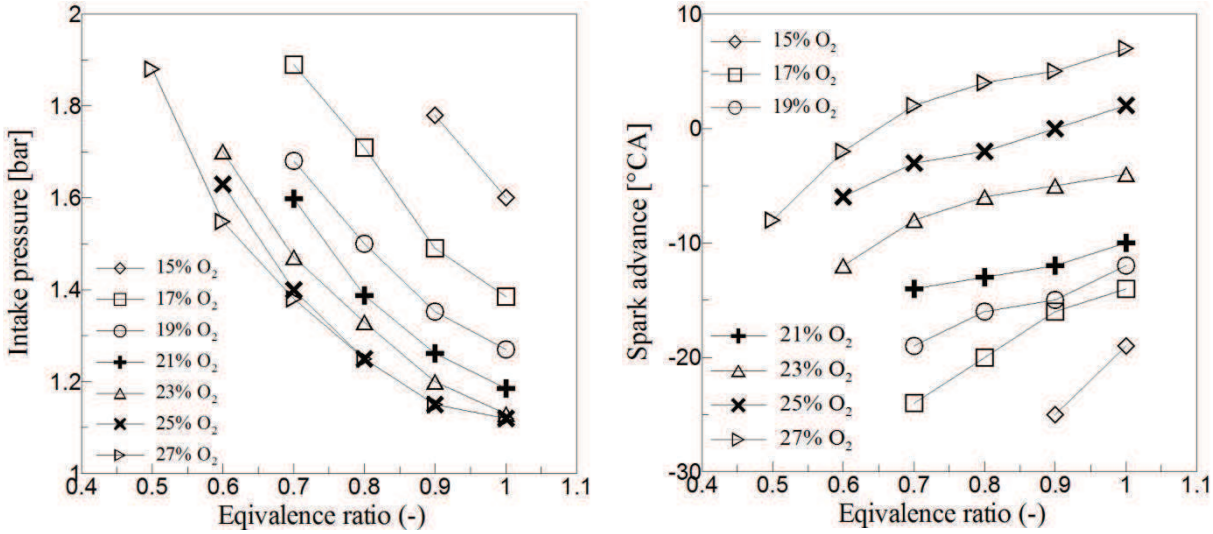

(a) (b)

Figure 4-7. Intake pressure(a) and spark advance (b) versus equivalence ratio for different cases of O_2 percentages

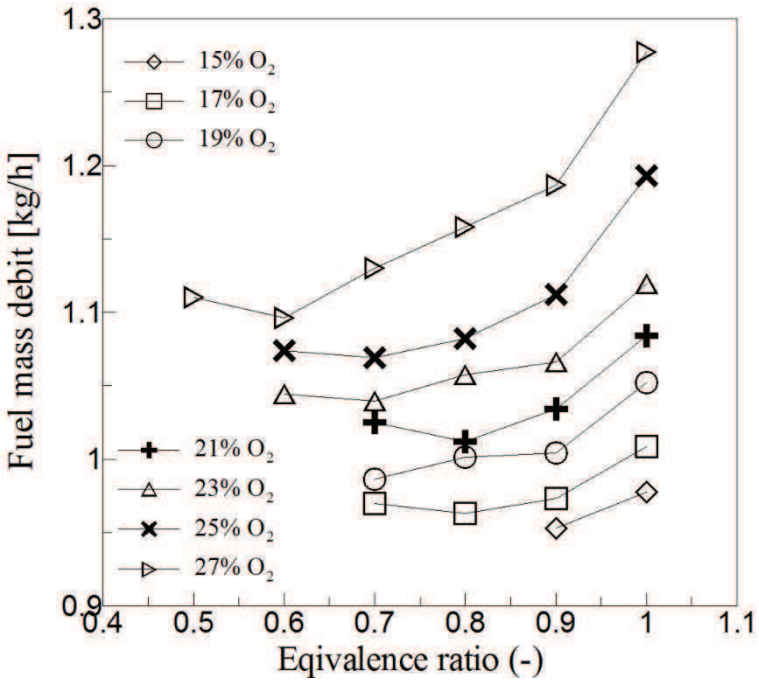

Figure 4-8. Fuel mass flow rate versus equivalence ratio for different cases of O_2 percentages

4.5.3 Calibration of in-cylinder pressure

Experimental and simulated cylinder pressure curves for different engine loads with engine regime at 1400 rpm are presented in following figures.

In ***Figure 4-9a, 5-9b, 5-9c,*** the in-cylinder pressure is showed for different cases of oxygen percentage at stoichiometric equivalence ratio, 15% O_2, 21% O_2 and 27% O_2 respectively. The discrepancies can be found in ***Figure 4-9***a, especially for the cases of IMEP 8 and 10 bar, which may due to the spherical evolution assumption of flame propagation inside the combustion volume. For high nitrogen dilution mixture, the flame evolution in cylinder becomes irregular, which phenomena have been presented in the work of Landry (Landry 2009). However, good calibration results can be found in ***Figure 4-9 b and 5-9c*** for 21% O_2 and 27 O_2 respectively. The simulated results show a good agreement with our experimental data, which indicates that, the evolution of the burning velocity and then the heat release rate is well described for all cases(Bougrine et al. 2011).

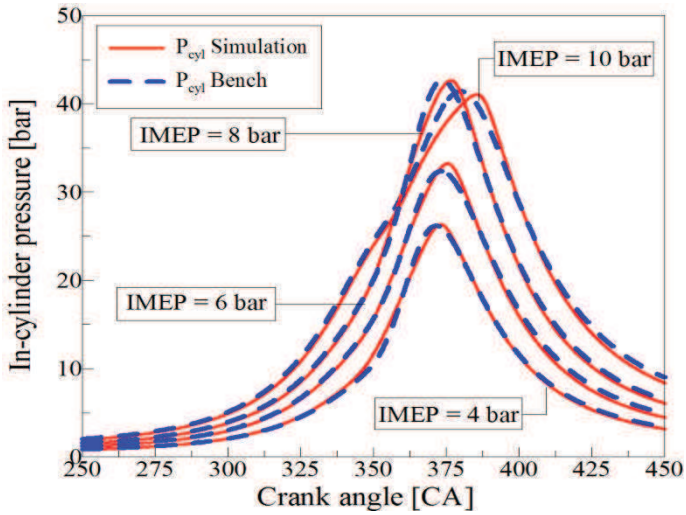

Figure 4-9a. ϕ=1, 15% O2

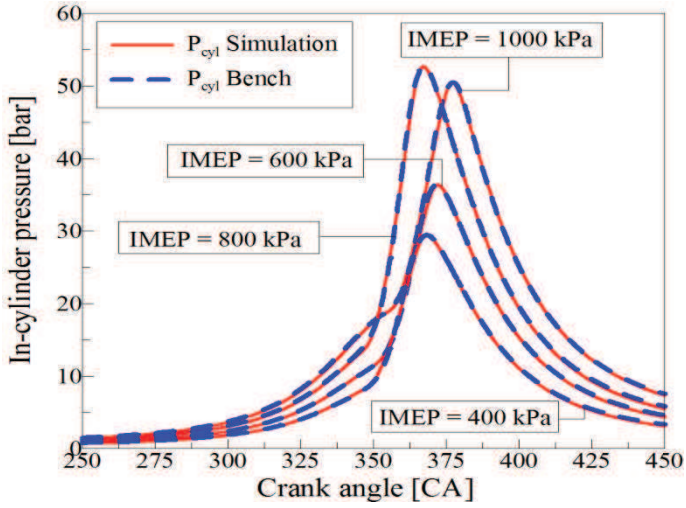

Figure 4-9b. ϕ=1, 21% O2

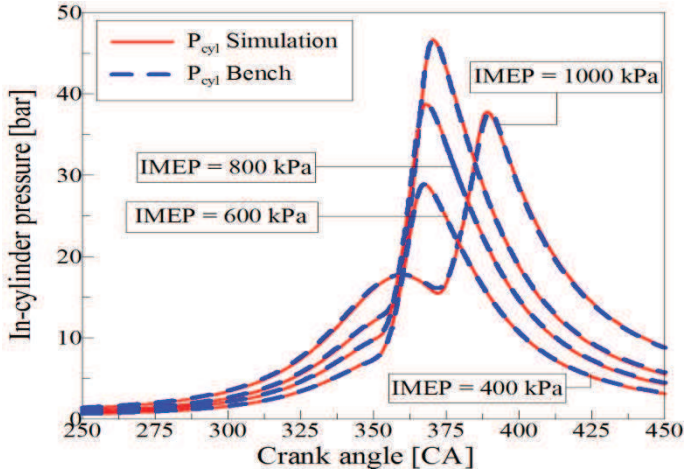

Figure 4-9c. ϕ=1, 27% O2

Figure 4-9. Comparison between experimental and simulated cylinder pressure curve for different engine load at 1400 rpm.

In ***Figure 4-10***, the in-cylinder pressure is showed for different cases of oxygen percentage at IMEP = 10 bar, 15% O_2, 21% O_2 and 27% O_2 respectively and for different equivalence ratio until lean operating limit at the constant load. The intake pressures of smaller equivalence ratio mixture are bigger than the larger ones in order to maintain the IMEP at 10 bar, which are indicated in the figures with the arrow symbols. For lean mixture, for instance, $\phi = 0.9$ in figure 5.5 (a), $\phi = 0.7$ in ***Figure 4-10*** (b), and $\phi = 0.5$ in ***Figure 4-10*** (c), the simulation results have a certain discrepancy compare to experimental data. These errors may also due to the hypothesis of spherical propagation of flame. Moreover, the high intake pressure level was found for the case of $\phi = 0.6$ and 0.5 the maximum pressure is not well predicted, which can also be found in the previous study of Richard et al.(Richard et al. 2009). The compression ratio is calibrated by pure compression process as described in section 4.5.1. A little different of calibrated value has been found for different intake pressure level: higher calibrated value is found for higher intake pressure level. However, a fixed compression ratio is determined by minimizing the errors of all the in-cylinder pressure calibration cases. In this case, the fixed compression ratio produced a certain peak pressure error for lean mixture cases. For the cases of equivalence ratio near stoichiometry, the in-cylinder pressure is perfectly predicted.

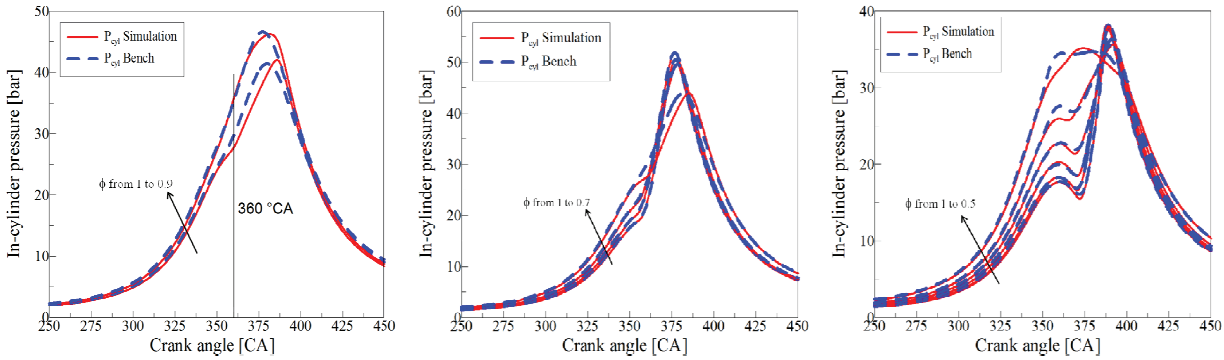

(a) IMEP =10 bar, 15% O_2 (b) IMEP =10 bar, 21% O_2 (c) IMEP =10 bar, 27% O_2

Figure 4-10. Comparison between experimental and simulated cylinder pressure curve for different equivalence ratio at 1400 rpm.

Relative error of IMEP and maximum in-cylinder pressure are presented in following figures.

In ***Figure 4-11***(a), IMEP relative error and max pressure relative error versus IMEP value for O_2 percentage from 15% to 27% are showed. The maximum value can be found in case of 15% O_2 for each case of IMEP. The difference among these cases are not every clear. The second figure (***Figure 4-11***b) shows the evolution of max in-cylinder pressure relative error versus IMEP. Only two points are greater than 1%, which are the case of $IMEP = 6\ bar$, 15% O_2 and $IMEP = 10\ bar$, 17% O_2.

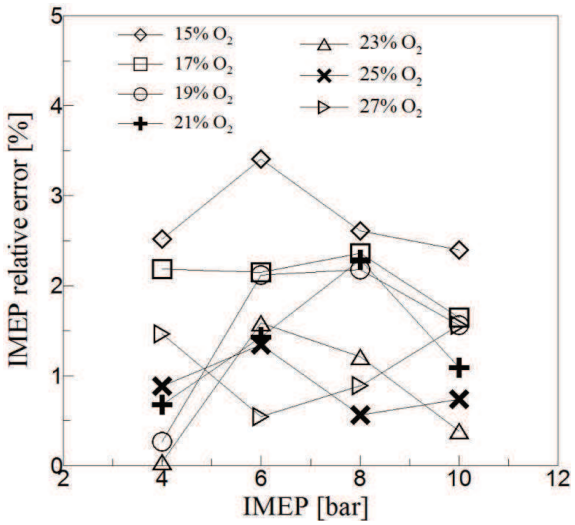

Figure 4-11a

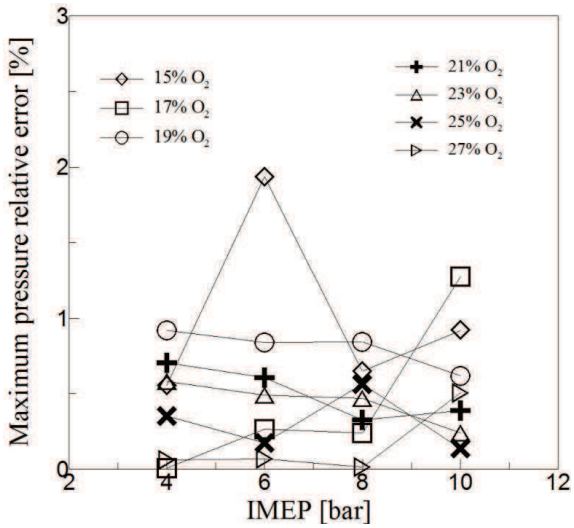

Figure 4-11b

Figure 4-11. Relative error of IMEP (a) and maximum in-cylinder pressure (b) as function of IMEP.

In ***Figure 4-12***, IMEP relative error (***Figure 4-12***a) and max pressure relative error (***Figure 4-12***b) versus equivalence ratio for O_2 percentage of 15%, 21% and 27% are showed. The large values of IMEP relative error and max pressure error are found at 15% O_2. However, IMEP relative errors are not exceed 3% for all cases, and max pressure relative errors are less than 2%.

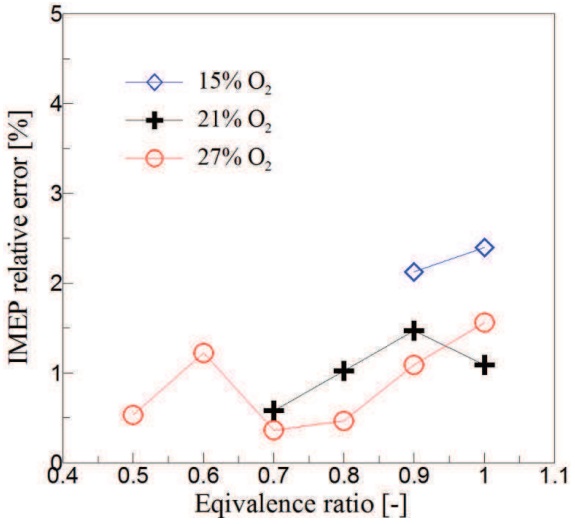

Figure 4-12a

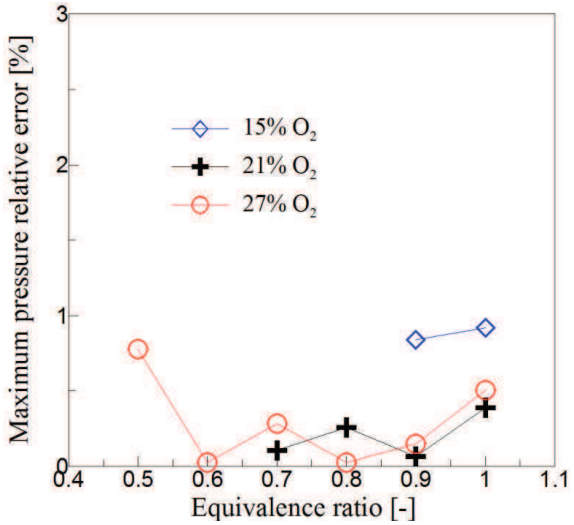

Figure 4-12b

Figure 4-12. Relative error of IMEP (a) and maximum in-cylinder pressure (b) as function of equivalence ratio.

In ***Figure 4-13***, IMEP relative error (***Figure 4-13***a) and (***Figure 4-13***b) maximum pressure relative error versus O_2 percentage for different cases of IMEP are presented. The large values of IMEP relative error and maximum pressure relative error are found at 15% O_2. The small values of IMEP absolute errors are situated near 23%O_2. The max pressure relative error roughly decreases with increasing of O_2 percentage. And it is important to note that the model simulates well the O2 variation, as the errors are less than 5% for maximum of pressure and less than 2% for IMEP.

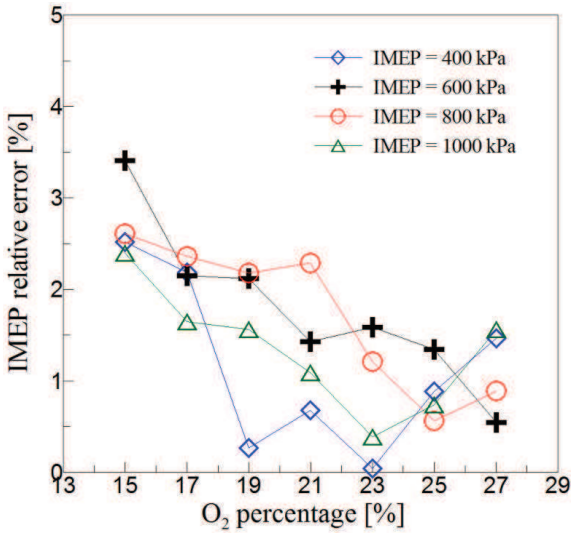

Figure 4-13a

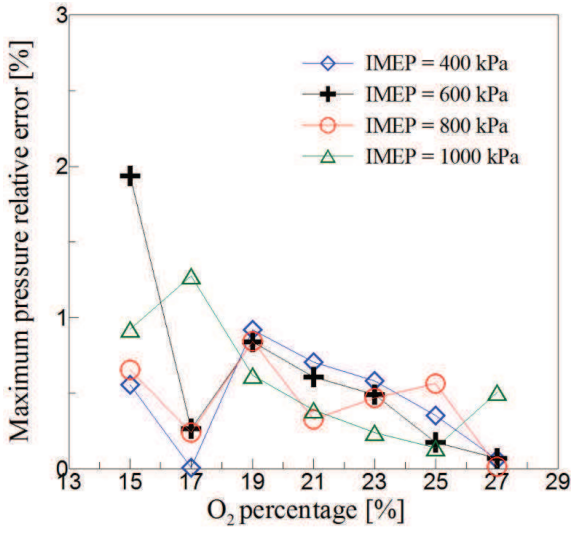

Figure 4-13b

Figure 4-13. Relative error of IMEP (a) and maximum in-cylinder pressure (b) as function of O_2 precentage.

The maps of the integral length scale (lt) and the tumble number (N_{tumble}) values are showed in ***Figure 4-14*** to ***Figure 4-16***. The integral length scale is the characteristic length corresponding to the biggest turbulent structure which produces the turbulent energy. The experimental estimation of l_t in optical SI engine is previously studied in our laboratory using PIV (particle image velocimetry) technology (Foucher 2002; Landry 2009). In their studies, the determination of lt for one spatial coordinate (i.e. x direction) is based on: $l_t = \int_0^{x(f=0)} f(x)dx$ with $f(x) = \frac{\overline{u'(x_0)u'(x)}}{u'^2}$ where f(x) is auto-correlation function. Compare to the experimental determination of l_t, l_t determined by the numerical calibration here is less accurate. The precision of lt determination needs not only a good representation of flame wrinkling model but also a fine laminar burning velocity correlation.

Three cases of the integral length and the tumble number are discussed below. In AMESim model: l_t is assumed as integral length scale at spark timing, and it remains constant for the whole combustion stroke. For different spark timing (which is related to piston-cylinder head distance), lt evolves theoretically as: it decreases when the distance between piston and cylinder head decreases. This evolution is also found by the experimental study of Hong et al. (Hong et al. 1997), in which the integral length scale decreases intensively after the IVO. In ***Figure 4-14***, lt and N_{tumble} are plotted as function of IMEP. Except the cases of 15% O_2 and 17% O_2, lt decreases with the increase of IMEP. The decrease trend of l_t is also found in the paper of Richard (Richard et al. 2009). This is mainly due to the spark timing is more advanced for lower IMEP, which means higher piston-cylinder head distance and then higher l_t value. For N_{tumble} value, with the increase of IMEP, a slight decrease was found for almost of study

cases, except 15% O_2 and 17% O_2. The Tumble value can be considered as quasi-constant compare to the magnitude of decrease trend of l_t.

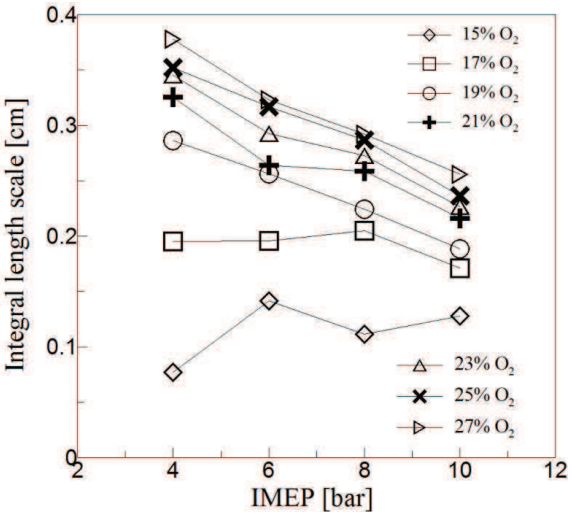

Figure 4-14a

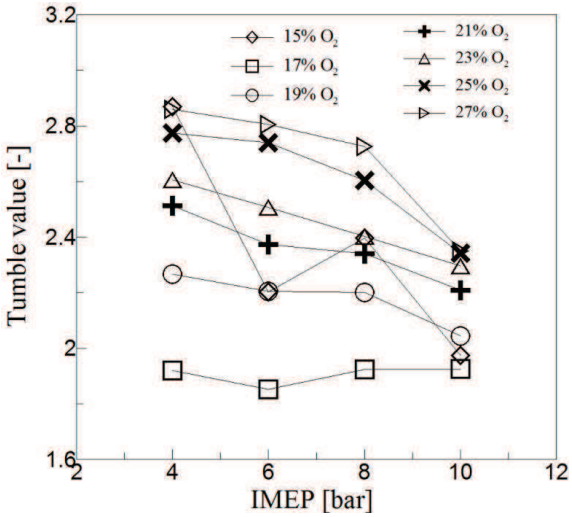

Figure 4-14b

Figure 4-14. integral length scales and tumble values obtained by optimizing the in-cylinder pressure.

In ***Figure 4-15***, the integral length and the tumble number versus equivalence ratio are presented for 15%, 21%, and 27% O_2 respectively. The integral length increases with increasing of the equivalence ratio except for the point 23%O_2, $\phi = 0.6$. The overestimation of this point is essentially due to the calibration error during combustion stroke. However, for this operation point, as showed in the graph on the lower side, the tumble number has a good coherence with the other points. The effects of this two parameters to in-cylinder pressure is: when the tumble number increases, the maximum in-cylinder pressure increases as well; when the integral length decreases, the peak position is advanced (IFP Engine library (IFP-EN 2008)). The tumble number value is quite smooth because the factor α is employed for well calibration the maximum in-cylinder pressure.

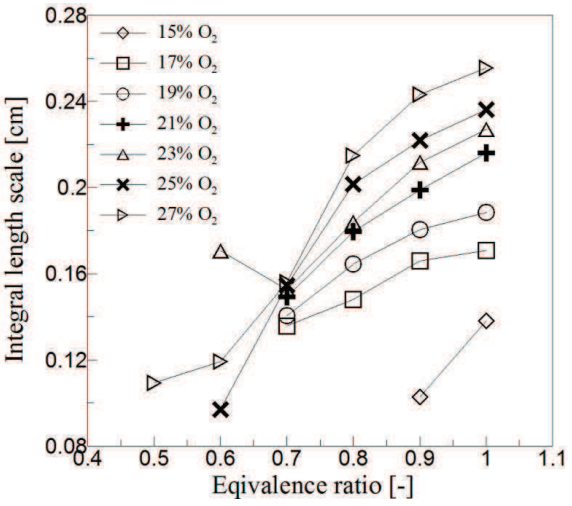

Figure 4-15a

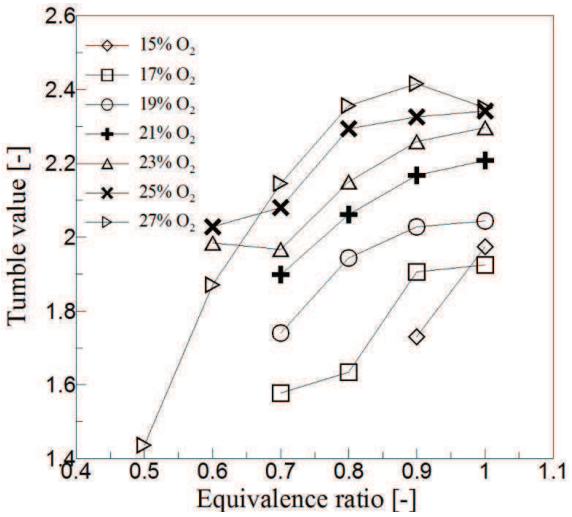

Figure 4-15b

Figure 4-15. integral length scales and tumble values obtained by optimizing the in-cylinder pressure at IMEP=10 bar.

In ***Figure 4-16***, the integral length and the tumble number versus O_2 percentage are presented for IMEP from 4 to 10 bar. With the increase of O_2 percentage, the integral length increases as well. The tumble value increases with O_2 percentage except the cases of 15% O2.

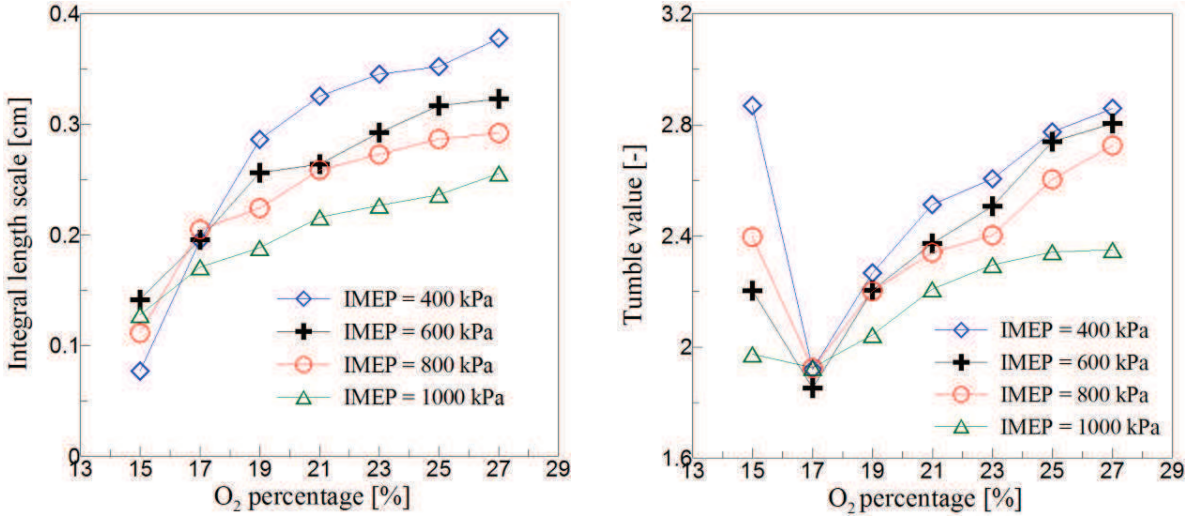

Figure 4-16. integral length scales and tumble values obtained by optimizing the in-cylinder pressure at unit equivalence ratio.

Although some operation points are beyond the general tendency, the evolution of the integral length scale and the tumble number is smooth when the IMEP, equivalence ratio and O_2 percentage are varied. Thus, reasonable values of l_t and N_{tumble} can be obtained by interpolation of the data in look-up tables, in order to transient engine operations.

Integral length scales and tumble values versus intake pressure for IMEP at 10 bar are presented in ***Figure 4-17***. Regardless of O_2 percentage and equivalence ratio, both of the two numbers have a decreasing tendency with the increasing of the intake pressure. lt and N_{tu} are fitted linearly and some exception points of l_t are found for in case of low equivalence ratio or low O_2 percentage.

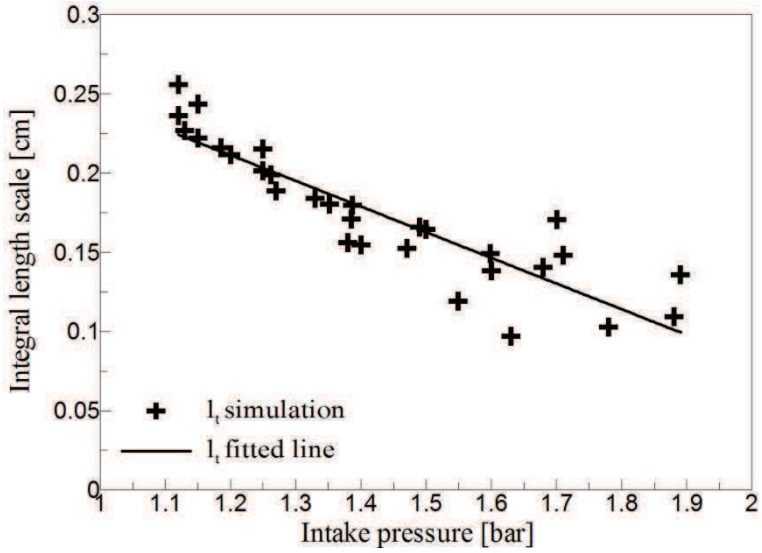

(a)

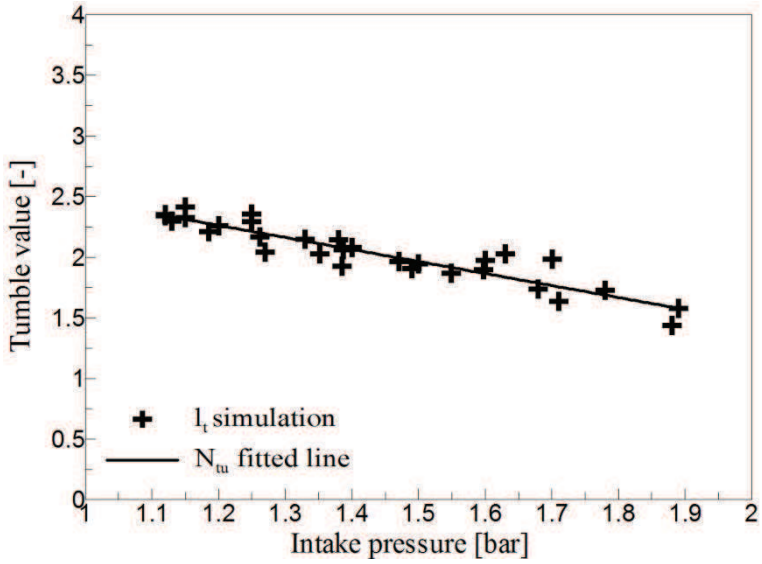

(b)

Figure 4-17. integral length scales (a) and tumble values (b) versus intake pressure for IMEP at 10 bar.

4.5.4 Combustion characteristics

Effect of O_2 percentage on combustion characteristics

The evolution of calculated in-cylinder pressure at stoichiometric equivalence ratio and IMEP=1000 kPa for different cases of O_2 percentage are presented in ***Figure 4-18***. The in-cylinder pressure is started at the spark ignition degree with the operation conditions listed in ***Table 4-3***. The increase in O_2 percentage results in a decrease in intake pressure while maintaining the same IMEP. However, for 27% O_2, in order to maintain IMEP at 10 bar, the intake pressure was kept at the same value as for 25% O_2 while increasing spark timing to prevent knock. For relatively high O_2 percentages, engine operation was limited by knock phenomena, which can be seen in the in-cylinder pressure plot. To avoid engine knock, the higher spark timing was set for higher oxygen enrichment.

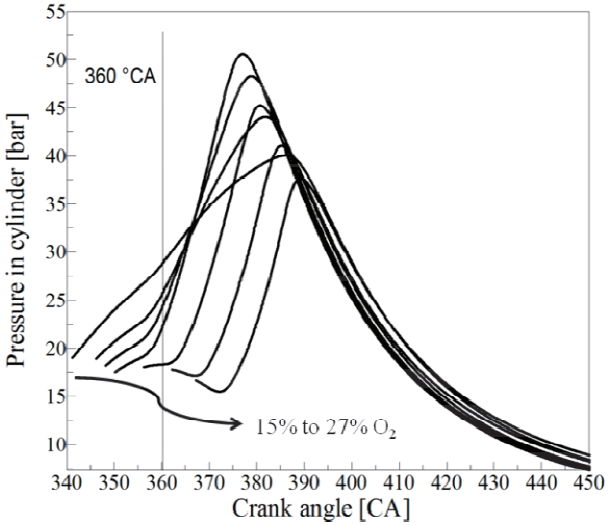

Figure 4-18. Evolution of the mean in-cylinder pressure at stoichiometric and IMEP=1000kPa

Figure 4-19 presents laminar burning velocities versus crank angle degree with different O_2 percentages. The laminar burning velocity increases as a function of O_2 percentage. Compared to 15% O_2, the laminar burning velocity of 27% O_2 is more than 8 times higher. The reasonable results of laminar burning velocity under engine operation conditions were obtained thanks to the reliability of the experimental correlation proposed by Galmiche et al.(Galmiche et al. 2012).

O_2 %	Intake pressure [bar]	Spark timing [°CA]	Fuel mass flow rate [kg/h]
15	1.60	-19	0.98
17	1.39	-14	1.01
19	1.27	-12	1.05
21	1.19	-10	1.08
23	1.13	-4	1.12
25	1.12	2	1.19
27	1.12	7	1.28

Table 4-3. Operating conditions for combustion analysis

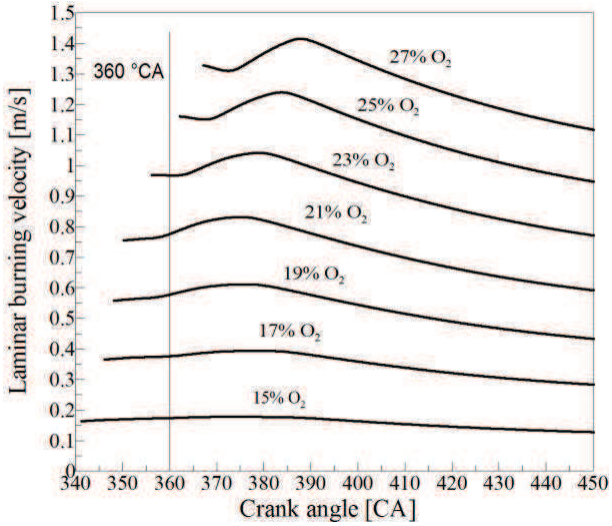

Figure 4-19. Laminar burning velocity versus crank angle degree with different O_2 percentages at stoichiometric and IMEP=1000kPa

The evolution of the flame surface and flame wrinkling versus crank angle degree for different O_2 percentages at stoichiometry and IMEP=1000kPa are plotted in ***Figure 4-20***. A previous experimental study (Mounaïm-Rousselle et al. 2013) showed that dilution enhances flame-turbulence interactions and that the corrugation generated through dilution occurs at smaller scales than the integral length scales. This phenomenon is well produced in the present simulation, as shown in ***Figure 4-20***a, for 15 and 17 % O_2, which corresponds to 26.87% and 17.65% of EGR respectively. The flame surface is much higher than in the case of lower dilution or oxygen enrichment. This tendency is mainly due to the high flame wrinkling in the case of high dilution, as presented in ***Figure 4-20***b.

Figure 4-21 shows the evolution of the turbulent flame velocity versus crank angle degree. The flame kernel growth is initially laminar like as described in (Heywood 1994) and once the flame has grown to more than 5 mm, it can become turbulent(Boulouchos et al. 1994).

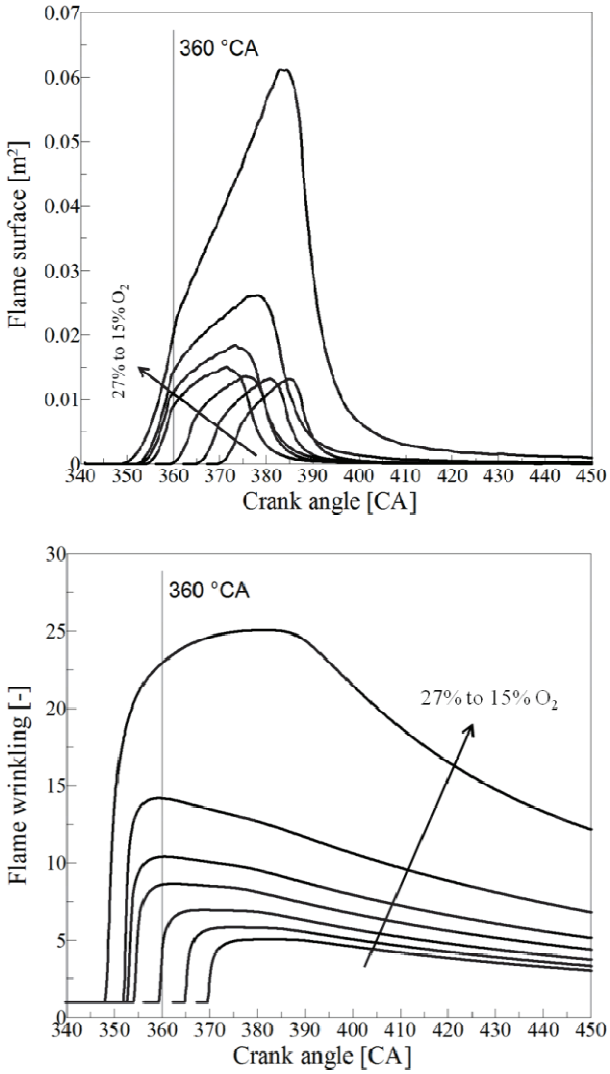

Figure 4-20. Flame surface (a) and flame wrinkling (b) versus Crank angle with different O_2 percentages at unit equivalence ratio and IMEP=1000kPa

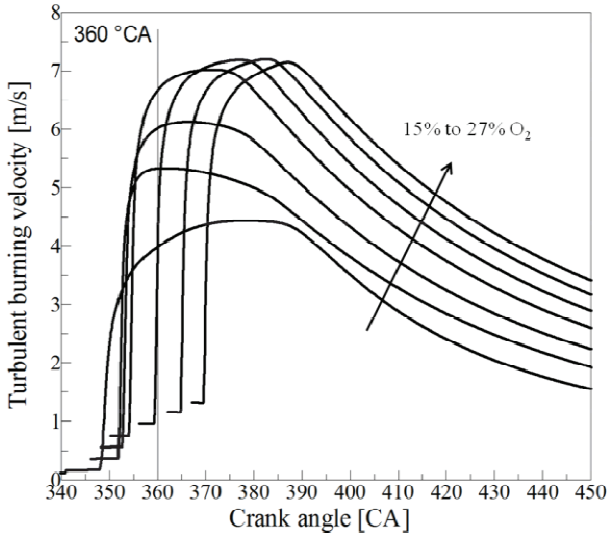

Figure 4-21. Evolution of turbulent flame velocity with different O_2 percentages at stoichiometric equivalence ratio and IMEP=1000kPa

Thus, based on the above findings, as the laminar burning velocity is much lower in the case of dilution, the laminar flame state lasts longer than with oxygen enrichment: about 7.5 CAD for 15% O_2, 5 CAD for 21% O_2 and 2.5 CAD for 27% O_2. Although substantial differences are found for laminar burning velocities (8 times higher with 27% O_2 compared to 15% O_2), the turbulent burning velocities show comparatively little difference (less than 2 times higher with 27% O_2 compared to 15% O_2). This is mainly due to the reverse evolution of flame wrinkling: the lower the O_2 percentage, the higher the flame wrinkling.

In order to characterize the combustion regime in Peters-Borghi diagram, the ratio of the characteristic length and velocity scales versus crank angle degree for different O_2 percentages is drawn in ***Figure 4-22***. As previously described, after the spark, the flame is initially 'laminar like'. And the duration of this phase is from about 2.5 to 7.5 CAD. So here, the curve is start at 10 CAD after spark timing (ex. 360+ST+10) for all the cases. Higher the value of l_t/δ_L is found for higher value of O_2 percentage, reversely for u'/S_L. Two crank angle degree cases of these ratios (10 CAD and 20 CAD after spark timing) are showed in ***Figure 4-23***.

Finally, in ***Figure 4-24***, the combustion is classified according the Peters-Borghi diagram which gives a deeper insight into the interaction between turbulence and the flame front. According to the study of Linse et al.(Linse et al. 2009), engine combustion is normally located in thin reaction zone and corrugated flamelets zone. Generally, the combustion of the earlier generation of SI engine takes place in the corrugated flamelet regime, while the combustion of the new generation engines takes place in the thin reaction zone (Wirth 1993). Higher turbulent level and charge motion are created when turbo charging and/or direct injection are used in new generation engines, which is the main reason corresponds to the different regime between new and earlier generation engines (Linse et al. 2009).

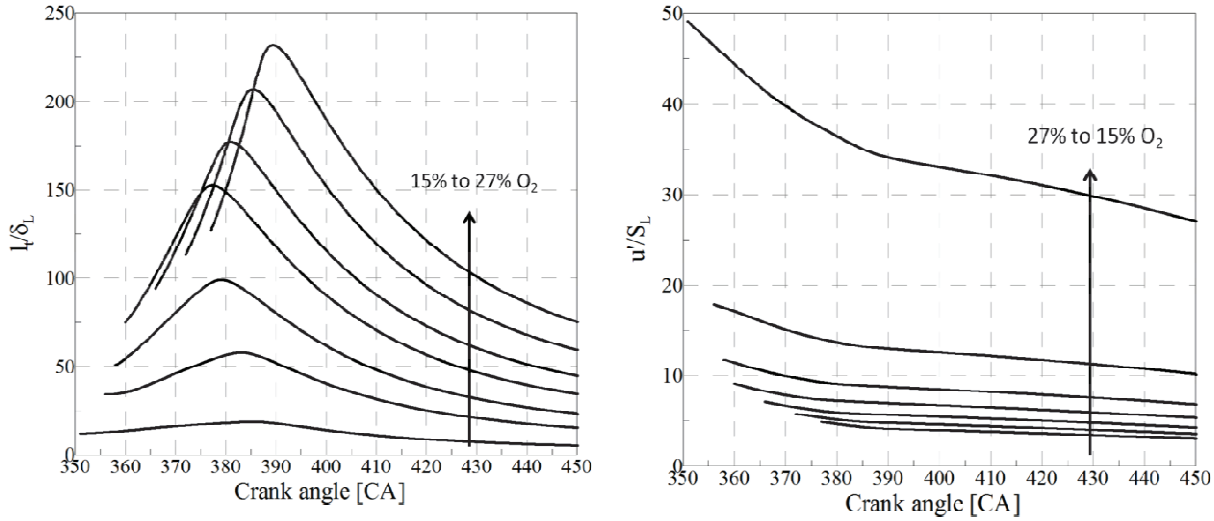

Figure 4-22. Ratio of the characteristic length and velocity scales versus crank angle degree for different O2 percentages.

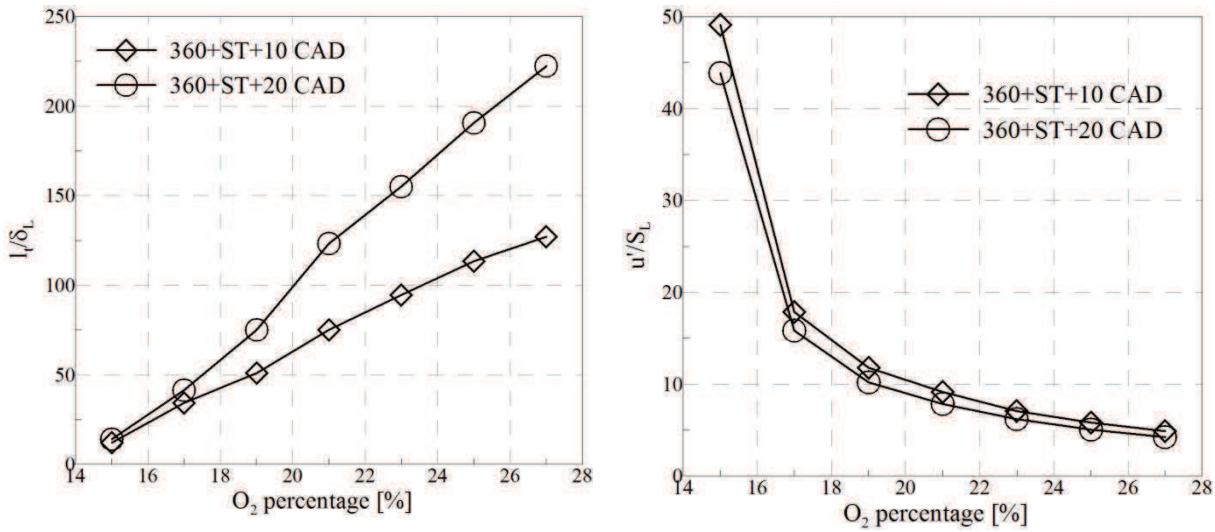

Figure 4-23. Ratio of the characteristic length and velocity scales versus O_2 percentage for two crank angle degree cases

In ***Figure 4-24***, from 15% O_2 to 27% O_2, the combustion trace passes from broken reaction zone to thin reaction zone, and finally to the corrugated flamelets zone. for the cases of 17% to 23% O_2, combustion takes place in thin reaction zone, which may mainly due to the tested engine is supercharged and the high turbulent level are produced. For the cases of 25% and 27% O_2, the combustion traces are mainly in corrugated flamelets zone. And for the case of 15% O_2, the combustion is occurred in broken reaction zone. Normally, flamelets theory is used for vehicle engine combustion simulation. The validation of flamelets theory has been determined by Poinsot et al. (Poinsot et al. 1991) based on direct simulation. Their results show that the resistance of flame front to vortices is underestimated by classical diagrams which neglect viscous, transient and curvature effects. The limit line of flamelets regime determined by Poinsot et al. is drawn as the v formed green line in ***Figure 4-24***. Therefore, for the case of 15% O_2, the spherical propagation of flame might not be well adapted, which gives a reasonable answer to the high level of in-cylinder calibration error (***Figure 4-9a).***

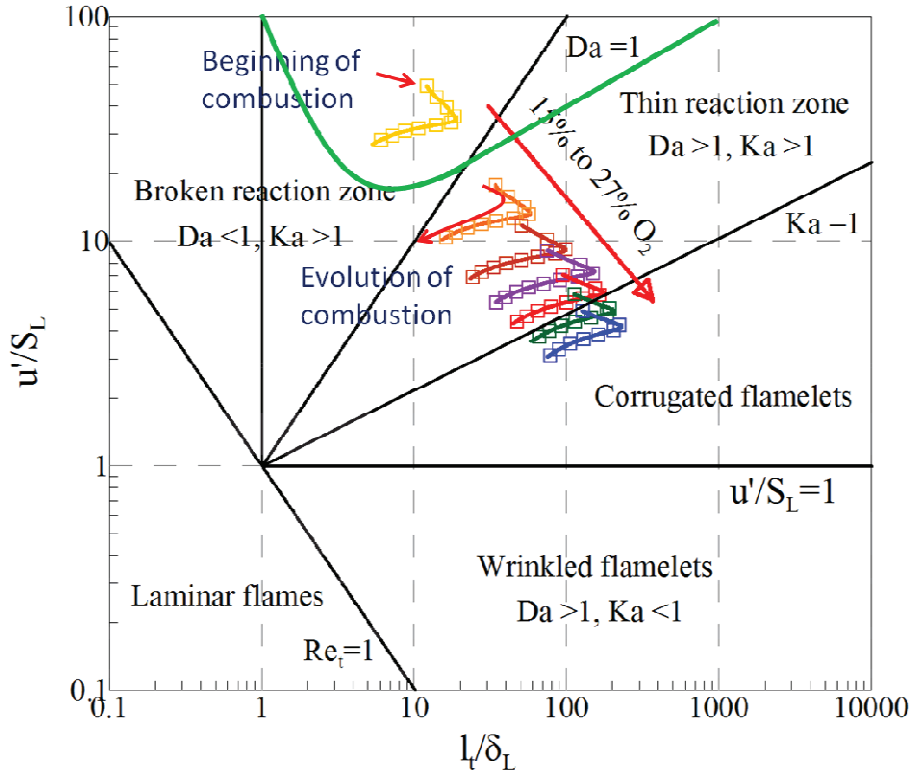

Figure 4-24. Comparison of the combustion traces in the Peters-Borghi diagram for different O_2 percentages

The effect of N_2 dilution on the combustion trace corresponds well with the previous study of Mounaïm-Rousselle (Mounaïm-Rousselle et al. 2013). Dilution makes the combustion trace towards to up-left side in de peters-borghi diagram. And the effect of O_2 enrichment which is firstly classified in Peters-Borghi diagram shows a reverse tendency compare to N_2 dilution. For all the operating cases, the combustion trace has a turning point. Compare to the simulation results of Linse et al. (Linse et al. 2009), the turning angle are smaller, which is caused by the simplification of l_t definition in AMESim model. l_t is supposed as a constant value and equal to its value at spark timing during the whole combustion stroke in the combustion model (Richard et al. 2009). While l_t normally depend on the distance between the piston and cylinder head. Nevertheless, the general tendency correspond well with the previous study of Linse et al. (Linse et al. 2009) and Mounaïm-Rousselle (Mounaïm-Rousselle et al. 2013).

Effect of equivalence ratio on combustion characteristics

The impact of equivalence ratio on the characteristic length and velocity scales is discussed below. The operation conditions are listed in ***Figure 4-25***. In order to maintain the IMEP, higher intake pressure is needed for lower equivalence ratio. And the sparking timing is optimized to have a lower SFC.

Equivalence ratio	Intake pressure [bar]	Spark timing [°CA]	Fuel mass flow rate [kg/h]
1.0	1.19	-10	1.084
0.9	1.26	-12	1.034

0.8	1.39	-13	1.012
0.7	1.60	-14	1.025

Figure 4-25. Operating conditions for combustion analysis

The ratio of the characteristic length and velocity scales versus crank angle degree and equivalence ratio are presented in ***Figure 4-26*** and ***Figure 4-27*** respectively. Higher equivalence ratio leads to higher l_t/δ_L value at same crank angle after spark. The tendency of the ratio of the characteristic length and velocity scales for lean mixture is similar to N_2 dilution cases that discussed above. Thus the combustion traces in Peters-Borghi diagram (***Figure 4-28***) show similar behavior compare to dilution cases (***Figure 4-24***). Similar combustion behavior is also found in our experimental results of CA10, CA50 and CA90 for these two cases (in section 2.6.6), which confirms the reliability of the simulation results of combustion traces in Perters-Borghi diagram. This similarity is mainly due to the reason that the access of O_2 in case of lean mixture which not participles the chemical reactions acts like N_2 dilution. The combustion traces are all situated in thin reaction zone for these cases.

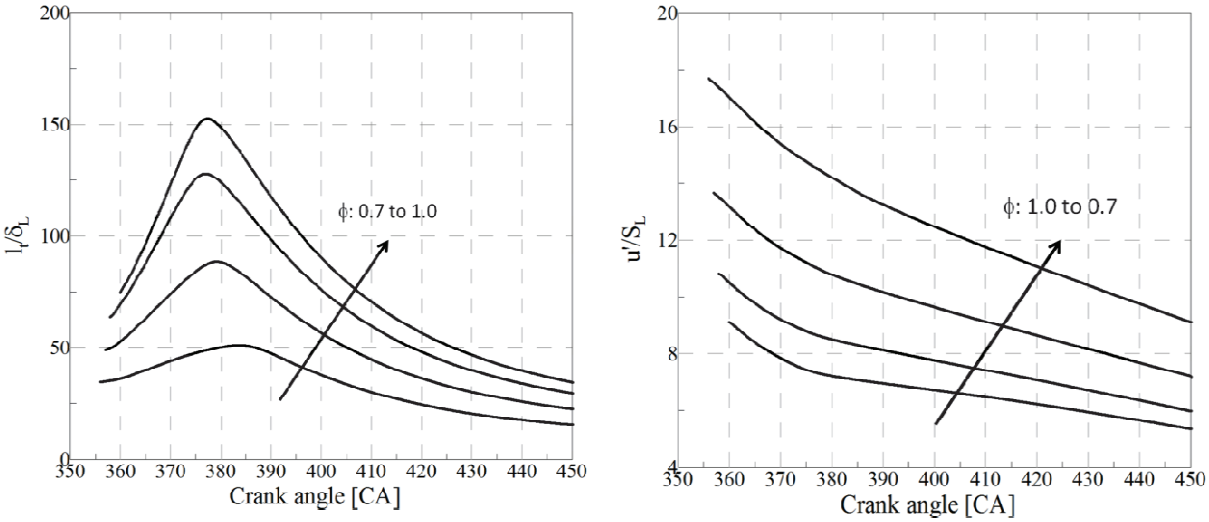

Figure 4-26. Ratio of the characteristic length and velocity scales versus crank angle degree for different equivalence ratios.

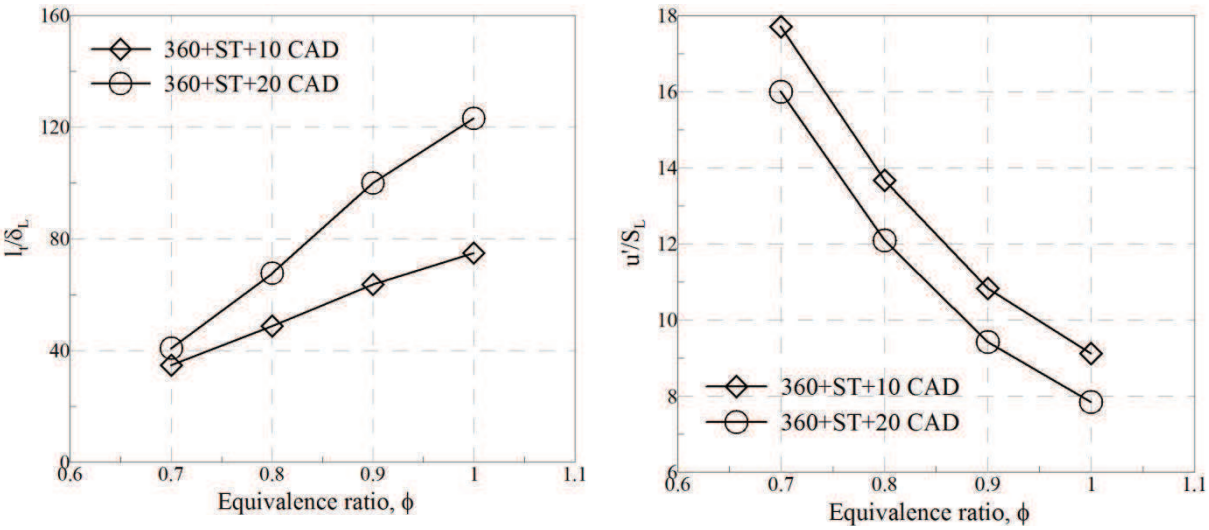

Figure 4-27. Ratio of the characteristic length and velocity scales versus equivalence ratio for two crank angle degree cases

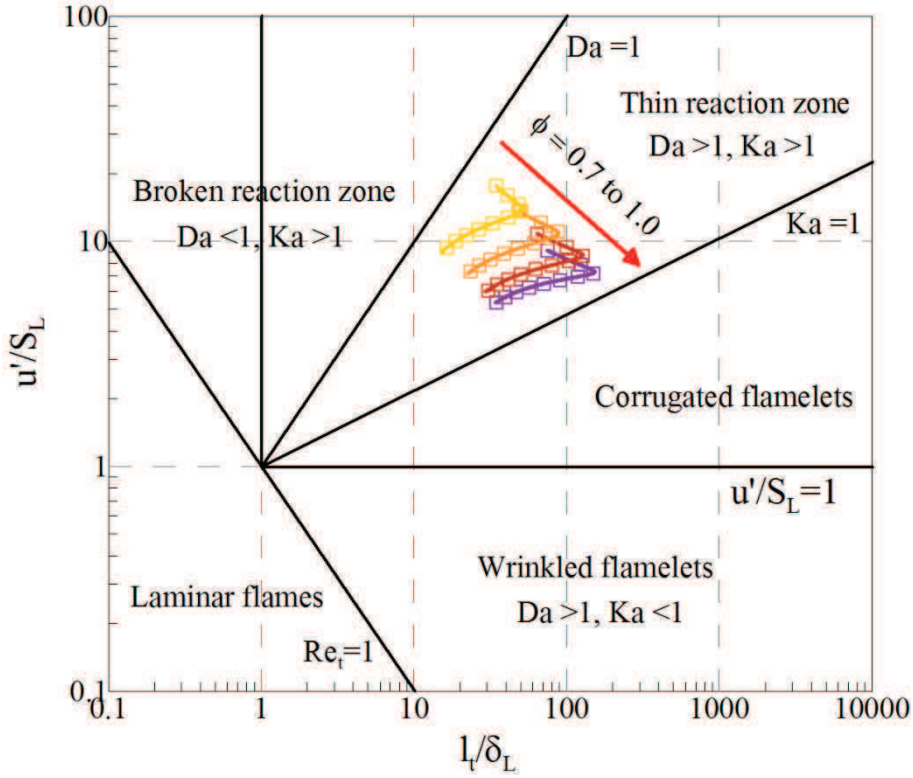

Figure 4-28. Comparison of the combustion traces in the Peters-Borghi diagram for different equivalence ratios at IMEP=10 bar

Effect of IMEP on combustion characteristics

Finally, the effect of IMEP on combustion characteristics is discussed. The operating conditions of different IMEP at 21% O2 and unit equivalence ratio are listed in ***Figure 4-29***. With increase of IMEP, intake pressure, spark timing and fuel mass debit are all increased.

IMEP	Intake pressure [bar]	Spark timing [°CA]	Fuel mass flow rate [kg/h]
4 bar	0.59	-21	0.513
6 bar	0.77	-16	0.678
8 bar	0.99	-15	0.885
10 bar	1.19	-10	1.084

Figure 4-29. Operating conditions of different IMEP for combustion analysis

In ***Figure 4-30***, the ratio of the characteristic length and velocity scales versus crank angle for different IMEP are presented. The evolution of l_t/δ_L trace between different IMEP is not clear at the low crank angle degree, which is mainly affected by the different spark timing for different IMEP. The evolution of l_t/δ_L and u'/S_L versus crank angle are similar to the two previous cases because these parameters are all depend on the in-cylinder thermodynamic properties. In ***Figure 4-31***, the ratio of the characteristic length and velocity scales versus

IMEP are presented. The ratio l_t/δ_L increases quasi linearly when IMEP increase. The increase of l_t/δ_L is due to the laminar flame thickness, which decreases by the density increase with higher intake pressure level (Linse et al. 2009). With the constant assumption of l_t, l_t/δ_L is nearly proportional to the unburned gas density (Linse et al. 2009). The ratio u'/S_L is nearly constant, which is because the variation of both u' and S_L are minimal by IMEP variation. For S_L, the effect of residual gas has two opposite influences. High level of residual gas percentage decrease the laminar flame velocity by a factor about $(1 - 2.1\chi_{\text{residual}})$, whereas the residual gas can also increase the global in-cylinder temperature and leads to higher laminar flame velocity. Thus, even the residual gas decreases from about 5% to 10% of total in-cylinder mass by the increase of IMEP from 4 to 10 bar, the effect of residual gas S_L is minimal.

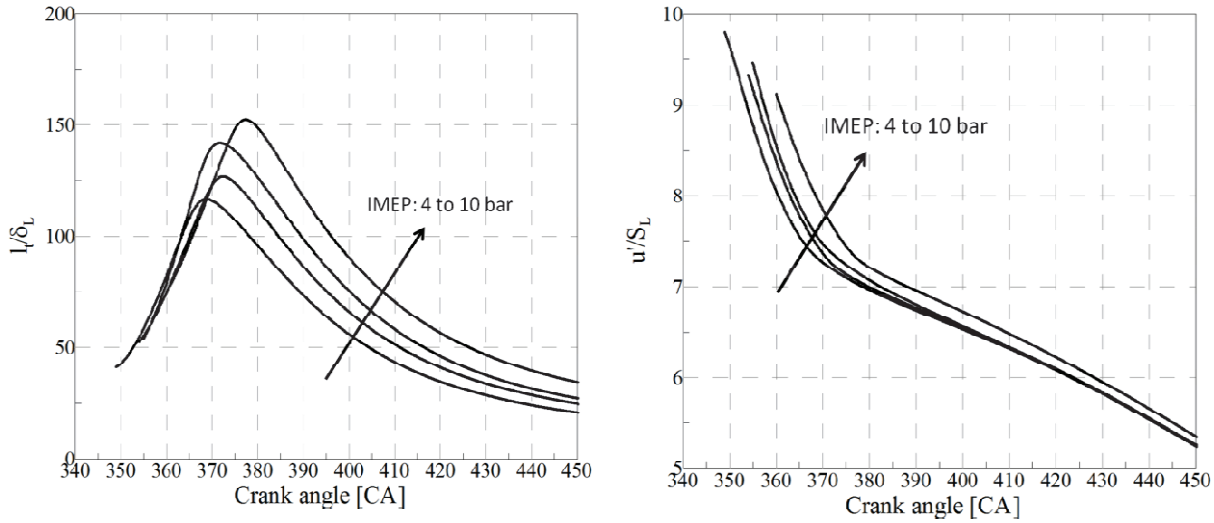

Figure 4-30. Ratio of the characteristic length and velocity scales versus crank angle degree for different IMEP.

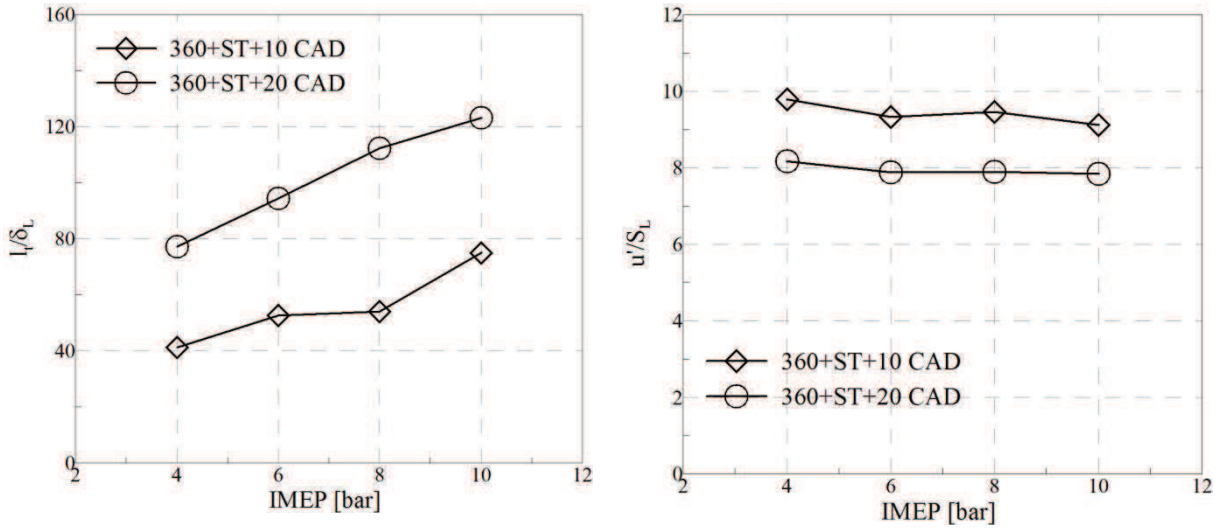

Figure 4-31. Ratio of the characteristic length and velocity scales versus IMEP for two crank angle degree cases

Due to quasi-linear variation of l_t/δ_L and to quasi-constant variation of u'/S_L, the combustion trace shift horizontally towards the right side in the Peters-Borghi diagram (***Figure 4-32***) this

implicate that changes in flame structure by load variation are principally affected by thermodynamic properties (Linse et al. 2009).

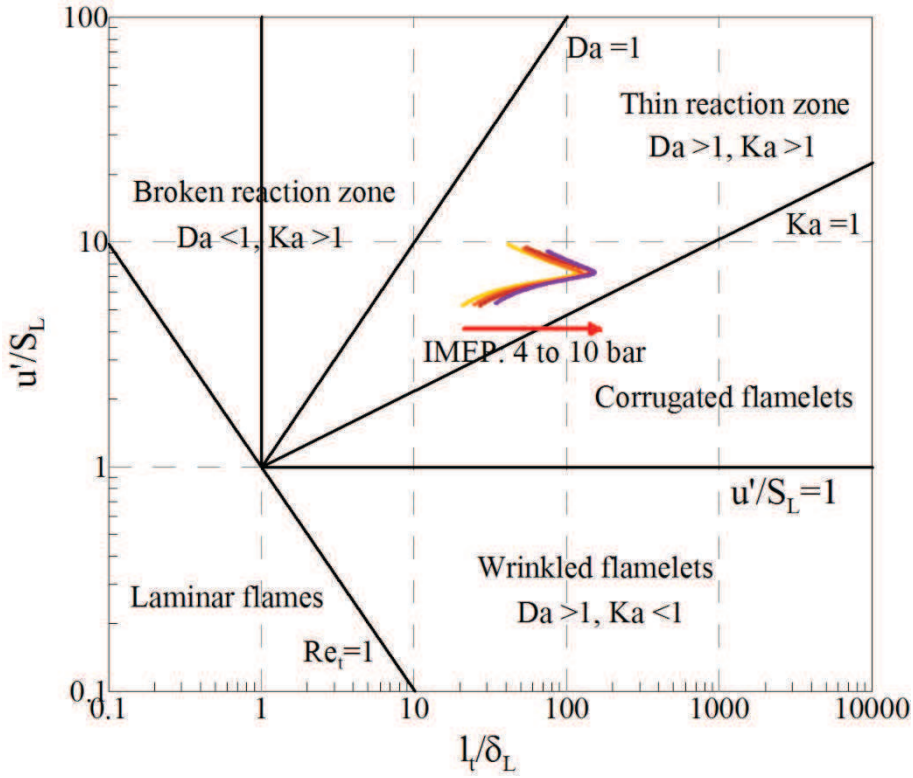

Figure 4-32. Comparison of the combustion traces in the Peters-Borghi diagram for different equivalence ratios

Parametric study of combustion characteristics

In this part, parametric study of combustion characteristics is investigated. In ***Figure 4-33***, the evolution of in-cylinder pressure varying laminar flame speed is presented. In all these graphs, the black lines present the reference case of in-cylinder pressure which has been calibrated with experimental results. And the red line is the supposed cases with variations of different parameter factor of laminar flame speed. The laminar flame speed is varied from 0.7 S_L to 1.3 S_L. The augmentation of laminar flame speed results in higher in-cylinder pressure for all the cases. Especially for the case of 15% O_2, this tendency is even more obvious, which is mainly due to higher flame wrinkling. Turbulent flame velocity is much higher with laminar flame speed increase.

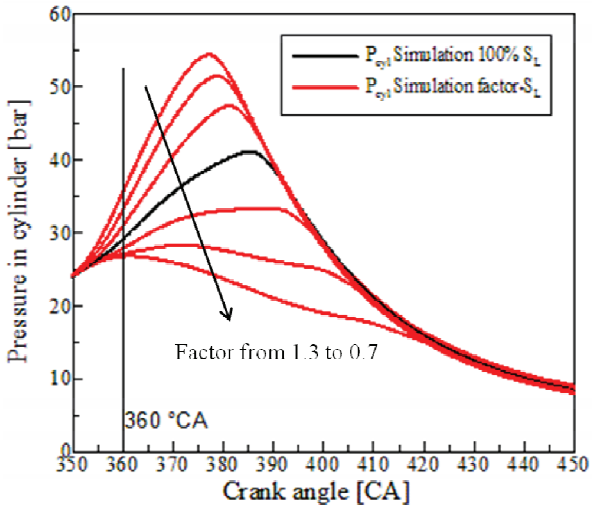

15% O2, ϕ=1.0

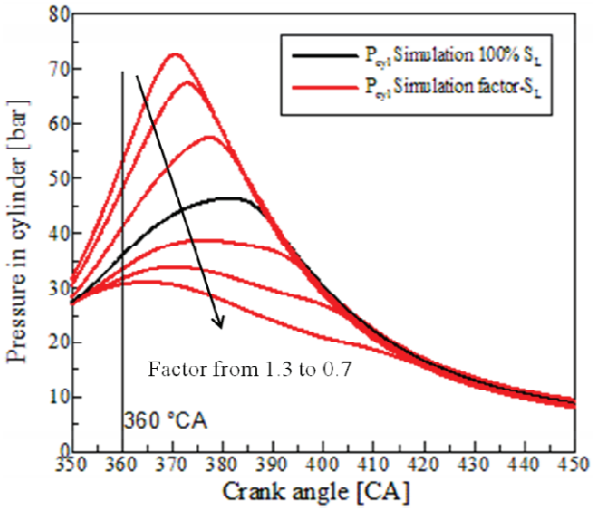

15% O2, ϕ=0.9

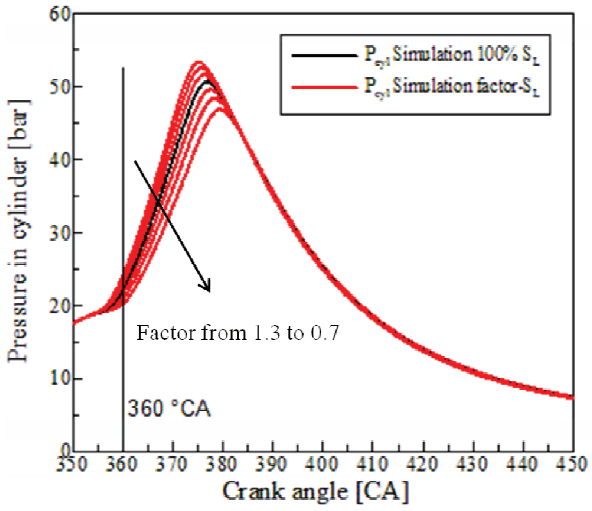

21% O2, ϕ=1.0

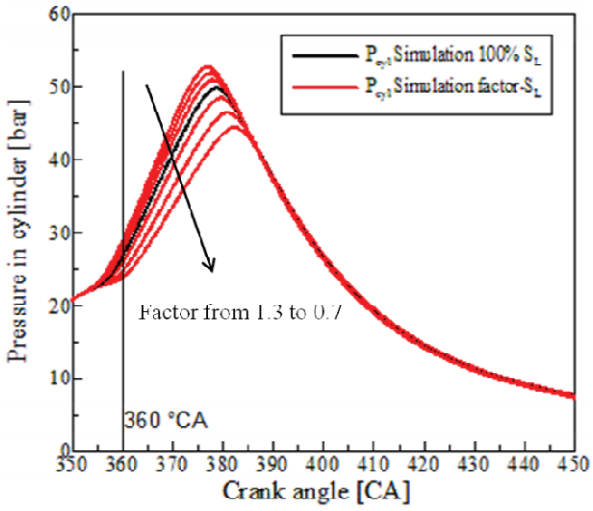

21% O2, ϕ=0.8

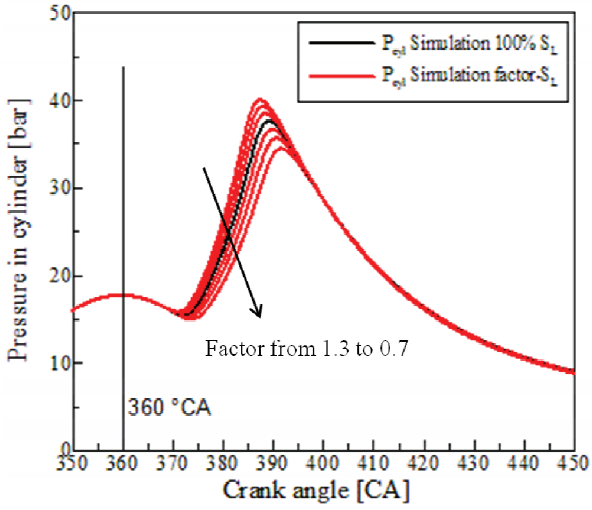

27% O2, ϕ=1.0

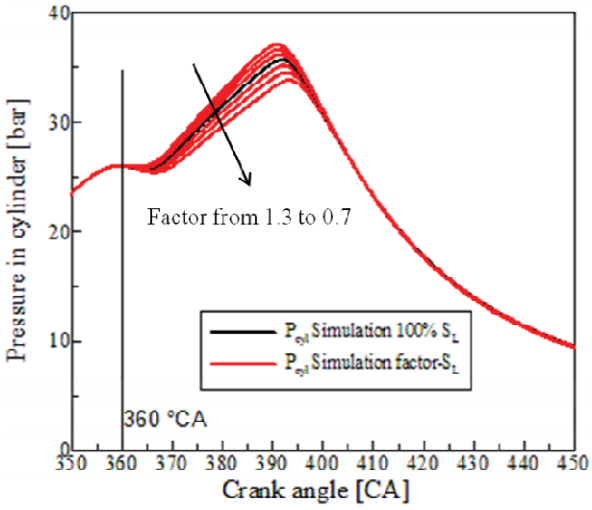

27% O2, ϕ=0.6

Figure 4-33. Evolution of in-cylinder pressure varying laminar flame speed with two different cases of equivalence ratio at IMEP=10bar

The evolution of in-cylinder pressure versus spark advance is presented in ***Figure 4-34***. The variation of spark advance is CAD of the reference point ± 6 CAD with the step of 2 CAD. As expected, the increase of spark advance leads to higher maximum in-cylinder pressure value. As the as the effect of knock on heat release is not concerned in the model, the in-cylinder pressure does not influenced by the knock occurrence even though strong knock is predicted for some cases.

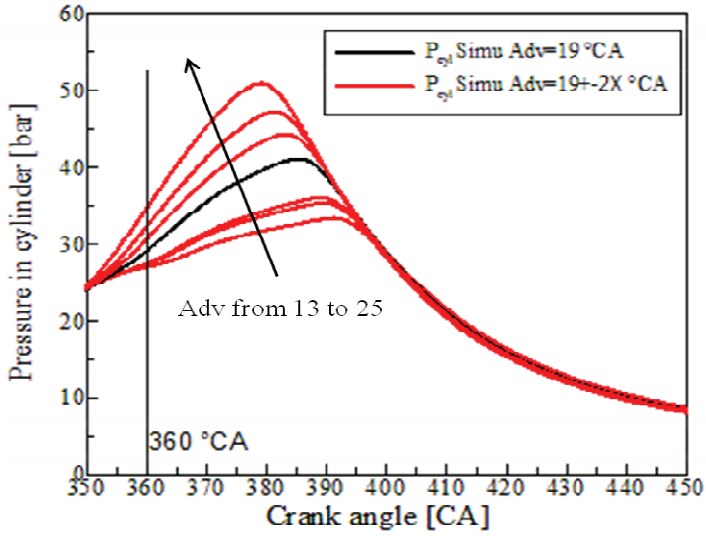

15% O_2

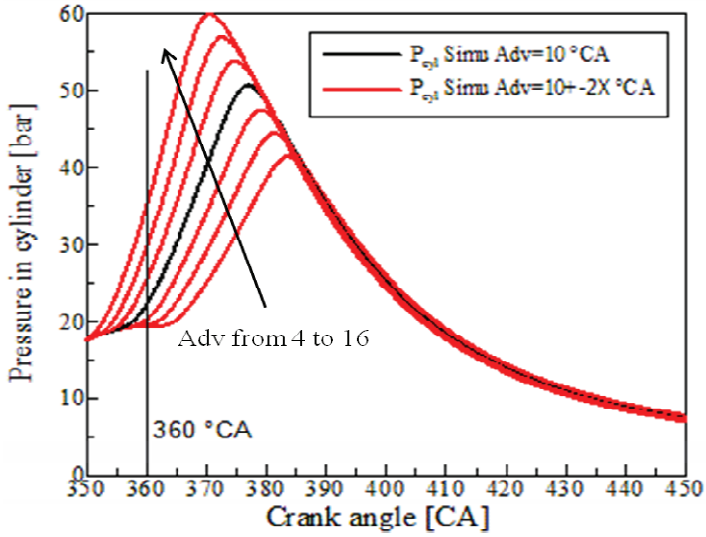

21% O_2

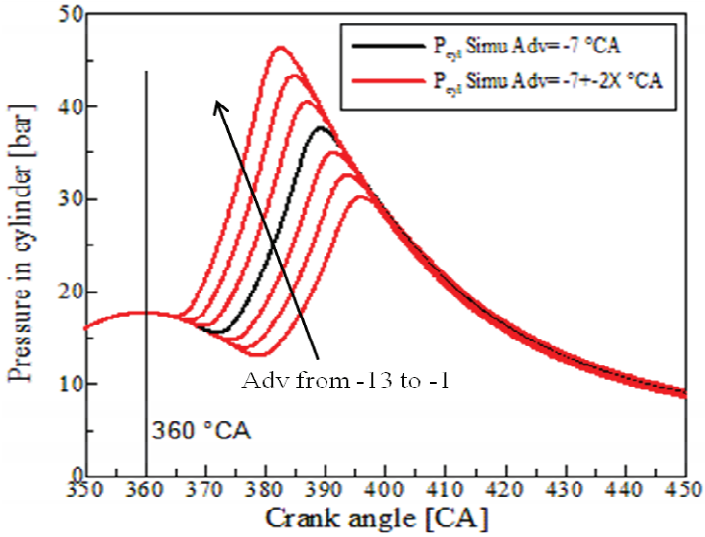

27% O_2

Figure 4-34. evolution of in-cylinder pressure varying spark ignition advance for three different cases of O2 percentage at IMEP=10bar and stoichiometric equivalence ratio (X=1, 2, 3).

The effect of intake temperature on in-cylinder pressure is described in ***Figure 4-35***. The intake temperature is varied from 40°C to 100°C, which represents to the reference intake temperature (T_{adm}) ± 30°C with the step of 10°C. Two principle effects might be involved by the increase of intake temperature: the first effect is that the increase of intake pressure will potentially increase the laminar burning velocity which accelerates the heat release rate. However, with the same intake pressure, higher intake temperature leads to less in-cylinder air/fuel mass which may effectively decrease the power density. For 15%O_2, the increase of intake temperature results in slightly higher in-cylinder pressure at the beginning phase combustion stroke, which may be due to the first effect as described above. Whereas, the pressure is lower at the later phase of combustion stock, which is probably due to the second effect. For 21% and 27% O_2, the first effect is not obvious compare to 15% O_2; the main reason is the in-cylinder pressure is very sensible to laminar burning velocity for 15% O_2 as presented in ***Figure 4-33***. Lower intake temperature gives higher maximum in-cylinder pressure for the two cases.

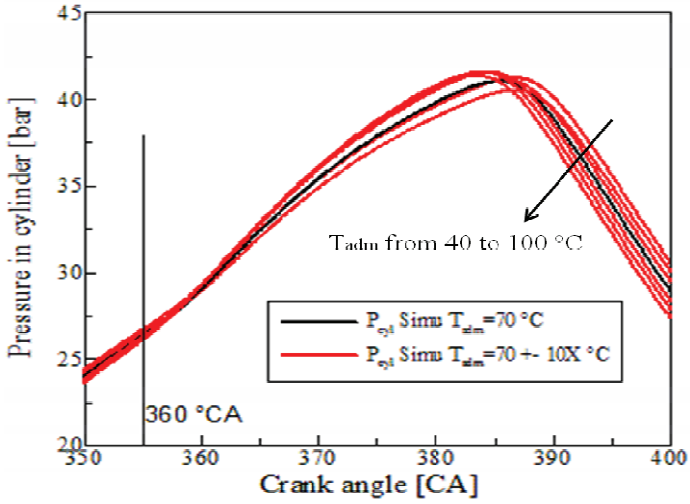

15% O_2

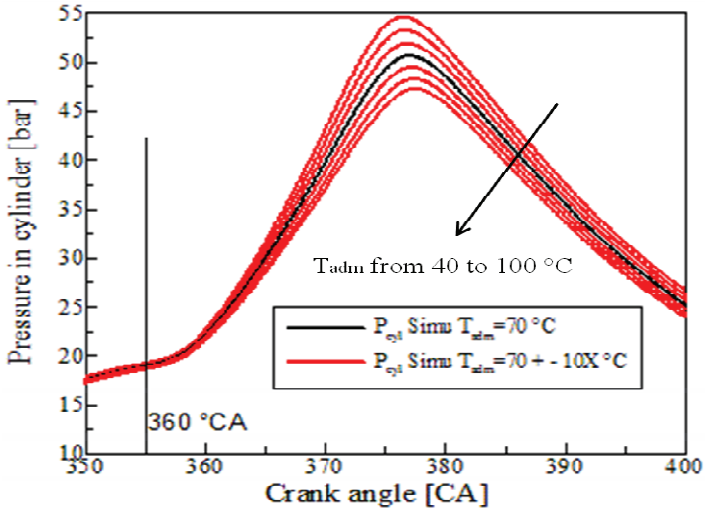

21% O_2

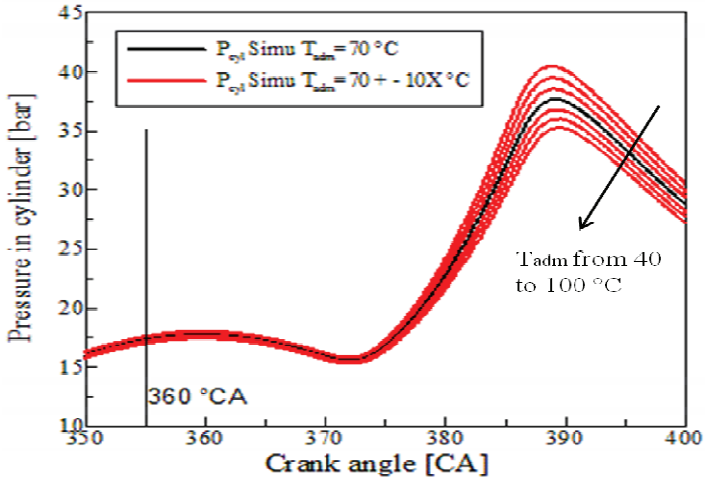

27% O_2

Figure 4-35. Evolution of in-cylinder pressure varying the intake temperature for three different cases of O_2 percentage at IMEP=10bar and stoichiometric equivalence ratio (X=1, 2, 3)

Laminar burning velocity versus crank angle for the two different cases described above is depicted in ***Figure 4-36***. Three cases of spark advance (Adv_{ref} – 6CAD, Adv_{ref}, Adv_{ref} +6CAD) and intake temperature ($T_{intake,ref}$ - 30K, $T_{intake,ref}$, $T_{intake,ref}$ + 30K) for each O_2 percentage are presented. The increase of spark advance incites higher in-cylinder temperature, therefore the laminar burning velocity increase as well for all the three cases of O_2 percentage. However, compare to the effect of O_2 percentage on laminar burning velocity, the 6 CAD increase of spark advance is minimal. On the right hand of figure, the effect of intake pressure on laminar burning velocity is presented. As expected, the increase of temperature leads to higher laminar burning velocity.

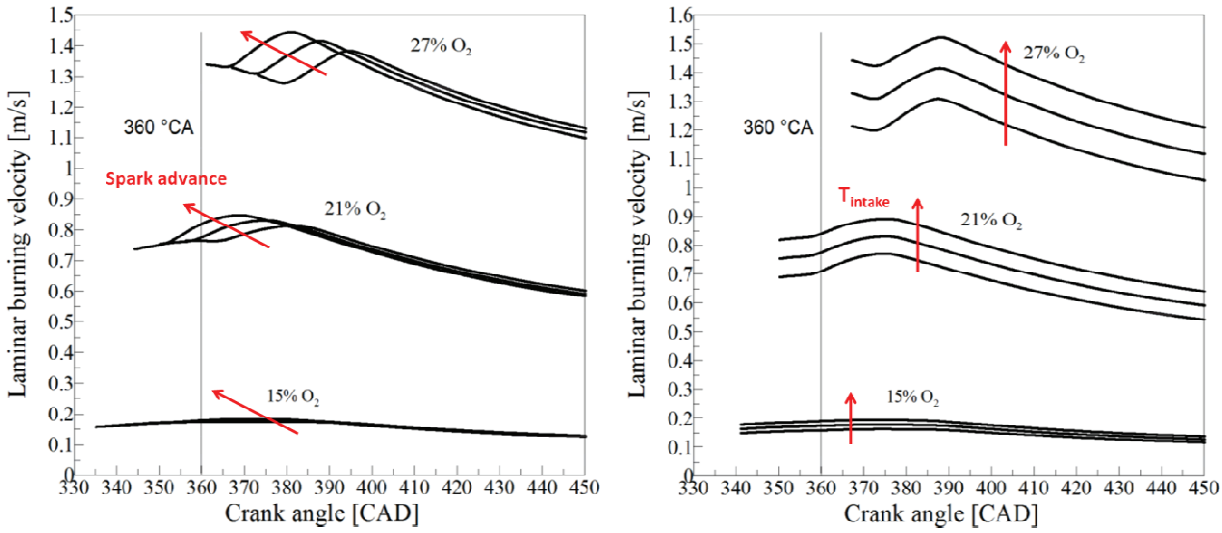

Figure 4-36. Laminar burning velocity versus crank angle for two different cases. Left: variation of spark advance, Right: variation of intake temperature

In *Figure 4-37*, the influence of spark advance and intake temperature on combustion characteristics is described. The parametric study shows that by increasing spark advance the combustion trace is shifted to right-up side, and by increasing intake temperature it is shifted to down side.

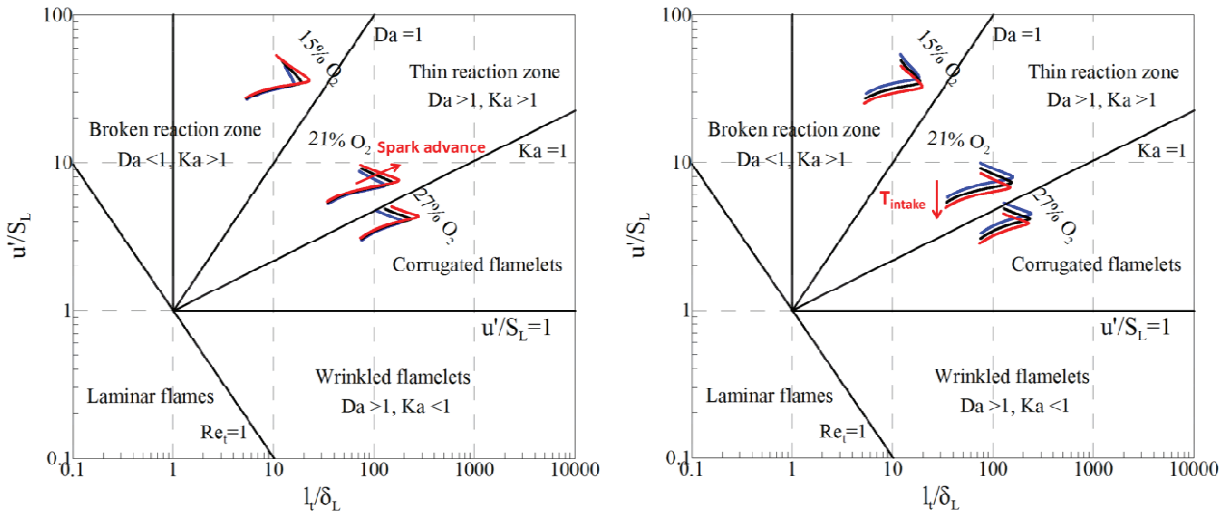

Figure 4-37. Behavior of spark advance (left) and intake temperature (right) in Peters-Borghi diagram.

4.5.5 Knock estimation and sensitivities

In this section, knock estimation is discussed by using both experimental and simulation method. In order to investigate the effect of different parameter on knock, knock and in-cylinder pressure sensitivities are investigated by varying the laminar flame speed, auto-ignition delay, degree of spark advance and other parameters.

Knock estimation

Knock prediction is performed by using an empirical correlation which depends on engine parameters and in-cylinder mixture thermodynamic properties. In order to gives a better

adaptation of engine working with O_2 controlling, a new correlation based on the previous correlation (Richard et al. 2009) is used. For 21% O_2, the correlation used here gives the same data as the previous correlation of Richard (Richard et al. 2009). As the correlation is used for various application conditions, it is not obvious to have a fine prediction of knock intensity. However, this correlation is quite useful to avoid the engine knock limit when engine is operated and also investigate the impact of different engine parameters on knock occurrence.

Experimental estimation of knock intensity (KI) is simply conducted by analyzing in-cylinder pressure oscillation with two knock indicators which is commonly used in the literature (Brecq et al. 2003; Rahmouni et al. 2004; Saikaly et al. 2010; Galloni 2012). These two knock indicators are MAPO and IMPO, the former one is the maximum amplitude of pressure oscillations, and the later one is the integral of modulus of pressure oscillations. MAPO related to the peak of the pressure oscillations due to the knock, and IMPO represents the energy contained in the high frequency oscillation of the pressure signal. The formulas of these two indicators are listed respectively as:

$$MAPO = \frac{1}{N}\sum_1^N max_{\theta_i,\theta_{i+W}}\left|\tilde{P}\right| \qquad \text{Equation 4-28}$$

$$IMPO = \frac{1}{N}\sum_1^N \int_{\theta_i}^{\theta_{i+W}}\left|\tilde{P}\right| d\theta \qquad \text{Equation 4-29}$$

Where N is number of investigated cycle, θ_i is the crank angle corresponding to the beginning of the calculation window, W is the length of the calculation window, and $\tilde{P}$ is the filtered pressure. To make sure the reliability of estimated KI value, noise measurement instrument is also installed upside the tested engine to give a comparable value of KI for different operation points.

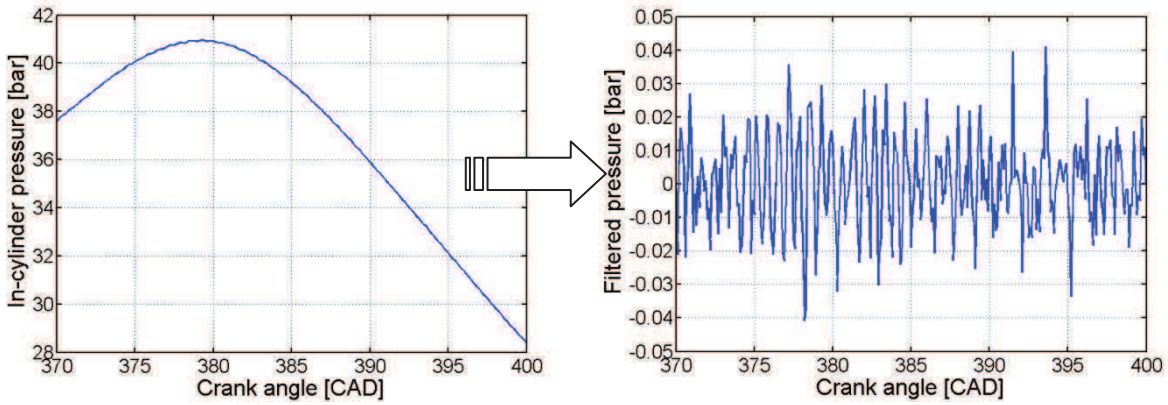

15% O_2

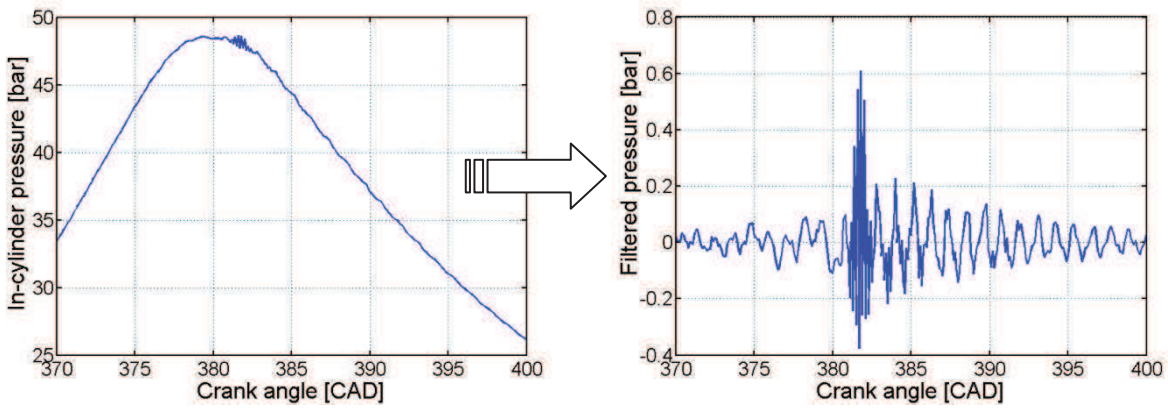

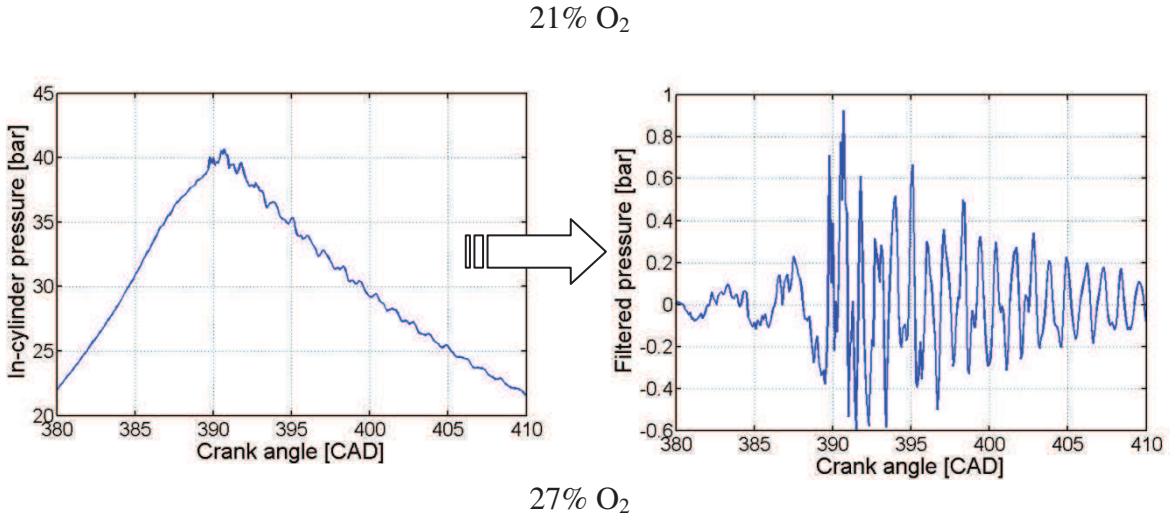

Figure 4-38. Examples of absolute (left hand) and high-passed filtered with 4 kHz cut-off frequency (right hand) cylinder pressure traces at IMEP 10 bar and $\phi = 1$.

Figure 4-38 shows the examples of absolute (left hand) and high-passed filtered with 4 kHz cut-off frequency (right hand) cylinder pressure traces for three cases (15% O_2, 21% O_2, 27% O_2). The magnitude of the example of 15% is much smaller than that of 21%, and 27% O_2. For 21% O_2 the maximum magnitude of filtered pressure is about 0.6 bar and that of 27% O_2 is 0.9 bar. The value of the maximum magnitude may be affected by the frequency of the high passed filter; therefore it can only be treated as a comparative value but not an absolute one. The oscillation of the filtered pressure of 27% O_2 last longer than that of 21% O_2. However, one or several engine cycle can't give a decisive value for the knock indicators due to important cycle to cycle variation. Thus 100 cycles of in-cylinder pressure were recorded during experimental tests. Filtered cylinder pressure traces for 100 consecutive cycles at IMEP 10 bar and $\phi = 1$ are presented in ***Figure 4-39***.

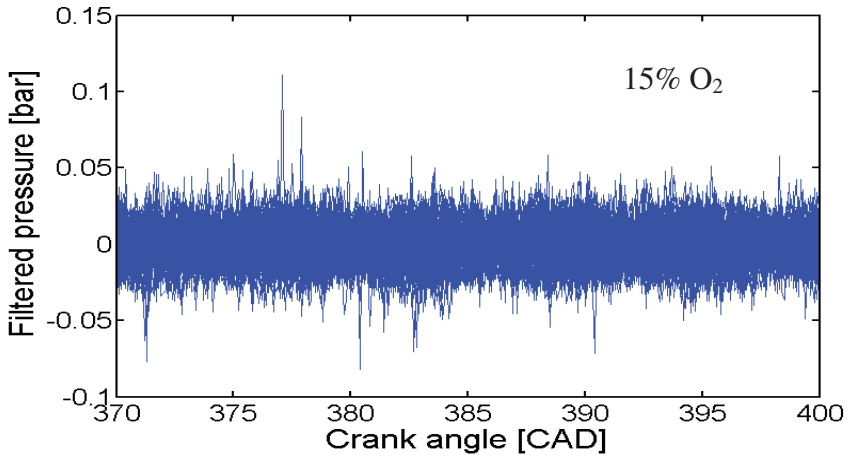

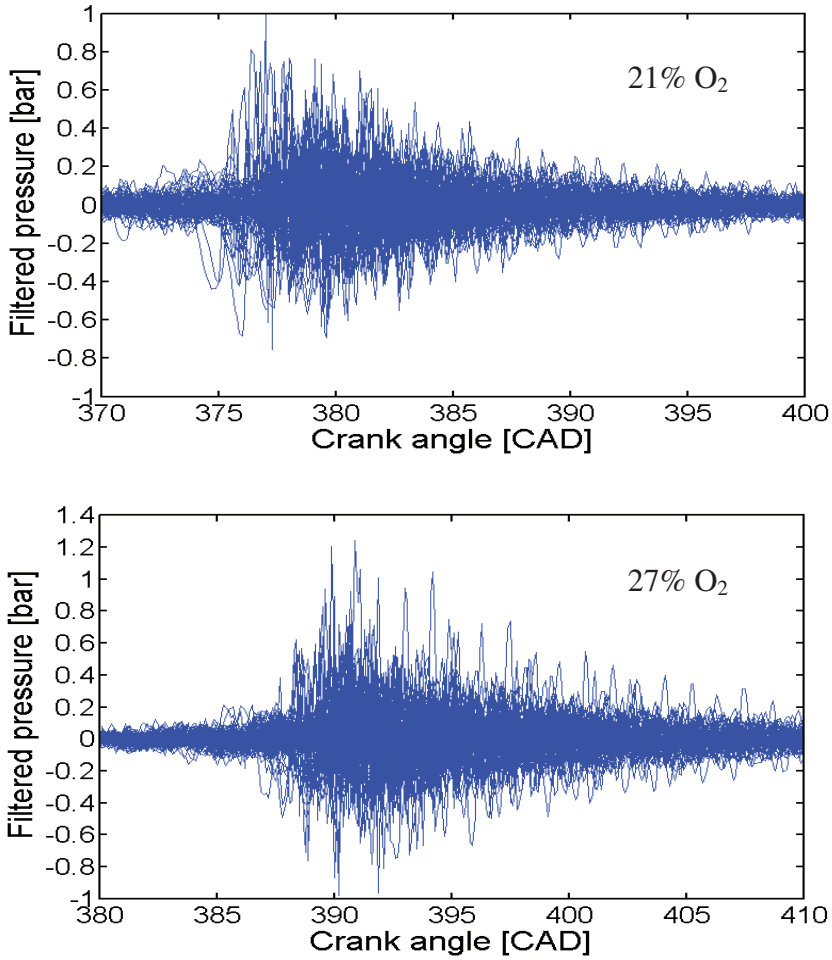

Figure 4-39. High-passed filtered cylinder pressure traces for 100 consecutive cycles at IMEP 10 bar and ϕ = 1.

In ***Figure 4-40***, absolute values of experimental indicators MAPO, IMPO, (left) and normalized MAPO, IMPO, simulated KI (right) versus O_2 percentage are presented. The absolute values of MAPO and IMPO show big difference, whereas the tendencies are quite similar. In this study, the length of the calculation window W is 40 CAD. For different value of W, IMPO gives different value: higher W accompanies with higher IMPO value. However, MAPO are nearly constant once the maximum pressure oscillation is captured within the calculation window W. High value of MAPO and IMPO are found in the side of the oxygen enrichment, and the biggest value are found at 25% O_2. This indicated that the efficiency of the oxygen enrichment is limited by knock, whereas for N_2 dilution, knock has few influence. This can also explain that the oxygen enrichment gives higher specific fuel consumption (SFC) for high IMEP cases (ex. 10 bar and some cases of 8 bar IMEP).

On the right hand of ***Figure 4-40*** the normalized MAPO, IMPO, simulated KI are described. In order to have a comparable value for these three values, all of these values are normalized by their maximum ones. The simulated KI is calculated using the new correlation described in section (4.2.6), which corrects all the experimental MAPO data of 10 bar IMEP. The maximum value of KI (max (KI)) here is 0.925 which situated in 23% O_2, so in the graph the KI/ (max (KI)) is 1.0 for 23% O_2. The simulation data gives reasonable value compare to experimental indicators, although some discrepancy is found. Normally, almost of the knock

occurred in our study is in the 'trace knock' regime ($0.5 \leq KI < 1$), as the medium knock is normally avoided to protect tested engine during the manipulation. Moreover, the medium knock may also affect the engine efficiency, therefore increase SFC. So during the operation, in the case of high knock, intake pressure or spark advance should be decreased to minimize the knock to 'trace knock' or 'no knock' regime. As the intake pressure or spark advance are change during the operation, KI also is affected by the operator. For example, KI value of 27% O_2 is smaller than 23 and 25% O_2, which is because smaller spark advance is set to prevent knock. The trace knock is found for oxygen enrichment and 21% O_2 (with KI=0.52) and no knock is found in the case of N_2 dilution.

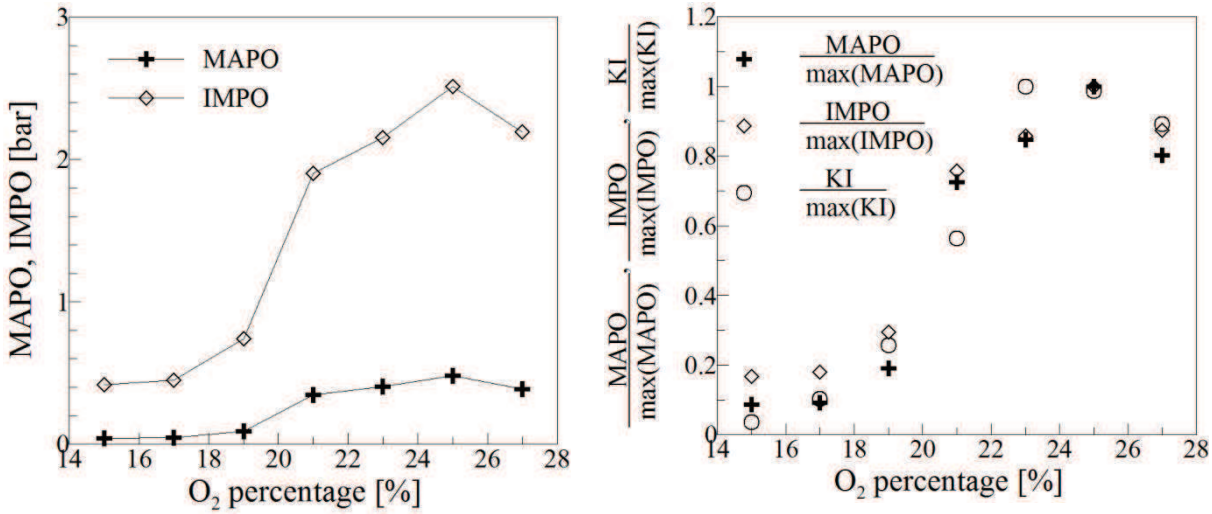

Figure 4-40. Absolute values of experimental indicators (left) and normalized MAPO, IMPO, simulated KI (right) versus O_2 percentage

Knock sensitivities

In ***Figure 4-41***, the evolution of knock intensity KI by varying laminar flame speed and auto-ignition delay is presented. In the case of 15% O_2, regardless the variation of delay or laminar burning velocity factor, KI has a very small value which means no knock is occurred. For 21% O_2 the increase of laminar burning velocity factor has very little affect on KI. And quasi constant is observed.

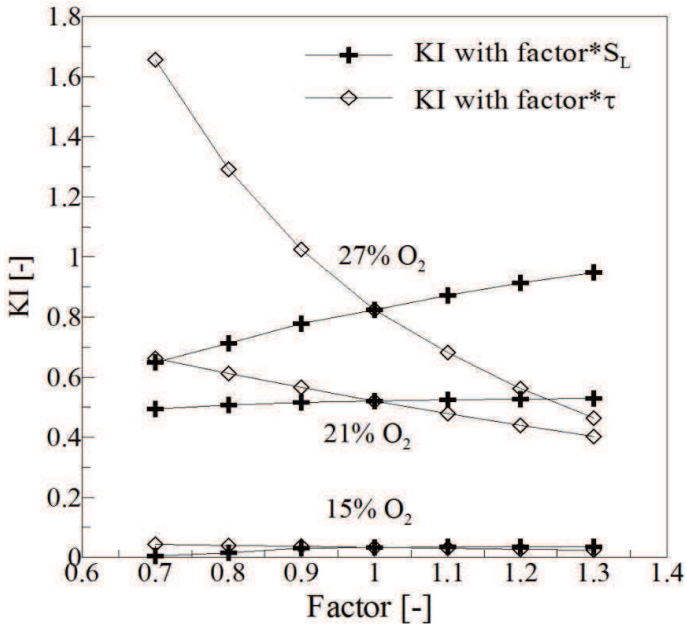

Figure 4-41. Evolution of knock intensity (KI) by varying laminar flame speed and auto-ignition delay

The increase of laminar burning velocity has two opponent effects as showed in $KI = C_1.\left(\frac{\chi_{O_2}}{0.21}\right)^{\alpha}(1 - bmf.\max(1,\emptyset))(\Pi - 1)\sqrt{1 - \frac{\theta_k + \beta(0.21 - \chi_{O_2})}{c_2 - \gamma(0.21 - \chi_{O_2})}}N_{eng}$: on the one side, higher burning velocity leads to more rapid pressure and temperature increase which may makes the value of θ_k smaller and then favorite the knock occurrence. On the other side, burned mass fraction at knock onset is bigger when laminar burning velocity is higher, which may decrease the KI value. Thus, the effect of laminar burning velocity maybe have different trend for KI value. For 27% O_2, the increase of laminar burning velocity gives higher KI value, whereas these points are situated in trace knock zone. The effect of auto-ignition delay is more clear compare to laminar burning velocity. The increase of delay leads to lower KI for all the cases. Especially for 27%, a factor of 0.9 incites 20% increase of KI. This indicates that it is extremely important to have a good estimation of auto-ignition delay for knock prediction.

The evolution of KI by varying spark advance is presented in ***Figure 4-42***. The reference spark advance are 19, 10, -7 CAD respectively for 15%, 17%, 27%O_2. For 15% O2 the variation of spark advance has little effect on KI, whereas KI is strongly influenced by spark advance for 27% O_2. By advancing 2 CAD more, the knock might be transformed from trace knock to strong knock, which is also observed during our experimental operations. Thus, the much efficient way for decreasing KI is to advance less. In the case of 21% O_2, a slight increase of KI is found.

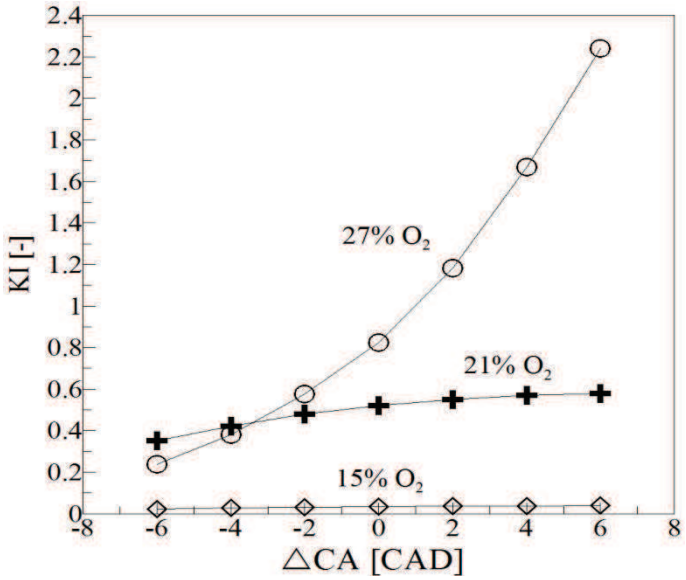

Figure 4-42. Evolution of knock intensity (KI) by varying spark advance with adv= Adv_{ref} +ΔCA

Although the increase of intake temperature might be decrease the maximum in-cylinder pressure as described above especially for the cases of 21% O_2 and 27% O_2, the KI is still increase due to high dependence of auto-ignition delay to temperature (***Figure 4-43***).

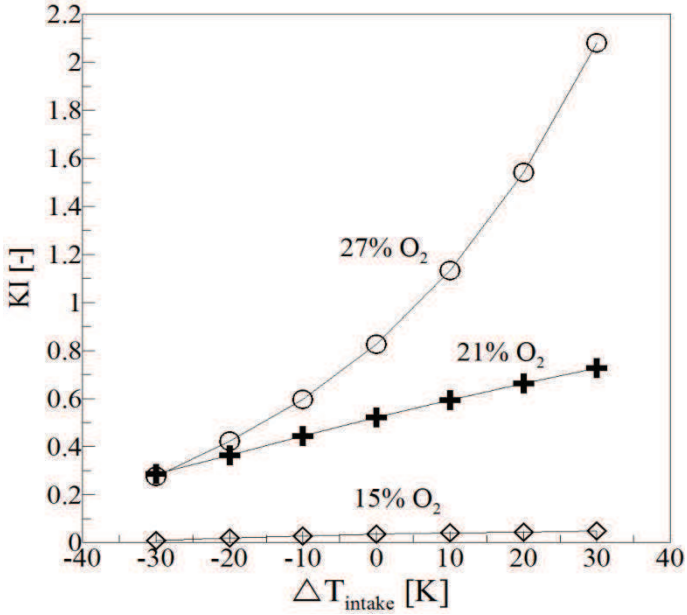

Figure 4-43. Evolution of knock intensity (KI) by varying intake temperature with T_{intake}= $T_{intake,ref}$ +ΔT_{intake}

4.6 Conclusions

The numerical simulation was conducted with the AMESim software by taking into account the effect of O_2 control. In-cylinder pressure was well reproduced, although discrepancies can

be found for high levels of dilution. The flame surface of high dilution cases is much greater than that with lower dilution or oxygen enriched cases. Therefore, turbulent flame velocities show few differences compared to laminar ones. The effects of O_2 percentage, equivalence ration and IMEP on combustion characteristics were discussed respectively according to the Peters-Borghi diagram. The last part of this chapter was focused on knock estimations and sensitivities. Experimental estimation of knock was carried out by using two commonly used indicators: MAPO and IMPO. The simulation data of KI calculating by the new correlation correspond well with experimental indicators. It was demonstrated that oxygen-enriched combustion is limited by knock onset. Finally, knock sensitivities were investigated by varying laminar burning velocity, auto-ignition delay, intake temperature and spark advance.

5 Conclusions and perspectives

Conclusions

Nowadays, car manufacturers still lead researches on renewable technologies facing to the energy shortage and pollutant emission problems. One of the promising solutions is 'downsizing' with turbo-charger. However, this concept is unfortunately limited by 'knock' phenomenon (abnormal combustion) for SI engine as the super-charge induces high temperature and high pressure conditions. In this context, this phd work is focused on the study of oxygen controlled combustion in downsized SI engine. On the one hand, oxygen-enriched combustion can improve engine power density with the same intake pressure level. Thus, oxygen-enriched combustion can be used either as a booster to increase engine output or as a combustion enhancer when the engine operates at low loads or in cold start conditions. On the other hand, low oxygen concentration in air (or N_2 dilution) can be considered as an alternative to exhaust gas recirculation (EGR). The knock occurrence while applying oxygen controlled combustion is also discussed.

In our literature review (chapter one), several new technologies responding to fuel economy and pollutant emissions are introduced. As turbulent flow regime is strongly presented in spark ignition engine, an important part of this chapter aims at presenting the basic knowledge of turbulence and turbulent premixed combustion. By several dimensionless numbers, the turbulent combustion can be classified into several different regimes according to Peters-Borghi diagram: wrinkled flamelets, corrugated flamelets, thin reaction and broken reaction regime. The abnormal combustion is then introduced, especially the knock phenomenon. Finally, the application of oxygen controlled combustion in downsized engine is presented.

In the second chapter, experimental study of oxygen controlled combustion was discussed. The characteristic of single-cylinder SI engine, (PSA EP6) and the engine control and measurement systems were described in details. Experimental results showed that for low load (mean effective pressure of 400 and 600 kPa), oxygen enrichment can improve fuel efficiency, whereas for relatively high IMEP, N_2 dilution is better. It is important to note that oxygen enrichment can enlarge the lean limit: for 27% O_2, the combustion is still stable at equivalence ratio of 0.5 with COV_{imep} smaller than 5% for all engine loads. The HC emission decreases with the increase in the O_2 percentage and the lowest value are always found at 27%O_2 for every fixed equivalence ratio. But in this case, NOx emissions increase. The CO emissions are mainly affected by equivalence ratio, especially for equivalence ratio near stoichiometic. They decrease in lean condition due to the increase in O_2 concentration that helps the oxidation of CO into CO_2, this phenomenon can be confirmed by the CO_2 emissions: for equivalence ratio neat unit value, the increase of CO_2 emissions at equivalence ratio from 0.9 to 1.0 are less obvious compared to general tendency due to some CO is not converted to CO_2.

Laminar premixed combustion play an important role for both experimental and numerical investigations of SI engine combustion. Thus, main part of the third chapter is devoted to estimate the laminar combustion parameters for the mixture of isooctane/O_2/N_2/CO_2 at stoichiometric equivalence ratio. The volume fraction of O_2 was varied from 21 to 29% and CO_2 was varied from 0 to 28%. The experimental study was carried out by using spherical combustion chamber at atmospheric pressure and the temperature of 373 K. Both linear and non-linear method for post-treating were introduced and compared with each other. Numerical simulation was conducted using Cantera software with kinetic schemes of Hasse

(48 reactions and 29 species) and Jerzembeck (669 reactions and 99 species). Both experimental and numerical results showed that laminar flame burning velocities increase linearly with an increase of O_2 and decrease as a polynomial tendency with CO_2. Based on this observation, an experimental correlation is proposed for balancing the O_2 and CO_2 percentages with constant laminar burning velocities. The effect of O_2 enrichment and CO_2 dilution on adiabatic flame temperature is also discussed. CO_2 dilution can minimize the effect of O_2 enrichment on the increase of adiabatic flame temperature, which gives a perspective option to decrease NOx emission and knock occurrence tendency when O_2 enrichment is applied in SI engine.

The last part of this chapter is dedicated to the simulation study of auto-ignition delay, as fundamental parameter. As widely accepted, knock occurs due to the auto-ignition of the unburned gas before the arrival of flame front. Thus, auto-ignition delay is considered as a key parameter for knock prediction for both 0D (Soylu 2005) and CFD (Computational Fluid Dynamics) (Lafossas 2002) simulations. In our study, the auto-ignition delay was investigated for the mixture of isooctane/O_2/N_2/CO_2 by using detailed kinetics mechanism with Senkin tool. The chemical kinetic scheme of Curran (Curran et al. 2002) was used because of its wide range of validation and its good prediction comparing with numerous previous experimental results. Based on the data of the simulation study, a correlation of auto-ignition with traditional Arrhenius formula was proposed. This correlation would then be employed in AMESim for further simulation of knock. Simulation results showed that under certain initial condition of temperature and pressure, auto-ignition delay decreases with the increase of O_2 percentage and increase with the increase of CO_2. Compare with the effect of O_2 to auto-ignition delay, the addition of CO_2 is less important.

In the last chapter of the thesis, numerical simulations were carried out using commercial software AMESim. By calibrating the two turbulence parameters (i.e. integral length scale and number of tumble value), the in-cylinder pressure was well simulated. Three cases of combustion analysis were discussed according to the Peters-Borghi diagram:

- Effect of O_2 percentage on combustion characteristics: The laminar burning velocity increases as a function of O_2 percentage. The value of 27% O_2 is more than 8 times higher compare to 15% O_2. The turbulent flame surface of high dilution cases (i.e. 15% and 17% O_2) is much higher than in the case of lower dilution or oxygen enrichment due to the higher flame wrinkling. Thence, the turbulent burning velocities show comparatively (less than 2 times higher than 27% O_2 compare to 15% O_2) less difference compare to laminar ones. In order to give a deeper insight into the interaction between turbulence and flame, the combustion is classified according the Peters-Borghi diagram. The combustion trace passes from broken reaction zone to thin reaction zone, and finally to the corrugated flamelets zone by varying the O_2 precentage for 15% to 27%. Only for the case of 15% O_2, the combustion is take place in broken reaction zone in which the spherical propagation of flame may not well adapted.

- Effect of equivalence ratio on combustion characteristics: higher equivalence ratio leads to higher l_t/δ_L value and lower u'/S_L at same crank angle after spark timing. The combustion traces in Peters-Borghi diagram show similar behavior compare to dilution cases.

- Effect of IMEP on combustion characteristics: the combustion trace shifts horizontally towards the right side in the Peters-Borghi diagram due to the quasi-linear variation of l_t/δ_L and quasi-constant variation of u'/S_L. This implicate that changes in flame structure by load variation are principally affected by thermodynamic properties (Linse et al. 2009).

The last part of this chapter was focused on knock estimations and sensitivities. Experimental estimation of knock was carried out by using two commonly used indicators: MAPO and IMPO. The simulation data of KI calculating by the new correlation correspond well with experimental indicators. It was demonstrated that oxygen-enriched combustion is limited by knock onset. Finally, knock sensitivities were investigated by varying laminar burning velocity, auto-ignition delay, intake temperature and spark advance.

Perspectives

This thesis leads to numerous perspectives:

- As demonstrated in this thesis, oxygen enrichment is limited by knock occurrence. Thus, oxygen enrichment with CO_2 dilution can be used to prevent or minimize knock occurrence. Several advantages were found in our thesis for CO_2 dilution when O_2 enrichment is applied: As CO_2 has high value of Cp, it can decrease the in-cylinder temperature which is considered as a main factor of knock occurrence.

- Alternative fuels, especially those with a high octane number (natural gas, ethanol, synthetic fuels, and etc.) can be employed when oxygen enrichment is applied. High laminar burning velocities of oxygen enrichment can be profitable for the fuel that has low laminar burning velocities to ameliorate the engine efficiency. Whereas the nature of high octane number can prevent knock occurrence even though oxygen enrichment is applied.

- Realize the real Decarbonised SI engine (DSIE) concept: this work will be carried out under our future project named ‘MACDOC’ (Moteur à Allumage Commandé Downsizé à taux d’Oxygène Contrôlé). The real membrane will be produced to adapt the engine application. And the new dilution concept will be compared to the traditional EGR systems.

Conclusions et perspectives (version français)

Conclusions

Face à la diminution de la ressource d'énergie primaire et la limitation des émissions de polluants, les constructeurs automobiles mènent des recherches sur des technologies innovantes pour le développement de véhicule du futur. L'une des solutions prometteuses est le concept de 'downsizing', qui peut être obtenu par l'utilisation d'un turbocompresseur. Cependant, l'utilisation de ce concept est malheureusement limité par un phénomène préjudiciable, le 'cliquetis' (combustion anormale). En effet, les moteurs à Allumage Commandés (AC) super-chargés induisent des conditions de haute pression et haute température pouvant amener des combustions non contrôlées qui peuvent être destructrices pour le moteur. Ce travail de thèse a été axé dans ce contexte : l'impact du taux contrôlé d'oxygène sur le contrôle de la combustion dans un moteur à allumage commandé 'downsizé'. En effet, la combustion enrichie en oxygène permet d'améliorer le rendement du moteur avec le même niveau de pression d'admission. Ainsi, enrichie en oxygène, la combustion peut être utilisée soit comme un booster pour augmenter le rendement du moteur ou comme un activateur de combustion lorsque le moteur fonctionne à faible charge ou dans des conditions de démarrage à froid. D'autre part, une faible concentration en oxygène dans l'air (soit une dilution de N_2) peut être une alternative à la recirculation des gaz d'échappement (EGR), qui peut être difficile techniquement. L'objectif de ce travail est de quantifier l'impact du contrôle de l'oxygène sur la combustion rencontrée dans un moteur à allumage à commande à partir de résultats issus de différents dispositifs expérimentaux et d'une modélisation obtenue à partir du logiciel AMESIM.

Une première partie de ce travail a consisté en l'étude expérimentale sur moteur monocylindre. Il a été montré qu'à faible charge, l'enrichissement en oxygène améliore le rendement du carburant alors que, pour des charges plus élevées, la dilution est le meilleur moyen d'optimisation. Il est important de noter que l'enrichissement en oxygène peut augmenter la plage de fonctionnement en limite pauvre: pour 27% O_2, la combustion est toujours stable à la richesse 0.5 pour l'ensemble des charges du moteur. Les émissions d'HC diminuent avec l'augmentation du pourcentage d'O_2 avec une valeur minimale à 27% d'O_2 quelle que soit la richesse, mais avec une augmentation des émissions de NOx. Quant aux émissions de CO, elles ne sont que faiblement affectées par l'augmentation de la concentration en O_2, ce qui permet l'oxydation du CO en CO_2.

La combustion dans les moteurs à allumage commandé étant de type combustion turbulente de prémélange, la seconde partie de cette étude a été consacrée à l'estimation des paramètres de combustion laminaire pour évaluer l'impact du taux d'O_2, sur un mélange stoechiométrique d'isooctane/O_2/N_2/CO_2. La fraction volumique d'O_2 a varié de 21 à 29% et celle du CO_2 de 0 à 28%. L'étude expérimentale a été réalisée dans une chambre de combustion sphérique à la pression atmosphérique et à la température de 373 K. Les résultats numériques, obtenus en utilisant le logiciel Cantera avec deux schémas cinétiques (Hasse et Jerzembeck) et expérimentaux ont montré que la vitesse de la flamme laminaire augmente de façon linéaire avec une augmentation d'O2 et diminue comme une tendance polynomiale avec CO_2. Partant de ce constat, une corrélation expérimentale a été proposée pour équilibrer les pourcentages d'O_2 et de CO_2. L'effet de l'enrichissement O_2 et de la dilution de CO_2 sur la température de flamme adiabatique a été également discuté. L'utilisation du CO_2 comme diluant peut ainsi minimiser l'effet néfaste de l'enrichissement d'O_2 sur l'augmentation de la température de flamme adiabatique, ce qui ouvre une perspective pour réduire les émissions

de NO_x et ainsi minimiser le risque de cliquetis lors de l'enrichissement O_2, appliqué dans le moteur à allumage commandé.

La probabilité de risque de cliquetis étant liée à la compétitivité entre la vitesse de combustion laminaire et le délai d'auto-inflammation, celui-ci a été estimé en utilisant le mécanisme cinétique détaillé de Curran avec l'outil Senkin, schéma utilisé en raison de sa large gamme de validation et de sa bonne prédiction. A partir des résultats obtenus de la simulation, une corrélation permettant de prédire le délai d'auto-inflammation selon la concentration d'O2 a été proposée, basée sur le modèle classique d'Arrhenius. Cette corrélation a été utilisée pour la dernière partir du travail, la simulation sous AMESim afin de simuler le cliquetis. Les résultats des simulations ont ainsi montré que, dans certaines conditions initiales de température et de pression, le délai d'auto-inflammation diminue avec l'augmentation du pourcentage d'O_2 et augmente avec l'augmentation de CO_2. Comparativement à l'effet d'O_2 sur le délai d'auto-inflammation, l'ajout de CO_2 a moins d'impact.

La dernière partie de ce travail a été consacrée à des simulations numériques à partir du logiciel commercial AMESim. En calibrant les deux paramètres de turbulence (c'est à dire échelle de longueur intégrale et la valeur de tumble), la pression dans le cylindre a été bien simulée. Trois cas d'analyse de combustion ont été discutés selon le schéma de combustion-turbulente de Peters-Borghi, résumant ainsi les conclusions principales de ce travail:

- Effet du pourcentage d'O_2 sur des caractéristiques de combustion: la vitesse de la combustion laminaire augmente en fonction du pourcentage d'O_2. La surface de la flamme turbulente pour des cas de dilution élevés est beaucoup plus élevée. La conséquence est qu'en fait, les vitesses de combustion turbulente sont moins affectées par la concentration d'O_2 (moins de 2 fois plus élevé que 27% O_2 comparer à 15%). A partir du diagramme de Peters-Borghi, la combustion se déplace de la zone de flammes épaissies à la zone de flammes plissées-épaissies puis vers la zone de flammes plissées avec poches lorsque pourcentage O_2 varie de 15% à 27%. Dans le cas de 15% d'O_2, la combustion prend place dans la zone de réaction de flammes épaissies.

- Effet de la richesse sur les caractéristiques de combustion: l'augmentation de richesse entraîne une augmentation de l_t/δ_L et une diminution de u'/S_L au même angle vilebrequin après l'allumage. Les traces de combustion dans le diagramme Peters-Borghi montrent un comportement similaire à celui de l'effet de dilution.

- Effet de la charge sur les caractéristiques de combustion: selon la charge, la combustion se décale horizontalement vers la droite dans le diagramme Peters-Borghi due à la variation quasi-linéaire de l_t/δ_L et variation quasi-constante de u'/S_L, cela implique que des changements dans la structure de la flamme par variation de charge sont principalement dus aux les propriétés thermodynamiques.

A partir de la modélisation, les estimations et les sensibilités aux cliquetis ont pu être obtenues et comparées à l'estimation expérimentale. Il a été démontré que combustion enrichie en oxygène est limitée par l'apparition du cliquetis.

Perspectives

Ce travail de thèse ouvre de nombreux champs de perspective:

- L'enrichissement en oxygène est limité par l'apparition du cliquetis. Ainsi, l'enrichissement en oxygène avec dilution en CO_2 peut être utilisé pour prévenir ou minimiser cette apparition. Plusieurs avantages ont été trouvés d'utiliser la dilution du CO_2 lorsque l'enrichissement O_2 est appliqué et en particulier la diminution de la température dans le cylindre, considérée comme le principal facteur de survenue de cliquetis.

- L'enrichissement de l'oxygène peut être un atout pour l'utilisation de carburants alternatifs, en particulier ceux avec faible indice d'octane, permettant l'augmentation de la vitesse laminaire pour améliorer le rendement du moteur.

- Réaliser le concept réel de moteurs dé-carbonées à partir de la maitrise d'la concentration d'oxygène et de dilution par le CO2 par exemple. Ce travail sera effectué dans le projet ANR 'MACDOC' (Moteur à Allumage commande avec le taux d'Oxygène Contrôle). La technique membranaire de séparation de l'air sera évaluée afin d'évaluer l'application du moteur. Ce nouveau concept de dilution sera comparé avec les systèmes d'EGR traditionnels.

References

Abu-Qudais, M. (1996). "Exhaust gas temperature for knock detection and control in spark ignition engine." Energy Conversion and Management **37**(9): 1383-1392.

Babkin, V., A. V'yun, et al. (1967). "Determination of burning velocity from the pressure record in a constant-volume bomb." Combustion, Explosion, and Shock Waves **3**(3): 221-225.

Balusamy, S., A. Cessou, et al. (2011). "Direct measurement of local instantaneous laminar burning velocity by a new PIV algorithm." Experiments in fluids **50**(4): 1109-1121.

Baritaud, T. (1989). "Combustion and Fluid Dynamic Measurements in a Spark Ignition Engine: Effects of Thermochemistry and Velocity Field; Turbulent Flame Speeds." SAE Technical Paper (892098).

Bechtold, J. and M. Matalon (2001). "The dependence of the Markstein length on stoichiometry." Combustion and Flame **127**(1): 1906-1913.

Blint, R. J. (1986). "The relationship of the laminar flame width to flame speed." Combustion Science and Technology **49**(1-2): 79-92.

Blumenthal, R., K. Fieweger, et al. (1996). "Gas Dynamic Features of Self Ignition of Non Diluted Fuel/Air Mixtures at High Pressure." Combustion Science and Technology **113**(1): 137-166.

Boger M., V. D., Boughanem H. (1998). "DNS Analysis of FSD concept for LES of turbulent premixed combustion." Proceedings of the 27th Symposium (Int.) on Combustion, The Combustion Institute: pp.917-925.

Borghi, R. and D. Escudie (1984). "Assessment of a theoretical model of turbulent combustion by comparison with a simple experiment." Combustion and Flame **56**(2): 149-164.

Bougrine, S. (2012). 0-DIMENSIONAL MODELING of the COMBUSTION of ALTERNATIVE FUELS in SPARK IGNITION ENGINES. IFP Energies nouvelles, Laboratoire EM2C du CNRS et de l'ECP.

Bougrine, S., S. Richard, et al. (2011). "On the combination of complex chemistry with a 0-D coherent flame model to account for the fuel properties in spark ignition engines simulations: Application to methane-air-diluents mixtures." Proceedings of the Combustion Institute **33**(2): 3123-3130.

Boulouchos, K., T. Steiner, et al. (1994). Investigation of flame speed models for the flame growth period during premixed engine combustion, Society of Automotive Engineers.

Bradley, D., P. Gaskell, et al. (1996). "Burning velocities, Markstein lengths, and flame quenching for spherical methane-air flames: a computational study." Combustion and Flame **104**(1): 176-198.

Bradley, D., R. Hicks, et al. (1998). "The measurement of laminar burning velocities and Markstein numbers for Iso-octane–Air and Iso-octane–n-Heptane–Air mixtures at elevated temperatures and pressures in an explosion bomb." Combustion and Flame **115**(1): 126-144.

Brecq, G., J. Bellettre, et al. (2003). "A new indicator for knock detection in gas SI engines." International Journal of Thermal Sciences **42**(5): 523-532.

Buckmaster, J. (1977). "Slowly varying laminar flames." Combustion and Flame **28**: 225-239.

Caton, J. A. (2005). "Use of a cycle simulation incorporating the second law of thermodynamics: results for spark-ignition engines using oxygen enriched combustion air." SAE Technical Paper: 01-1130.

CITEPA (2010). Inventaire des émissions de polluants atmposphériques en France. Rapport national d'inventaire, www.citepa.org, 2010., CITEPA.

Clavin, P. (1985). "Dynamic behavior of premixed flame fronts in laminar and turbulent flows." Progress in Energy and Combustion Science **11**(1): 1-59.

Colin, O., A. Benkenida, et al. (2003). "3d Modeling of Mixing, Ignition and Combustion Phenomena in Highly Stratified Gasoline Engines." Oil & Gas Science and Technology - Rev. IFP **58**(1): 47-62.

Coombe, H. S. and S. Nieh (2007). "Polymer membrane air separation performance for portable oxygen enriched combustion applications." Energy Conversion and Management **48**(5): 1499-1505.

Curran, H., P. Gaffuri, et al. (2002). "A comprehensive modeling study of iso-octane oxidation." Combustion and Flame **129**(3): 253-280.

Dagaut, P., M. Reuillon, et al. (1993). "High pressure oxidation of liquid fuels from low to high temperature. 1. n-Heptane and iso-Octane." Combustion Science and Technology **95**(1-6): 233-260.

Damköhler, G. (1940). "Der einfluß der turbulenz auf die flammengeschwindigkeit in gasgemischen." Zeitschrift für Elektrochemie und angewandte physikalische Chemie **46**(11): 601-626.

Davidson, D. F., B. M. Gauthier, et al. (2005). "Shock tube ignition measurements of iso-octane/air and toluene/air at high pressures." Proceedings of the Combustion Institute **30**(1): 1175-1182.

Davidson, D. F., M. A. Oehlschlaeger, et al. (2002). "Shock tube measurements of iso-octane ignition times and OH concentration time histories." Proceedings of the Combustion Institute **29**(1): 1295-1301.

Davis, S. and C. Law (1998). Laminar flame speeds and oxidation kinetics of< i> iso</i>-octane-air and< i> n</i>-heptane-air flames. Symposium (International) on Combustion, Elsevier.

Descieux, D. and M. Feidt (2007). "One zone thermodynamic model simulation of an ignition compression engine." Applied Thermal Engineering **27**(8–9): 1457-1466.

Dooley, S. (2008). Galway, National University of Ireland,, . **Ph.D. dissertation**.

Dubreuil, A. (2008). Etude expérimentale du processus de combustion dans un moteur Diesel à accès optiques fonctionnant en charge homogène. Orleans, Orleans university. **doctorat**.

Ettefagh, M. M., M. H. Sadeghi, et al. (2008). "Knock detection in spark ignition engines by vibration analysis of cylinder block: A parametric modeling approach." Mechanical Systems and Signal Processing **22**(6): 1495-1514.

F.-A. Lafossas, O. Colin, et al. (2005). "Application of a New 1D Combustion Model to Gasoline Transient Engine Operation." SAE Technical Paper (2005-01-2107).

Favre, E., R. Bounaceur, et al. (2009). "A hybrid process combining oxygen enriched air combustion and membrane separation for post-combustion carbon dioxide capture." Separation and Purification Technology **68**(1): 30-36.

Ferguson, C., Ed. (1986). Internal combustion engines applied thermosciences, John Wylely & Sons.

Fieweger, K., R. Blumenthal, et al. (1994). "Shock-tube investigations on the self-ignition of hydrocarbon-air mixtures at high pressures." Symposium (International) on Combustion **25**(1): 1579-1585.

Fieweger, K., R. Blumenthal, et al. (1997). "Self-ignition of S.I. engine model fuels: A shock tube investigation at high pressure." Combustion and Flame **109**(4): 599-619.

Foucher, F. (2002). Etude expérimentale de l'interaction flamme-paroi: application au moteur à allumage commandé.

Freeh, J., K. Kumar, et al. (2004). "Laminar Flame Speeds of Preheated iso-Octane/Air and n-Decane/Air Flames Using Digital Particle Image Velocimetry."

Friedman, R. and W. C. Johnston (1950). "The Wall-Quenching of Laminar Propane Flames as a Function of Pressure, Temperature, and Air Fuel Ratio." Journal of Applied Physics **21**(8): 791-795.

Galloni, E. (2012). "Dynamic knock detection and quantification in a spark ignition engine by means of a pressure based method." Energy Conversion and Management **64**(0): 256-262.

Galmiche, B., F. Halter, et al. (2012). "Effects of high pressure, high temperature and dilution on laminar burning velocities and Markstein lengths of iso-octane/air mixtures." Combustion and Flame **159**(11): 3286-3299.

Gauthier, B. M., D. F. Davidson, et al. (2004). "Shock tube determination of ignition delay times in full-blend and surrogate fuel mixtures." Combustion and Flame **139**(4): 300-311.

Grandin, B., Denbratt, I., Bood, J., Brackmann, C. et al. (2000). "The Effect of Knock on the Heat Transfer in an SI Engine: Thermal Boundary Layer Investigation using CARS Temperature Measurements and Heat Flux Measurements." SAE Technical Paper (2000-01-2831).

Guezennec, Y. and W. Hamama (1999). "Two-Zone Heat Release Analysis of Combustion Data and Calibration of Heat Transfer Correlation in an I. C. Engine." SAE Technical Paper (1999-01-0218).

Gulder, Ö. L. (1983). "Laminar burning velocities of methanol, isooctane and isooctane/methanol blends." Combustion Science and Technology **33**(1-4): 179-192.

Gupta, M., S. Bell, et al. (1996). "An investigation of lean combustion in a natural gas-fueled spark-ignited engine." Journal of energy resources technology **118**(2).

Halstead, M. P., L. J. Kirsch, et al. (1977). "The autoignition of hydrocarbon fuels at high temperatures and pressures—Fitting of a mathematical model." Combustion and Flame **30**(0): 45-60.

Halter, F., T. Tahtouh, et al. (2010). "Nonlinear effects of stretch on the flame front propagation." Combustion and Flame **157**(10): 1825-1832.

Hasse, C., M. Bollig, et al. (2000). "Quenching of laminar iso-octane flames at cold walls." Combustion and Flame **122**(1–2): 117-129.

He, X., M. T. Donovan, et al. (2005). "An experimental and modeling study of iso-octane ignition delay times under homogeneous charge compression ignition conditions." Combustion and Flame **142**(3): 266-275.

He, X., B. T. Zigler, et al. (2006). "A rapid compression facility study of OH time histories during iso-octane ignition." Combustion and Flame **145**(3): 552-570.

Heywood, J. (1994). Combustion and its modeling in spark-ignition engines. International symposium COMODIA.

Heywood, J. B., Ed. (1988). Internal combustion engine fundamentals, McGraw-Hill International Editions.

Hong, C. and D. Chen (1997). "Direct measurements of in-cylinder integral length scales of a transparent engine." Experiments in fluids **23**(2): 113-120.

Huang, Y., C. Sung, et al. (2004). "Laminar flame speeds of primary reference fuels and reformer gas mixtures." Combustion and Flame **139**(3): 239-251.

Hudson, C., X. Gao, et al. (2001). "Knock measurement for fuel evaluation in spark ignition engines." Fuel **80**(3): 395-407.

IFP-EN (2008). IFP-Egine library. **Rev 8A**.

Jerzembeck, S., N. Peters, et al. (2009). "Laminar burning velocities at high pressure for primary reference fuels and gasoline: Experimental and numerical investigation." Combustion and Flame **156**(2): 292-301.

Kahandawala, M. S., S. A. Corera, et al. (2006). "Investigation of kinetics of iso-octane ignition under scramjet conditions." International journal of chemical kinetics **38**(3): 194-201.

Kajitani, S., E. Clasen, et al. (1993). "Partial-load and start-up operations of spark-ignition engine with oxygen enriched air."

Kajitani, S., E. Clasen, et al. (1993). "Partial-load and Start-up Operations of Spark-ignition Engine with Oxygen Enriched Air." SAE Technical Paper **932802**.

Kajitani, S., N. Sava, et al. (1992). A spark ignition engine operated by oxygen enriched air, Society of Automotive Engineers.

Karim, G. A. (2004). "A dimensionless criterion for predicting the onset of knock in spark ignition engine 2004." SAE Paper(2004-01-1992).

Kawahara, N., Tomita, E., and Roy, M. (2009). "Visualization of Autoignited Kernel and Propagation of Pressure Wave during Knocking Combustion in a Hydrogen Spark-Ignition Engine." SAE Technical Paper(2009-01-1773).

Kobayashi, H., T. Tamura, et al. (1996). Burning velocity of turbulent premixed flames in a high-pressure environment. Symposium (International) on Combustion, Elsevier.

Kolmogorov, A. N. (1941). Dissipation of energy in locally isotropic turbulence. Dokl. Akad. Nauk SSSR.

Komninos, N. P., D. T. Hountalas, et al. (2007). "A parametric investigation of hydrogen hcci combustion using a multi-zone model approach." Energy Conversion and Management **48**(11): 2934-2941.

Konig, G., R. R. Maly, et al. (1990). Role of exothermic centers on knock initiation and knock damage.

Koros, W. J. and R. T. Chern (1987). "Separation of gaseous mixtures using polymer membranes." Handbook of separation process technology: 862-953.

Kumar, K., J. Freeh, et al. (2007). "Laminar flame speeds of preheated iso-octane/O2/N2 and n-heptane/O2/N2 mixtures." Journal of propulsion and power **23**(2): 428-436.

Lafossas, F.-A., M. Castagne, et al. (2002). "Development and Validation of a Knock Model in Spark Ignition Engines Using a CFD code." SAE Technical Paper (2002-01-2701).

Lafossas, F., Castagne, M., Dumas, J., and Henriot, S. (2002). "Development and Validation of a Knock Model in Spark Ignition Engines Using a CFD code." SAE Technical Paper 2002-01-2701.

Landry, L. (2009). Experimental study of spark ignition engine mode under high pressure and high dilution. Laborary PRISME. Orléans, Orléans université. **Doctor**

Linse, D., C. Hasse, et al. (2009). "An experimental and numerical investigation of turbulent flame propagation and flame structure in a turbo-charged direct injection gasoline engine." Combustion Theory and Modelling **13**(1): 167-188.

Livengood, J. C. and P. C. Wu (1955). "Correlation of autoignition phenomena in internal combustion engines and rapid compression machines." Symposium (International) on Combustion **5**(1): 347-356.

Lounici, M. S., K. Loubar, et al. (2011). "Investigation on heat transfer evaluation for a more efficient two-zone combustion model in the case of natural gas SI engines." Applied Thermal Engineering **31**(2–3): 319-328.

Mallard, E. and H. L. Chatelier (1983). "Recherches sur la Combustion des MClanges Gazeux Explosifs." Annales des Mines **8ème Serie**: pp. 274.568.

Markstein, G. H. (1951). "Experimental and theoretical studies of flame front stability." J. Aero. Sci **18**: 199-209.

Matalon, M. and B. Matkowsky (1982). "Flames as gasdynamic discontinuities." Journal of Fluid Mechanics **124**(1): 239-259.

Mazas, A. N., B. Fiorina, et al. (2011). "Effects of water vapor addition on the laminar burning velocity of oxygen-enriched methane flames." Combustion and Flame **158**(12): 2428-2440.

Merola, S. S. and B. M. Vaglieco (2007). "Knock investigation by flame and radical species detection in spark ignition engine for different fuels." Energy Conversion and Management **48**(11): 2897-2910.

Metghalchi, M. and J. C. Keck (1982). "Burning velocities of mixtures of air with methanol, isooctane, and indolene at high pressure and temperature." Combustion and Flame **48**: 191-210.

Millo, F. a. F., C. (1998). "Knock in S.I. Engines: A Comparison between Different Techniques for Detection and Control." SAE Technical Paper(982477).

Minetti, R., M. Carlier, et al. (1996). "Comparison of oxidation and autoignition of the two primary reference fuels by rapid compression." Symposium (International) on Combustion **26**(1): 747-753.

Minetti, R., M. Ribaucour, et al. (1996). "Autoignition Delays of a Series of Linear and Branched Chain Alkanes in the Intermediate Range of Temperature." Combustion Science and Technology **113**(1): 179-192.

Mittal, G. (2006). A RAPID COMPRESSION MACHINE – DESIGN, CHARACTERIZATION, AND AUTOIGNITION INVESTIGATIONS, Case Western Reserve University.

Mittal, G. and C.-J. Sung (2008). "Homogeneous charge compression ignition of binary fuel blends." Combustion and Flame **155**(3): 431-439.

Mittal, G. and C.-J. Sung* (2007). "A RAPID COMPRESSION MACHINE FOR CHEMICAL KINETICS STUDIES AT ELEVATED PRESSURES AND TEMPERATURES." Combustion Science and Technology **179**(3): 497-530.

Mogi, K., K. Hashizume, et al. (1998). "Analysis and avoidance of pre-ignition in S.I. gasoline engines." JSAE Review **19**(1): 9-14.

Mounaïm-Rousselle, C., L. Landry, et al. (2013). "Experimental characteristics of turbulent premixed flame in a boosted Spark-Ignition engine." Proceedings of the Combustion Institute **34**(2): 2941-2949.

Müller, U. C., M. Bollig, et al. (1997). "Approximations for burning velocities and markstein numbers for lean hydrocarbon and methanol flames." Combustion and Flame **108**(3): 349-356.

Ng, H. K., R. R. Sekar, et al. (1993). The potential benefits of intake air oxygen enrichment in spark ignition engine powered vehicle, Society of Automotive Engineers.

Noda, T., K. Hasegawa, et al. (2004). "Development of Transient Knock Prediction Technique by Using a Zero-Dimensional Knocking Simulation with Chemical Kinetics." SAE Technical Paper (2004-01-0618).

Oehlschlaeger, M., D. Davidson, et al. (2004). "Shock tube measurements of branched alkane ignition times and OH concentration time histories." International journal of chemical kinetics **36**(2): 67-78.

Peters, N. (1988). Laminar flamelet concepts in turbulent combustion. Symposium (International) on Combustion, Elsevier.

Peters, N. (1999). "The turbulent burning velocity for large-scale and small-scale turbulence." Journal of Fluid Mechanics **384**(1): 107-132.

Petersen, E., M. Lamnaouer, et al. (2007). 26th International Symposium on Shock Waves. Goettingen.

Poinsot, T., D. Veynante, et al. (1991). Diagrams of premixed turbulent combustion based on direct simulation. Symposium (International) on Combustion, Elsevier.

Poinsot, T., D. Veynante, et al. (1991). "Quenching processes and premixed turbulent combustion diagrams." Journal of Fluid Mechanics **228**(561-606): 230.

POOLA, R. B., et al. (1995). Utilizing Intake-Air Oxygen-Enrichment Technology to Reduce Cold-Phase Emissions. New York, NY, ETATS-UNIS, Society of Automotive Engineers.

Poola, R. B., H. K. Ng, et al. (1995). Utilizing intake-air oxygen-enrichment technology to reduce cold-phase emissions, Argonne National Lab., IL (United States).

Poola, R. B., R. Sekar, et al. (1996). The effects of oxygen-enriched intake air on FFV exhaust emissions using M85, Argonne National Lab., IL (United States).

Poola, R. B., K. C. Stork, et al. (1998). "Variable Air Composition with Polymer Membrane–A New Low Emissions Tool." SAE Paper **980178**.

Powling, J. (1949). "A new burner method for the determination of low burning velocities and limits of inflammability." Fuel **28**(2): 25-28.

Quader, A. (1978). "Exhaust Emissions and Performance of a Spark Ignition Engine Using Oxygen Enriched Intake Air." Combustion Science and Technology **19**(1-2): 81-86.

Rahmouni, C., G. Brecq, et al. (2004). "Knock rating of gaseous fuels in a single cylinder spark ignition engine." Fuel **83**(3): 327-336.

Rakopoulos, C. D. and C. N. Michos (2008). "Development and validation of a multi-zone combustion model for performance and nitric oxide formation in syngas fueled spark ignition engine." Energy Conversion and Management **49**(10): 2924-2938.

Rakopoulos, C. D., C. N. Michos, et al. (2008). "Availability analysis of a syngas fueled spark ignition engine using a multi-zone combustion model." Energy **33**(9): 1378-1398.

Richard, S., S. Bougrine, et al. (2009). "On the reduction of 3D CFD combustion model to build a physical 0D model for simulating heat release, knock and pollutants in SI engines." Oil & Gas Science and Technology - Rev. IFP **64**(3): 223-242.

Richard, S., O. Colin, et al. (2007). "Towards large eddy simulation of combustion in spark ignition engines." Proceedings of the Combustion Institute **31**(2): 3059-3066.

Ryan, T. W. and S. S. Lestz (1980). "The laminer burning velocity of isooctane, n-heptane, methanol, methane and propane at elevated temperature and pressures in the presence of a diluent." SAE Paper(800103).

Saikaly, K., O. Le Corre, et al. (2010). "Preventive knock protection technique for stationary SI engines fuelled by natural gas." Fuel Processing Technology **91**(6): 641-652.

Sakai, Y., H. Ozawa, et al. (2007). "Effects of Toluene Addition to Primary Reference Fuel at High Temperature." SAE Technical Paper **2007-01-4104**.

Scott, S. G. (2009). "A chemical kinetically based ignition delay correlation for iso-octane covering a wide range of conditions including the NTC region." Combustion and Flame **156**(6): 1248-1262.

Shen, H.-P. S., J. Vanderover, et al. (2008). "A shock tube study of iso-octane ignition at elevated pressures: The influence of diluent gases." Combustion and Flame **155**(4): 739-755.

Sivashinsky, G. (1977). "Nonlinear analysis of hydrodynamic instability in laminar flames—I. Derivation of basic equations." Acta Astronautica **4**(11): 1177-1206.

Soylu, S. (2005). "Prediction of knock limited operating conditions of a natural gas engine." Energy Conversion and Management **46**(1): 121-138.

Spalding, D. (1955). "some fundamentals of combustion."

Tahtouh, T., F. Halter, et al. (2009). "Measurement of laminar burning speeds and Markstein lengths using a novel methodology." Combustion and Flame **156**(9): 1735-1743.

Tanaka, S., F. Ayala, et al. (2003). "Two-stage ignition in HCCI combustion and HCCI control by fuels and additives." Combustion and Flame **132**(1–2): 219-239.

Trapy, J. (1981). "Transferts thermiques dans les moteur à combustion interne, measure et modélisation." Revue Générale de Thermique **Vol. 233**.

Van Blarigan, A., R. Seiser, et al. (2012). "Working fluid composition effects on methane oxycombustion in an SI-engine: EGR vs. CO_2." Proceedings of the Combustion Institute.

Vanhove, G., G. Petit, et al. (2006). "Experimental study of the kinetic interactions in the low-temperature autoignition of hydrocarbon binary mixtures and a surrogate fuel." Combustion and Flame **145**(3): 521-532.

Verhelst, S. and C. G. W. Sheppard (2009). "Multi-zone thermodynamic modelling of spark-ignition engine combustion – An overview." Energy Conversion and Management **50**(5): 1326-1335.

Vermeer, D. J., J. W. Meyer, et al. (1972). "Auto-ignition of hydrocarbons behind reflected shock waves." Combustion and Flame **18**(3): 327-336.

Walton, S. M., X. He, et al. (2007). "An experimental investigation of iso-octane ignition phenomena." Combustion and Flame **150**(3): 246-262.

Williams, F. A. (1974). "A review of some theoretical considerations of turbulent flame structure." Agard Conference Proceeding: N°164.

Winklhofer, E. (2009). Self Ignition and Irregular Combustion Events in SI engines. Graz Austria, AVL List GmbH.

Wirth, M. (1993). Die turbulente flammenausbreitung im ottomotor und ihre charakteristischen längenskalen. RWTH Aachen.

Wu, Y.-Y. and K. D. Huang (2007). Improving the Performance of a Small Spark-Ignition Engine by Using Oxygen-Enriched Intake Air. Proceedings of the 2007 Small Engine Technology Conference, Society of Automotive Engineers, Niigata, Japan.

Würmel, J., E. J. Silke, et al. (2007). "The effect of diluent gases on ignition delay times in the shock tube and in the rapid compression machine." Combustion and Flame **151**(1–2): 289-302.

Yahyaoui, M., N. Djebaïli-Chaumeix, et al. (2007). "Experimental and modelling study of gasoline surrogate mixtures oxidation in jet stirred reactor and shock tube." Proceedings of the Combustion Institute **31**(1): 385-391.

Yu, G., C. Law, et al. (1986). "Laminar flame speeds of hydrocarbon+ air mixtures with hydrogen addition." Combustion and Flame **63**(3): 339-347.

Zhen, X., Y. Wang, et al. (2012). "The engine knock analysis – An overview." Applied Energy **92**(0): 628-636.

Zheng, J. and J. A. Caton (2012). "Use of a single-zone thermodynamic model with detailed chemistry to study a natural gas fueled homogeneous charge compression ignition engine." Energy Conversion and Management **53**(1): 298-304.

Zhou, J. X., M. Cordier, et al. (2011). "Experimental estimate of the laminar burning velocity of iso-octane in oxygen-enriched and CO_2-diluted air." Combustion and Flame **158**(12): 2375-2383.

Zhu, D., F. Egolfopoulos, et al. (1989). Experimental and numerical determination of laminar flame speeds of methane/(Ar, N< sub> 2</sub>, CO< sub> 2</sub>)-air mixtures as function of stoichiometry, pressure, and flame temperature. Symposium (International) on Combustion, Elsevier.

6 ANNEXES

The theoretical operation of the 4-stroke SI engine is based on the Beau de Rochas cycle. It includes four phases as following:

a. Intake stroke

The first stroke of the SI engine is also known as the suction stroke because the piston moves from TDC to BDC (downward direction in the cylinder) creating depression in the cylinder. The inlet valve opens as a result of piston movement, and the vaporized fuel mixture enters the combustion chamber. The inlet valve closes at the end of this stroke.

Gas velocities are rather high (the speed of sound can be achieved by passage of the valve) and the inertia of the gas cannot be neglected. Because of this and also because there are losses on the induction system, the cylinder filling is not achieved completely: the filling of a natural motor is less than unity. To improve this rate, the inertia of the gas is taken into account by advancing the opening the intake valve before TDC. These offsets are a few degrees and the importance depends on the range of engine operating regime. Regardless of the inlet pressure in the intake system, the amount of mixture allowed depends on the throttle opening, which also determines the pressure upstream valves. The engine load is related to the intake pressure.

b. Compression stroke

In this stroke, both valves are closed and the piston starts its movement to the minimum volume position (upward direction in the cylinder) and compresses the fuel mixture. The pressure in the cylinder increases without combustion, they expect fully open from 10 to 20 bar at TDC, as the compression ratio. Ignition occurs few moments before TDC (10 to 40 V) to take into account the time necessary for the development of combustion. The direct injection engines perform their partial charges by adjusting the amount of fuel injected, which means that in the combustion chamber, the load distribution is heterogeneous so that locally a small amount of fuel may be associated with a small amount of air and the mixture is combustible. The design and aerodynamics of internal chambers combustion determine the formation of the mixture and its location, which must also be close to a spark plug. The full costs are obtained against returning to a homogeneous charge filling the entire volume of the cylinder.

c. Power stroke

The spark plug ignites the fuel mixture and burns when the piston reaches the minimum volume position. The fuel produces power that is transmitted to the crank shaft mechanism. The combustion pressure is growing rapidly and normally reaches its highest value at ten degrees of crank ankle; the gases are very hot at that time (2000 to 3000 K) so that heat transfer of the walls is intense. The piston then descends to the PMB, pressure and gas temperature decrease at the same time, the work is provided to the piston. The expansion ratio is critical to performance.

d. Exhaust stroke

In the end of the power stroke, the exhaust valve opens. During this stroke, the piston starts its movement to the minimum volume position. The open exhaust valve allows the exhaust gases to escape the cylinder. At the end of this stroke, the exhaust valve closes, the inlet valve opens, and the sequence repeats in the next cycle. Four stroke engines require two revolutions. To account for the inertia of the gases, the exhaust can be opened somewhat before the BDC and close after TDC. There may be few and moments during which the intake and exhaust are open simultaneously, this is called the valve overlap. It is particularly important that the engine works at high speed.

The cycle described above is often represented as a diagram. This diagram named Clapeyron diagram is a representation of states of a fluid through curves which giving the fluid pressure in terms of its volume. The area enclosed by the abscissa of the curve and two points in the evolution of fluid is the working fluid during processing. The blue surface in ***Figure 6-1*** corresponds to a part of the engine work. The engine work is given by

$$W_{i\_cyl} = -\int P_{cyl}\, d\, V_{cyl} \qquad \text{Equation 6-1}$$

Where the left term is called the indicated work, which is measured firstly by Watt using steam engine and the recorder is called Watt indicator. In the right term, P_{cyl} is the in-cylinder pressure, and V_{cyl} is the cylinder volume.

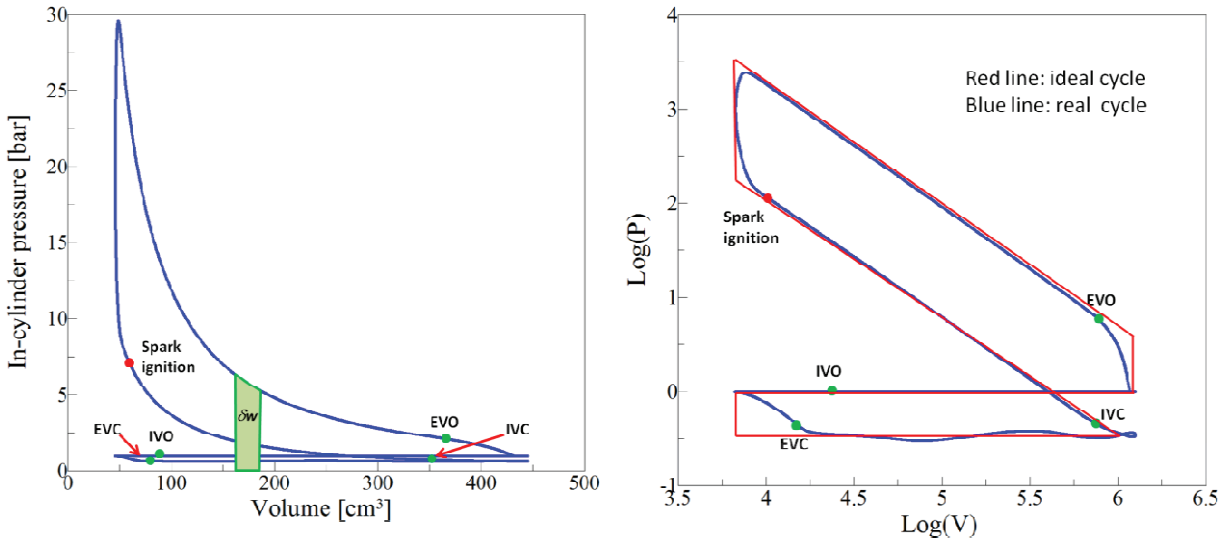

Figure 6-1. An example of Clapeyron diagram with operating conditions as: engine speed 1400 rpm, Pintake = 0.6 bar, Spark advance = 21 CAD

Normally, the engine work is expressed negative, because the energy of in-cylinder system decreases. This energy is than transformed to mechanical energy to provide vehicle running. Thus inversely, as viewed from the crankshaft, the work can be considered as positive when the energy of in-cylinder system decreases, because the crankshaft receives the energy. As showed in the above figure, the pink surface corresponds to the high loop pressure; it represents the work done by the engine. The orange area is the low loop pressure; it is the necessary work to introduce the fresh mixture into the cylinder. The right hand of figure 1.3

represents a real engine cycle and its cycle envelope using a Clapeyron diagram in which the charges are considered as isochors and polytropic.

Engine efficiencies and energy losses

As viewed from the crankshaft, the work can be considered as positive when the energy of in-cylinder system decreases, because the crankshaft receives the energy, then the equation (2.2) can be expressed as:

$$W_i = \int P_{cyl}\, d\, V_{cyl}$$

The thermal work is the energy which the fuel delivers theoretically by complete combustion, and it can be expressed:

$$W_{th} = 1000.M_C.PCI$$

Where M_C is mass of the fuel introduced per engine cycle, and PCI is fuel heating value. The effective work $W_e$is deduced by:

$$W_e = 4\pi C$$

Where C is the engine torque. Several parameters are introduced to express different engine energy efficiency.

- Theoretical thermal efficiency of the spark ignition engine can be deduced from Beau de Rochas cycle, which supposes that the admission and exhaust strokes are isobaric, the combustion take place at constant volume, and the compression and power stroke are considered as adiabatic. Thus the thermal efficiency can be expressed by dividing the work supplied by the system to the combustion heat release:

  $$\eta_{thth} = \frac{W_{thth}}{W_{th}} = 1 - \frac{1}{\tau^{\gamma-1}}$$

  Where W_{tot} is the thermal work supplied theoretically by the system, Q_{comb}^{th} is the combustion heat release with the constant volume assumption, τ is the compression ratio, and $\gamma = C_P/C_v$ is the adiabatic constant.
- Indicated efficiency is the ratio of the indicated work to the theoretical thermal work of the fuel:

  $$\eta_i = \frac{W_i}{W_{th}}$$
- Mechanical efficiency is the ratio of the effective work to the indicated work:

  $$\eta_m = \frac{W_e}{W_i}$$

  This parameter characterizes the mechanical losses by friction and the energy expended by the auxiliary.
- Global efficiency is expressed as the ratio of the effective work to the theoretical thermal work:

  $$\eta_g = \frac{W_e}{W_{th}}$$
- Combustion efficiency is the ratio between the total energy released in the form of useful heat or work during the combustion and the theoretical thermal work:

  $$\eta_c = \frac{Q}{W_{th}}$$

  This efficiency is calculated specially from the exhaust gas analysis.
- 'Rendement de forme' is the ratio of the indicated work to the theoretical thermal work of the theoretical cycle:

  $$\eta_f = \frac{W_i}{W_{thth}}$$

It characterizes the difference between the cycle which could be realized theoretically and the cycle actually realized by engine, due to pumping losses of the gas stream, wall heat loses, the inertia of the gas columns, and the pressure wave in the pipes etc…

Thus, the relation among these efficiencies can be expressed:

$$\eta_g = \eta_i \times \eta_m$$
$$\eta_i = \eta_{thth} \times \eta_f$$

Engine puissance, specific fuel consummation and mean pressure indicators

Indicated puissance is defined by dividing the indicated work by the time required to complete a cycle engine.

$$P_i = W_i . N/120$$

Where P_i is the indicated puissance, N is engine rotation speed with the unit of round per minute. Similarly, the effective puissance is expressed:

$$P_e = W_e . \frac{N}{120} = C_e . \omega$$

ω is rotation speed in rad/s, C_e is effective engine torque, normally it is measured by engine test bench.

Specific fuel consummation is noted in grams of fuel per kilowatt per hour (g/kW/h). The lower it is the better fuel chemical energy transforms into mechanical energy. There are two kinds of specific fuel consummations:

a. Effective specific consummation: $Esc = \frac{consummation\ (g/h)}{P_e\ (kW)}$, where consummation of fuel can be measured by mass flow meter
b. Indicated specific consummation: $Isc = \frac{consummation\ (g/h)}{P_i\ (kW)}$

Indicated mean pressure is the average pressure produced in the combustion chamber during the operating cycle. It is calculated by:

$$IMEP = \frac{W_i}{V_d} = \frac{1}{V_d} \oint_{cycle} P_{cyl} \, . \, dV_{cyl}$$

Where V_d is the displaced volume of the cylinder. It represents a constant pressure that should be applied on the piston to obtain the indicated work. Then indicated engine torque can be expressed by:

$$C_i = \frac{W_i . n_{cyl}}{4\pi} = \frac{MIP . V_d . n_{cyl}}{4\pi}$$

Where n_{cyl} is the number of cylinders. Friction torque then can be defined by C_i and C_e:

$$C_{fr} = C_i - C_f$$

By analogy with IMP, mean effective pressure can be expressed as:

$$MEP = \frac{C_e . 4\pi}{V_d . n_{cyl}}$$

Then the mean fictive pressure can be defined by:

$$MFP = IMP - MEP$$

Etude de l'impact du taux d'oxygène sur la combustion en moteur à allumage commandé downsizé

Aujourd'hui, les constructeurs automobiles continuent de chercher les technologies renouvelables face à la pénurie d'énergie et les problèmes d'émission de polluants. Un moyen important pour optimiser l'économie de carburant et réduire les émissions polluantes des moteurs à allumage commandés est le concept 'downsizing'. Cependant, ce concept est limité par le phénomène de cliquetis du aux conditions de haute température et haut pression.
Dans cette étude, le contrôle de la concentration d'oxygène dans l'air est proposé. Car d'une part, la combustion enrichie en oxygène permet d'améliorer la densité de puissance de moteur avec le même niveau de pression d'admission. Cela permet soit de 'booster' la combustion pour augmenter la puissance du moteur ou de l'activer lorsque le moteur fonctionne à faible charge ou dans des conditions de démarrage à froid. D'autre part, une faible concentration en oxygène dans l'air (ou dilution de N_2) par un système membranaire peut être considérée comme une alternative à la recirculation des gaz d'échappement.
Les expériences ont été effectuées dans un moteur monocylindre 'downsizing' avec différents taux d'oxygène et richesse. L'étude de l'impact du contrôle de la concentration d'oxygène sur les caractéristiques de combustion et d'émissions a été effectuée pour plusieurs charges en fonctionnement optimum pour limiter la consommation spécifique de carburant.
L'effet de la concentration en oxygène sur les caractéristiques de combustion du moteur a été simulé en utilisant le logiciel commercial AMESim avec le modèle de combustion développé par IFP-EN. En mettant en œuvre des corrélations de la vitesse de combustion laminaire, déterminées au préalable durant ce travail, et délai d'auto-inflammation, les pressions dans les cylindres sont parfaitement calibrés avec une erreur maximale inférieure à 2% et l'intensité du cliquetis a pu être prédite.

Mot clés : moteurs à allumage commandé, downsizing, cliqutis, combustion enrichie en oxygène, vitesse de combustion laminaire, délai d'auto-inflammation, AMESim.

The study of the oxygen controlled combustion in downsized SI engine

Nowadays, car manufacturers continue to lead researches on new technologies facing to the energy shortage and pollutant emission problems. A major way to optimise fuel economy and reduce pollutant emissions for Spark-Ignition (SI) engines is the downsizing concept. However, this concept is unfortunately limited by 'knock' phenomena (abnormal combustion) due to high temperature and high pressure in-cylinder conditions.
In the present study, control the oxygen concentration in air is proposed. Indeed, on the one hand, oxygen-enriched combustion can improve engine power density with the same intake pressure level. Thus, oxygen-enriched combustion can be used either as a booster to increase engine output or as a combustion enhancer when the engine operates at low loads or in cold start conditions. On the other hand, low oxygen concentration in air (or N_2 dilution) can be considered as an alternative to exhaust gas recirculation (EGR).
The experiments were carried out in a downsized single-cylinder SI engine with different rates of oxygen and equivalence ratios. The study of the impact of controlling oxygen concentration on the combustion characteristics and emissions was performed at several loads by optimizing the spark advance and the intake pressure to maintain the load and obtain a minimum value of indicated Specific Fuel Consumption (SFC).
The effect of oxygen concentration on the engine combustion characteristics was simulated by using the commercial software AMESim, with the combustion model developed by IFP-EN. By implementing correlations for the laminar burning velocity, determined previously during this study, and auto-ignition delay data base, the in-cylinder pressures were perfectly calibrated with a maximum pressure relative error less than 2%, and the knock intensity was predicted.

Keywords: Spark-Ignition engines, downsizing, oxygen-enriched combustion, exhaust gas recirculation, knock, laminar burning velocity, auto-ignition delay, AMESim.

Service: DINQ/DRIA/SARA/STEO/PCEL
2 Route de Gizy
78943 Vélizy Vilacoublay

8 rue Léonard de Vinci
75072 Orléans Cedex 2